TÉCNICO LISBOA

**UNIVERSIDADE DE LISBOA**

**INSTITUTO SUPERIOR TÉCNICO**

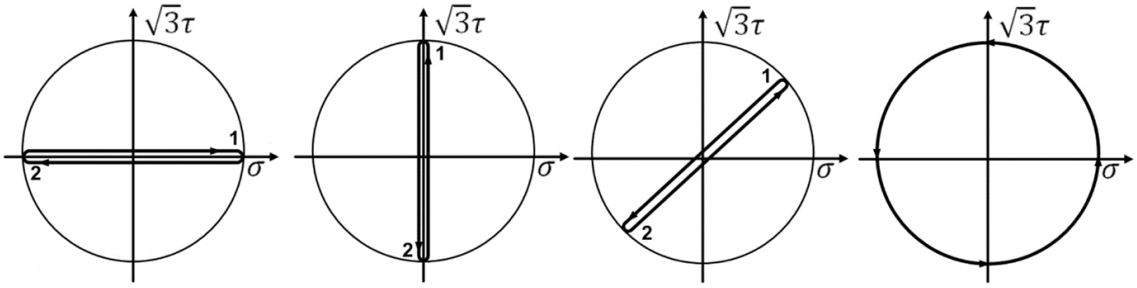


# Multiaxial Fatigue

## Damage Analysis of Complex Loading Paths

**Vitor Manuel Rodrigues Anes**

**Supervisor**: **Doctor** Luís Filipe Galrão dos Reis
**Co-Supervisor**: **Doctor** Manuel José Moreira de Freitas

Thesis approved in public session to obtain the PhD Degree in
**Mechanical Engineering**

**Jury final classification: Pass with Distinction**

**Jury**

**Chairperson:** Chairman of the IST Scientific Board
**Members of the Committee:**
**Doctor** Paulo Manuel Salgado Tavares de Castro
**Doctor** José Domingos Moreira da Costa
**Doctor** Nuno Manuel Mendes Maia
**Doctor** Luís Filipe Galrão dos Reis

**2015**

TÉCNICO LISBOA

**UNIVERSIDADE DE LISBOA**
**INSTITUTO SUPERIOR TÉCNICO**

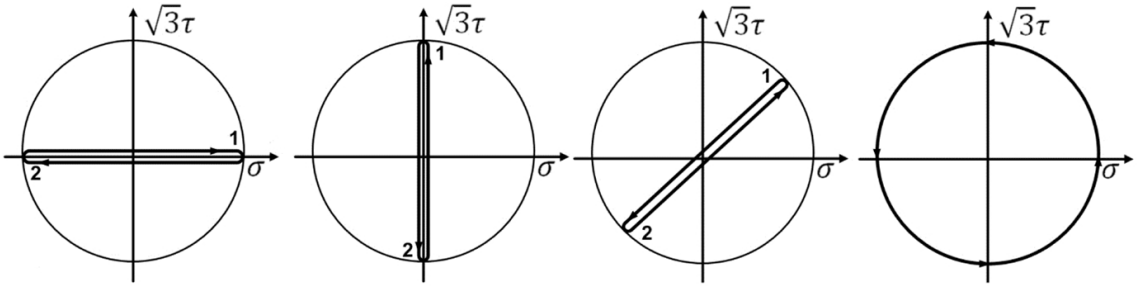


# Multiaxial Fatigue

## Damage Analysis of Complex Loading Paths

**Vitor Manuel Rodrigues Anes**

**Supervisor**: **Doctor** Luís Filipe Galrão dos Reis
**Co-Supervisor**: **Doctor** Manuel José Moreira de Freitas

Thesis approved in public session to obtain the PhD Degree in
**Mechanical Engineering**

**Jury final classification: Pass with Distinction**

**Jury**

**Chairperson:** Chairman of the IST Scientific Board
**Members of the Committee:**
**Doctor** Paulo Manuel Salgado Tavares de Castro, Professor Catedrático da Faculdade de Engenharia, da Universidade do Porto
**Doctor** José Domingos Moreira da Costa, Professor Associado (com Agregação) da Faculdade de Ciências e Tecnologia, da Universidade de Coimbra
**Doctor** Nuno Manuel Mendes Maia, Professor Associado (com Agregação) do Instituto Superior Técnico, da Universidade de Lisboa
**Doctor** Luís Filipe Galrão dos Reis, Professor Associado do Instituto Superior Técnico, da Universidade de Lisboa

**2015**

*To my Shining Stars*

***Ana, Raquel, and João***

*If any of you lack wisdom, let him ask of God, that giveth to all men liberally, and upbraideth not; and it shall be given him.*

*James 1:5*

*The Holy Bible, King James version.*

# Multiaxial Fatigue

Damage analysis of complex loading paths

**Vitor Manuel Rodrigues Anes**

## Abstract

This thesis proposes a new set of models to improve multiaxial fatigue characterization. The research main objective was to create physical based methodologies to characterize multiaxial fatigue damage under random loading conditions, which is one of the greatest challenges in multiaxial fatigue life assessment. To achieve this goal, five interconnected criteria were developed in this work, namely a cyclic elastic-plastic model, a non-proportional sensitivity parameter, a new equivalent shear stress, a new multiaxial cycle counting method, and a fatigue crack initiation model. Series of fatigue tests were performed to characterize two different materials, i.e. an high-strength steel (42CrMo4) and a magnesium alloy (AZ31B-F), in order to scrutinize their multiaxial fatigue behaviour, including crack initiation planes under proportional and non-proportional loading conditions. Regarding other types of loading such as asynchronous, sequential, variable amplitude, mean stress, and stress gradients, it was used a third-party fatigue data collected from literature. The methods developed here were correlated with state-of-the-art criteria and with experimental data. Based on the achieved results it can be concluded that the proposed methods are easy to implement, easy to understand, and have improved results comparatively to the state-of-the-art criteria.

**Keywords:** Multiaxial random fatigue, Fatigue damage, Fatigue life assessment, Multiaxial cycle counting, Loading paths, Equivalent shear stress, Non-proportionality, Cyclic plasticity, Multiaxial elastic-plastic model, Fatigue crack initiation.

# Fadiga Multiaxial

Análise de dano em histórias de carregamento complexas

**Vitor Manuel Rodrigues Anes**

## Resumo

Esta tese propõe um novo conjunto de modelos para melhorar a caracterização e avaliação do dano em fadiga multiaxial. Ao logo deste trabalho foram criadas metodologias de modo a caracterizar vários fenómenos presentes em fadiga multiaxial sob condições de carregamento aleatórios, sendo este um dos actuais desafios em fadiga multiaxial. Para isso, foram desenvolvidos neste trabalho cinco critérios interligados, nomeadamente um modelo de plasticidade cíclica, um parâmetro de sensibilidade não-proporcional, uma nova tensão equivalente, um novo método de contagem de ciclos em fadiga multiaxial e um modelo de previsão de iniciação de fissuras por fadiga. Foram realizados testes de fadiga multiaxial num aço de alta resistência (42CrMo4) e numa liga de magnésio (AZ31B-F) a fim de caracterizar e avaliar o seu comportamento á fadiga sob cargas cíclicas assim como os seus planos de iniciação de fissura sob diferentes condições de carga, nomeadamente carregamentos proporcionais e não proporcionais. Para outro tipo de carregamentos, tais como, carregamentos assíncronos, sequenciais, amplitude variável e carregamentos com gradiente de tensões e tensão média, os dados experimentais foram obtidos a partir da literatura. As estimativas dos métodos propostos foram correlacionadas com as dos modelos usados na literatura e com os dados experimentais. A partir dos resultados obtidos pode-se concluir que os métodos propostos são fáceis de implementar, fáceis de entender e têm melhor estimativas de vida á fadiga, comparativamente ao desempenho encontrado nos critérios disponíveis na literatura.

**Palavras chave:** Fadiga multiaxial aleatória, Dano por fadiga, Avaliação de vida a fadiga, Contagem multiaxial de ciclos, Histórias de carregamento, Tensão equivalente de corte, Não-proporcionalidade, Plasticidade cíclica, Modelo multiaxial elastoplástico.

# Acknowledgements

I would like to thank my advisor, Dr. Luis Reis, who has believed in my capability to go forward until the end of this journey. His guidance, encouragement and continuous support through the course of this work was a driven force that pushed me forward in calm and turbulent times.

I also would like to thank to my co-advisor, Dr. Manuel Freitas, for his time and valuable advices. His comments are valuable information that does not come in books; they helped me to interpret the scientific language of multiaxial fatigue and to identify the milestones of this work.

This dissertation could not be done without the support of my advisors, to them my deepest appreciation.

I want to thank Yoann Lage for his friendship, encouragement, and support in the vibration tests at the vibration lab of the DEM-IST, with emphasis on technical and practical aspects, as well as in some theoretical aspects.

I want to thank Mr. Pedro Alves, technician of the (LTO) laboratory of the DEM-IST, for the time and effort; their support and willingness to help in the experimental tests was much appreciated.

I would like to thank my colleagues at the mechanical department of the Instituto Superior Técnico at Lisbon University for their friendship, companionship, and support.

Finally, I would like to thank my family for all their support and encouragement throughout this journey.

# Agradecimentos

Quero de agradecer ao meu orientador, Dr. Luis Reis, que acreditou na minha capacidade de seguir em frente até o final desta jornada. A sua orientação, incentivo e apoio contínuo ao longo do curso deste trabalho foram uma força impulsionadora que me motivaram a seguir em frente tanto em tempos calmos como em turbulentos.

Quero também agradecer ao meu co-orientador, Dr. Manuel Freitas, pelo o seu tempo e conselhos valiosos. Os seus comentários foram e são sabedoria que não vem nos livros, ajudaram-me a interpretar a linguagem do mundo da fadiga multiaxial e a identificar quais os caminhos que deveria seguir para levar a bom porto este trabalho.

Esta dissertação não poderia ter sido feita sem o apoio de meus orientadores, para eles o meu profundo apreço.

Quero agradecer ao Yoann Lage pela sua amizade, encorajamento e apoio no laboratório de vibrações do DEM-IST, com particular ênfase em aspectos técnico-práticos assim como em alguns aspectos teóricos.

Ao Sr. Pedro Alves do laboratório de técnicas oficinais (LTO) do DEM-IST, pelo seu tempo e esforço, o seu apoio e vontade de ajudar nos testes experimentais foram muito apreciados.

Aos meus colegas do departamento de engenharia mecânica do Instituto Superior Técnico da Universidade de Lisboa pela sua amizade, companheirismo e apoio.

Finalmente, agradeço à minha família por todo o apoio e incentivo ao longo desta jornada.

# Contents

# List of Figures

# List of Tables

# Publications

Author's publications in peer reviewed journals and international conference proceedings that are related with the research work developed in this thesis.

## Peer reviewed journals

1. V. Anes, L. Reis, M. de Freitas, "Random accumulated damage evaluation under multiaxial fatigue loading conditions", Fracture and Structural Integrity 2015, vol. 33, pp. 309-318.

2. Vitor Anes, Luis Reis, Manuel Freitas, "Asynchronous Multiaxial Fatigue Damage Evaluation", Procedia Engineering 2015, vol. 101, pp. 421-429.

3. Vitor Anes, Luis Reis, Manuel Freitas, "Multiaxial Fatigue Damage Accumulation under Variable Amplitude Loading Conditions". Procedia Engineering 2015, vol. 101, pp. 117-125.

4. V. Anes, L. Reis, B. Li, M. de Freitas, "Evaluation of the AZ31 cyclic elastic-plastic behaviour under multiaxial loading conditions", Fracture and Structural Integrity 2014, vol. 30, pp. 282-292.

5. V. Anes, L. Reis, B. Li, M. Fonte, M. de Freitas, "New approach for analysis of complex multiaxial loading paths". International Journal of Fatigue 2014, vol. 62, pp. 21-33.

6. V. Anes, L. Reis, B. Li, M. Freitas, "Crack path evaluation on HC and BCC microstructures under multiaxial cyclic loading". International Journal of Fatigue 2014, vol. 58, pp. 102-113.

7. Anes V, Reis L, Li B, Freitas M, Sonsino C. "Minimum circumscribed ellipse (MCE) and stress scale factor (SSF) criteria for multiaxial fatigue life assessment". Theoretical and Applied Fracture Mechanics 2014, vol. 73, pp. 109–19.

8. Anes V, Reis L, Li B, Freitas M. "New approach to evaluate non-proportionality in multiaxial loading conditions". Fatigue & Fracture of Engineering Materials & Structures 2014, vol. 37, pp. 1338–54.

9. Anes V, Reis L, Li B, de Freitas M. "New cycle counting method for multiaxial fatigue". International Journal of Fatigue 2014, vol. 67, pp. 78–94.

10. Anes V, Reis L, de Freitas M. "A new criterion for evaluating multiaxial fatigue damage under multiaxial random loading conditions". Advanced Materials Research 2014, vol. 891, pp. 1360–1365.

11. Reis L, Anes V, de Freitas M. "AZ31 magnesium alloy multiaxial LCF behavior: theory, simulation and experiments". Advanced Materials Research 2014, vol. 891, pp. 1366–1371.

12. L. Reis, V. Anes and M. Freitas, "Loading cycle analysis regarding multiaxial fatigue life assessment", Structural integrity and life 2014, vol. 14, pp. 177-183.

13. L. Reis, V. Anes, B. Li, and M. de Freitas, "Characterizing the cyclic behaviour of extruded AZ31 magnesium alloy". Materials Science Forum 2013, vol. 730, pp. 727–732.

14. L. Reis, V. Anes, B. Li, and M. de Freitas, "Effect of non-proportionality in the fatigue strength of 42CrMo4 steel". Materials Science Forum 2013, vol. 730, pp. 757–762.

15. L. Reis, V. Anes, B. Li, and M. de Freitas, "Damage accumulation due to sequential loading effect". Procedia Engineering 2011, vol. 10, pp. 1396–1401.

16. Luis Reis, Vítor Anes, Bin Li, Manuel Freitas,"Efeito da sequência de cargas axial e de torção na previsão de vida em fadiga multiaxial". APAET Mecânica Experimental 2011, Vol 19, pp. 1-7.

## Conference proceedings

1. L. Reis, V. Anes and M. Freitas, "Fatigue damage under complex multiaxial loading conditions", XIV Portuguese Conference on Fracture, Régua, Portugal 2014.

2. Manuel Freitas, Luis Reis, and Vitor Anes, "AZ31 Magnesium alloy elastoplastic behavior under multiaxial loading conditions", 1st Cluster workshop in materials and nanotechnology book of abstracts, Lisbon, Portugal 2013.

3. V. Anes, L. Reis, B. Li and M. Freitas, "The critical aspect of cycle's definition in multiaxial fatigue conditions",The Tenth International Conference on Multiaxial Fatigue & Fracture (ICMFF10), Kyoto, Japan 2013.

4. V. Anes, L. Reis, B. Li and M. Freitas, "Multiaxial fatigue behaviour (HCF and LCF) of AZ31 magnesium alloy", The Tenth International Conference on Multiaxial Fatigue & Fracture (ICMFF10), Kyoto, Japan 2013.

5. Vitor Anes, Luis Reis, Bin Li, M. de Freitas, "Az31 magnesium alloy plasticity behaviour on a Crack initiation Process under multiaxial loading conditions", International Conference Materiais 2013 book of abstracts, Coimbra, Portugal 2013.

6. V. Anes, L. Reis, B. Li and M. Freitas, "The shear stress space influence in multiaxial fatigue life evaluation", 13th International Conference on New Trends in Fatigue and Fracture (NT2F13), Moscow, Russia 2013.

7. V. Anes, L. Reis, B. Li, M. Fonte, and M. Freitas, "A new Stress methodology under multiaxial loading conditions for fatigue life evaluation", XXX Encuentro del Grupo Espanol de fractura, Toledo, Spain 2013.

8. L. Reis, V. Anes, B. Li, and M. Freitas, "Fatigue crack path evaluation on two different micro-Structures HC and BCC under multiaxial loading", Crack Paths (CP 2012), Gaeta, Italy 2012.

9. V. Anes, L. Reis, B. Li, and M. Freitas, "Az31 Magnesium alloy mechanical behaviour under low-cycle fatigue regime", XIII Portuguese Conference on Fracture, Coimbra, Portugal 2012.

10. L. Reis, V. Anes, B. Li, and M. Freitas, "Evaluation of multiaxial fatigue loading paths in different shear stress spaces", 1st International Conference of the International Journal of Structural Integrity, Oporto, Portugal 2012.

11. L. Reis, V. Anes, B. Li, and M. Freitas, "Multiaxial sequential effect under proportional and non-proportional loading conditions on 42CrMo4 fatigue damage", XIII Portuguese Conference on Fracture, Coimbra, Portugal 2012.

12. V. Anes, L. Reis, B. Li, and M. Freitas, "Comportamento mecânico do aço estrutural 42CrMo4 em condições de fadiga multiaxial", 10º Congresso Iberoamericano de Engenharia Mecânica, Oporto, Portugal 2011.

13. L. Reis, V. Anes, B. Li, and M. de Freitas, "The influence of tension/torsion load sequences on fatigue life and early crack propagation of 42CrMo4 steel", XXVIII Encuentro del Grupo Espanol de fractura, Gijon, Spain 2011.

14. L. Reis, V. Anes, B. Li and M. Freitas. "Effect of non-proportionality in the fatigue strength on 42CrMo4 steel". VI International Materials Symposium MATERIAIS 2011, Guimarães, Portugal 2011.

15. L. Reis, V. Anes, B. Li and M. Freitas. "Characterizing the mechanical behaviour of extruded AZ31 magnesium alloy". VI International Materials Symposium MATERIAIS 2011, Guimarães, Portugal 2011.

# Acronyms and abbreviations

| | |
|---|---|
| **AISI** | American Iron and Steel Institute |
| **ASM** | American Society for Metals |
| **ASME** | American Society of Mechanical Engineers |
| **ASTM** | American Society for Testing and Materials |
| **BM** | Brown-Miller |
| **BS** | British Standards |
| **DEM** | Department of Mechanical Engineering |
| **EESH** | Effective Equivalent Stress Hypothesis |
| **FEM** | Finite Element Method |
| **FS** | Fatemi-Socie |
| **HCF** | High Cycle Fatigue |
| **HIS** | Elastic-plastic phenomenological model based in hysteresis loops |
| **IST** | Instituto Superior Técnico |
| **LCF** | Low cycle Fatigue |
| **MCE** | Minimum Circumscribed Ellipse |
| **MCC** | Minimum Circumscribed Circle |
| **NP** | Non-proportional |
| **PP** | Proportional |
| **PT** | Pure Tension |
| **PS** | Pure Shear |
| **SAR** | Stress amplitude ratio or strain amplitude ratio |
| **SAE** | Society of Automotive Engineers |
| **SHM** | Structural Health Monitoring |
| **S-N** | Curve for Stress versus Number of cycles at failure |
| **SIH** | Shear Stress Intensity Hypothesis |
| **SSF** | Stress Scale Factor |
| **SWT** | Smith-Watson-Topper |
| **UL** | University of Lisbon |
| **VSE** | Virtual Strain Energy |
| **vcc** | Virtual Cycle Counting |
| **WB** | Wang & Brown multiaxial cycle counting method |

# Notation

| | |
|---|---|
| $\alpha$ | Additional hardening |
| $b$ | Fatigue strength exponent |
| $b_\gamma$ | Fatigue strength exponent in torsion |
| $\beta$ | Flexural fatigue limit |
| $c$ | Fatigue ductility exponent |
| $c_\gamma$ | Fatigue ductility exponent in torsion |
| $C_a$ | Maximum shear stress amplitude |
| $\Delta\varepsilon,\ \Delta\varepsilon_n$ | Normal strain range |
| $\Delta\varepsilon_1, \Delta\varepsilon_2, \Delta\varepsilon_3$ | Principal strain range |
| $\Delta\varepsilon_x, \Delta\varepsilon_y, \Delta\varepsilon_z$ | Normal strains range in the x-y-z referential |
| $\Delta\varepsilon_e$ | Normal elastic strain range |
| $\Delta\varepsilon_{NP}$ | Normal strain range under non-proportional loadings |
| $\Delta\varepsilon_p$ | Plastic normal strain |
| $\Delta\gamma_{xy}, \Delta\gamma_{yz}, \Delta\gamma_{xz}$ | Shear strains range in the x-y-z referential |
| $\Delta\gamma$ | Shear strain range |
| $\Delta\gamma_{max}$ | Maximum shear strain range |
| $\Delta\sigma_1, \Delta\sigma_2, \Delta\sigma_3$ | Principal stress range |
| $\Delta\sigma$ | Axial stress range |
| $\Delta\sigma_n$ | Normal stress range |
| $\Delta\tau$ | Shear stress range |
| $\Delta W_H$ | Range of shear energy |
| $\Delta\tau_{oct}$ | Octahedral shear stress range |
| $\Delta W$ | Range of total strain energy |
| $\Delta W_I$ | Energy range from normal stresses |
| $\Delta K$ | Range of stress intensity factor |
| $\Delta K_{ef}$ | Range of effective stress intensity factor |
| $\delta$ | Phase shift |
| $\delta_{xy}$ | Phase shift between normal and shear stresses/strains |
| $E$ | Young's modulus |
| $eq.$ | Equivalent index |
| $\varepsilon$ | Normal strain |
| $\varepsilon_n$ | Normal strain on a given plane |
| $\varepsilon_{max}$ | Maximum normal strain on a given plane |
| $\varepsilon_{min}$ | Minimum normal strain on a given plane |
| $\varepsilon_{x0}$ | Initial normal strain |

| | |
|---|---|
| $\varepsilon_x, \varepsilon_y, \varepsilon_z$ | Normal strains in the x-y-z referential |
| $\varepsilon_1, \varepsilon_2, \varepsilon_3$ | Principal strains |
| $\varepsilon_\theta$ | Normal strain on plane $\theta$ |
| $\varepsilon_{nom}$ | Nominal normal strain |
| ${\varepsilon_f}'$ | Fatigue ductility coefficient |
| $f_{NP}$ | Non-proportionality factor |
| $f_0$ | Fatigue limit in repeated bending |
| $f_{-1}$ | Fatigue limit in tension/compression |
| $\gamma$ | Shear strain |
| $\gamma_{max}$ | Maximum shear strain |
| $\gamma_{xy}, \gamma_{yz}, \gamma_{xz}$ | Shear strains in the x-y-z referential |
| $\gamma_{xy0}$ | Initial shear strain |
| $\gamma_1, \gamma_2, \gamma_3$ | Principal shear strains |
| $\gamma_\theta$ | Shear strain on plane $\theta$ |
| ${\gamma'}_f$ | Coefficient of cyclic ductility in torsion |
| $G$ | Shear modulus |
| $HV$ | Vickers hardness |
| $J_2$ | Second invariant of the deviatoric tensor |
| $\sqrt{J_{2,a}}$ | Square root of the amplitude of J2 |
| $\sqrt{J_{2,m}}$ | Square root of the mean value of J2 |
| $k_t$ | Stress concentration factor |
| $k_{F-S}$ | Fatemi-Socie k parameter |
| $K$ | Monotonic strength coefficient |
| $K'$ | Cyclic strength coefficient |
| $N_{max}$ | Maximum normal stress |
| $N_{a,eq}$ | Equivalent normal stress amplitude |
| $n$ | Monotonic hardening exponent |
| $n_i$ | Number of loaded cycles |
| $N_{f_i}$ | Fatigue life of the loading path $i$ |
| $n'$ | Cyclic hardening exponent |
| $\nu$ | Poisson coefficient |
| $\nu_e$ | Poisson coefficient from elastic strains |
| $\nu_p$ | Poisson coefficient from plastic strains |
| $N$ | Number of cycles |
| $N_f$ | Number of cycles at rupture (fatigue life) |
| $P_H$ | Hydrostatic pressure |
| $P_{H,med}$ | Mean hydrostatic pressure |
| $P_{H,\max}$ | Maximum hydrostatic pressure |
| $R$ | Stress ratio |
| $R_a$ | Radius of the major axis of the ellipse |
| $R_b$ | Radius of the minor axis of the ellipse |
| $\sigma$ | Normal stress |
| $\sigma_a$ | Normal stress amplitude |
| $\sigma_y$ | Yield strength |
| $\sigma_{ut}$ | Ultimate tensile strength |

| | |
|---|---|
| $\sigma_H$ | Hydrostatic stress |
| $\sigma_{H,m}$ | Mean hydrostatic stress |
| $\sigma_{H,\max}$ | Maximum hydrostatic stress |
| $\sigma_{f'}$ | Fatigue resistance coefficient |
| $\sigma_{\max}$ | Maximum normal stress |
| $\sigma_{med}$ | Normal stress mean value |
| $\sigma_{\min}$ | Minimum normal stress |
| $\sigma_{nom}$ | Nominal stress |
| $\sigma_n$ | Normal stress |
| $\sigma_{n,max}$ | Maximum normal stress |
| $\sigma_r$ | Rupture stress |
| $\sigma_x, \sigma_y, \sigma_z$ | Normal stresses in the x-y-z referential |
| $\sigma_{xa}, \sigma_{ya}, \sigma_{za}$ | Normal stress amplitudes in the x-y-z referential |
| $\sigma_{x,med}, \sigma_{y,med}, \sigma_{z,med}$ | Normal stresses mean values in the x-y-z referential |
| $\sigma_{x0}$ | Initial normal stress |
| $\sigma_1, \sigma_2, \sigma_3$ | Principal stresses |
| $\sigma_{eq}$ | Equivalent stress |
| $\sigma_{i,relative}(t)$ | von Mises relative time-history |
| $\sigma_i(t)$ | Wang and Brown normal stress time-history |
| $\sigma_{eq,OP}$ | Equivalent stress of a non-proportional loading path |
| $\sigma_{eq,PP}$ | Equivalent stress of a proportional loading path |
| $S$ | Fatigue limit |
| $\tau$ | Shear stress |
| $\tau_a$ | Shear stress amplitude |
| $\tau_{a,MCE}$ | MCE method shear stress amplitude |
| $\tau_m$ | Shear stress mean value |
| $\tau_{xy}, \tau_{yz}, \tau_{xz}$ | Shear stresses in the x-y-z referential |
| $\tau_{xy0}$ | Initial shear stress |
| $\tau_{\gamma\varphi}$ | Shear stress on plane $\gamma\varphi$ |
| $\tau_{max}$ | Maximum shear stress |
| $\tau_i(t)$ | Wang and Brown shear stress time-history |
| $\tau_{oct}$ | Octahedral shear stress |
| $\tau_{f'}$ | Shear fatigue strength coefficient |
| $t_{-1}$ | Fatigue limit under fully reversed torsion |
| $t$ | Time |
| $T_a$ | Shear stress amplitude |
| $T$ | Period |
| $w_n$ | Natural frequency |
| $W$ | Energy |
| $W_e$ | Elastic energy |
| $W_p$ | Plastic energy |

# Chapter 1

# Introduction

Structural health monitoring (SHM) is a discipline of science that aims to monitor structural integrity of structures and mechanical components in order to avoid unexpected failures. This is a very important subject, because it allows preventing the loss of human lives, invested money in structures, and also prevents assurance payments due to collateral damages from accidents; therefore SHM has social and economic impacts in society. Structures and/or mechanical components may fail during service due to several reasons such as fabrication defects, assembly defects, impacts, and cyclic incremental effects. Fabrication and assembly defects can be monitored during the quality inspection but loading effects do not, however, these effects can be monitored in to two ways: first, at design stages, it is taken into account a representative loading pattern that structures or/and mechanical components are usually subjected to. Next, with the right design criteria and the aforementioned loading patterns, structures and mechanical components are designed for reliability. The second way is the monitoring of accumulated damage in structures/components in order to make maintenance decisions; structural components can be replaced or maintained based in the damage accumulation information gathered with SHM techniques. Both ways are complement to each other, one to be used in structures design and the other to evaluate structural damage accumulation taking into account the usage regimen in the field. Damage evaluation in the field is very important because the usage regime can be quite different from the one considered in design stages. In both approaches, mechanical design and SHM, it is required reliable methods to evaluate structural damage and integrity. Essentially, these methods aims to monitor/estimate the loading pattern influence in the material strength. Load level and load type are two loading factors that have great influence in the structures strength. They cause different damage regimes, especially under multiaxial loading conditions, which is the most common stress state in the usage field. Figure 1.1 shows the Eschede train disaster occurred on June 1998 in Germany, the train derailed due to a fatigue crack in one wheel. It remains the worst high speed rail disaster until now. After the accident, the Deutsche Bahn (German railway

company, the second-largest transport company in the world) stated that it paid more than 30 million U.S. dollars to the victims families and survivors. Due to this accident all wheels with similar design where replaced by another model, the German railway company had large costs with this unexpected preventive action.

**Figure 1.1:** Train disaster in 1998, Eschede, Germany, 101 deaths and 88 injuries [1].

Figure 1.2 shows a Trent 900 Rolls-Royce aircraft turbine, commonly used in the airbus A380, completely destroyed due to a fatigue crack in an oil feed-pipe.

**Figure 1.2:** Rolls-Royce Trent 900 engine failure, Singapore, Changi Airport in 2010 [2].

Contrary to what has happened in the Eschede disaster, there were no fatalities neither injuries. After the accident Airbus sought to be compensated from Rolls-Royce due to the disruption of the Quantas airline service, and pondered to not sign new contracts for new engines. In 2011, Quantas announced that had agreed to be compensated with 100 million U.S. dollars; the repair cost was estimated in 145 million. Many accidents like the aforementioned ones can be avoided with an effective monitoring of structural integrity. Materials multiaxial fatigue characterization plays an important role

in structural monitoring being one SHM keystone among others. Multiaxial fatigue is a scientific field that has captured, during decades, the attention of the scientific community. The scientific concern regarding this subject starts in the beginning of the last century where due to mechanical failures in the field, engineers started to investigate the materials fatigue phenomena. But, it was in the mid-70s that occurred the fatigue zenith being one of the most important scientific fields in materials characterization at that time. Since then, many efforts have been made in order to achieve a multiaxial fatigue criterion that be able to capture all fatigue damage mechanisms in all kinds of materials and loading conditions. The pursuit of such criterion has been a hard task, with some highs and downs during the last decades. The estimates inconsistency of multiaxial fatigue criteria have been a screenplay that registers the scientific struggle to solve the multiaxial fatigue problem. Some multiaxial fatigue models have good results for one kind of material, but for other ones their results are not satisfactory. This evidence creates a lack of confidence in multiaxial fatigue criteria because their ability to accurately estimate materials fatigue strength, without making specific fatigue tests, is very low. Therefore, it is required specific experimental tests to perform a fine tuning of such criteria. This inaccuracy led to their segmentation, where multiaxial fatigue models are classified according to their performance for each kind of material, and loading conditions. Thus, the main problems in multiaxial fatigue characterization remains nowadays unsolved due to several constraints.

One reason to have such difficult problem is the different fatigue responses (or fatigue damage responses) obtained in different kind of materials under the same loading conditions. Also, for the same material, different loading conditions lead to different damage regimes. These damage regimes are a result of many factors, such as material lattice (micro-structure), surface finishing, mechanical cyclic properties, among others. It is well known that materials change their cyclic properties during cyclic loadings in the field [3], thus knowing their cyclic mechanical behaviour is of utmost importance to estimate local stress states. Furthermore, the materials cyclic properties may change under different environments, for instance, high or/and low temperatures, oxidation, abrasion or even corrosion have huge influence in the materials monotonic and cyclic mechanical properties. However, some multiaxial fatigue models are unable to account for material cyclic evolution (material hardening/softening) to perform fatigue life assessment. Nowadays, there is no multiaxial fatigue criterion that be able to update the materials cyclic properties to evaluate multiaxial fatigue damage on the fly, which is very important feature in SHM. Despite that, one reason that has been delayed solid achievements in multiaxial fatigue characterization is the difficulties found in the local stress/strain measurements due to technical limitations. An accurate record of the materials stress state is very important because all reasoning around multiaxial fatigue criteria is based on those measurements.

In the last decade some improvements were made in strain/stress measurements, for instance 3D video extensometers begin to be used in order to measure multiaxial stress

gradients and their time evolution during cyclic loadings, and fatigue crack initiation and growth processes. Until few years ago, stress/strains measurements were mainly performed in a single material point due to the limitations of conventional extensometers, which are unable to measure stress/strain gradients. On the other hand, the video extensometer solution can monitor stress/strain gradients, but due to resolution problems and applicability issues in conventional fatigue specimens, this measurement tool proved to be a costly solution and difficult to manage in order to obtain accurate data. Besides those measurement difficulties, the spot identification of the crack initiation process in smooth samples is also difficult to achieve, because it is not known the location of the crack initiation spot in order to focus the record video camera, especially in crack nucleation regimens where fatigue cracks are too small to be seen with naked eye. This constraint had brought difficulties in the interpretation of the crack initiation process in smooth specimens under multiaxial loading conditions, to overcome this problem has been made small notches at the specimen throat to fix the initiation spot, but this solution has some shortcomings related to local hardening resulted from the machining process that influences the crack growth results. Due to these reasons and other ones, it can be concluded that a recipe for all materials fatigue response remains in pursuit until today. Thus, the unachieved goals across years of pursuit may be the cause of the lack of motivation and innovation in multiaxial fatigue research at the end of the last century, the lack of innovative experimental tests published in multiaxial fatigue journals justifies this observation. Meantime, a new era of new materials arrived to the scientific community and high-tech industry; smart materials, and materials subject to tremendous loads in new harsh environments, had led to pushing up the motivation of the scientific community to a new level in multiaxial fatigue characterization.

Smart materials are nowadays used in mechanical actuators; they change their mechanical properties by changing their micro-structure through mechanical deformation and heating. This micro-structure change leads to different mechanical responses and therefore also leads to different multiaxial fatigue behaviours and damage accumulation regimens. Moreover, the materials used in spacecraft are subjected to severe operating conditions, i.e. to enter into the atmosphere they are subjected to intense loads and heat. In this materials the allowed number of loading cycles is much reduced compared to the ones found in conventional applications. To assure reliability in such operative regimes, structural components must be inspected and replaced regularly despite being very expensive. Thus, it is necessary to have a decision tool to help in replacement decisions, like a damage accumulation criterion, for instance. In the near future it is envisioned de use of spacecraft on a regular bases which will require an accurate characterization of the materials strength variation under such adverse operative conditions. Another example is the high speed railways, in this case the high velocities leads to spend the material cyclic strength in a few years. Nanotechnology developments have allowed the fabrication of nano components,

but multiaxial fatigue nano-characterization practically does not exist yet. Several works have been presented in this matter [4], but they are very basic with huge constraints. New materials and their inherent technologies bring always with them new challenges in materials characterization, which cannot be ignored.

In contemporary times, a strong trend has emerged in order to replace some structural components traditionally made of metal by composites. With this rising trend, the multiaxial fatigue in composites is emphasized, being one major structural concern. Structural fatigue behaviour in composites brings new challenges in multiaxial fatigue characterization, i.e. new type of tests and new theoretical concepts are required to capture the physical behaviour of multiaxial damage accumulation processes, which are quite different from the ones found in metals. Due to feasibility issues, multiaxial fatigue research has been developed until now based on experiments conducted to analyse the mechanical behaviour of metals; therefore multiaxial fatigue characterization in composites is a relatively new subject.

Nowadays, materials research is driven by industrial needs, due to that, it has been focused on metals and alloys used in specific industrial branches such as power generation, aerospace, transportation, marine and offshore structures. Essentially, the aforementioned research is built on the fatigue and crack growth under different load conditions in high cycle fatigue (HCF) and low cycle fatigue (LCF) regimens. Loading paths effects in materials cyclic elastic-plastic behaviour, stress level and residual stresses (internal measurements) are the key research areas driven by industrial activities where the fatigue damage and crack growth characterization is required. Therefore, reliable methods to modulate materials fatigue behaviour under analytical, computational, and theoretical approaches, remains in pursuit by the scientific community. Its purpose is to obtain reliable tools that allow understanding fatigue mechanisms and to estimate the materials fatigue strength and their inherent crack initiation and growth processes.

## 1.1 Motivation

The present research aims to push forward reliable methodologies in multiaxial fatigue characterization. The main objective is to develop tools that yield reliable multiaxial fatigue estimates in mechanical design stages and in structural health monitoring procedures. The solutions found in the industry regarding this subject are very basic with unsatisfactory results, due to that it is commonly used high safety factors in mechanical design to deal with uncertainty, which leads to heavier structures, increase of fuel consumption and $CO_2$ emissions.

The transportation industry has been one of the biggest players in the $CO_2$ emissions reduction by funding research in light materials. They pursue a combination of high strength and low-density properties in structural materials; however achieving an optimal

material remains a paramount goal under pursuit. Nowadays, a 3-litre car is an achievable, goal but now the newest goal is to achieve a 1-litre car. Under this research dynamics, the weight saving is of major concern. Despite the improvement in fuel consumption and inherent vehicle performance being an economical approach and a driving force from the customer side, the reduction of fuel consumption is also motivated by legislative rules to reduce primary energy consumption and environmental impact.

In the recent past, the alternative to energy savings was the lower aerodynamic drag approach having been a path exhaustively explored. However, a new one has been adopted based on structural weight reduction. Structural weight reduction requires a compromise between the material properties and the structural components geometry, under this required equilibrium a fully understanding of cyclic, monotonic, and elastic-plastic properties is required as well as the fully understanding of the fatigue behaviour under these loading conditions.

## 1.2 Research objectives

This research aims to characterize fatigue damage under multiaxial loading conditions for a wide range of loading types. The ultimate goal is to use the developed methods in mechanical design and structural health monitoring procedures. This research was developed having always in mind a final industrial application, it was avoided abstract and complex solutions (when possible) and it was given always primacy to simple, and ease to implement methodologies. To characterize random fatigue damage, it is needed to cover a broad number of concepts related to multiaxial fatigue. As a matter of fact, it is not possible to deal with random accumulated damage without considering all of them. Figure 1.3 shows the fatigue pyramid for random fatigue characterization. In this pyramid each level depends on all levels below and each level has within a wide number of concepts regarding materials science.

Random multiaxial fatigue damage is a complex subject that has been handled in a segmented way, i.e. each level of the fatigue pyramid has been studied and analysed in a separated way without an evident interconnection between them. In literature, it can be gather information related to each subject inherent to each level of the fatigue pyramid, but they are usually studied and presented in a separated way. Therefore, subjects like damage accumulation, damage parameters, cyclic properties, multiaxial cycle counting methods among others, are concepts that capture partially the fatigue phenomena when considered separately, however they have not been presented in literature in a synergistic way. Nevertheless, to analyse and estimate random multiaxial fatigue life it is necessary to account with all of them. Therefore, in this research, it is explored several key aspects of multiaxial fatigue damage in order to gather, in a synergistic way, concepts and physical phenomena to characterize random multiaxial fatigue damage. A key question may arise

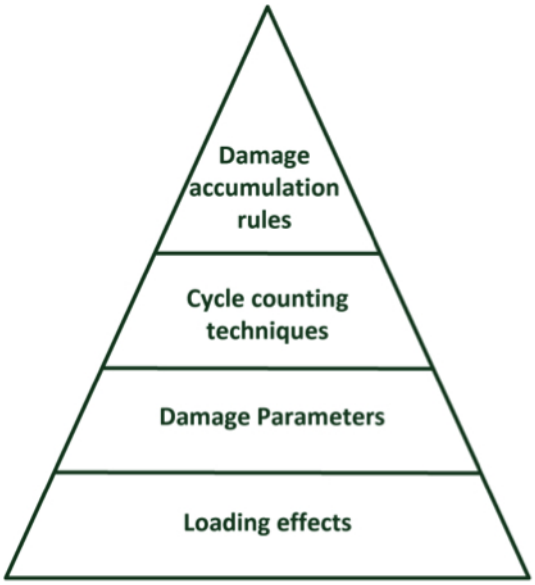


**Figure 1.3:** Fatigue levels of random fatigue characterization.

about this work, why it is important such task, why it is important to evaluate and account random multiaxial fatigue damage? In the actual state-of-the-art there is no such synergistic models that allow the evaluation of random multiaxial fatigue damage in a reliable way. Moreover, it is of utmost importance to account multiaxial damage in the field where random loadings show to be the most realistic loading regimen, which are the cases of car suspensions, wind energy harvest towers, or fighter jets, for instance. The added value of this research is to bring new models that capture several physical phenomena related to fatigue and use then to characterize random multiaxial fatigue damage. Going deeper in the explanation, it can be said that the cornerstone of this research is based in the fact that in the actual state-of-the-art the loading path effects on the materials fatigue strength remains to be fully understood. Moreover, cannot be found in literature any tool that allows to quantify the loading path effects in a reliable way. For instance, the equivalent stress concept under multiaxial loading conditions is independent from the loading path type, i.e. it can be reached the same equivalent stress with different combinations of normal, and shear stresses, for the same stress level. However, experimental results show that the fatigue strength varies with different combinations of normal and shear stress amplitudes, even for the same equivalent stress amplitude. Thus, fatigue life estimates of equivalent stress criteria under multiaxial loading conditions give inconsistent results. Moreover, the same conclusion can be extrapolated for any other multiaxial damage parameter, such as critical plane or invariant criteria. In the present author opinion, this is the main problem that has hindered the fully characterization of multiaxial random fatigue in the last years. In the base of the fatigue pyramid shown in Figure 1.3, one can find the level 1, here it is studied the loading effect on the material cyclic response. For level 1, the thesis objective is to develop an elastic-plastic cyclic model, and a non-proportional sensitivity parameter; this two contributions will allow to update the

cyclic material response in level 2 (damage parameter criteria). Next up, level 2, covers the damage parameter concept, other research objective of this thesis is to reach a multiaxial fatigue damage parameter capable to account for multiaxial damage effects resulting from several loading path types such as: sequential, proportional, non-proportional, and stress gradient effects among others. Next, at level 3, a cycle counting technique is developed to account for variable amplitude and loading block damage using the damage parameter developed in level 2. In level 4, it is studied damage accumulation rules for random loadings damage characterization. This synergistic way to account with each pyramid level is an important feature because under random multiaxial loading conditions all of these pyramid levels may be activated in a sequential or simultaneous way.

Another research objective is to achieve a crack initiation model capable to estimate critical planes, i.e. the direction of the crack initiation plane, having into account the random loading conditions, and being sensitive to the loading path trajectory. This feature is also important because it will allow to help the identification of crack initiation planes in failure analysis. Another question may be raised regarding the research objectives: it can be found in literature any models or techniques for the four levels of the pyramid? The answer is yes, there are plenty of models published in literature; however all of them do not have into account the path trajectory type as is considered in this research, which is one of the contributions of this thesis, among others. Figure 1.4, summarizes the synergistic process of evaluating random multiaxial fatigue proposed here.

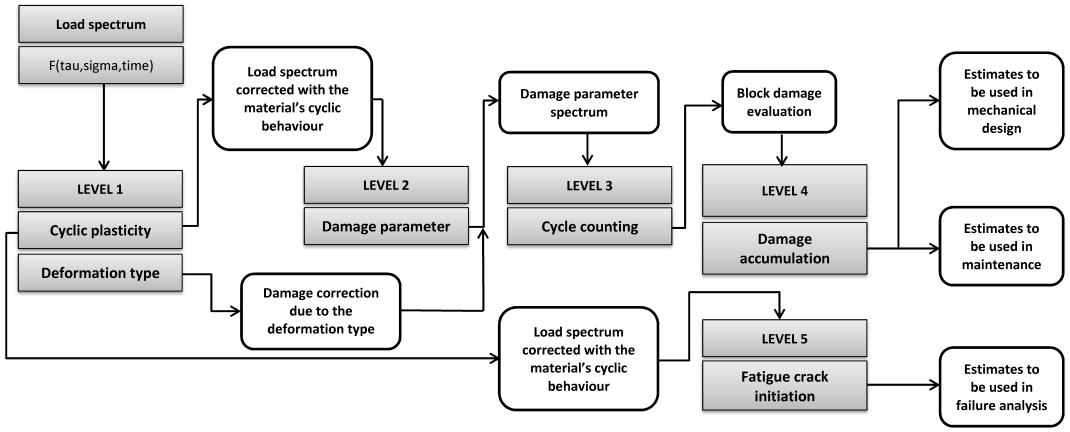


**Figure 1.4:** Fatigue estimates process under random loading conditions.

## 1.3 Research conceptual framework

The thesis statements are presented in the next paragraphs; these statements are the foundations that support all research work presented here.

### 1.3.1 Fatigue characterization

A fatigue model must have into account all aspects inherent to the material fatigue damage process. Must be able, in a synergistic way, to account for cyclic damage factors when they are acting isolated or simultaneously. Only in this way, it is possible characterize random fatigue. Therefore, a fatigue model must be able to estimate fatigue lives under constant, variable and random amplitudes, and under uniaxial and multiaxial loading conditions. Here it is stated that a fatigue model should comprises a set of criteria for fatigue. Due to that, in this research it is pursued models for each one of the fatigue pyramid level present in Figure 1.3.

### 1.3.2 Fatigue fracture

A fatigue fracture surface is an important record of the fatigue process where several physical phenomena occur at nucleation and crack growth. In several materials, fatigue crack nucleation takes most of the fatigue life-time; during this process the material cyclic plasticity has a major influence in the material fatigue strength. Therefore, it is expected that the stress time evolution at nucleation spot be quite different from the nominal one. Thus, it is hypothesized here, that the loading path type has a huge influence on the cyclic plastic mechanism and therefore on the crack initiation plane. With this in mind, the influence of the loading path type on the direction of the crack initiation plane is analysed here. Moreover, the stress time histories used to estimate fatigue lives must be updated with a cyclic $k_t$.

### 1.3.3 Damage parameter

Damage parameter is a fatigue quantity/measure based in physical principles that aims to capture an unitary damage to be processed in cycle counting methods and/or damage accumulation criteria. This parameter concept is the cornerstone to all fatigue branches found in literature. If this parameter do not capture the unitary damage, it will be very difficult to obtain coherent results in cycle counting and damage accumulation methodologies. The most used and appreciated type is the equivalent stress, which reduces a multiaxial stress state (usually represented by a stress tensor) to a scalar, however under multiaxial loading conditions equivalent stress approaches have some shortcomings. Despite their popularity, equivalent stresses do not capture the loading path influence on the materials fatigue strength. This shortcoming results from the equivalent stress concept, where it is only considered the maximum value obtained within the loading path. Moreover, the loading signal loss verified in equivalent stress criteria also negatively influences the estimates of these criteria. Furthermore, the state-of-the-art of equivalent stress criteria under multiaxial loading conditions considers that the stress scale factor, which reduces the normal and shear damages to the same damage scale is a constant

parameter. These are some reasons among others for their poor performance to capture fatigue damage in multiaxial loading conditions. It is stated here that the stress scale factor concept (SSF) is not captured by a constant and is strongly dependent of the loading path type, stress level and material type.

### 1.3.4 Non-proportionality evaluation

Materials have different cyclic responses under different loading paths and stress levels; they may harden, soft or have a mix of both cyclic responses. In literature, the material non-proportionality is evaluated under high plastic strains. However, experimental observations lead to conclude that the material non-proportional response is a cyclic property that is intrinsic to the material type, and must be determined considering their S-N curves. Here, it is stated that a new material property, the material non-proportional sensitivity can be measured considering the material S-N curves under proportional and non-proportional loading conditions. Moreover, the aforementioned non-proportional sensitivity can be used to update fatigue damage parameters.

### 1.3.5 Cycle counting methodology

Cycle counting is an important technique to interpret fatigue damage accumulation and a hard topic to deal with. As a matter of fact, there are very few cycle counting methods for multiaxial loading conditions, and the ones that can be found in literature are based in the Rainflow method, which in turn is based in uniaxial hysteresis loops. By definition, hysteresis loops are based in the stress/strain relation, therefore under multiaxial loading conditions it will be required the use of an equivalent stress and an equivalent strain to perform such analysis. However, it is well-known that the actual equivalent stress/strain concept for multiaxial damage assessment do not capture the damage physical behaviour as mentioned in sub-Section 1.3.3. Therefore, cycle counting methods based in this concept and based in the Rainflow cycle counting method do not showed so far very good results. Here, it is stated that, contrary to what is found in literature, it is possible to deal with complex loading paths by using a non-Rainflow cycle counting method in synergy with an damage parameter time evolution.

### 1.3.6 Damage accumulation

Damage accumulation rules are important procedures to estimate fatigue strength under complex loading paths. Usually, they compute the unitary damage captured by the damage parameter in association with a cycle counting method. It is stated here that if the damage parameter and cycle counting method really capture the unitary damage, thus the damage accumulation rule should be linear. It is found in literature some examples of non-linear damage accumulation rules, but in the present author opinion,

those approaches aim to capture the damage accumulation without having into account the physical damage mechanisms within the material. Therefore, it is hypothesised here that the Palmgren-Miner linear damage rule can be used to capture fatigue damage accumulation under random loading conditions.

### 1.3.7 Random loadings

In the field, many structures and mechanical components are subjected to constant, variable and random amplitudes. These loading conditions lead to different degrees of complexity in damage characterization, but a fatigue criterion must be able to capture fatigue damage in those regimens. Also, multiaxial fatigue criteria must be able to capture fatigue damage on the fly and not be only used as fatigue life estimators in design stages. Here, is stated that the aforementioned fatigue tools presented in the previous sub-Sections can be synergistic arranged to evaluate fatigue damage in constant, variable and random amplitude loading conditions. Moreover, it is also possible to reach a fatigue model that be able, in real time, to capture the material damage accumulation in order to be used in maintenance and replacement decisions (structural health monitoring).

### 1.3.8 Cyclic elastic-plastic model

Cyclic plasticity is quite different from the quasi-static one. This type of plasticity is the one that results from cyclic loadings with stress amplitudes much lower than the materials yield stress. Therefore stress states considered in design stages may change during service without notice. In some materials that change may result in the materials hardening but in other ones may result in the materials softening which may reduce the material strength. However, some materials also show a mixed behaviour that is dependent of the stress level involved in the cyclic loading process. Thus, in literature cannot be found cyclic elastic-plastic criteria that are able to fully capture the mechanical properties variation due to cyclic loadings. Thus, here is stated that it is possible to reach a elastic-plastic model for multiaxial loading conditions that be able to capture the material cyclic behaviour variation, and can be used to update the material stress state.

## 1.4 Scholarly and practical significance

The research theme present here is a topic of current international research; the outcomes of this research are important for the scientific community as well as for the industry, with them it becomes possible to evaluate more efficiently fatigue damage accumulation taking into account loading paths effects. Every year a countless number of conferences are held worldwide regarding each level of the fatigue pyramid shown in Figure 1.3, which is an indicator of the research dynamics in this subject. Nevertheless, the major novelty of this research is based in the use of an equivalent stress to capture the loading effects in the

materials damage. This research adds to the present state-of-the-art new methodologies and new concepts for evaluating materials damage accumulation. Moreover, this research improves the understanding of multiaxial fatigue by making a critical literature review, explaining the new concepts proposed here, and connecting them with the ones found in literature. Also, it is envisioned the use of the outcomes of this research in the industry, where it is increased the structures/components safety by using the techniques developed here. This means that people such as faculty members and industry employees will use the set of fatigue tools developed here, as well as continue to develop it.

## 1.5 Research methodology

This research was carried out within a framework of approaches using scientific methods to achieve unbiased and objective results. It was collected, analysed and interpreted information to answer the research questions. The type of research is a pure research type where it is performed systematic studies towards the understanding of fundamental aspects of phenomenological results in multiaxial fatigue, which may or may not have practical application, however at the end the objective is to transfer the acquired knowledge to practical applications with an industrial partner. This is a correlational and explanatory research where is sought clarify the relationships between several phenomenological aspects of materials science. The inquire mode was a mix of structured and unstructured approaches, where a quantitative research is used to define the main guidelines, and a qualitative research is adopted to have flexibility in all aspects of the research process.

### 1.5.1 Research questions

This research aims to find a new set of models to improve the fatigue damage accumulation characterization and evaluation under multiaxial and random loading conditions. In the following is presented the research question of this research.

1. Does the random multiaxial fatigue models, which can be found in literature, have the required mechanisms to have into account the loading path effects in fatigue damage accumulation?

2. Does the random multiaxial fatigue models be able to estimate the direction of the crack initiation plane? These models have into account the local stress state variation due to cyclic plasticity?

3. Is there an equivalent stress damage parameter that has into account the loading type? Does the equivalent stress damage approach a reliable way to be used in random damage accumulation?

4. In literature, non-proportionality is commonly evaluated using an equivalent stress, however in this way the stress level is increased under non-proportional loadings,

comparatively to the proportional ones, which is an inaccurate way to evaluate the material non-proportionally. Is it possible to evaluate non-proportionality without making this error?

5. Is it possible to create a non-Rainflow cycle counting method for multiaxial loading conditions? Will it have better results? Will it be easier to implement?

6. Does the Palmgren-Miner rule an adequate damage accumulation rule to be used in random accumulated damage evaluation? The damage accumulation under random conditions is linear?

7. Typically, in literature each of the aforementioned topics are studied separately like independent subjects. Will it be possible to create a unified fatigue model that has into account all the aforementioned fatigue subjects?

8. will it be possible to implement a random multiaxial fatigue model that has into account the stress states updated through a cyclic plasticity model?

### 1.5.2 Literature review

A literature review in specialized journals and conference proceedings was carried out. This stage was very important because it allowed to understand the maturity of the state-of-the-art of the subjects focused in this thesis. Moreover, it allowed the understanding and learning of the scientific language commonly used by the scientific community. This task proved to be very important because research is strongly based in communication. Materials science have many concepts and definitions that are used to define new ones, therefore getting a right and good communication is a fundamental task when we start in a research field. Although being a first step, the literature review must be always updated during the research project. This continuous update will allow the comparison between the developed work and the new research proposed by peers. Also, new research outcomes gathered from literature can somehow help the improvement of the developed work. A continuous literature review brings clarity and focus to the research, also it supports the developed methodologies and contextualises the research findings.

### 1.5.3 Collecting data

In this research, it was performed several multiaxial fatigue tests using the multiaxial fatigue testing machine of the department of the mechanical engineering (DEM) of the Instituto Superior Técnico (IST) at Universidade of Lisbon (UL). In these experiments two materials were analysed, namely: the high strength steel 42CrMo4, and the magnesium alloy AZ31B-F. Moreover, it was gathered and analysed a legacy of 20 years of experiments made by the research group lead by Professor Manuel Freitas at DEM-IST. The collected data was the results of multiaxial fatigue tests performed using three materials, the

42CrMo4, Ck45, and AISI 303. Additionally, it was gathered complementary experimental fatigue data from literature; in this case, the materials were the structural steels Ck45, C40, and the aluminium alloy 2024-T4. All experiments were documented in order to allow peers to perform the same experimental tests performed here. By doing this, it is clarified the achieved results and experimental procedures.

### 1.5.4 Data Analysis

The purpose of this analysis is to validate the achieved models and inherent methodologies for a broad number of materials and loading conditions described above. After having the fatigue data, a reflexive period was considered to analyse the results and identify physical patterns that justifies the studied physical phenomena. In this research a fundamental premise was adopted, i.e. all conclusions, models and methodologies must be validated using experimental data. Also, all hypothesized ideas that were not validated by experiments were identified; in these cases, it was explicitly referred the need of validation by experiments.

### 1.5.5 Correlation and interpretation

To check the added value of this research to the scientific knowledge, it was performed a performance comparison between the most used models in literature and the methodologies achieved in this research.

### 1.5.6 Preparation of the final report

The research outcomes have been published in specialized journals and presented in conferences; with this, the results obtained during the investigation were being shown to the scientific community. This procedure proved to be very rewarding, because opinions and ideas were received during the research period. Moreover, the achieved experimental and theoretical results were scrutinized by peers. Also a final document was produced (this PhD thesis) to gather together all research information and outcomes.

## 1.6 Research Plan

In order to achieve the research objective several milestones were defined as follows:

1. Attain an elastic-plastic cyclic criterion that can be able to capture the materials cyclic behaviour under uniaxial and multiaxial loading conditions. This model must estimate for each stress level and loading path type the local stress/strain relation in order to update stress/strain time histories. Under uniaxial loading conditions, the stress/strain relation can be analysed using an hysteresis loop, but under multiaxial loads such concept does not exist. In this task a new concept to characterize multiaxial stress/strain states must be attained.

2. Attain a criterion that be able to capture the loading paths effects in the materials fatigue strength, namely the non-proportional effect. The equivalent stress, pointed out in the next point, must be able to be updated with the results of this task.

3. Attain an equivalent stress criterion sensitive to the material and loading path type. The equivalent stress must be able to be updated with the materials cyclic behaviour.

4. Attain a cycle counting method able to capture uniaxial and multiaxial loading cycles. Preferable this criterion should be a non-Rainflow based methodology. Rainflow based cycle counting methods use hysteresis loops, but under multiaxial conditions does not exist. In literature can be found multiaxial cycle counting methods based in the Rainflow methodologies. However, in such concept, usually it is separated the normal and shear stresses time histories to reduce a multiaxial loading into two uniaxial ones, and then it is applied the Rainflow cycle counting method to such stress time histories. Under such procedure, the combined damage effect of normal and shear loadings is missing. Therefore, a multiaxial cycle counting method that has into account the aforementioned combined damage is required.

5. Attain a damage accumulation criterion that is able to account with uniaxial and multiaxial damage under any loading type.

6. Attain a variable amplitude fatigue life criterion based in the achieved equivalent stress and cycle counting method.

7. Attain a random fatigue life criterion based in the achieved variable amplitude fatigue life criterion.

8. Being a stress based fatigue criterion closely related to crack nucleation, attain at yearly crack stages (micro notches) the $k_t$ variation with the loading path type and the inherent effect on the local stress states.

9. Being the fatigue crack topography an important record of the fatigue process, attain a relation between the direction of the crack initiation plane (critical plane) and the loading type taking into account the material's cyclic behaviour.

## 1.7 Research report outline

The research report (PhD thesis) is structured in 9 chapters as follows:

- Chapter 1 starts with an overview regarding the fatigue research evolution over time. It is presented some drawbacks and future trends in research and industrial environments regarding materials fatigue characterization. It is also presented the most important problems that had created some difficulties to the progress of fatigue characterization. In addition, it is identified the problems to be solved in this work and presented the research objectives, next up it is presented the thesis statements

that are the research cornerstones from which all research work is based, finally it is presented the thesis outline.

- Chapter 2, in this chapter, it is performed a reviewing of the state-of-the-art in several aspects of multiaxial fatigue. The most important information regarding the topics mentioned in the research objectives are gathered together in order to identified the available tools in multiaxial fatigue characterization. The objective is to identify their drawbacks and inconsistencies in order to perform a benchmark between the state-of-the-art and the research results obtained here.

- Chapter 3, presents the research contribution to level 1 depicted in Figure 1.3. Here, it is presented and discussed the thesis proposals regarding a cyclic elastic-plastic model and a new way to account cyclic non-proportionality. It is presented and demonstrated all formulae and physical principles behind each model.

- Chapter 4, presents a new damage parameter, which is an equivalent shear stress, this new equivalent stress is the research contribution to the pyramid level 2. In this chapter it is explained the physical foundation of this parameter and it is performed a comparison between the state-of-the-art criteria and the developed equivalent stress performance.

- Chapter 5, presents the research contribution to level 3. This contribution is a new cycle counting method, named as virtual cycle counting (vvc), which is based in the equivalent shear stress proposed in Chapter 4. The vcc method performance is compared with two multiaxial cycle counting methods for a wide number of loading paths. The fatigue data used here were obtained from the in house experiments (42CrMo4) and from a third party data (Ck45, and C40).

- Chapter 6, presents the level 4 research contribution. Here, the outcomes from level 1, 2 and 3 were joined together to estimate variable amplitude damage accumulation. Moreover, a new method to deal with random loading conditions is presented. In this chapter, it was performed fatigue life correlations for the aluminium alloy 2024-T4 using a third party fatigue data.

- Chapter 7, presents a thesis sub-objective where it is investigated an alternative way to obtain a fundamental parameter (the SSF damage map) of the proposed equivalent shear stress. Here, it is investigated the possibility to obtain fatigue parameters using modal analysis, i.e. using the material damping values.

- Chapter 8, presents the research contribution to level 5. Here it is proposed methodologies and new criteria that relates loading histories with the direction of crack initiation plane. Also, here it is presented the experimental fractography results, which were correlated with the estimates of the state-of-the-art, and with the estimates of the proposed models.

- Chapter 9, in this chapter it is registered the overall conclusions and pointed out some ideas for future works.

## 1.8 Final comments

This chapter aims to line up a set of reasoning, which in the present author opinion, will lead to achieve a set of tools to be used in the characterization of damage accumulation under multiaxial and random loading conditions. These tools are very important under the scope of structural health monitoring procedures and mechanical design, especially in the transportation industry; this is so, because the available solutions have unsatisfactory correlations with the results obtained in the field. This research will contribute to the improvement of the mechanical design and maintenance of metal structures/components in order to increase their reliability. Moreover, the structural reliability increase will also increase the final users confidence, which is an important factor of sustainability in the transportation industry.

# Chapter 2

# Literature review

## 2.1 Introduction

In this chapter, it is performed a literature review regarding the materials phenomenological behaviour under the scope of multiaxial fatigue. Moreover, it is focused on several criteria and their methodologies that are commonly used in the scientific community to characterize multiaxial fatigue damage. As discussed in the previous chapter, to deal with this subject it is needed to cover a broad number of concepts usually tackled in a separated way in literature. One of the novelties of this work is to gather all these concepts in one approach as a multiaxial fatigue package for random loading conditions. This chapter presents the state-of-the-art regarding these concepts, at first sight it may seem to be fragment concepts but in reality, under random loading conditions, they are always needed and interconnected. Recalling Figure 1.3 from Chapter 1, the fatigue pyramid is divided by four levels or four major themes, namely: the material constitutive behaviour, damage parameter, cycle counting techniques, and damage accumulation rules. Usually, each level is studied and developed horizontally, however each level has bridges in the vertical direction that interconnect those levels, where the upper level needs information from the lower ones.

Analysing these levels and their interconnections, we have the material constitutive behaviour which is the base level of the pyramid in which it is covered the quantitative and phenomenological behaviours in material due cyclic loads. For instance, the material hardening and softening are concepts that aim to characterize the material hardness variation due to cyclic loadings. In these cases, the cyclic yield stress may increase or decrease accordingly to the material type. These cyclic variations are very important and must be taken into account, because the stress states depend on the actual capability of response of the material to external loads.

In the pyramid's second level, damage parameters need accurate stress states obtained in level 1. This input is also important because it allows the damage parameter criterion

to capture unitary damages based on physical phenomena interpretations. The output from level 2 is the input of level 3, in level 3 it is used unitary damages within the cycle counting techniques, therefore pyramid's level 3 needs the damage reference from level 2. Finally, accumulated damage estimates for complex loadings are computed at level 4. In this level, it is accounted the cycle counting techniques output in order to be used in damage accumulation rules.

In level 4, it is performed the decision of replace or not to replace a mechanical component or structure, which is based on damage accumulation estimates. The scope of level 4 is mainly related to the field loading regimens, in other hand mechanical design usually goes only to the pyramid level 3. Therefore, this Chapter is divided in four sections, one for each pyramid level presented in Figure 1.3.

This review is focused on the most important models, criteria and concepts commonly found in literature, however in some cases the author may go further in the research deep. Nevertheless, one more topic was added to the literature review, which is related to the estimates of the crack initiation plane. Fatigue is always related to crack initiation and crack growth process. Therefore fatigue crack is an evidence of the fatigue phenomena. Moreover, the loading path type deeply influences the direction of the crack initiation plane. In this sense, the relation between the crack initiation plane and the loading path type was also covered here.

## 2.2 Level 1 - Phenomenological cyclic behaviour

### 2.2.1 Loading paths

In the lab, a loading path is a loading trajectory performed by a fatigue testing machine that loads the testing sample. This trajectory results from the combination of normal and shear stresses, which may load the material in many different ways. Materials have different responses accordingly to the load trajectory even for the same stress level, due to that multiaxial fatigue strength is strongly related with the loading path shape.

Essentially, there are two types of loadings from which all loadings can be set, i.e. the proportional and non-proportional loadings. The main characteristic that differentiates both loading types is the variation or not of the principal directions. Non-proportional loadings have their principal directions changing along the loading period, but in proportional loadings they remain fixed. Regarding the loading effect on the material, these two loading types cause different fatigue damages.

In proportional loadings, the material is loaded in one particular plane (direction) given by the stress amplitude ratio. On the other hand, non-proportional loadings activate more than one loading plane in the material, due to that non-proportional loadings causes additional phenomenological effects such as non-proportional hardening [5].

Figure 2.1 shows an example of proportional and non-proportional loading paths typically considered in literature to evaluate materials fatigue strength under multiaxial loading conditions. Figure 2.2 shows the variation of the normal and shear stresses across their loading period.

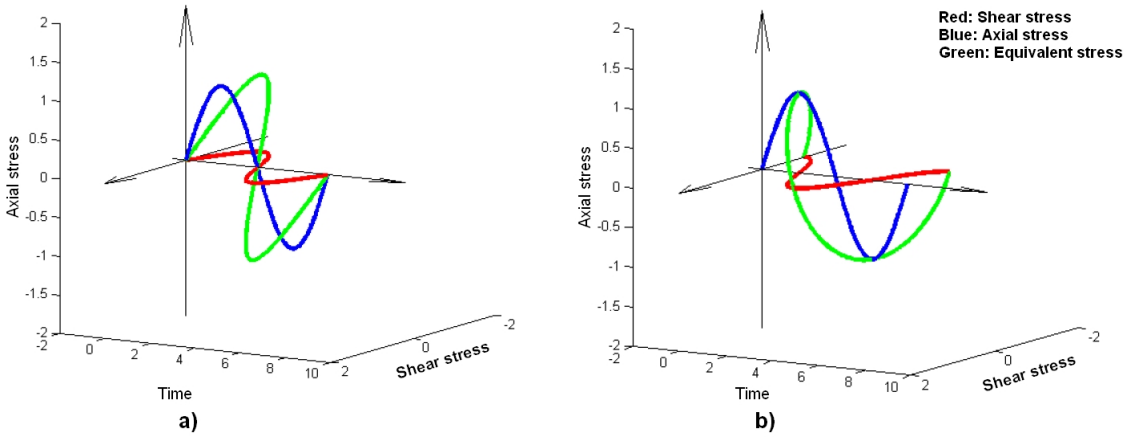


**Figure 2.1:** Three-dimensional time variation of a) Proportional loading, and b) Non-Proportional loading [6].

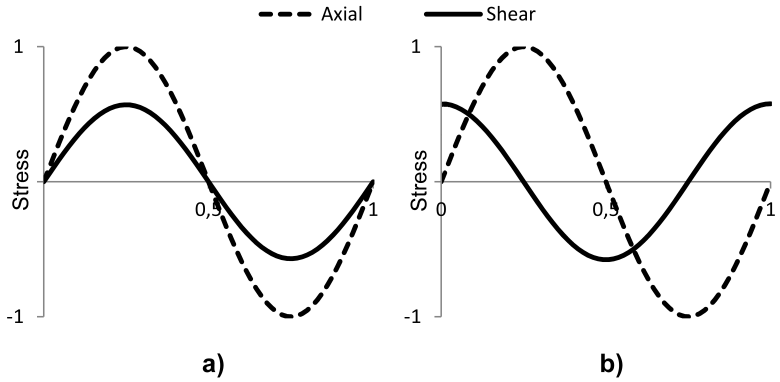


**Figure 2.2:** a) Proportional loading time variation, and b) Non-Proportional loading time variation.

One way to represent multiaxial loading paths is to use the von Mises stress space. Figure 2.3 shows the normal and shear stresses time evolution for a loading period depicted in the von Mises stress space; the loading path trajectory is obtained by removing the time axis and projecting the amplitudes of the normal and shear stresses into the plane tau-sigma (axis of shear and normal stresses). Usually, stress spaces have different scales in each axis, in the case of von Mises stress space, the tau axis used to represent the shear stress, has a scale given by the constant $\sqrt{3}$ constant. Therefore, the shear stress time variation of a loading path is multiplied by this constant to be represented in the von Mises stress space. The reasoning of the stress space scale is based in the experimental evidence in which different damage mechanisms can be obtained under uniaxial loading conditions (axial and shear).

This way to represent loading paths is very straightforward and gives a quick overview about the loading path shape. Moreover, the loading path representation in a stress space allows the direct identification of the loading path type i.e. proportional or non-proportional. Some multiaxial fatigue criteria are based in the loading path shape depicted in the von Mises stress space, which is the cases of the MCE [7], and MCC [8] criteria for biaxial loading conditions.

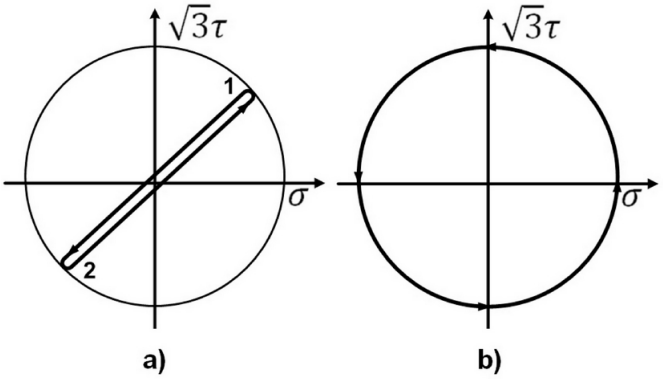


**Figure 2.3:** a) Proportional and b) non-proportional loading paths depicted in the von Mises stress space.

The loading paths shown in Figure 2.3 are a combination of normal and shear stresses with a sinusoidal variation in time. These type of loadings are periodical and it is very easy to identify their loading period, i.e. their loading cycle. However, in some loading paths the loading cycle identification is much more difficult, which is the cases of loading blocks or loading spectra. Loading blocks are loading trajectories in which it can be identified proportional and non-proportional branches; it is possible to create other loading cycles (loading blocks) based in proportional and non-proportional loading types [9], for example the sequential loading effect has been analysed in literature by a combination of proportional loadings as presented in Figure 2.4.

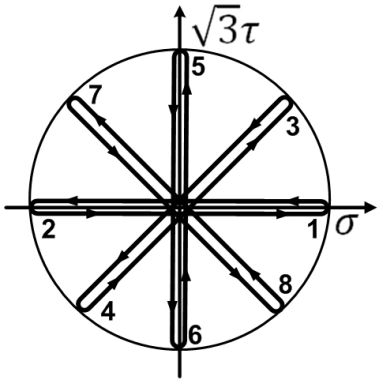


**Figure 2.4:** Non-proportional loading block with proportional loading branches.

Figure 2.4 shows a combination of proportional loadings with different stress amplitude ratios, this loading block is established using eight proportional loading branches. In an

overall point of view this loading block is a non-proportional loading with its principal directions changing during the loading period, but each loading branch is a proportional loading. Asynchronous loadings are other type of loading paths in which the frequency of a multiaxial loading component (normal stress or shear stress) is different from the other one, please see Fig.(s) 2.5 to 2.7 .

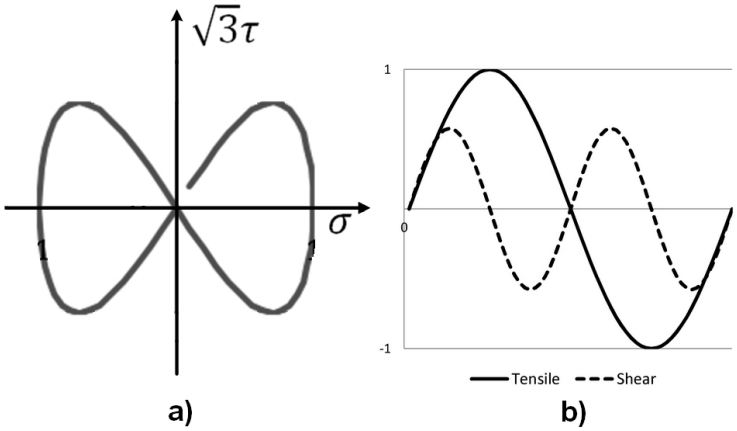


**Figure 2.5:** Asynchronous loading with shear stress frequency two times higher than the normal stress frequency a) Loading path depicted in the von Mises stress space b) Stress time evolution.

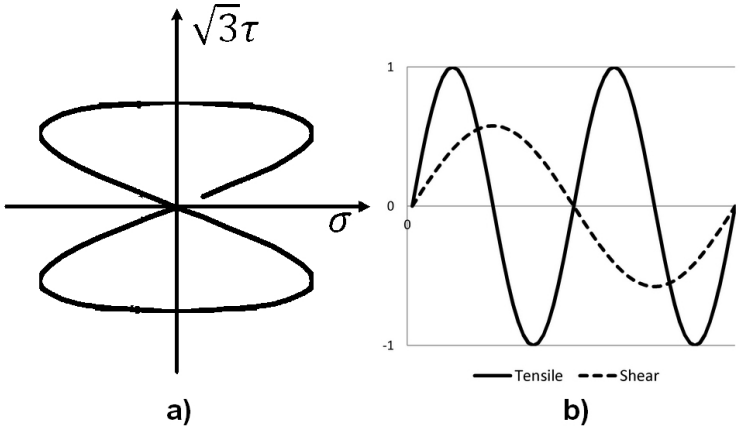


**Figure 2.6:** Asynchronous loading with normal stress frequency two times higher than the shear stress frequency a) Loading path depicted in the von Mises stress space b) Stress time evolution.

Fig.(s) 2.5 and 2.7 show asynchronous loading paths in which the loading frequency of the shear stress component of the multiaxial loading is higher than the normal one. In these cases, the shear stress has more loading cycles than the normal stress, this feature brings some challenges to the loading cycle interpretation. For instance in Figure 2.7 b), it is depicted five loading cycles for the shear stress and only one for the normal stress. In this case how many cycles can be accounted within the loading path? Five from the shear stress time evolution? or one from the normal stress? or none of these two options? These types of loadings are non-proportional and with them it is possible to have normal and shear damages in different proportions, within a non-proportional loading.

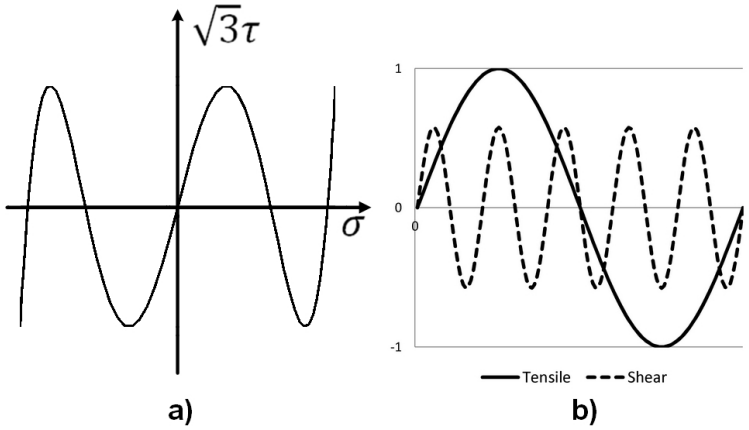


**Figure 2.7:** Asynchronous loading with shear stress frequency five times higher than the normal stress frequency a) Loading path depicted in the von Mises stress space b) Stress time evolution.

Other type of loading can be achieved by entering with mean stress in proportional and non-proportional loadings. Mean stress is very important and can change substantially the fatigue damage pattern [10]. Figure 2.8 presents a proportional a) and non-proportional b) loading with mean stress, where tensile mean stresses usually decreases the material cyclic strength and the compression ones increase that strength [11]. This is so because, compressive mean stresses promote the fatigue crack closing and the tensile ones facilitate the crack growth. Regarding steady shear stresses, their damage effect is not so obvious, but some authors stated that the shear mean stress also influences the materials fatigue strength accordingly to the stress level [12].

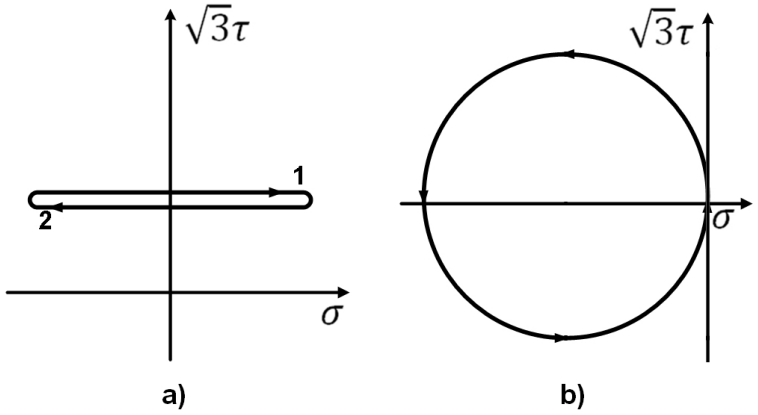


**Figure 2.8:** Multiaxial loading paths with mean stress a) Normal stress with steady shear stress b) Non-proportional loading path with mean normal stress in compression.

### 2.2.2 Cyclic hardening

Material hardening is the material phenomenological response to external loads, being particular sensitive to the load level, and load type. Essentially, the internal micro plasticity, due to cyclic loadings, changes the material strength, their fatigue behaviour, and crack initiation patterns. Therefore, materials at first loading cycles search for a

stable response, which is a stress-strain relation set out accordingly to the external load type. After the material cyclic accommodation to the first loading cycles the stress state is maintained during the remaining time of the loading period, if the loading pattern is not changed meantime. Under strain control loading conditions, the material hardening leads to the increase of the required stress values to maintain the same strain amplitude i.e. the cyclic elongation is maintained during the loading period if the load level is increased. On the other hand, under a stress control loading conditions, a constant stress amplitude results in the decrease of the strain amplitude due to the material hardening. This subject is very important because the material accommodation (or response to the loading) will influence the stress states, therefore the relation between stresses and strains becomes non-linear under elastic cyclic loadings. Constitutive cyclic plasticity models have hardening rules to account with this phenomenon. Figure 2.9 presents the hardening effect in the stress amplitude values for a constant strain amplitude, here it can be seen the increase of the stress amplitude required to maintain a constant strain amplitude under cyclic loadings.

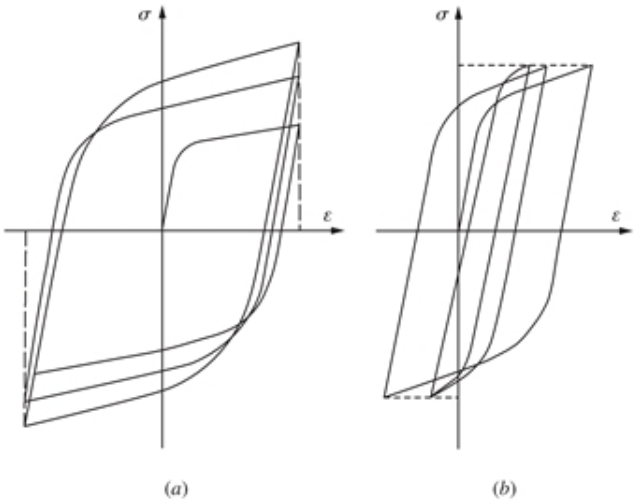


**Figure 2.9:** Uniaxial hysteresis loops in cyclic hardening: a) constant strain amplitude, and b) constant stress amplitude[13].

The material hardening behaviour is strongly dependent on the loading type; some works in literature focus this subject especially under non-proportional loading conditions [14, 15]. Figure 2.10 depicts a non-proportional hardening evolution under strain control. As it can be seen in Figure 2.10 b) the strain limits are maintained constant, but the normal and shear stresses increase until reach stable values, please see Figure 2.10 a).

### 2.2.3 Cyclic softening

Material softening, due to cyclic loadings, is the opposite phenomenon described for the cyclic hardening concept. In this case, the material strength is cyclically reduced, please see Figure 2.11. On the left side of Figure 2.11, one can find the cyclic strain variation

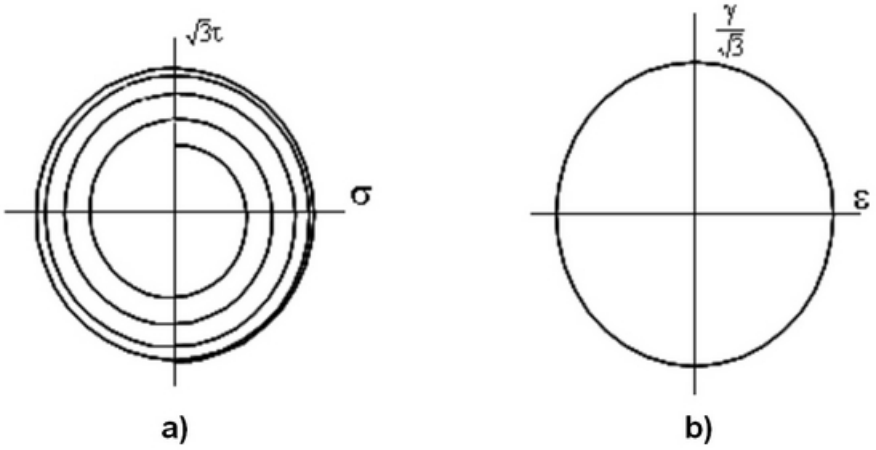


**Figure 2.10:** Non-proportional hardening under strain control, a) Stress evolution, b) Strain evolution [16].

in time, their amplitude is maintained across the loading period. However, in the right side, is depicted the stress-strain variation where the stress a amplitude decreases under constant strain limits, as seen in Figure 2.11. Therefore, from a stress control point of view, constant stress amplitudes will increase the inherent strain amplitude in materials that cyclically soften, which may lead to higher plasticity. Moreover, higher strains increase the crack initiation potential; thus, this type of materials is much more susceptible to failure than the ones that cyclically harden. Nevertheless, structural materials typically harden; therefore this subject is not so focused in literature as is the cyclic hardening phenomenon.

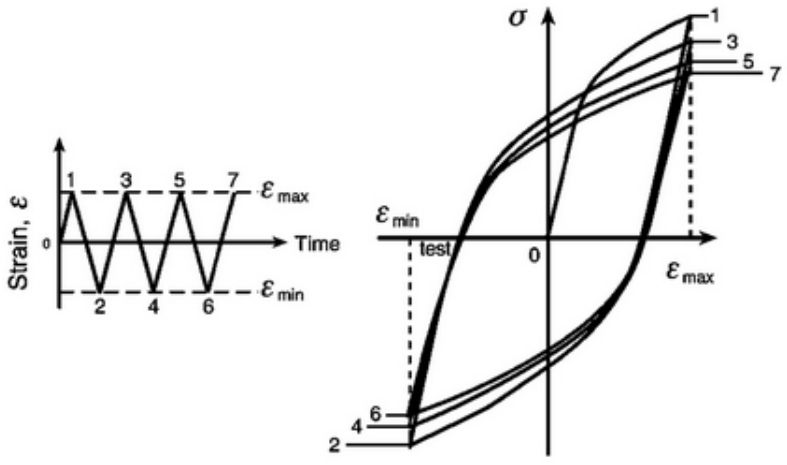


**Figure 2.11:** Material softening under strain control [17].

### 2.2.4 Non-proportional cyclic effect

Analysing the state-of-the-art in non-proportional cyclic effects, one can conclude that the generalized way to deal with non-proportionality is to find a factor that in some way corrects a damage parameter criterion. None of the multiaxial fatigue criteria found in literature deal with non-proportional cyclic effects by default; their

fatigue life estimates without any correction shows unsatisfactory results in fatigue life correlation for non-proportional loadings. There are several physical phenomena within non-proportional loadings, which increases their phenomenon complexity. Moreover, the non-proportional physical concept remains under study because there are different types of non-proportionality, which is the cases of non-proportionality under mean and steady stresses, for instance. Therefore, the appreciated concept of one damage parameter to capture the additional damage due non-proportionality remains a difficult task to be accomplished. Non-proportionality is strongly related to the loading path type, therefore, it has been evaluated in literature based in loading path shapes. Multiaxial fatigue criteria are generally insensitive to non-proportionality, i.e. the criteria procedures do not distinguish between proportional and non-proportional loadings conditions. However, non-proportionality induces a different fatigue damage than the one achieved under proportional loading conditions [16], thus it is required further investigations in this matter.

Under proportional loading conditions fatigue damage occurs on a specific loading plane, because the principal stress directions remain fixed during the loading period, thus the highest fatigue damage occurs mainly on a specific plane of the material. However, under non-proportional loading regimens, fatigue damage occurs in different directions of the material, due to the principal directions variation along the loading path. The principal directions variation results from the fact that under non-proportional loading conditions, the maximum stresses, from the biaxial loading components, do not occur at same time instant, during the loading period. This time lag between the maximum values of the normal and shear stresses is a result of the so called non-proportional phase shift. Non-proportional loadings can activate the entire material slip, where by local cyclic plasticity, the mechanical properties are cyclic changed. This phenomena is the so called non-proportional cyclic hardening.

The materials non-proportionality is usually characterized based on the material non-proportional cyclic hardening coefficient [16, 18]. This coefficient is usually determined considering two specific multiaxial loading cases, namely: the non-proportional loading with a $90^{o}$ of phase shift and the typical proportional loading, both with $SAR = 45^{o}$. For each total equivalent strain within a predefined strain range, it is inspected the equivalent stress values under proportional and non-proportional loading conditions. These values are obtained when, at each total strain, a cyclic stable behaviour is reached. With these values, it is measured the material non-proportional response to non-proportional loadings.

From the above discussion, it can be concluded that the equivalent strain-stress concept used to characterize non-proportional cyclic hardening has within a fixed damage scale between normal and shear strains.

This is so, because the aforementioned damage scale is within the equivalent concept used

to evaluate the non-proportional cyclic hardening coefficient, for instance in the von Mises equivalent stress the shear stresses are multiplied by $\sqrt{3}$, which means that the shear stresses cause a damage $\sqrt{3}$ times greater than the normal stresses.

Thus, the stress space damage scale used in the equivalent stress concept affects the non-proportional interpretation and their characterization. The fixed damage scale in the stress space, as in the case of the von Mises stress space, estimates in the same way the proportional and non-proportional damage, moreover also considers the same damage scale for any kind of materials, which is a quite inaccurate approach.

Considering the aforementioned and described reasoning, one question may be raised: how to avoid inaccurate interpretations resulted from the analysis process of the non-proportionality effect in the material strength, since the stress space concept have some shortcomings such as fixed damage scale for all type of loadings and load levels? For instance, and considering the von Mises stress space, it is usual to consider the same equivalent stress/strain under proportional and non-proportional loadings to inspect their different fatigue damages.

This procedure to evaluate non-proportionality increases the stress level of the multiaxial components in the non-proportional loading case. However, if it is maintained the proportional shear and normal stress levels and adding a phase angle between normal and shear stresses time evolution (phase shift), the maximum equivalent stress under these conditions will be less than the one found in the proportional loading case. Thus, for the same normal and shear stress levels the introduction of and phase angle will reduce the equivalent stress value.

But, if it is compared proportional and non-proportional damages for the same value of equivalent stress and strain, as seen in non-proportional cyclic hardening concept, part of non-proportional damage have nothing to do with the non-proportionality effect, but with the increase of the stress level required in the non-proportional loading case in order to reach the proportional equivalent stress/strain. Thus, the material non-proportional cyclic hardening determined as mentioned above is a biased attempt to measure the material non-proportional capability and has been considered a material cyclic parameter.

The material non-proportional cyclic hardening is considered in literature as a non-proportional reference to deal with non-proportional loadings being updated accordingly to the loading path non-proportional level. In order to evaluate non-proportionality, some coefficients were proposed in literature, the non-proportional hardening coefficient $\alpha$ is one example of that [16]. This coefficient attempts to capture the maximum non-proportional effect through the ratio of the 90$^{o}$ out of phase equivalent stress to the proportional equivalent stress obtained at stabilized stress-strain curves. In Figure 2.12 a) is depicted the way in which the $\alpha$ parameter is determined. In order to generalize the $\alpha$ parameter for any kind of non-proportional loading cases Socie and

Marquis [16] conceived the idea that the entire loading path trajectory, depicted in a stress space, can be enclosed by an ellipse. Then, the ratio of the minor to major axis of the ellipse that encloses the loading path history is the so called non-proportional factor, $F$. This factor has been used to quantify the non-proportionality level within a loading path, which has been used to correlate the material non-proportional cyclic hardening behaviour. Figure 2.12 b) presents the $F$ factor concept.

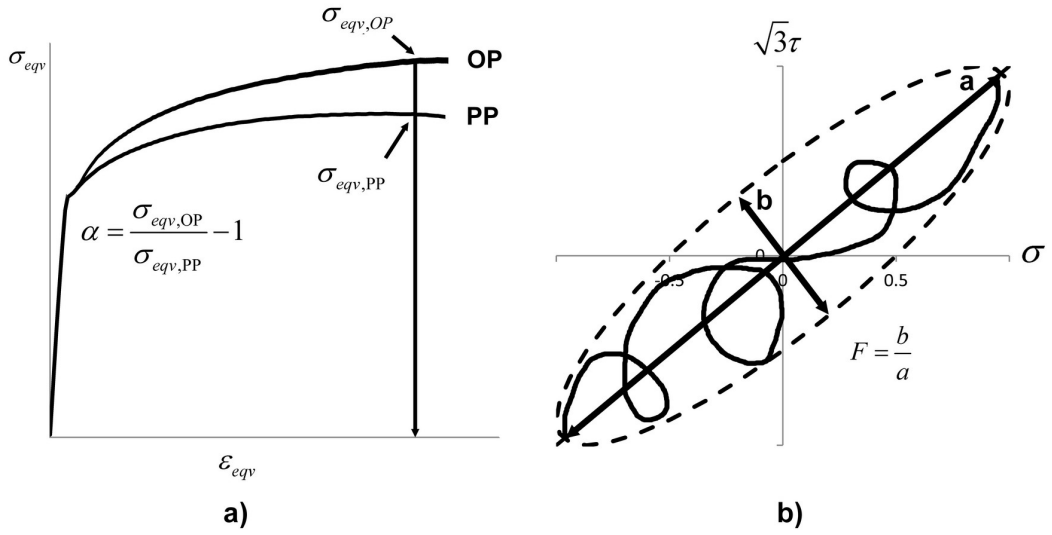


**Figure 2.12:** a) Non-proportional cyclic hardening parameter, $\alpha$ b) Non-proportional factor concept, $F$.

Under proportional loadings, the aforementioned ellipse ratio, please see Figure 2.12 b), is undetermined thus the $F$ parameter is equal to 0. For the highest non-proportionality level, i.e. phase shift equal to 90°, the $F$ parameter is equal to 1. This non-proportional concept, considers that all other non-proportional loadings (different from the 90° out of phase loading case) has a non-proportional factor ranging between 0 and 1.

Regarding the $\alpha$ parameter concept, it can be concluded that this parameter is insensitive to the non-proportionality within a generic loading path because it is only based on two specific loading cases [16]. In this sense, the $F$ parameter is a step forward in the evaluation of non-proportionality. The $F$ factor can be used to update an equivalent stress, $\bar{\sigma}$ as follows in Eq. 2.1.

$$\bar{\sigma} = K^{'} (1 + \alpha \cdot F) (\bar{\varepsilon_p})^{n^{'}} \tag{2.1}$$

where $\alpha$ is the non-proportional hardening coefficient, $\bar{\varepsilon_p}$ is the plastic strain, $F$ is the non-proportionality factor, the $K^{'}$ and $n^{'}$ are the coefficient and exponent of the stress-strain curve equation.

Kanazawa et al. [19] proposed another non-proportional factor that has into account

the non-proportionality from phase shift and stress amplitude ratios. The idea of this concept is to capture the slip damage mechanisms in all different loaded planes obtained under non-proportional loading conditions. In order to do that, the authors correlated the proportional shear strain with the non-proportional one. Eq. 2.2 presents the Kanazawa rotation factor to characterize the additional non-proportional damage, considering the proportional damage as reference. This rotation factor is defined as the ratio of the shear strain at 45º in the maximum shear strain range direction to the maximum shear strain range.

$$F^2 = \frac{\lambda^2 + (1+\nu)^2 - \sqrt{\left((1+\nu)^2 - \lambda^2\right)^2 + \left(2\lambda\,(1+\nu)\cos(\phi)\right)^2}}{\lambda^2 + (1+\nu)^2 + \sqrt{\left((1+\nu)^2 - \lambda^2\right)^2 + \left(2\lambda\,(1+\nu)\cos(\phi)\right)^2}} \tag{2.2}$$

Where, $\lambda$ represents the strain amplitude ratio $\gamma_a/\varepsilon_a$ , $\nu$ is the Poisson's ratio and $\phi$ is the phase angle. Figure 2.13 shows two types of non-proportional loading histories evaluated by the Kanazawa rotation factor in the Tresca stress space. Figure 2.13 a) shows loading histories with the same stress amplitude ratio and with different phase angles, and Figure 2.13 b) and c) depicts several non-proportional loading histories with different stress amplitude ratios and with 90º as phase shift angle.

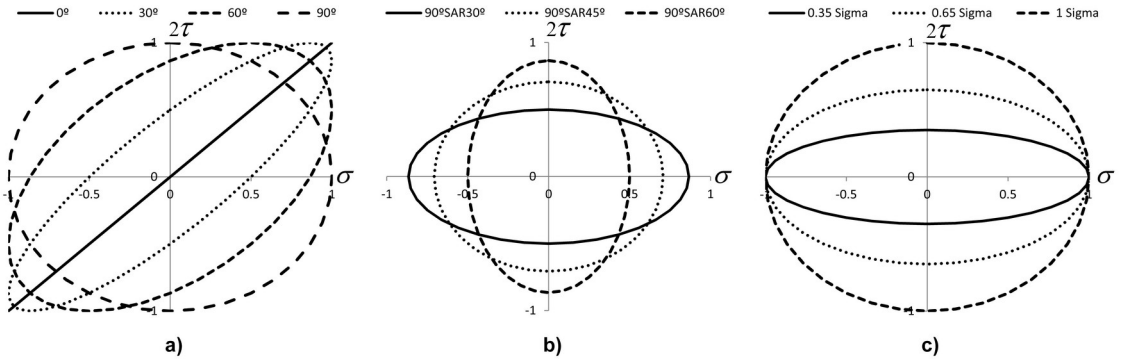


**Figure 2.13:** Different non-proportional loading paths a) Fixed SAR with phase angle variation, b) SAR variation with fixed phase angle c) SAR variation with fixed phase angle and fixed normal stress amplitude.

Some observations can be made about these two criteria, based in the reasoning discussed about the non-proportionality assessment. Firstly, both criteria are defined under a stress space concept; in particular the Socie and Marquis criterion is defined under the von Mises stress space, and the Kanazawa rotation factor is defined in the Tresca stress space. It can be concluded that the damage scale that enables to reduce both normal and shear stresses to the same stress space, is a constant factor under proportional and non-proportional loading damage characterization; moreover, that damage scale is equal for every material.

Thus, the stress space damage scale between normal and shear damages is independent from the loading and material type. Another shortcoming associated to the Socie and Marquis's non-proportional concept is related to the non-univocal behaviour of the $F$ factor. The $F$ factor concept yields the same value for different non-proportional damages mechanisms. For example, in Figure 2.13 b) and c) it is possible to obtain the same $F$ value under different stress amplitude ratios. However, it is well-known that the damage obtained under different stress amplitude ratios is quite different, since the material slip system is activated in different ways in such loading conditions [20]. Thus, the $F$ factor concept does not capture in full the non-proportional damage inherent to a generic loading path. Moreover, the non-proportional hardening coefficient, the $\alpha$ parameter, is defined as the ratio between the equivalent stress at 90º out of phase and the proportional equivalent stress for the same equivalent strain. The following relation gives the non-proportional hardening coefficient:

$$\alpha = \frac{\sigma_{eq,OP}}{\sigma_{eq,PP}} - 1 \tag{2.3}$$

As aforementioned, the non-proportional hardening coefficient, $\alpha$, obtained in expression 2.3 does not capture the material non-proportional response under several levels of non-proportionality. Moreover, in order to have the same equivalent strain under non-proportional and proportional loading conditions, it is necessary to increase the stress level under non-proportional loadings. Therefore, the $\alpha$ coefficient does not quantify uniquely the material response due to non-proportionality, but also takes into account the stress amplitude increase, which adds an additional damage to the non-proportional one. Despite the above drawbacks $\alpha$ coefficient has been widely used as reference to the material response under the most severe non-proportional loading conditions. From here it can be concluded that the non-proportionality characterization using $\alpha$ and $F$ coefficients has some shortcomings resulted from the stress space paradigm and its damage scale because these coefficients are strongly related to the stress damage scale between shear and normal stresses. Therefore, it can be concluded that it is required a new way to evaluate the non-proportionality found in multiaxial loading paths by avoiding the shortcomings identified here.

## 2.3 Level 1 - Plasticity

### 2.3.1 Cyclic plasticity models

In general, plasticity models take into account 3 dynamic mechanisms to follow the material response under cyclic plastic deformation [21]. One of those mechanisms is the yield function that estimates the material yield behaviour. Before the material yield occurs, the linear relation between strains and stresses is given by the Young's modulus, i.e.

the Hook's law governs the stress-strain relation. However, this law is not sensitive to the material response under plastic strains, therefore a yield function is used to determine when the material yielding occurs, and to cyclically update stress-strain relations. The most common yield function derives from the von Mises equivalent stress, where a combination of principal stresses on the octahedral plane establishes the yield stress boundary. The second mechanism found in plasticity models is the flow rule; this conceptual rule is established based on constitutive equations where stresses and strains are computed in incremental plasticity procedures, where the next plastic deformation is dependent on the prior value. This rule is generally based on the Drucker's postulate [22–24], where the plastic strain increments are normal to the yield surface defined by the yield function. The last mechanism is the hardening rule, which establishes the changes on the yield surface during the plastic deformation [21, 25].

#### 2.3.1.1 Chaboche

The Chaboche plasticity model [26] is a non-linear kinematic hardening model, where the yield function, $F$, is given through the following equation, Eq. 2.4.

$$F = \sqrt{\frac{3}{2}(s-\alpha) : (s-\alpha)} - k = 0 \tag{2.4}$$

Where $s$ is the deviatoric stress, $\alpha$ is the back stress, and $k$ is the yield stress [25, 27]. In this plasticity model the kinematic hardening is governed through the back stress tensor, which in turn is related to the yield surface translation. The back stress tensor equations are present in Eq.(s) 2.5 and 2.6.

$$\{\alpha\} = \sum_{i=1}^{n} \{\alpha_i\} \tag{2.5}$$

$$\{\Delta\alpha\}_i = \frac{2}{3} C_i \left\{\Delta\varepsilon^{pl}\right\} - \gamma_i \{\alpha_i\} \Delta\bar{\varepsilon}^{pl} + \frac{1}{C_i}\frac{dC_i}{d\theta}\Delta\theta \{\alpha\} \tag{2.6}$$

where $\Delta\varepsilon^{pl}$ is the accumulated plastic strain, $\theta$ is the temperature, and $C_i$ and $\gamma_i$ are the Chaboche material parameters. In Eq. 2.6 the hardening modulus and back stress variation (recall term) are represented by the first and second terms respectively. The third term is related with the temperature variation. In the commercial software, Ansys, the Chaboche plasticity model allows to use various kinematic models and material constants, where the $C_1$ and $\gamma_1$ are inputs for one kinematic model, however extra sets of $C$ and $\gamma$ can be added. The $C_1$ and $\gamma_1$ parameters aim to capture the material cyclic behaviour, and can be determined through stress-strain tests under stabilized hysteresis loops (usually under uniaxial loading conditions). With the plastic strain values and the inherent recall

term, which is the difference between the stress amplitude and the material cyclic yield stress defined by the total strain of a given load, the relation between $C_1$ and $\gamma_1$ can be obtained by making a fitting of experimental data using Eq. 2.7.

$$\frac{\Delta\sigma}{2} - \mathrm{k} = \frac{\mathrm{C}_1}{\gamma_1}\tanh\left(\gamma_1\frac{\Delta\varepsilon^{pl}}{2}\right) \tag{2.7}$$

The fitting procedures allows to determine the unknown variables of Eq. 2.7, including the constants $C1$ and $\gamma 1$ .

#### 2.3.1.2 Jiang and Sehitoglu

The Jiang & Sehitoglu plasticity model [21, 28, 29] is also a non-linear kinematic hardening model that incorporates an Armstrong-Frederick type hardening rule, in order to capture the Bauschinger effect on the cyclic plastic deformation. This model was firstly implemented with the purpose of capture the cyclic ratcheting phenomena, which is a progressive and directional plastic deformation when a material is subjected to asymmetric loadings under stress-controlled regimens, which makes this model a good candidate to modelling elastic-plastic behaviour of magnesium alloys, please see Figure 2.14.

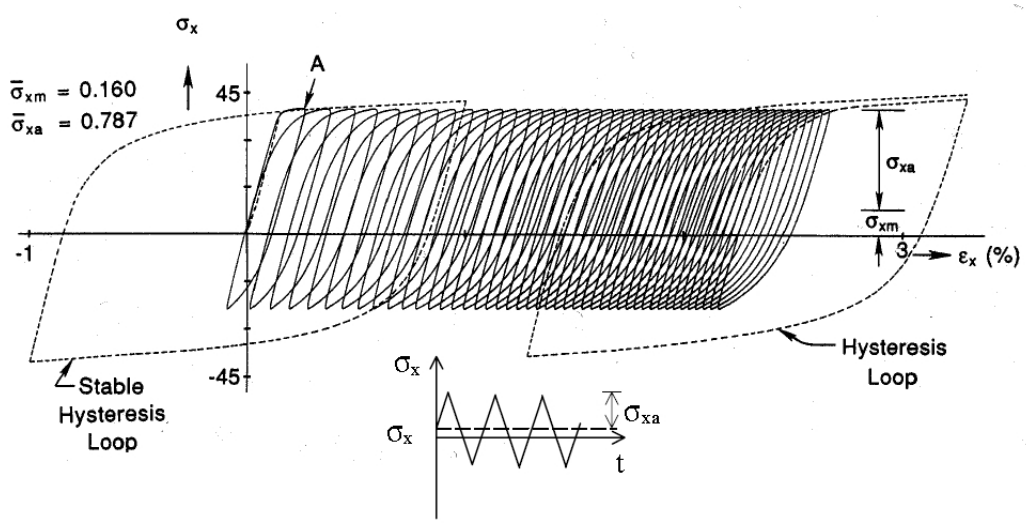


**Figure 2.14:** Normal strain ratcheting response under uniaxial loading conditions with mean stress and stress control [30].

One peculiarity associated to this model is the inclusion of a non-proportional hardening parameter (similar to the ones discussed in the previous section, i.e. $\alpha$ and $F$), to capture the additional resistance due to the non-proportional hardening found in materials subjected to non-proportional loading and plastic strains. This non-proportional hardening parameter is very similar to the $\alpha$ parameter described in Eq. 2.3. Also, it is introduced the memory concept on the material behaviour simulation in order to describe the strain range dependency from the plastic cyclic hardening. The Jiang & Sehitoglu

plasticity model also considers several others physical based mechanisms to capture cyclic phenomena, such as: a yield function, which considers a combinations of stresses that will lead to plastic deformations; a flow rule, that model a relationship between the stresses and plastic strains during plastic deformation;a hardening rule, which defines the yield criterion changes under plastic straining, stress relaxation and load redistribution in the stressed volume. The model key equations are presented in Eq.(s) 2.8 to Eq. 2.11. The yield function, $F$ is expressed as follows:

$$F = \left(\tilde{S} - \tilde{\alpha}\right) : \left(\tilde{S} - \tilde{\alpha}\right) - 2k^2 = 0(1) \tag{2.8}$$

Where $\tilde{S}$ is the deviatoric stress tensor, $\tilde{\alpha}$ is the back stress and $k$ is the yield stress. The flow rule is given in Eq. 2.9.

$$d\tilde{\varepsilon}^p = H \left\langle d\tilde{S} : \tilde{n} \right\rangle \tilde{n}(2) \tag{2.9}$$

Where $\tilde{\varepsilon}^p$ is the exterior normal unit. The hardening rule is presented in Eq. 2.10

$$\tilde{\alpha} = \sum_{i=1}^{M} \tilde{\alpha}^i(3) \tag{2.10}$$

Material memory contained in the back stress terms is given by the plastic modulus function presented in Eq. 2.11.

$$H = \sum_{i=1}^{M} c^i r^i \left[1 - \frac{\left|\tilde{\alpha}^i\right|^{X^{i+1}}}{r^i} \tilde{L}^i : \tilde{n}\right] + \sqrt{2}\frac{dk}{dp} \tag{2.11}$$

where $c^i$, $r^i$, and $X^i$ are non-negative scalar functions, $dp$ is the equivalent plastic strain increment, $\tilde{n}$ is the exterior unit normal to the yield surface, $\tilde{\alpha}^i$ is the material memory, $\tilde{L}^i$ is a function based on the $\tilde{\alpha}^i$ values, and $dk$ is the yield stress variation.

## 2.4 Level 2 - Damage parameters

### 2.4.1 Introduction

In mechanical design, the concept of equivalent stress is greatly appreciated because it allows, in an easy way, to interpret a three-dimensional stress state. The von Mises equivalent stress is one example of that, being widely used in static fail-safe design and many times is also used as a base for multiaxial loading paths interpretation. The major characteristic of this equivalent stress is the stress scale factor (SSF) between normal and

shear stresses [31, 32], namely in a simplified relation $\sqrt{3}\tau = \sigma$. This relationship is corroborated by the fact that experimentally, and for most materials, the value of the shear stress required to cause the material yield is smaller than the value of the normal stress [33]. In multiaxial fatigue analysis, the von Mises stress scale factor was adopted by several models; the ASME code is one example [34]. The ASME criterion is similar to the von Mises equivalent stress with the difference of using stress amplitudes instead of using instantaneous values [3].

A key point in the multiaxial fatigue damage interpretation is to find out the relationship between the fatigue damage caused by the normal and shear stress components of a multiaxial loading. The combined effect quantification of those stress components is very important to capture multiaxial fatigue damage, which is very different from the uniaxial one [8, 16, 35, 36]. The majority of multiaxial fatigue models somehow seek to establish this damage relationship between normal and shear stress components [37–44]. For example, in the Crossland [39] and Sines [45, 46] invariant criteria, the combined damage effect from multiaxial load components is quantified through the summation of the maximum amplitude of the second deviatoric invariant, with the hydrostatic stress. The hydrostatic stress in both criteria is corrected based on the fatigue limits obtained under pure shear and tension-compression loading conditions, aiming to perform a stress scale between normal and shear stress components by reducing both damages to the same damage scale.

The concept of damage stress scale, firstly, used in the von Mises yield criterion through the ratio of the normal to shear stresses under static failure conditions, is adopted in the multiaxial fatigue criteria by using the ratio of axial to shear fatigue limits. The use of this approach is quite common in the multiaxial fatigue field; multiaxial fatigue models such as Dang Van [47, 48], McDiarmid [49, 50], Papadopoulos [8], Matake [51], Carpinteri & Spagnoli [52, 53] among others, are some examples of the generalization of the damage scale concept in the combined damage formulations of normal and shear stresses. Some critical plane criteria also use the damage scale concept to account for the combined effect between normal and shear strains; for example the Fatemi-Socie model corrects on the critical plane the maximum shear strain amplitude through the ratio of the maximum normal stress to the material yield strength [54].

The Brown and Miller [55] criterion also defines its damage parameter by adding the amplitudes of shear and normal strains calculated in the critical plane, where it is corrected the normal strains amplitude through the $S$ parameter obtained for each type of material under a low cycle fatigue regime. To determine the critical plane in these models (critical plane models) a search of the plane direction where the damage parameter reaches its maximum value is performed. This search is mainly based on the Mohr's circle projections of the stress tensor in various directions, being a pure mathematical exercise; therefore

it is not taking into account the material fatigue properties in the critical plane search [16]. Due to that, in some cases, the experimental direction of the crack initiation plane has been different from the critical plane models estimates, as reported in literature [3]. However, some critical plane models such as Carpinteri & Spagnoli criterion [52, 53], takes in consideration a fatigue anisotropy approach and includes material properties in the critical plane search methodology. In this criterion, the critical plane is firstly determined using a specific formulation to capture fatigue anisotropy and then it is performed the projection of the normal and shear stress amplitudes on that plane to compute the damage parameter.

Previous studies clearly show that the loading path trajectory has a strong influence in the materials fatigue life, leading to conclude that the stress amplitudes by itself cannot justify the damage process [20, 33, 34, 56–58]. Furthermore, the material properties generally used, namely yield stress ratio or fatigue limit ratio $f_{-1}/\tau_{-1}$ are not sensitive to the physical damage process inherent to the loading path shape. This properties are determined under uniaxial conditions, and are used for all kinds of loading paths, uniaxial and multiaxial [54]. Therefore, the damage scale effect between shear and normal stresses along the loading path trajectory is missing.

Other approach, where it is taken into account the loading path effect, can be found in fracture mechanics, the analysis of fatigue crack growth is related to the stress intensity factor (SIF) variation. In a multiaxial approach, the equivalent stress intensity factor is usually obtained by adding the SIF factors inherent to the activated fatigue crack modes along the loading period [59, 60]. However, these factors are not directly added, they are also corrected in order to capture the combined effect in a multiaxial fatigue crack growth process. The combined effect of stress intensity factors also remains unclear and it is difficult to quantify the physical damage behaviour under a three-dimensional fatigue crack process.

The materials ability to resist a multiaxial cyclic loading is deeply related to the loading path trajectory, and not only related to the normal and shear stress amplitudes. This directional capability to cyclically resist to a cyclic loading is a material property that cannot be ignored and must be quantified.

### 2.4.2 Equivalent stress

The scientific community research in the multiaxial fatigue field remains under pursuit of an optimal criteria to estimate fatigue life under multiaxial loading conditions. Several criteria have been developed and proposed in the literature [16], however, some of them are difficult to implement and have many constraints. Due to that, and due to the difficulties found in the verification and validation of these criteria their use has being limited to their authors. Moreover, many models proposed in the literature are validated by the

own author data and usually are not corroborated with other authors lab work. In this context, a simple multiaxial fatigue method is of prime importance to create a more general methodology to be validated and used by other researchers and engineers in an easy way.

There are about three main categories in multiaxial fatigue characterization, i.e. critical plane, stress invariants and integral approaches [61]. The most common equivalent stress approaches are based in the yield criteria to evaluate fatigue damage. These approaches are the maximum principal stress, maximum shear stress (Tresca), and the octahedral stress commonly known as the von Mises equivalent stress. The performance of these equivalent stresses have some limitations regarding their capability to capture fatigue damage, however they are very appreciated and used due to their straightforward usability. Moreover, for few materials and loading paths these approaches have acceptable correlations. Nevertheless, their use in non-proportional loading conditions is not advised. Under such loading conditions the principal axes directions vary during the loading period, however, equivalent stress approaches do not have mechanisms to account this feature.

One reason for this shortcoming is settled in the yield criteria formulations used to define equivalent stresses, which were developed for static loading conditions and later adopted to be used to assess multiaxial fatigue. Essentially, the only difference between the yield criteria (static equivalent stresses) and equivalent stress approaches for fatigue is the loading pattern. Usually, they are used accordingly to the material ductility, for instance the von Mises equivalent stress are used to evaluate ductile materials and the maximum principal stress to evaluate materials with a fragile fatigue crack behaviour such as cast iron. Principal stresses used in these equivalent stresses are determined based in a referential rotation (or elemental cube rotation) in such way that the rotated stress tensor has only normal stresses. This rotation eliminates the shear stress components and defines the principal axes directions. These normal stresses (principal stresses) are ordered accordingly to their decreasing value as follows in expression 2.12:

$$\sigma_1 > \sigma_2 > \sigma_3 \tag{2.12}$$

Therefore for two-dimensional stress state the principal stresses are calculated as follows in Eq.(s) 2.13 and 2.14.

$$\sigma_1 = \frac{\sigma_x + \sigma_y}{2} + \sqrt{\left(\frac{\sigma_x - \sigma_y}{2}\right)^2 + {\tau_{xy}}^2} \tag{2.13}$$

$$\sigma_2 = \frac{\sigma_x + \sigma_y}{2} - \sqrt{\left(\frac{\sigma_x - \sigma_y}{2}\right)^2 + {\tau_{xy}}^2} \tag{2.14}$$

The principal directions are given by Eq. 2.15.

$$\tan(2\theta_p) = \frac{2\tau_{xy}}{\sigma_x - \sigma_y} \tag{2.15}$$

where $\theta_p$ is the rotation of the stress tensor axes in order to eliminate any shear stresses.

#### 2.4.2.1 Maximum principal stress theory

The idea behind this theory is that failure occurs when the maximum principal stress reaches the value of the material tensile yield stress. Therefore, for a given stress state, the principal stresses are calculated and compared with the material yield stress. Under cyclic loading conditions the maximum principal stress within a loading cycle is the equivalent stress used to estimate fatigue damage. Eq. 2.16 presents the formulation for this equivalent stress.

$$\Delta\sigma_{eq} = \Delta\sigma_1 \tag{2.16}$$

In this way, a multiaxial stress state is reduced to a uniaxial one by considering the highest principal stress time variation.

#### 2.4.2.2 Maximum shear stress theory

Similarly to the maximum principal stress theory, the maximum shear stress theory uses the principal stress time variation to estimate fatigue damage. In this criterion, it is considered that the fatigue damage results only from shear stresses (Tresca hypothesis). Eq. 2.17 presents the equivalent stress from this criterion.

$$\Delta\tau_{13} = \frac{\Delta\sigma_{eq}}{2} = \frac{\Delta\sigma_1 - \Delta\sigma_3}{2} \tag{2.17}$$

#### 2.4.2.3 Boiler and pressure vessel code

The ASME Boiler and Pressure Vessel code Procedure [62] is based on the von Mises hypothesis, but employs the stress difference between to two arbitrary instants $t_1$ and $t_2$ within the loading period:

$$\Delta\sigma_{eq} = \frac{1}{2\sqrt{2}}\sqrt{(\Delta\sigma_x - \Delta\sigma_y)^2 + (\Delta\sigma_y - \Delta\sigma_z)^2 + (\Delta\sigma_z - \Delta\sigma_x)^2 + 6\left(\Delta{\tau_{xy}}^2 + \Delta{\tau_{yz}}^2 + \Delta{\tau_{xz}}^2\right)} \tag{2.18}$$

where the equivalent stress range $\Delta\sigma_{eq}$ is maximized with respect to time. In some non-proportional loadings Eq. 2.18 yields lower equivalent stress ranges comparatively

to in-phase loadings with same stress level, this feature increases the fatigue life estimates for non-proportional loadings, which is in contradiction with experimental results.

#### 2.4.2.4 Maximum octahedral shear stress

This criterion is also based in the principal stresses time variation. In this case, it is considered a plane equally inclined to the principal axis. Next up, the norm resulted from the three principal stresses is projected into this plane, the octahedral plane. Under cyclic loadings, this projection forms a trajectory from which it is measured the maximum octahedral shear stress amplitude in time. Eq. 2.19 presents the formulation for this equivalent stress.

$$\Delta\sigma_{eq} = \frac{1}{\sqrt{2}}\sqrt{\left(\Delta\sigma_1 - \Delta\sigma_2\right)^2 + \left(\Delta\sigma_2 - \Delta\sigma_3\right)^2 + \left(\Delta\sigma_3 - \Delta\sigma_1\right)^2} = \Delta\tau_{oct}\frac{3}{\sqrt{2}} \tag{2.19}$$

This equivalent stress is unsuitable to be used under non-proportional loading conditions, because the shear stress amplitude is calculated in the octahedral plane, and under non-proportional loadings the direction of this plane changes in time, therefore the octahedral shear stress values time variation are within several octahedral planes. Due to this fact, it is not possible measure the octahedral shear stress amplitude in one octahedral plane. Therefore, under non-proportional loading conditions, Eq. 2.19 gives ambiguous results.

#### 2.4.2.5 Effective equivalent stress hypothesis (EESH)

Sonsino [63, 64] proposed a hypothesis for ductile materials under multiaxial loading conditions where fatigue damage is estimated by an equivalent stress. This equivalent stress is a modification of the von Mises equivalent stress in order to account the size effects and their different stress gradients. Eq. 2.20 presents the EESH formulation for proportional loadings.

$$\sigma_{eq}\left(\delta_{xy} = 0^{\mathrm{o}}\right) = \sqrt{\sigma_{xa}^2 + \sigma_{ya}^2 + f3\tau_{xya}^2} \tag{2.20}$$

Where $f$ is a parameter that has into account the gradient effect from bending and torsion loading conditions, the $f$ parameter is determined as follows in Eq. 2.21.

$$f = \frac{\sqrt{\sigma_{xa}^2 + \sigma_{ya}^2 - \sigma_{xa}\sigma_{ya}}}{\sqrt{3}\tau_{xya}} \tag{2.21}$$

#### 2.4.2.6 von Mises

The von Mises yield criterion is based on the assumption that only shear stress cause plastic flow and hydrostatic stress cause no effect on the yield process [65]. Under this approach, the shear stress is measured through the second deviatoric stress invariant, generally represent as $J_2$. This equivalent stress, despite being a yield criterion, has been widely used as a simple and feasible multiaxial fatigue model. Moreover, its graphic representation of its variation during the load period is very representative of the loading path type, where it is possible to measure an equivalent stress amplitude, which can be used as a multiaxial fatigue parameter. This approach has known shortcomings, particularly in out-of-phase loading cases. Considering a general stress tensor given in Eq. 2.22, the deviatoric stress tensor is computed by removing the equivalent hydrostatic pressure component from the stress tensor as follows in Eq.(s) 2.23 to 2.25.

$$S_{ij} = \begin{bmatrix} \sigma_{xx} & \tau_{xy} & \tau_{xz} \\ \tau_{yx} & \sigma_{yy} & \tau_{yz} \\ \tau_{zx} & \tau_{zy} & \sigma_{zz} \end{bmatrix} \tag{2.22}$$

$$D_{ij} = S_{ij} - I \cdot \frac{tr\left(S_{ij}\right)}{3} \tag{2.23}$$

Thus, the second deviatoric stress tensor invariant is given by:

$$J_2 = \frac{1}{2} D_{ij} \cdot D_{ji} \tag{2.24}$$

In terms of principal stresses:

$$J_2 = \frac{1}{2}\left(\left(\sigma_1 - \sigma_2\right)^2 + \left(\sigma_2 - \sigma_3\right)^2 + \left(\sigma_3 - \sigma_1\right)^2\right) \tag{2.25}$$

Considering the uniaxial case, were $\sigma_1 = \sigma_0$ and $\sigma_2 = \sigma_3 = 0$, it is obtained the following expression:

$$J_2 = \frac{1}{3}(\sigma_0)^2 \sqrt{J_2} = \frac{\sigma_0}{\sqrt{3}} \tag{2.26}$$

Through this expression, it is obtained, for a specific loading case i.e. pure axial, one relation between normal and shear stresses. Considering this result, the material yielding will occur when $\sqrt{J_2}$ exceeds the yield stress in pure shear conditions i.e. $\sqrt{J_2} = k$, thus Eq. 2.27 is valid.

$$\sqrt{3}k = \sigma_0 \tag{2.27}$$

Therefore, the von Mises damage stress scale is given by $\frac{1}{\sqrt{3}}$, indicating that the shear stress necessary to cause yielding is 1.73 times lower than the normal stress. This is a purely theoretical result, being independent of the material monotonic and cyclic properties, however, it has good results fro quasi-static loading conditions.

### 2.4.3 Invariant stress

The invariant criteria are based on the premise that a generic stress tensor can be split into two other stress tensors, i.e. the deviatoric and the hydrostatic tensors. Another premise adopted in these models, is the assumption of the crack nucleation process results mainly from the shear stress/strain contribution in the HCF regimen. Moreover, it is also assumed that the hydrostatic stress has a secondary role during the fatigue process. Under this paradigm, the shear stress amplitude assessment is of prime importance and is usually determined based in the deviatoric stress tensor. The invariant approaches evaluate the shear stress amplitude in the $\pi$ plane, which can be updated with the hydrostatic stress contribution as seen in some multiaxial criteria, such as Sines [66] , Crossland [39], or Dang Van [47], for instance.

Conventionally, the shear stress amplitude is usually evaluated by the Longest Projection (LP) approach or by the Minimum Circunscribed Circle (MCC) computed in the von Mises shear stress space in which the equivalence $\tau = \sigma/\sqrt{3}$ or the Tresca equivalence $\tau = \sigma/2$ are used under multiaxial loading conditions to reduce both normal and shear damages to the same damage scale [67]. Based on experiments it was found out that the damage scale between shear and the normal stresses may vary significantly depending on the material type.

For example, the ratio of the torsion fatigue limit to the bending fatigue limit varies from 0.5 for mild metals to 1 for brittle metals [16]. However, invariant models do not have this physical evidence in to account and use a damage scale independent from the material type.

Every second rank tensor can be decomposed into a deviatoric and a hydrostatic component as follows:

$$\sigma_{ij} = s_{ij} + p\delta_{ij} \tag{2.28}$$

Where $s_{ij} = \sigma_{ij} - p\delta_{ij}$ is the deviatoric tensor, $p = \frac{1}{3}\sigma_{kk}$ is the hydrostatic one, and $\delta_{ij}$ is the kronecker delta. Therefore, the deviatoric invariants are calculated as follows:

$$J_1 = s_{kk} = 0 \tag{2.29}$$

$$J_2 = \frac{1}{2} s_{ij} s_{ji} \tag{2.30}$$

$$J_3 = \det(s_{ij}) \tag{2.31}$$

The tensor invariants are calculated as follows:

$$I_1 = \sigma_{kk} \tag{2.32}$$

$$I_2 = \frac{1}{2} (\sigma_{ii}\sigma_{jj} - \sigma_{ij}\sigma_{ji}) \tag{2.33}$$

$$I_3 = \det(\sigma_{ij}) \tag{2.34}$$

#### 2.4.3.1 Crossland criterion

In the Crossland criterion [39], the shear stress amplitude is obtained through the second invariant of the deviatoric stress tensor, contrary to the observed in the von Mises yield criterion, this one considers that the fatigue damage results from the shear stress amplitude and from the maximum value of the hydrostatic stress computed during the loading period. The damage parameter is determined through the addition of both deviatoric and hydrostatic stresses using a stress scale factor (SSF) to reduce the hydrostatic stress to the shear stress space (reduce normal stress damage to the shear damage scale). The failure is expected to occur when the damage parameter exceeds the material fatigue limit in pure shear loading conditions. The Crossland criterion formulation is given in Eq.(s) 2.35 to 2.37.

$$\sqrt{J_{2_a}} + \frac{\beta}{\alpha} \cdot \sigma_{H,\max} \leq \frac{f_{-1}}{\alpha} \tag{2.35}$$

$$\alpha = \frac{f_{-1}}{t_{-1}}; \beta = 3 - \sqrt{3}\frac{f_{-1}}{t_{-1}} \tag{2.36}$$

$$\sqrt{J_{2_a}} + \left(3\frac{t_{-1}}{f_{-1}} - \sqrt{3}\right)\sigma_{H,\max} \leq t_{-1} \tag{2.37}$$

In this criterion, the stress scale factor is given by $3\frac{t_{-1}}{f_{-1}} - \sqrt{3}$, which is a constant value defined through the uniaxial fatigue stress limits in tension and shear.

#### 2.4.3.2 Sines criterion

The Sines criterion [46] is very similar to the Crossland criterion; here the damage parameter is defined through the summation of the shear stress amplitude and the mean hydrostatic stress. The shear stress amplitude is computed by the square root of the amplitude of the deviatoric's second invariant. In this criterion the hydrostatic stress is also reduced to the shear stress space using a stress scale factor. The damage parameter is given by the following Eq.(s):

$$\sqrt{J_{2_a}} + \frac{\beta}{\alpha} \cdot \sigma_{H,\mathrm{m}} \leq \frac{f_{-1}}{\alpha} \tag{2.38}$$

$$\alpha = \frac{f_{-1}}{t_{-1}}; \beta = 6\frac{f_{-1}}{f_0} - \sqrt{3}\frac{f_{-1}}{t_{-1}} \tag{2.39}$$

The original formulation of the Sines criterion uses the axial fatigue limit in repeated bending, which is a seldom parameter difficult to obtain in literature which can be a shortcoming to implement this model. However, it can be used the modified Goodmann line to estimate the repeated bending limit. Figure 2.15 shows a repeated bending loading where it can be identified the loading amplitude and its mean stress.

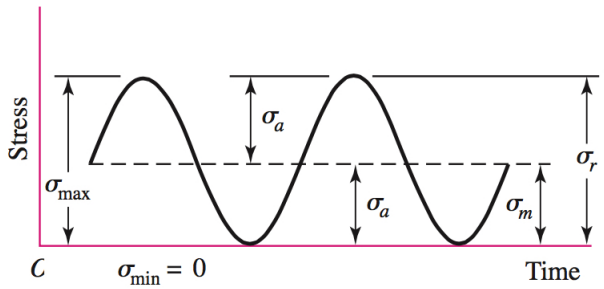


**Figure 2.15:** Illustration of a repeated bending loading with its stress amplitude and mean stress [68].

The Goodman line is as follows in Eq. 2.40 [68].

$$\frac{\sigma_a}{f_{-1}} + \frac{\sigma_m}{\sigma_{ut}} = 1 \tag{2.40}$$

Replacing $\sigma_a$ and $\sigma_m$ by $f_0$ in Eq. 2.40 it yields:

$$\frac{f_0}{f_{-1}} + \frac{f_0}{\sigma_{ut}} = 1 \tag{2.41}$$

Solving for $f_0$ Eq. 2.41 it yields Eq. 2.42,

$$f_0 = \frac{1}{\frac{1}{f_{-1}} + \frac{1}{\sigma_{ut}}} \tag{2.42}$$

Multiplying the right side of Eq. 2.42 by $f_{-1}$ it is obtained Eq. 2.43 from which it is estimated $f_0$.

$$f_0 = \frac{f_{-1}}{1 + \frac{f_{-1}}{\sigma_{ut}}} \tag{2.43}$$

where $\sigma_{ut}$ is the material ultimate tensile strength. Eq. 2.44 shows the Sines criterion adapted to the most common materials properties. In this model the fatigue failure is expected to occur when the damage parameter exceeds the uniaxial shear fatigue limit. This criterion is unsuitable to be used as equivalent stress because their SSF is only dependent on the tension compression fatigue limit; being usually used as a on-off fatigue model to estimate failure or no failure conditions for infinite life. Therefore, this criterion is unsuitable to be used in finite fatigue life estimates.

$$\sqrt{J_2}_a + \left(\sqrt{3}\frac{f_{-1}}{\sigma_{ut}}\right)\sigma_{H,\mathrm{m}} \leq t_{-1} \tag{2.44}$$

In this criterion, the stress scale factor is given by: $\sqrt{3}\frac{f_{-1}}{\sigma_{ut}}$.

#### 2.4.3.3 Vu criterion

Vu et al. [69] proposed an invariant equivalent stress for the high cycle fatigue regime (more than $10^4$ cycles). The central piece of their model is the introduction of the mean value of the second invariant of the deviatoric tensor, $J_{2mean}$. As stated by the authors, with the introduction of this parameter it is possible to capture several loading effects such as non-proportionality, effect of mean normal stresses, and fatigue damage from asynchronous loadings. The authors divided this criterion accordingly to the material ultimate tensile strength, $\sigma_{ut}$. Eq.(s) 2.45 and 2.46 presents the formulation for this criterion.

For $\sigma_{ut} < 750MPa$; $\gamma_1 = 0.65$; $\gamma_2 = 0.8636$, the equivalent stress takes the following shape:

$$f = \sqrt{\gamma_1 J_2^{'}(t)^2 + \gamma_2 J_{2,mean}^2 + \gamma_3 \left( I_{1,a} + I_{1,m} \right)} < \beta \tag{2.45}$$

For $\sigma_{ut} > 750MPa$; $\gamma_1 = 0.3$; $\gamma_2 = 1.7272$, the Vu equivalent stress is as follows:

$$f = \sqrt{\gamma_1 J_2^{'}(t)^2 + \gamma_2 J_{2,mean}^2 + \gamma_3 \left( I_{1,a} + \frac{f_{-1}}{t_{-1}} I_{1,m} \right)} < \beta \tag{2.46}$$

Where $\gamma_1, \gamma_2, \gamma_3$ and $\beta$ are material parameters determined by experiments; $J_2^{'}(t)$ and $J_{2,mean}$ aims to account the phase shift effect within non-proportional loadings, and shear stress effects. $I_{1,a}$ and $I_{1,m}$ aims to account the effects of the hydrostatic stress such as amplitude level and mean values.

#### 2.4.3.4 Kakuno-Kawada criterion

Kakuno and Kawada [70] developed an invariant criterion taking into account the hydrostatic amplitude and their mean value. The criterion formulation is as follows:

$$\sqrt{J_{2,a}} + k\sigma_{H,a} + \lambda\sigma_{H,m} \leq \mu \tag{2.47}$$

Where $k = \frac{(3t_{-1})}{f_{-1}} - \sqrt{3}$ , $\lambda = \frac{(3t_{-1})}{f_0} - \sqrt{3}$ , and $\mu = t_{-1}$. $t_{-1}$ is the fatigue limit under fully reversed torsion, $f_{-1}$ is the fatigue limit under fully reversed bending, and $f_o$ is the fatigue limit under repeated bending (zero to tension).

#### 2.4.3.5 Minimum circumscribed ellipse (MCE)

The minimum circumscribed ellipse approach (MCE) [7, 71] was proposed to compute the effective shear stress amplitude taking into account the non-proportional loading effects. The MCE concept is based on a minimum circumscribed ellipse construction around the loading path trajectory represented on the deviatoric stress space, usually the von Mises stress space. The MCE shear stress amplitude is given by:

$$\sqrt{J_{2,a}} = \sqrt{R_a^2 + R_b^2} \tag{2.48}$$

where $R_a$ and $R_b$ are the lengths of the major and minor semi-axis of the minimum circumscribed ellipse, respectively. The MCE approach proposed in [7, 71] gives very good prediction for sinusoidal stress wave forms and so on, but may be very conservative for some special multiaxial loading paths. For example, for the triangular shear stress paths shown in Figure 2.16, the original procedure of the MCE approach had the drawback in

which it is obtained the same "minimum ellipse" for both stress paths A and B, even when the length $\delta$ of the stress path B becomes very small as shown in Figure 2.16 a). This drawback leads to the same measure of shear stress amplitude in the two different paths A and B, which gives very conservative results in loading path B.

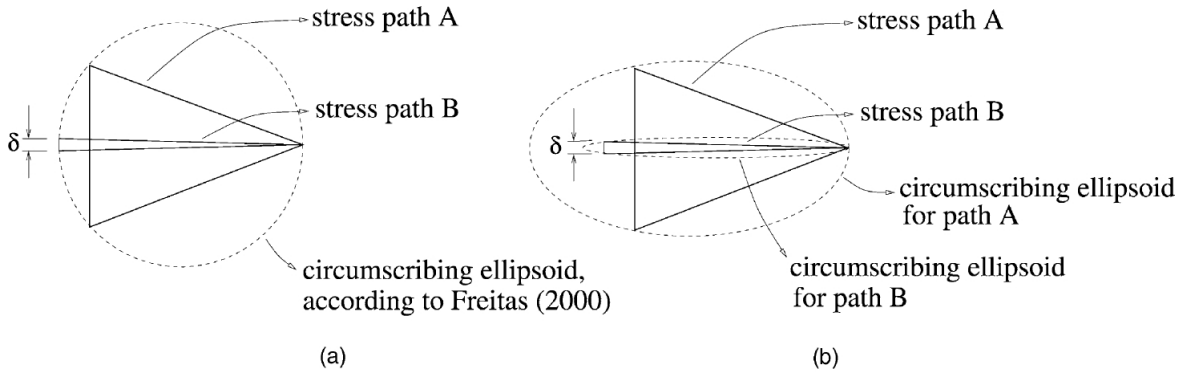


**Figure 2.16:** a) Drawback of the original MCE procedure proposed by Freitas et al., b) Circumscribing ellipsoid [72] .

In order to overcome the described drawback in the original MCE approach, a modified procedure was proposed in [71]. In this modification, the Minimum Circumscribed Circle (MCC) is firstly found and the major semi-axis $R_a$ is determined as shown in Figure 2.17, then it is calculated the maximum normal distance to the major semi-axis, $R_a$ , in the circumscribed loading. This distance was named as $R_b$ and is defined as depicted in Figure 2.17.

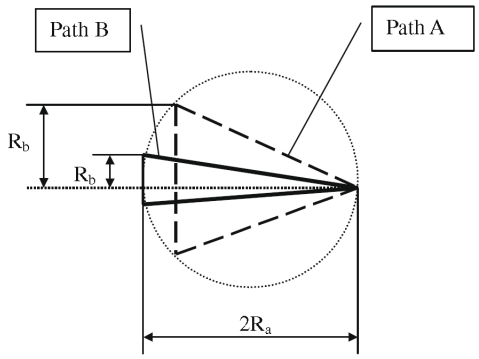


**Figure 2.17:** Modified procedure of the MCE approach for determining $R_a$ and $R_b$ [71].

This modified procedure of the MCE approach introduces the "minimum circumscribed rectangle" (MCR) approach to overcome the drawback depicted in Figure 2.16 a). Figure 2.18 shows that different $R_a$ and $R_b$ values can be evaluated for the same rectangle loading path by two approaches. The MCR approach gives $R_a$ values much more sensitive to the loading path shape than the MCE approach. Therefore, the modified procedure of the MCE approach (The MCR approach) is able to give more accurate results.

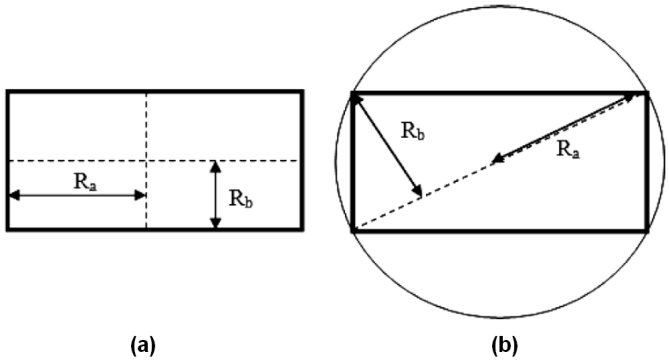


**Figure 2.18:** (a) Illustration of the differences between the evaluated Ra and Rb values by the minimum circumscribed rectangle approach (MCR) and (b) by the modified procedure of the MCE approach, for the same rectangle loading path shown [71].

The shear stress amplitude determined using the MCE approach can be used in invariant criteria such as Sines or Crossland as follows in Eq. 2.49.

$$\sqrt{J_{2,a}} + \alpha \cdot \sigma_H \leq \beta \tag{2.49}$$

where $\alpha$ is the stress scale factor that reduces the fatigue damage from normal stresses to the shear damage scale, $\sigma_H$ is the hydrostatic stress, which is set according to the multiaxial criterion to be used, i.e. the Sines criterion uses the mean hydrostatic stress, and the Crossland uses the maximum hydrostatic stress. The $\beta$ parameter is the material fatigue strength in pure shear. The stress scale factor represented here by the $\alpha$ parameter is selected accordingly to the models Sines or Crossland.

### 2.4.4 Critical plane damage parameter

The critical plane approach had great popularity in the last years due to the simple physical concept involved around their methodology, which ease to understand and ease to implement in numeric simulations. It is common to find in the literature multiaxial energy models based on critical plane formulations [73, 74] or even integral ones [61, 75, 76]. Integral approaches are based in mean stresses within a elementary volume, where the fatigue damage is accounted in all possible material planes [8, 61]. The main methodology in critical plane approaches is to find the critical plane where the damage parameter reach their maximum value.

Basically, the multiaxial loading components, normal and shear stresses, are projected in each plane using the Mohr's circle, then the damage parameter is computed accordingly to each criterion.

Also, in critical plane models it is used the damage stress scale concept i.e. on each plane, the shear component of a given critical plane damage parameter is updated with the normal

component previously reduced to the shear damage scale using a stress scale factor, this procedure can be found in critical plane criteria such as Findley [77], Fatemi-Socie [54, 73], among others. Despite the popularity achieved by this approach, critical plane criteria have some shortcomings. In some loading cases, the same stress amplitude can be obtained for different planes, indicating several critical planes, i.e. several directions for the crack initiation plane. However, fractographic examinations of samples tested in such loading conditions generally indicate only one crack initiation spot. The critical plane is identified by an angle (direction), usually represented as $\theta$, please see Figure 2.19. The search of this angle is usually performed within the range $[0, \pi]$. Moreover, the stresses and strains in each plane $\theta$ are determined using the Mohr's circle as follows in Eq.(s) 2.50 to 2.53.

$$\sigma_\theta = \frac{\sigma_x + \sigma_y}{2} + \frac{\sigma_x - \sigma_y}{2}\cos(2\theta) + \tau_{xy}\sin(2\theta) \tag{2.50}$$

$$\tau_\theta = \frac{\sigma_x - \sigma_y}{2}\sin(2\theta) - \tau_{xy}\cos(2\theta) \tag{2.51}$$

$$\varepsilon_\theta = \frac{\varepsilon_x + \varepsilon_y}{2} + \frac{\varepsilon_x - \varepsilon_y}{2}\cos(2\theta) + \frac{\gamma_{xy}}{2}\sin(2\theta) \tag{2.52}$$

$$\frac{\gamma_\theta}{2} = \frac{\varepsilon_x - \varepsilon_y}{2}\sin(2\theta) - \frac{\gamma_{xy}}{2}\cos(2\theta) \tag{2.53}$$

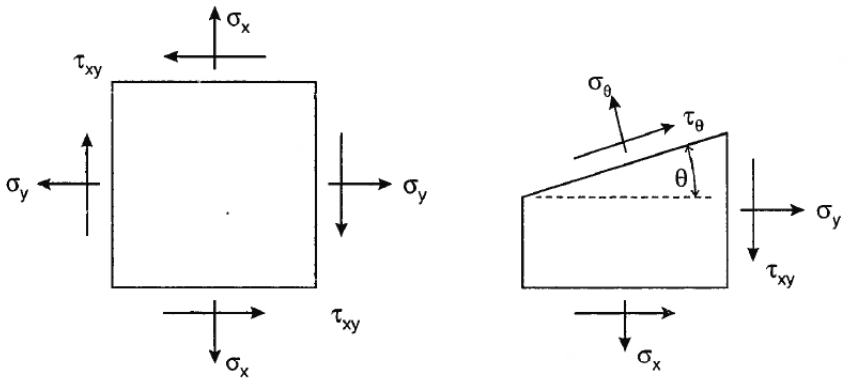


**Figure 2.19:** Plane stress loading of a plate [16].

#### 2.4.4.1 Critical plane criteria - Stress based models

**Findley**

Findley [77, 78] proposed a critical plane criterion to estimate the orientation of the fatigue crack initiation plane the material's fatigue strength under multiaxial loading conditions.

The critical plane is identified by determining the plane with the maximum damage parameter, which formulation is given in Eq. 2.54.

$$\max_{\theta} \left(\tau_a + k\sigma_{a,\max}\right) \tag{2.54}$$

Where $\tau_a$ is the shear stress amplitude determined on a plane $\theta$, $\sigma_{n,\max}$, is the maximum normal stress on that plane and $k$ is a stress scale factor. The fatigue life can be estimated using the maximum Findley parameter which is an equivalent shear stress computed in the critical plane. Fatigue life estimates for this criterion are obtained using Eq.(s) 2.55 and 2.56.

$$\tau_a + k\sigma_{a,\max} = \tau^*(N_f)^b \tag{2.55}$$

$$\tau^* = \sqrt{1+k^2}\tau' \tag{2.56}$$

Where $\tau'$ is the torsional fatigue strength coefficient, and the $\sqrt{1+k^2}$ is correction factor typically equal to 1.04.

In this criterion, the update of the normal stress to the shear damage scale is computed through the $k$ parameter, which is determined by experiments accordingly to the material fatigue strength ratio given by $\sigma_{a,R=-1}/\tau_{a,R=-1}$ . The $k$ parameter is determined as follows in Eq. 2.57:

$$\frac{\sigma_{a,R=-1}}{\tau_{a,R=-1}} = \frac{2}{1+\frac{k}{\sqrt{1+k^2}}} \tag{2.57}$$

Typically, the $k$ parameter varies between 0.2 and 0.3 for ductile materials.

### Matake criterion

This criterion [51] is a typical critical plane model, it considers the maximum shear stress amplitude added to the maximum normal stress updated through a stress scale factor. The critical plane is identified through the plane in which the maximum damage parameter occurs. Comparing this criterion with the invariant methods, the deviatoric second invariant amplitude is replaced by the critical plane shear stress amplitude, and the hydrostatic stress is replaced by the maximum normal stress on a given plane. The criterion takes the following form:

$$\alpha \cdot C_a + \beta \cdot N_{\max} \leq f_{-1} \tag{2.58}$$

$$\alpha = \frac{f_{-1}}{t_{-1}}; \beta = 2 - \frac{f_{-1}}{t_{-1}} \tag{2.59}$$

where:

$$\frac{\beta}{\alpha} = 2 \cdot \frac{t_{-1}}{f_{-1}} - 1 \tag{2.60}$$

The Matake criterion in the shear stress space is as follows in Eq. 2.61:

$$C_a + \left(2 \cdot \frac{t_{-1}}{f_{-1}} - 1\right) N_{\max} \leq t_{-1} \tag{2.61}$$

In this case the SSF parameter is given by: $2 \cdot \frac{t_{-1}}{f_{-1}} - 1$.

**McDiarmid criterion**

The McDiamid criterion [49, 50] is also based on the critical plane approach, having the particularity to consider two crack propagation modes, case A and case B. In case A, the crack propagation occurs along the surface, and in case B, the propagation occurs from the outside surface towards their inside. The criterion formulation is presented in Eq. 2.62:

$$\frac{\tau_a}{\tau_{A,B}} + \frac{\sigma_{n,\max}}{2 \cdot \sigma_{ut}} = 1 \tag{2.62}$$

where $\tau_A$ is the shear fatigue strength of case A crack growth, $\tau_B$ is for case B, and $\sigma_{ut}$ is the material ultimate tensile strength. Eq. 2.63 presents the McDiamid criterion to estimate fatigue lives under multiaxial loading conditions.

$$\tau_a + \left(\frac{\tau_{A,B}}{2 \cdot \sigma_{ut}}\right) \sigma_{n,\max} = \tau_{A,B} \tag{2.63}$$

where the stress scale factor is given by: $\frac{\tau_{A,B}}{2 \cdot \sigma_{ut}}$

### Dang Van criterion

Dan Van [47, 48] proposed a mesoscopic criterion considering the volume approach, which was posteriorly simplified through a mix of invariant and critical plane type criteria. In this model, it is performed a critical plane search based in the maximum value of the shear stress amplitude. Then, the normal stress component is computed in the critical plane through the hydrostatic stress assessment, which due to their physical definition can be considered as equal in all planes. This model is computed as follows in Eq.(s) 2.64 and 2.65.

$$C_a + \frac{\beta}{\alpha} \cdot \sigma_{H,\max} \leq t_{-1} \tag{2.64}$$

$$\alpha = \frac{f_{-1}}{t_{-1}}; \beta = 3\left(1 - \frac{f_{-1}}{2 \cdot t_{-1}}\right) \tag{2.65}$$

Here, the stress scale factor is based in the material fatigue limits, and is given by: $3\left(\frac{\tau_{-1}}{f_{-1}} - \frac{1}{2}\right)$.

### Carpinteri-Spagnoli criterion

Carpintery et al. [52, 53] proposed a critical plane criterion with atypical mechanism for the critical plane search. In this model, the critical plane is defined through a particular formula based on material properties, then the shear and normal stress amplitudes are calculated in this plane. The normal stress amplitude is determined based on a weight function with the possibility to account for mean stress values through the Goodman diagram procedures. In this model, the normal stress is considered as an equivalent normal stress. Moreover, in this model it is performed a linkage between the material properties and the critical plane search, which is a special feature that cannot be found in typical critical plane models. Furthermore, the damage parameter is obtained by considering the root mean square of the biaxial loading components, contrary to that is seen in previous models where the equivalent damage parameter results from adding shear and normal stresses updated to the shear stress space. Eq. 2.66 presents the Carpintery-Spagnoli criterion.

$$\left(\frac{C_a}{t_{-1}}\right)^2 + \left(\frac{N_{a,eq}}{f_{-1}}\right)^2 = 1 \tag{2.66}$$

Reduced to the shear stress space, the criterion takes the form:

$$C_a{}^2 + \left(\frac{t_{-1}}{f_{-1}} N_{a,eq}\right)^2 = (t_{-1})^2 \tag{2.67}$$

In this case the stress scale factor is given by: $\frac{t_{-1}}{f_{-1}}$.

#### 2.4.4.2 Critical plane criteria - Strain based models

**Fatemi-Socie**

Fatemi and Socie [54] proposed a strain based model based in the critical plane concept. Here, the shear strain amplitude and maximum normal stress is determined in each plane, then the shear stress amplitude is multiplied by the ratio of the maximum normal stress to the material yield stress, as shown in Eq. 2.68. The critical plane orientation is estimated with the maximum Fatemi-Socie damage parameter.

$$\left[\frac{\Delta\gamma}{2}\left(1 + k_{F-S}\frac{\sigma_{n,\max}}{\sigma_y}\right)\right]_{\max_\theta} \tag{2.68}$$

where $\Delta\gamma/2$ is the maximum shear strain amplitude on plane $\theta$, $\sigma_{n,\max}$ is the maximum normal stress on that plane, $\sigma_y$ is the material monotonic yield strength and $k$ is the sensitivity factor that depends on the stress level. Some authors of strain based models show some sensibility to the fact that the stress scale factor is not constant, which is the cases of Fatemi-Socie and Brown-Miller criteria. However, they only cover the stress level influence on the stress scale factor variation. In the Fatemi-Socie model that variation is given by the sensitivity factor, $k$, which formulation is presented in Eq. 2.69

$$k = \left[\frac{\frac{\tau_f^{'}}{G}(2N_f)^{b\gamma} + \gamma_f^{'}(2N_f)^{c\gamma}}{1.3\frac{\sigma_f^{'}}{E}(2N_f)^b + 1.5\varepsilon_f^{'}(2N_f)^c} - 1\right]\frac{K'(0.002)^{n'}}{\sigma_f^{'}(2N_f)^b} \tag{2.69}$$

where one can see that $k$ is not constant and vary with fatigue life. For finite fatigue live estimates, the authors suggests $k = 0.3$, however $k = 1$ has also been used [3].

**Brown and Miller**

Brown and Miller performed a deep review in multiaxial fatigue criteria and concluded that the octahedral shear strain and maximum shear strain criteria do not describe effectively the low-cycle fatigue behaviour.To better understand this matter, the authors conducted combined tension and torsion tests and concluded that it is needed two strain parameters accordingly to the type of fatigue crack nucleation and growth. Brown and Miller [55] proposed two criteria for each type of fatigue crack, given in Eq.(s) 2.70 and 2.71.

For A type cracks:

$$\left(\frac{\Delta\gamma}{g}\right)^{j} + \left(\frac{\varepsilon_n}{h}\right)^{j} = 1 \tag{2.70}$$

For B type cracks:

$$\frac{\Delta\gamma}{2} = const. \tag{2.71}$$

Where $g$, $h$ and $j$ are material parameters. The $j$ parameter is set according to the material ductility, i.e. for brittle materials $j$ is equal to 1, and for ductile materials $j$ is equal to 2. Figure 2.20 presents each crack type and inherent loading.

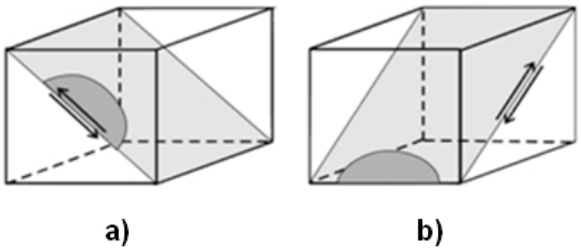


**Figure 2.20:** a) Case A crack mode; b) Case B crack mode [16].

The authors simplified the formulation of the case A crack initiation mode and proposed the equivalent shear strain criterion shown in Eq. 2.72.

$$\frac{\Delta\hat{\gamma}}{2} = \frac{\Delta\gamma_{\max}}{2} + S\Delta\varepsilon_n \tag{2.72}$$

Where the $S$ parameter is the normal strain effect coefficient, being calculated using Eq. 2.73 for a given material. This parameter is dependent on the temperature.

$$S = \frac{\frac{\tau_{\mathrm{f}}^{'}}{\mathrm{G}}(2\mathrm{N_f})^{\mathrm{b}\gamma} + \gamma_{\mathrm{f}}^{'}(2\mathrm{N_f})^{\mathrm{c}\gamma} - (1+\upsilon_{\mathrm{e}})\,\frac{\sigma_{\mathrm{f}}^{'}}{\mathrm{E}}(2\mathrm{N_f})^{\mathrm{b}} - (1+\upsilon_{\mathrm{p}})\,\varepsilon_{\mathrm{f}}^{'}(2\mathrm{N_f})^{\mathrm{c}}}{(1+\upsilon_{\mathrm{e}})\,\frac{\sigma_{\mathrm{f}}^{'}}{\mathrm{E}}(2\mathrm{N_f})^{\mathrm{b}} + (1+\upsilon_{\mathrm{p}})\,\varepsilon_{\mathrm{f}}^{'}(2\mathrm{N_f})^{\mathrm{c}}} \tag{2.73}$$

In this model, fatigue life is estimate using Eq. 2.74.

$$\frac{\Delta\gamma_{\max}}{2} + S\,\underset{n}{\Delta\varepsilon} = A\frac{\sigma_f^{'}}{E}(2N_f)^{b} + B\varepsilon_f^{'}(2N_f)^{c} \tag{2.74}$$

Where $A = 1.3 + 0.7S$ and $B = 1.5 + 0.5S$.

**Lohr & Ellison**

Lohr and Ellison [79] proposed a critical plane model based in shear and normal strains calculated on a specific plane, the $\pi/4$ plane to surface. Contrary to the procedures found in a typical critical plane, where it is pursuit the plane with highest damage parameter, here the equivalent strain is computed in the plane of maximum shear strain. This equivalent strain criterion is given in Eq. 2.75.

$$\gamma^* + k\varepsilon_n^* = C \tag{2.75}$$

Where $k$, and $C$ are material constants, $\varepsilon_n^*$ is the strain normal to plane of $\gamma^*$, and $\gamma^*$ is the maximum shear strain on the plane $\pi/4$ to surface. The authors by experimental tests concluded that $k = 0.2$ for high strength steels.

#### 2.4.4.3 Combined models (Critical Plane plus Energy models)

**SWT criterion**

Smith et al. [80] proposed a model, known as SWT, to account the mean stress effect under uniaxial loadings. Later on, this model was extended to multiaxial loading conditions by Dr. Darrell Socie by evaluating the SWT parameter under multiaxial loading conditions using a critical plane approach [16]. The critical plane version of the SWT criterion is based on the principal strain range, and on the maximum normal stress evaluated on the plane of the principal strain range, please see Eq. 2.76.

$$\max_{\theta} \left(\sigma_n\right) \frac{\Delta\varepsilon_1}{2} \tag{2.76}$$

where $\sigma_n$ is the normal stress on a plane $\theta$, and $\Delta\varepsilon_1$ is the principal strain range calculated in that plane. This model do not have any stress scale factor, since only considers the normal stress contribution to the fatigue damage process.

**Liu criterion**

Liu [81] proposed an energy method to estimate fatigue life based on the virtual strain energy (VSE) concept. This model considers two approaches for two different types of fatigue crack modes, namely: a tensile failure mode (mode I), $\Delta W_I$, and a shear failure mode (mode II), $\Delta W_{II}$. In this criterion, failure is expected to occur in a given plane $\theta$ where it is computed the maximum VSE quantity. Accordingly to the fracture mode I, the parameter, $\Delta W_I$ is given by Eq. 2.77.

$$\Delta W_I = \max_{\theta} \left(\Delta\sigma_n \Delta\varepsilon_n\right) + \Delta\tau\Delta\gamma \tag{2.77}$$

For mode II, the parameter, $\Delta W_{II}$ is given by Eq. 2.78

$$\Delta W_{II} = \Delta\sigma_n \Delta\varepsilon_n + \max_{\theta} \left(\Delta\tau\Delta\gamma\right) \tag{2.78}$$

where $\Delta\tau$ and $\Delta\gamma$ are the shear stress range and shear strain range, respectively. $\Delta\sigma_n$ and $\Delta\varepsilon_n$ are the normal stress range and normal strain range, respectively. Also here, it is not used any damage scale between normal and shear loadings. Therefore, the normal and shear energies are added directly, in this way the Liu damage parameter has a damage scale different from the uniaxial damage curves.

### Glinka

Based on the Brown Miller damage parameter paradigm [55], Glinka [82, 83] proposed an energy parameter expressed by normal and shear strains evaluated on the critical plane. The Glinka's damage parameter is as follows in Eq. 2.79.

$$\Delta W^* = \frac{\Delta\tau}{2}\frac{\Delta\gamma}{2} + \frac{\sigma_n}{2}\frac{\Delta\varepsilon_n}{2} \tag{2.79}$$

In order to account with mean stress effects, authors modified Eq. 2.79 as follows:

$$\Delta W^* = \frac{\Delta\tau}{2}\frac{\Delta\gamma}{2}\left(\frac{\sigma_f^{'}}{\sigma_f^{'} - \sigma_{n,\max}} + \frac{\tau_f^{'}}{\tau_f^{'} - \tau_{n,\max}}\right) \tag{2.80}$$

This modification results from the experimental observation of the normal stresses effect in the fatigue crack process, where compressive normal stresses difficult the crack growth and normal stresses in tension promotes the crack growth process.

### Pan criterion

Pan et al. [84] proposed an update to the Glinka's damage parameter [82] in order to add the fatigue damage contribution of the normal strain energy. The authors concluded that the strain energy in the shear direction cannot be directly added to the normal one. For this reason they conducted experimental tests and achieved two coefficients to correct the normal strain energy contribution to the overall fatigue damage. Eq. 2.80 presents the formulation for the Pan criterion.

$$\Delta W^* = \frac{\Delta\tau\Delta\gamma}{4} + k_1 k_2 \frac{\sigma_n \Delta\varepsilon_n}{4} \tag{2.81}$$

where $k_1 = \sigma_f^{'}/\tau_f^{'}$ , and $k_2 = \varepsilon_f^{'}/\gamma_f^{'}$ .

**Varhani-Farahani**

Varhani-Farahani [85] proposed an energy fatigue damage parameter taking into account the summation of strain energy ranges calculated in the critical plane. Here, the critical plane is the one with maximum shear strain amplitude determined using the Mohr's circle. Next up, the damage parameter calculation is performed in that plane using the maximum stress and strains amplitudes, which are also determined using the Mohr's circle during the loading cycle. This model has the drawback of be only valid for plane stress states.

$$W = \frac{\Delta\sigma_n \Delta\varepsilon_n}{\sigma_f^{'}\varepsilon_f^{'}} + \frac{1 + \frac{\sigma_{n,m}}{\sigma_f^{'}}}{\tau_f^{'}\gamma_f^{'}} \Delta\tau_{\max} \Delta\left(\frac{\gamma_{\max}}{2}\right) \tag{2.82}$$

### 2.4.5 Integral criteria

#### 2.4.5.1 Papadopoulos criterion

This model [8] is also a mesoscopic criterion based in the volume damage at mesoscopic scale, as seen in the Dang Van criterion. In this approach, the shear stress amplitude is determined by the mean shear stress amplitude obtained in the mesoscopic volume. The fatigue damage of normal stresses is accounted in this criterion through the maximum hydrostatic stress. Eq. 2.83 presents the criterion formulation.

$$\alpha\sqrt{\langle {T^2}_a \rangle} + \beta \cdot \sigma_{H,\max} \leq f_{-1} \tag{2.83}$$

where

$$\alpha = \frac{f_{-1}}{t_{-1}}; \beta = 3 - \sqrt{3}\left(\frac{f_{-1}}{t_{-1}}\right) \tag{2.84}$$

Eq. 2.85 shows the Papadopoulos criterion based in the von Mises shear stress space.

$$\sqrt{\langle {T^2}_a \rangle} + \left(3\frac{t_{-1}}{f_{-1}} - \sqrt{3}\right)\sigma_{H,\max} \leq \tau_{-1} \tag{2.85}$$

The shear stress amplitude assessment, under biaxial loading conditions, is simplified by considering the maximum value of the von Mises equivalent stress during the loading

period depicted in the von Mises shear stress space. The maximum hydrostatic stress is determined through the maximum trace of the stress tensor obtained along the loading period. For biaxial loading conditions the criterion is as follows in Eq. 2.86:

$$\sqrt{\frac{{\sigma_a}^2}{3} + {\tau_a}^2} + \left(3\frac{t_{-1}}{f_{-1}} - \sqrt{3}\right) \cdot \max\left(\frac{I_1}{3}\right) \leq \tau_{-1} \tag{2.86}$$

Where the stress scale factor between normal and shear stresses is given by: $3\frac{t_{-1}}{f_{-1}} - \sqrt{3}$.

#### 2.4.5.2 Shear stress intensity hypothesis (SIH)

Zenner et al. [61, 86] developed the so called shear stress intensity hypothesis, being an integral damage approach. This approach is a high cycle fatigue criterion and aims to estimate fatigue limit for certain loading conditions. The foundations of this approach were settled in the works of Novoshilov [87] where the von Mises equivalent stress was modified. This equivalent stress is determined by considering the mean square of the shear stresses in all planes, Figure 2.21 depicts the definition of the angles used in the integration process.

$$\sqrt{\left(\frac{1}{4\pi}\int_{\gamma=0}^{\pi}\int_{\varphi=0}^{2\pi}\tau_{\gamma\varphi}^2 \sin(\gamma)\, d\gamma d\varphi\right)} \cong \sigma_{Mises} \tag{2.87}$$

This approach was further developed to their most known form, please see Eq. 2.88.

$$\sigma_{eq.a} = \sqrt{\frac{15}{8\pi}\int_{\gamma=0}^{\pi}\int_{\varphi=0}^{2\pi}\left[m_1\tau_{\gamma\varphi}^2\left(1 + m_2\tau_{\gamma\varphi m}^2\right) + m_3\sigma_{\gamma\varphi}^2\left(1 + m_4\sigma_{\gamma\varphi m}^2\right)\right]\sin(\gamma)\, d\gamma d\varphi} \tag{2.88}$$

Where the coefficients $m_1$ and $m_3$ are determined using the fatigue strength ratio (axial and shear) and $m_2$, $m_4$ are coefficients that have into account the material sensitivity to normal and shear mean stresses. The equivalent stress is thereby determined for each integration plane given by $\gamma\varphi$.

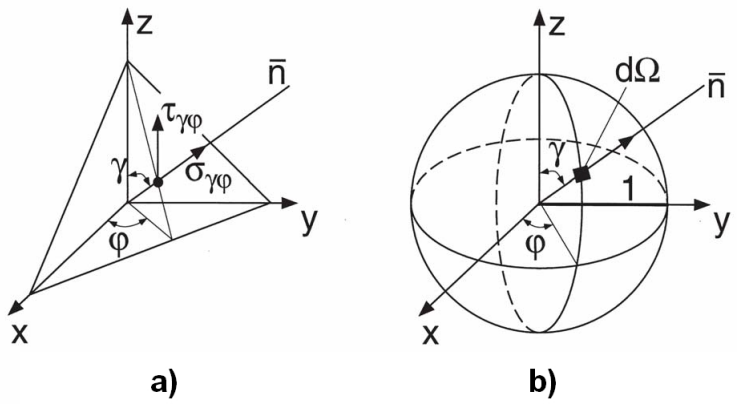


**Figure 2.21:** a) stress components in the intersection plane $\gamma\varphi$; b) surface representing all intersection planes in volume element [86].

## 2.5 Level 3 - Cycle counting

### 2.5.1 Introduction

Random fatigue damage is the ultimate challenge in materials damage characterization, especially under multiaxial loading conditions. Contrary to variable amplitude fatigue tests usually performed in the lab, in the field it is not possible to define in advance a loading block, because instantaneously the loading spectra are unknown. However, loading histories recorded in the field can be stored and interpreted as several loading blocks, where the inherit damage contribution to the final fatigue failure can be accounted. For each loading block extracted from a loading spectra, fatigue damage can be determined in order to update a total accumulated damage value, which can be updated during the service time. When the accumulated damager reaches a critical value the structure or machine component must be inspected and replaced. Under this paradigm, random fatigue damage is updated under service, however in design stages the field loading spectra may be not available. Nevertheless, it is possible to get a typical loading spectrum in order to estimate random fatigue damage in design stages. Therefore, random fatigue characterization can be decomposed into two main approaches, namely: damage accumulation from loading blocks and block extraction from loading spectra.

Generally speaking, cycle counting methods are usually related to block damage characterization. Very few multiaxial cycle counting methods can be found in the literature, and they are mainly based in the Rainflow cycle counting methodology or based in max-min procedures computed over a time variation of a multiaxial loading components (normal and shear stresses/strains), or even over an equivalent stress. In order to estimate the material fatigue strength the use of an equivalent stress is very appreciated due to the simplicity involved in their assessment, however this approach has some shortcomings related to loading block fatigue damage accumulation.

For multiaxial loading paths, the equivalent stress approaches establishes a stress value

representative of loading path damage, usually the maximum value [88]. This procedure leads to a "blind" approach which does not consider what happens along all loading period. For simple loading cases, the cycle definition is quite prompt where the damage reference can be captured using the maximum equivalent stress occurrence along the loading period. However, for more complex loading histories the fatigue life estimates under this approach are unsatisfactory. Therefore, the maximum equivalent stress damage reference is unsuitable to be used in loading blocks damage characterization, leading to non-conservative fatigue lives i.e. the block damage is greater than the one estimated by the maximum equivalent stress computed on the loading block. Thus, the block damage characterization must consider what happens during all loading trajectory. A loading block by definition is a complex loading composed by simple loading regions, this regions contribute to the overall damage under a damage accumulation point of view, thus only considering the maximum damage parameter within a loading block will not capture the overall damage. To handle with multiaxial cumulative damage it is usually used the Palmgren-Miner's rule or a similar rule, as is used in uniaxial loading conditions. Under multiaxial loading conditions, fatigue damage accumulation is evaluated by analysing the damage parameter evolution within the loading block from where it is extracted the inherent number of reversals verified on the loading block [16]. Thus, the critical aspect in the loading block cumulative damage assessment is centred in the equivalent stress or damage parameter used and in the cycle counting methodology, which in turn is related to the loading cycle definition.

Damage parameters must capture the material fatigue damage phenomena, this feature will allow to compute loading block fatigue damage as a summation of different type of damages identified within a loading block as given by the Miner's rule hypothesis. This is a important requirement because small variations of a damage parameter has huge influence in the fatigue life estimates, this is so because in S-N curves, a small variation in the damage parameter (stress level of the equivalent stress criteria) it is obtained a huge variation in the fatigue life estimates. However, cycle counting methodologies, found in literature, show to be independent from the magnitude of the damage parameter, being mainly based on the loading trajectory, which in turn yields equal results for all stress levels. But, experimentally it is observed that the damage inherent to each loading cycle is different under different stress levels, thus the damage of each loading cycle is not only dependent on the cycle definition but also on the stress level. For simple loadings where the loading cycle is easily identified, the stress level effect is captured by the damage parameter maximum value, but in the loading block cases is not.

Under low cycle fatigue assessment it is recommended the use of a strain based damage parameters to estimate loading block fatigue damage. In these cases, the computed strains can be updated with the material plasticity behaviour [89], where the loading trajectory is somehow corrected based on the load level. Therefore, for high levels of cyclic plasticity,

the cycle counting criteria yields different cycle counting results, because the damage parameter pattern changes accordingly to the cyclic plasticity model. However, in high cycle fatigue regime the cyclic plasticity involved in the fatigue process is negligible and due to that the shape of the loading trajectory is not significantly changed, therefore in high cycle fatigue regime, it is missing the cyclic plasticity contribution to overcome the stress level insensitivity found in cycle counting methodologies.

Usually, in fatigue testing machines, the cycle counting is performed by a block summation, the machine input establishes the loading trajectory which is repeated until the specimen test is totally separated or other testing condition. This is a quite prompt cycle counting methodology, where it is considered the loading block as one cycle even for different types of loading blocks, but the damage unit of those loading blocks can be quite different, even for the same stress level. Thus if the stress level is the same in both loading blocks and their fatigue life is quite different, then the cycle counting definition regarding loading blocks and random loadings must be re-analysed.

During years, cycle counting methods have not been a very studied issue, especially in multiaxial fatigue. The most known in this field have several years being the Rainflow cycle counting methodology, and it countless variants, the most used ones. These methodologies have acceptable results for the uniaxial loading cases (normal and shear), but under multiaxial loading conditions their results are questionable, however, new approaches and techniques to perform cycle counting under multiaxial loading are very few, specially multiaxial loading blocks [52, 90–92]. Some of them are critical plane based approaches where the Rainflow methodology is used to evaluate the stress/strains time evolution projected on each plane.

One example of the aforementioned cycle counting methodologies is the Bannantine and Socie methodology [93]. This method extracts the number of cycles of a loading path in the critical plane through a Rainflow routine, and a damage parameter time evolution usually the SWT or the Fatemi-Socie criteria are used for normal or shear dominant loadings, respectively. Under this approach some other works were developed in order to improve this multiaxial cycle counting methodology [91].

Multiaxial cycle counting methods based in critical plane approaches have some shortcomings associated with the fact that the normal and shear stresses contribution to the overall damage are analysed separately, which means that the time relation between shear and normal stresses is missing, i.e. these methods do not capture the combined effect always found in multiaxial loading conditions. Thus, the peak of each normal and shear stress reversals may occur in different instants within the loading period, which is the case of non-proportional loadings, but the overall damage is computed, using this procedures, as if they occur at the same time. The equivalent damage parameter approaches(equivalent stress/strain approaches) preserves the time relation between load components, but have

other shortcoming which is the sign lost, because an equivalent damage parameter is always positive. This is an important issue because a material damage reference (usually uniaxial S-N curves) is established based on a positive and negative reversals, which have different damage contributions to the overall damage found within a loading cycle, thus the loading sign lost may affect the Rainflow cycle counting results [90, 91]. Also, in normal stresses, negative signs are connected with compression and positive ones with tension identifying different damage mechanisms on material, moreover, positive or negative sign in shear loading doesn't lead to a different damage mechanisms. In order to overcome these issues Wang and Brown proposed a cycle counting method based in the Rainflow cycle counting methodology where it is used the von Mises relative equivalent strains in order to identify in the loading path history the inherent block reversals. This criterion also has some shortcomings which is the possibility to lose the maximum stress range during the loading time history [94, 95]. Meggiolaro et al. [90, 91] proposed a modification to the Wang and Brown criterion to overcome this issue and expands this methodology to the five-dimensional Euclidean space in order to guarantee that the highest relative strain amplitude is always accounted. Also Wei and Dong [96], proposed another cycle counting methodology based in the equivalent stress concept by performing a mapping of the equivalent stress time evolution in the space in order to overcome the missing path-dependency effect on fatigue damage assessment verified in the Wang and Brown criterion [94, 95, 97]. However, the cycle damage dependence on the stress level remains to be accounted on the loading block cycles extraction.

### 2.5.2 Multiaxial cycle counting

Uniaxial cycle counting is a well understood issue, the hysteresis loops interpretation to identify a load cycle is a method which had proved to be reliable in uniaxial fatigue damage characterization, however under multiaxial loading conditions such prompt method doesn't exist nowadays. However, some efforts were made in order to adapt the uniaxial cycle counting methodology such as the Rainflow algorithm to the multiaxial loading histories [98–100]. Bannantine and Socie and the Wang and Brown cycle counting methodologies are an example of that, despite being methodologies completely different they use the Rainflow concept to extract the number of cycles within a multiaxial loading history.

### 2.5.3 Bananntine and Socie

Bannantine and Socie [93] proposed a multiaxial cumulative damage model which is a mix of critical plane damage approach, a Rainflow cycle counting methodology [97, 101] and Miner's rule [88]. The main concept behind this criterion is based on the experimental evidence that some materials are more sensitive to normal strains than to shear ones and vice versa. The authors concluded that the normal and shear strains have different damage levels within the same material. Under this paradigm, the authors proposed to evaluate a

block damage under multiaxial loading conditions by considering normal strains or shear strains depending on the material damage sensitivity. Which is a attempt to eliminate the issue regarding the loss of the time dependence already discussed in previous sections. Thus, a multiaxial loading is projected into each plane of the critical plane search, and then the in-plane (shear) and normal strains are separately evaluated in each plane with a Rainflow based methodology. In this way it becomes possible to apply the uniaxial Rainflow cycle counting method to determine the number of reversals in each plane, and then evaluate the damage associated to them, in order to quantify the overall damage and critical plane direction. With this approach, the Rainflow cycle counting method can be associated with the strains time evolution, from where it can be identified the physical behaviour in the material, i.e. the Rainflow cycle counting on each plane can be fairly associate with the material hysteresis loops in that plane which it is the original main concept behind the Rainflow cycle counting methodology [36, 102, 103].

Regarding the damage accumulation from each block's reversal it can be accounted through any cumulative damage model. The most known and used is the Miner's rule, where it is performed a linear summation of each reversal contribution. For each set of reversals with same amplitude, can be computed their contribution to the overall damage by dividing the number of those reversals by the fatigue life estimate obtained through the damage parameter associated to those reversals amplitude.

Additional accumulative damage approaches based on the Miner's rule can be found in the literature [16, 101], which are mainly non-linear versions of the original version. However, that non-linearity, in the author's opinion, should be left to the damage parameter formulations, since S-N curves are already non-linear, and fatigue life estimates are always obtained from the relation between the damage parameter and the material S-N curve. As aforementioned, in the Bananntine and Socie model the damage parameter associated to the reversals extracted with the Rainflow methodology in the candidate plane, is determined using a specific critical plane criterion.

For instance, if the number of reversals is determined based in the normal strain time evolution evaluated in the candidate plane to critical plane, then a critical plane model based in normal strains must be considered. Likewise, if the in-plane strains are used to determine the number of reversal in the candidate plane, then a damage parameter based in shear strains should be used. For example, the reversals' damage can be estimated using the critical plane models present in Eq.(s) 2.89, and 2.90 [104], where Eq. 2.89 represents the Fatemi-Socie critical plane model, which is a shear strain-based model, and Eq. 2.90 represents the SWT, which is a normal strain-based critical plane model.

$$\max_{\theta}\left\{\frac{\Delta\gamma_{\max}}{2}\cdot\left(1+k\cdot\frac{\sigma_{n,\max}}{\sigma_y}\right)\right\}=\frac{\tau_f{}'}{G}(2N_f)^{b\gamma}+\gamma_f{}'(2N_f)^{c\gamma} \tag{2.89}$$

$$\max_{\theta}\left\{\sigma_{n,\max}\cdot\frac{\Delta\varepsilon_1}{2}\right\}=\frac{\sigma'^{2}_{f}}{E}(2N_f)^{2b}+\sigma'^{2}_{f}\varepsilon'(2N_f)^{b+c} \tag{2.90}$$

Socie et al. [16, 104] proposed evaluate the damage associated to a loading block by adding at each candidate plane the estimated damage from the normal and shear strains. This concept has two conceptual problems, the first one is the already discussed loss of time dependency between normal and shear stresses, the second one is the possibility of consider twice the same damage contribution to the overall damage.

For example, if the block damage at the candidate plane to critical plane, is evaluated for the in-plane load projections using the Fatemi-Socie criterion, and the SWT criterion is used for the perpendicular ones as suggested in [16, 104], then the normal stress contribution to the overall damage is double counted, because the normal damage contribution is accounted in both criteria as can be seen in Eq.(s) 2.89 and 2.90.

Despite the aforementioned conceptual problems, these models give a step forward by characterizing block damage by identifying the critical plane with the highest accumulated damage, determined by damage parameters based on shear and normal strains. The greatest difference between the highest damage parameter and the highest accumulated damage parameter is based on the fact that the highest damage parameter considers only the reversal with the highest amplitude in the loading block at a specific plane, in this case the damage of the remaining reversals are not considered. On the other hand, in the accumulated damage parameter concept, the damage from all reversals in a specific plane are accounted.

Figure 2.22 illustrates the Bannantine and Socie methodology used in to estimate fatigue life under multiaxial block loading conditions using a critical plane criteria.

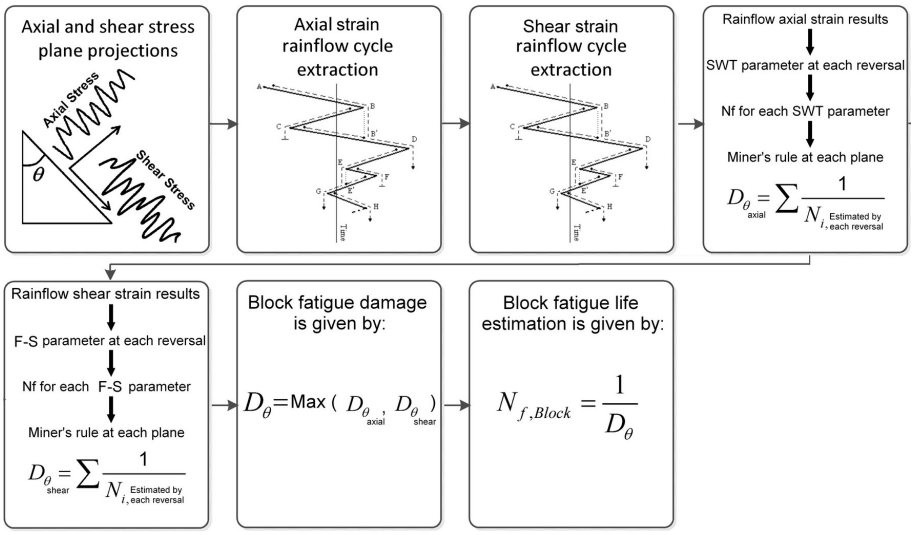


**Figure 2.22:** Bannantine and Socie framework to estimate block fatigue life.

### 2.5.4 Wang and Brown

Another concept used in multiaxial cycle counting techniques was proposed by Wang and Brown [98, 105, 106], where the loading cycles within a loading block are extracted through the von Mises equivalent strain time evolution. Contrary to the Bananntine and Socie methodology where the output gives the number of reversals and respective amplitudes, the Wang and Brown cycle counting method only identifies the region in the loading path trajectory (in the von Mises stress space) that belongs to each reversal. The damage parameter is then calculated to each extracted reversal. The use of an equivalent parameter as the von Mises equivalent strain have associated with it the loss of the loading sign, i.e. the equivalent strain is always positive regardless the compression, tension or shear stress direction, therefore several damage mechanisms are hidden by using this type of equivalent damager parameter. Regarding the fatigue damage interpretation, this is an important issue because the reading of the damage parameter time evolution can lead to wrong interpretations.

For example, the von Mises equivalent stress transforms a fully reversed load into a zero to maximum loading path, creating in such way a virtual mean stress that physically does not exist. In order to avoid this shortcoming Wang and Brown have proposed to make a Rainflow counting to the relative von Mises equivalent strains. Therefore, the von Mises equivalent strain time variation is computed to extract the loading cycles within a multiaxial loading block, then it is identified the maximum equivalent strain location in order to translate the origin of the time referential to that same location. This is the starting point to perform the Wang and Brown cycle counting methodology; the relative equivalent strain time variation is then calculated at each time by computing the norm between the instantaneous equivalent strain and the maximum equivalent strain value. After that, a Rainflow cycle counting is performed using the relative equivalent strain time variation, the cycle is extracted and then the relative equivalent strain is updated by removing from the loading history the information inherent to the extracted cycle. The remaining branches of the loading history are computed in the same way until there is no loading branch to compute.

With this method, it is obtained a kind of map that divides the normal and shear stress time evolution in loading regions, i.e. loading reversals. For each reversal it is used its normal and shear stress time evolution to performed a critical plane search to determine the maximum damage parameter of the reversal. Eq. 2.91 shows the Wang and Brown equation to estimate fatigue life. The left side of Eq. 2.91 represents the Wang and Brown critical plane damage parameter, the right side represents the material S-N curve.

$$\varepsilon \equiv \frac{0.5\left(\Delta\gamma_{\max}\right) + S\left(\delta\varepsilon_n\right)}{1+\nu^{'}+\left(1-\nu^{'}\right)S} = \frac{\sigma^{'}{}_f - 2\sigma_{n,mean}}{E}(2N_f)^b + \varepsilon^{'}{}_f(2N_f)^c \tag{2.91}$$

Where $\Delta\gamma_{\max}$, and $\delta\varepsilon_n$ are the shear strain range and the normal strain excursion between two turning points of the shear strain evolution on the plane of maximum shear, the parameter $S$ represents the influence of the normal strain to overall damage, the other parameters are the uniaxial strain lifetime equation constants. The parameter $S$ near the material fatigue limit is about 0.3, for half fatigue life the $S$ parameter takes the value 0.74 [16]. Afterwards, a cumulative damage rule must be considered in order to estimate the block damage, and the overall damage accumulation [107]. Figure 2.23 shows an illustrative example of the Wang and Brown cycle counting technique to determine the reversals region within a loading block. In Figure 2.23 a) it is presented the normal and shear loading components time variation; next up it is determined the von Mises strain time-variation as can be seen in Figure 2.23 b). The next step is to find the first maximum value of the von Mises equivalent strain time variation and translate the graph origin to that point, in Figure 2.23 c) it is shown the referential translation for the first maximum of the von Mises equivalent strain time evolution, named as point A.

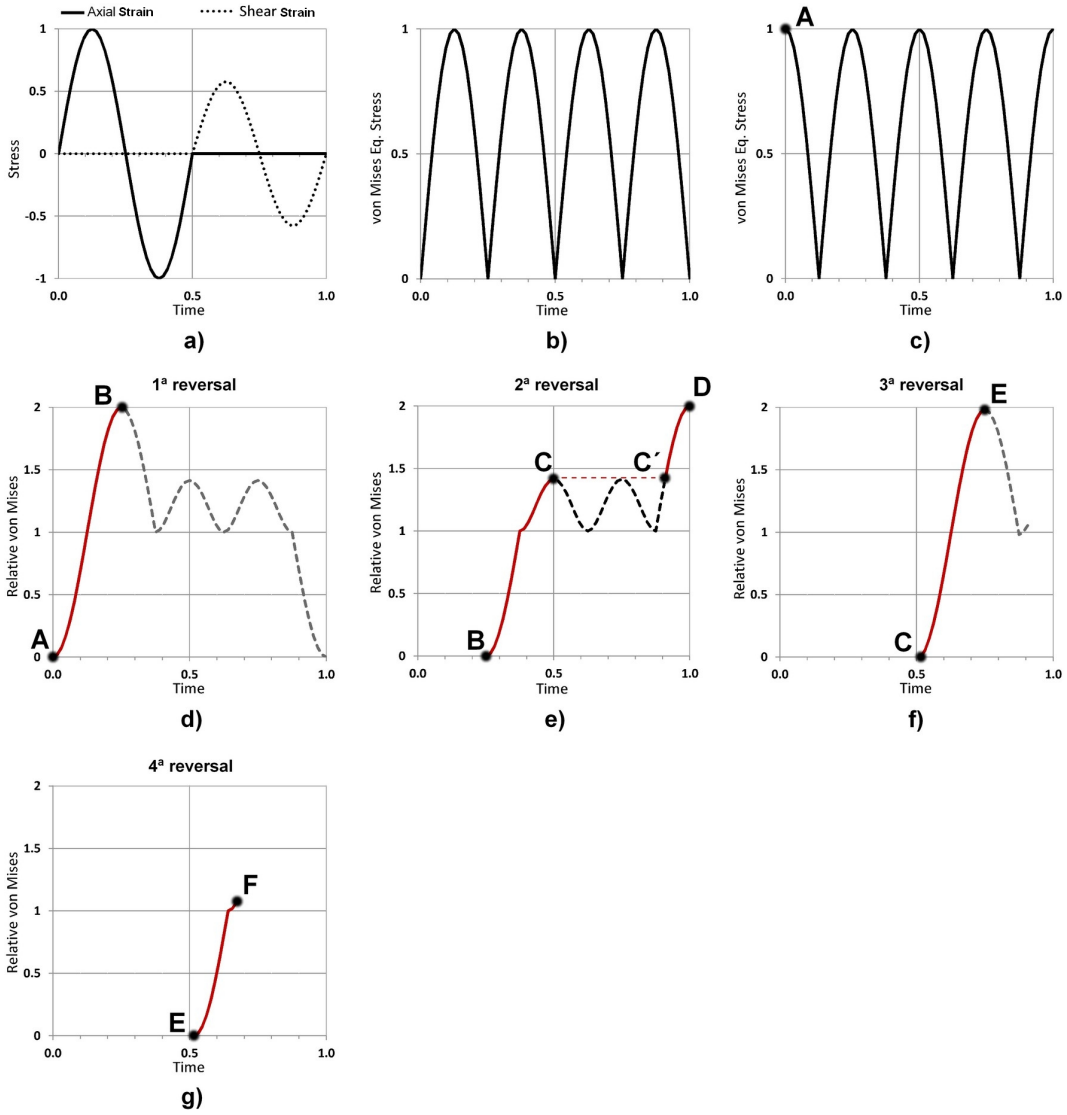


**Figure 2.23:** Illustrative example of the Wang and Brown reversals extraction procedure.

From here, it is determined the relative von Mises time-history, which is given by the following reasoning: The maximum value of the von Mises time evolution (point A) has two components, i.e. the normal and shear strains of point A. Now, consider the normal and shear strains time variation defined in the loading block, next up, subtract to the normal and shear strains time evolution the normal and shear strain values of point A. Next up, perform again the von Mises time-history using the new normal and shear strains time evolution. The result of this step can be seen in Figure 2.23 d), as expected, point A is now at the referential origin with normal and shear strains equal to zero, which yields a relative von Mises equivalent strain equal to zero. Next up, the reversal is extracted by removing from the normal and shear strain time evolution the values inherent to the reversal. Next the procedure to determine the relative von Mises time history starts from the beginner with the normal and shear stresses time variation updated. The relative von Mises time histories always starts at referential origin with relative strains equal to zero, because their calculation always starts at maximum values (points A, B, C, E depicted in Figure 2.23), in Eq. 2.92 it is shown the numeric methodology to determine the von Mises relative time-history.

$$\sigma_{i,relative}\left(t\right) = \sqrt{\left(\sigma_i\left(t\right) - \sigma_{\max}\right)^2 + 3 \cdot \left(\tau_i\left(t\right) - \tau_{\max}\right)^2} \tag{2.92}$$

In order to extract a reversal from the relative von Mises time history, it is selected the time history branch that starts from zero towards the closest peak, if the time-history begins to decrease the reversal extraction goes on the horizontal until the time history begins to increase again. If the horizontal extraction does not find any increasing time history segment, then the reversal ends at the exact point when the extraction initiates to become horizontal.

In Figure 2.23 d), it is shown the first reversal extraction, which is represented in red by the line AB; at this stage, there is no greater point than point B, thus the reversal was found, and the loading path must be updated i.e. must be removed from the loading block (normal and shear strains time variation) the normal and shear components time variation inherent to the reversal extracted. Then, the process starts again with the updated normal and shear strains time evolution; only one reversal is extracted for each relative time history.

Figure 2.23 e) shows the new relative minimum, the point B; the next reversal extraction reaches the point C; at this stage the von Mises time history decreases, therefore the red dot line goes horizontally to find point C', thus the reversal extraction continues to the end of the relative von Mises time history, which yields the second reversal through the points BCC'D. Next, the normal and shear strains time evolution must be updated again, the new relative minimum is now point C which grows until reach point E, being extracted

the 3rd reversal CE, please see Figure 2.23 f). Next up, the normal and shear strains time evolution is again updated by removing from the previous time evolution the normal and shear time evolution inherent to the reversal CE, then it is calculated the new relative von Mises time evolution, please see Figure 2.23 g). Next, the reversal extraction starts at point E and go towards point F. At this stage all loading path was covered and it was found all reversals within the loading block. In this example the loading block was split in four reversals.

#### 2.5.4.1 Wang and Brown fatigue life estimates of loading blocks

In order to estimate fatigue damage inherent to multiaxial loading blocks, the Wang and Brown cycle counting method identifies regions on the normal and shear strains time evolution that are representative of loading reversals. These regions are a kind of sub-loading paths inherent to each reversal. Each one of the archived sub-loading path must be considered as if it is a independent loading path, then for each one of these reversals the damage criteria is calculated. The Miner's rule is used to determine the loading block damage accumulation and consequently the block fatigue life can be estimated, as seen in Eq.(s) 2.93 and 2.94.

$$D_{block} = \sum_{i=1}^{\#reversals} \frac{1}{N_i} \tag{2.93}$$

Thus the block fatigue life can be estimated as follows:

$$N_{block} = \frac{1}{D_{block}} \tag{2.94}$$

## 2.6 Level 4 - Damage accumulation rules

The damage accumulation concept aims to capture fatigue damage from different loading paths, and stress levels. Although damage accumulation is always present even in simple loading paths, with constant amplitude, the complexity increases when the loading amplitude levels varies during a loading pattern. For instance, in constant amplitude and for simple loading paths, fatigue life can be directly estimated using a S-N curve, which is made for a specific loading type with a specific stress range, usually this range depends on the material type. However, if during the loading pattern the stress level changes or even the loading type, thus it is not possible to estimate fatigue life using directly the S-N curves with acceptable correlations. Thus, it is necessary to account the damage variation within a loading pattern and then compute the accumulated damage.

The first attempt to deal with this subject was made by Palmgren in 1924 [108] where he proposed a simple damage concept defined by the ratio between the number of cycles

loaded and the number of cycles to failure, estimated using the load level of the loaded cycles. Later on, in 1945 Miner [109] adopted this approach in their studies, becoming this approach known as the Palmgren-Miner rule. In this rule, it is considered that fatigue damage can be added linearly, however, soon it was published in literature several works reporting the inconsistency of the linear concept and their incorrect estimates in damage accumulation assessment. The linear damage rule (Palmgren-Miners's rule) is given in Eq. 2.95.

$$D_i = \frac{n_i}{N_{f_i}} \tag{2.95}$$

where, $n_i$ is the number of loaded cycles with the $i^{th}$ loading level, and $N_{f_i}$ is the fatigue life until failure for the $i^{th}$ load level. In this type of damage accumulation rules, it is estimate the failure occurrence when the summation of the damage fractions, $D_i$, computed at different loading levels equals one. Despite of its questionable performance, the Palmgren-Miner's rule has been widely used due to their simplicity and straightforward application. To improve their performance, many proposals based in the Palmgren-Miner rule modification have been proposed in literature.

Fatemi and Yang [110] made a exhaustive literature review in 1998 regarding this subject by covering about 50 fatigue damage accumulation models proposed between the Palmgren pioneer works in 1924 and the end of the 1990s. They found out, that before 1970, the damage accumulation models were mainly phenomenological in which the formulations were mainly based on empirical observations and experiments, after that period they become semi-analytical because the material damage mechanisms started to be considered to explain the damage accumulation phenomena. In their work Fatemi and Yang concluded that the damage accumulation models developed to improve the Palmgren-Miner rule can be divided into 6 categories, namely the linear and non-linear damage approaches, S-N curves modification, crack growth concept, continuum damage mechanics and energy models.

In 1953, Henry [111] proposed the first non-linear damage accumulation concept by changing the material endurance limit accordingly to the loading stress level. This approach was based in the experimental evidence in which the material properties change as the load level increases, therefore the author proposed to capture this variation by enter with the endurance limit in their formulations. Henry used their hypotheses to capture the sequential damage effect under a damage accumulation approach. One year after, in 1954, it was proposed the first non linear damage accumulation rule by Marco and Starkey [112] in order to capture the effect of the stress level in damage accumulation, Eq. 2.96 shows this rule.

$$D = \left( \frac{n_i}{N_{f_i}} \right)^{x_i} \tag{2.96}$$

where $x_i$ is a value related to the $i^{th}$ loading level obtained by experiments. Figure 2.24 depicts the Marco–Starkey non-linear theory regarding different values of the exponent $x_i$.

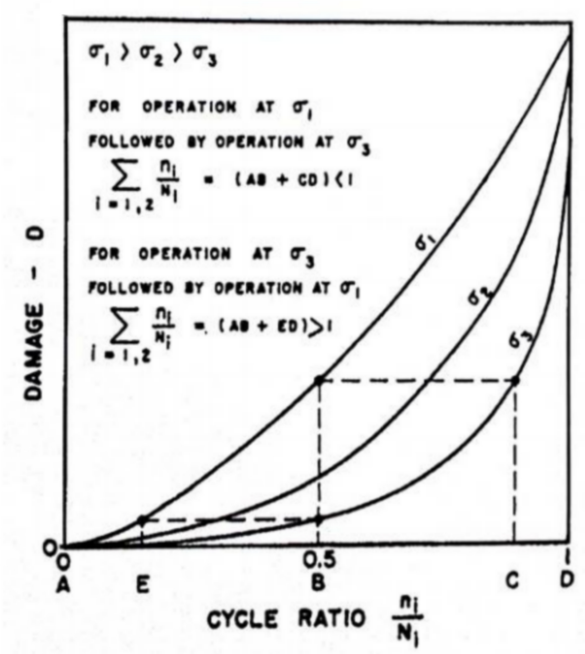


**Figure 2.24:** Nonlinear damage curves for the Marco–Starkey non-linear damage accumulation rule [112].

Next, in 1960 starts to appear the two stages damage concept with the works of Grover [113] where he uses one linear damage rule for crack initiation and other for crack propagation. In 1966, Manson [114] proposed the double linear damage rule which was based in the works of Grover. Figure 2.25 shows the Manson's approach to evaluate sequential damage accumulation.

Subramanyan [116] presented in 1976 the knee point-based approach, where the S-N slope is modified near the material endurance limit, this approach assumes that the endurance limit do not change during the damage accumulation process. In this approach, the S-N slope variation updates the remaining fatigue life after each stress level, however, in this rule the loading spectrum may have only two stress levels. In 1988, Kutt and Bienek [117], presents a review regarding damage accumulation rules based in statistical approaches. In 1990, Ben-Amoz [118] considers that fatigue is a statistical phenomenon, and uses the Subramanyan's approach by adopting the two scatter limits approach. These limits, a upper and lower bound, were created using the linear damage rule by making a upper and lower limit parallel to the S-N curve being updated with the Subramanyan approach. This approach was also implemented using non-linear fatigue life curves, having into account

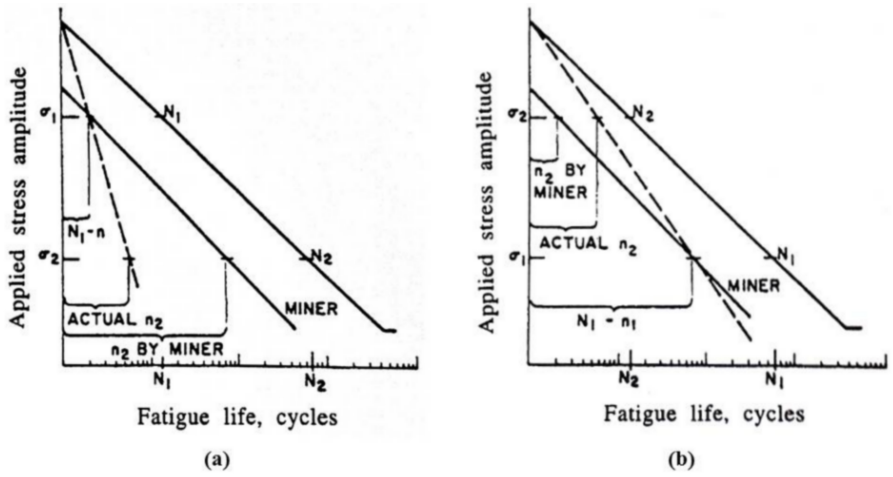


**Figure 2.25:** Manson's approach for two-step loading, a) High-Low b) Low-High[115].

crack initiation and crack propagation stages. Also here, the Ben-Amoz approach only covers damage accumulation for two stress levels as seen in the Subramanyan approach.

The use of a continuum damage approach to characterize damage accumulation was firstly emphasized by Chaboche [119] in 1988. This approach was based in the Chaboche's success to modelling creep damage using the continuum damage mechanics, which was later extended by the author to other damage regimes. Many other authors follow the continuum damage approach to cover damage accumulation such as Lemaitre and Plumtree [120], and Li et al. [121] among others. These models were designed based in the uniaxial damage characterization; however, these models extension to multiaxial fatigue damage accumulation have not had the same success verified under uniaxial loading conditions.

Recent works, continue to pursue the improvement of the Palmgren-Miner rule. For example, in 2007 Xue et al. [122] presents a damage plasticity model for ductile material based in experimental tests, containing a damage-related weakening factor to describe the material deterioration evolution due to cyclic loadings. In this approach, fatigue damage accumulation is accounted as a measure of deformability loss, having into account the load level, Lode angle, and a power law damage rule. This model estimates the failure occurrence when the damage accumulation equals 1. Also in 2008, Seweryn et al. [123] presents a damage accumulation rule that captures non-proportional damages, this rule is based in energy concepts and is updated with the material monotonic work-hardening curve, where the stress and strain tensor is determined using the hardening rule proposed by Mróz [118]. Here, the damage increment is updated having into account the energy dissipation increment and the first invariant of the stress tensor. The authors claim that their model requires a relatively small number of material parameters, which was stated as an advantage regarding other models found in literature.

In 2011, Casciati et al. [124] presented a pioneer work where is studied the fatigue damage accumulation in smart materials, with super elastic behaviour at positive temperatures.

In this study a Cu based shape memory alloy was cyclically loaded in order to create micro plasticity with residual strains. The author reported a loss of specific properties during each cycle. The authors correlated this loss with a non-linear damage accumulation approach based in the energy dissipation concept. In the same year, Yong Huang et al. [125] studied the damage accumulation in a carbon-manganese steel, the A42, which is commonly used in pipe components. The idea was to study damage accumulation in low cycle fatigue and gigacycle fatigue. To do that, the material was loaded under low cycle fatigue and then loaded with a gigacycle fatigue regime, being a typical loading regime in damage accumulation with two stress levels (two steps). It was reported that, the material fatigue life is increased by firstly perform a load at high stress levels and then change to lower levels. The author uses the continuum damage mechanics approach based in the Chaboche model to characterize the damage accumulation. The author also reported that the Chaboche damage model can describe the damage behaviour in LCF and VHCF.

In 2011, Rathore et al. [126] proposed a new methodology to model the probabilistic distribution of damage accumulation to improve the fatigue life estimates of structures and mechanical components. In this approach the damage accumulation is evaluated as a linear phenomenon. The authors underlined the possibility of their model to be extended to log-normal and Weibull distributions. In 2012, Zarrin-Ghalami et al. [127] studied the combination of Rainflow cycle counting, maximum principal strain, and Miner's linear cumulative damage rule to evaluate damage accumulation in a automotive cradle mount. The authors reported good results, with satisfactory predictions under variable amplitude loading tests.

Almost a century after the publication of the Palmgren-Miner's rule and after hundreds of published damage accumulation models, the simple Palmgren-Miner's rule continues to be used to characterize damage accumulation. Also in 2012, Huffman and Beckman [128], presents a new phenomenological technique to estimate fatigue life under variable amplitude loading. The authors use constant amplitude data to set-up their model and claim that there is no need of using a big amount of experimental data in their model set-up. They also reported (as seen in other authors) that overloads at the beginning of a loading history have more impact in fatigue lifetime than overloads at the end.

In 2013, El Aghoury and Gala [129], proposed a new concept to deal with damage accumulation under variable amplitude loading conditions, the VTCs (virtual life target curves). Their method is based in illustrative techniques and introduces a time dimension to the S-N curves. This method takes into account overloading effects and the authors claim that the method is able to deal with any loading pattern. This model needs to be calibrated with the material mechanical properties being pointed out good fatigue life estimates. Also in 2013, Taheri et al. [130], discuss the limitations of the linear damage accumulation rules, concluding that these rules yield non-conservative fatigue life estimates

for stainless steels. The reason found by the authors was based in the need of using a elastic-plastic law to capture the cyclic hardening found in austenitic steels. To overcome these issues the authors proposed a conservative model to account damage accumulation using the material cyclic strain-stress curve, they claim that in this way, it is not need a constitutive law to characterize the material cyclic plasticity. Despite the shortcomings pointed out by the authors regarding the linear damage accumulation approach, they end up using the Miner's rule to account damage accumulation. Hilgendorff et al. in 2013 [131] developed a damage accumulation approach based in microstructural damage mechanisms under resonant fatigue tests. They studied damage accumulation in a austenitic stainless steel (AISI 304) and correlated the fatigue damage with slip mechanisms of plastic deformation under very high cycle fatigue (HCF) loading conditions. They created a numerical model to simulate these microstructural mechanisms, which needs to be set-up by experimental tests. This model have into account slip mechanisms such as: sliding, slip irreversibility and cyclic hardening. The authors reported good agreement between estimates and experimental data. Wang and Yao [132] conducted experimental tests in the aluminium alloy LY12CZ under non-proportional loading conditions with different phase angles and two stress levels (two step loadings). To account damage accumulation under non-proportional loading conditions they propose a non-linear damage accumulation rule with a parameter ($\alpha$) that tunes the model accordingly to the phase shift level. The authors reported predictions within a scatter band with a life factor of two. Gao et al. [133] proposed a non-linear damage accumulation rule to account with the load interaction under variable amplitude loading conditions. The authors identify the limitations of the Palmgren-Miner's rule to capture those interactions. Based in the experimental data of two metallic materials, the authors validate their model and then correlated the results with other models estimates. Xia and Yao [134] goes further and evaluates state-of-the-art models in damage accumulation under variable amplitude and random loading conditions. To do that, they used sixteen loading paths with different loading effects such as: proportional, non-proportional, and stress level variation. The authors created a interesting methodology to implement random loadings in lab, by combining randomly the aforementioned sixteen loading paths. This is a unique work where for the first time it is studied fatigue damage accumulation under random loading conditions. In the past, many authors started to use wrongly the random concept to refer variable amplitude loading. Therefore, many works with titles referring to random loading conditions are in reality studies about variable amplitude loadings.

### 2.6.1 Final comments

During decades it has been pursued a damage accumulation model that be able do deal with damage accumulation. Many authors presented their way to deal with this subject but a consensual model remains in pursuit. However, many works continue to

use the Palmgren-Miner's rule to characterize damage accumulation despite their known shortcomings. In the present author opinion, this shortcomings are erroneously attributed to the linear damage accumulation approach because the non-linearity that characterizes fatigue damage must be captured through a damage parameter, and cycle counting techniques. Many authors try to capture non-linear damage behaviour using non-linear damage accumulation rules, but in fact they are fitting their experimental results for a particular loading conditions. Actually, the discussion around the Palmgren-Miner's rule shortcomings are usually focused on their non-conservative results, because it has been obtained damage accumulation estimates lower than 1 at failure. However, this can be explained by the scatter always found in fatigue life experiments. Therefore, if a damage parameter gives estimates within a scatter band with a life factor of two or even three (which is a very acceptable performance), it is logic that the estimated fatigue life,$N_{f_i}$, used to calculate the damage ratio, $\frac{n^i}{N_{f_i}}$, also varies accordingly to the aforementioned scatter bands. Thus, the Palmgren-Miner ratio is also influenced by a probabilistic factor always present in fatigue damage evaluation.

## 2.7 Level 5 Crack initiation plane

### 2.7.1 Introduction

Fatigue crack studies (fractography analysis) are very important because they allow to correlate stress levels and loading types with crack initiation planes and crack growth patterns. The crack initiation type and inherent growth may change accordingly to the stress level, and loading type. One example of that can be found in the experimental direction of the fatigue crack initiation obtained under proportional and non-proportional loading conditions. Typically, non-proportional loadings with $90^o$ phase shift, yields a experimental fatigue crack initiation at $0^o$ degrees, and in proportional loadings, the results may range between $12^o$ and $25^o$ degrees depending on the material type. This subject is of utmost importance in assurance inspections of structures or mechanical components after their fail. Performing a fractography analysis will allow to interpret what happened by inspecting the crack surface, which will allow to distinguish crack initiation and growth patterns from defects, impacts or the occurrence of high stress levels, among other causes.

Figure 2.26 depicts different fracture planes accordingly to the loading type for fragile materials, as can be seen the fracture plane direction varies significantly for each uniaxial loading type.

Figure 2.27 shows a fatigue crack under pure shear loading conditions performed in the lab. Figure 2.27 a) shows the crack grow path evolution and Figure 2.27 b) shows the fast fracture instant. Also under multiaxial loadings several fatigue crack initiations and growth patterns can be obtained by combination of the multiaxial loading components (normal and shear stress).

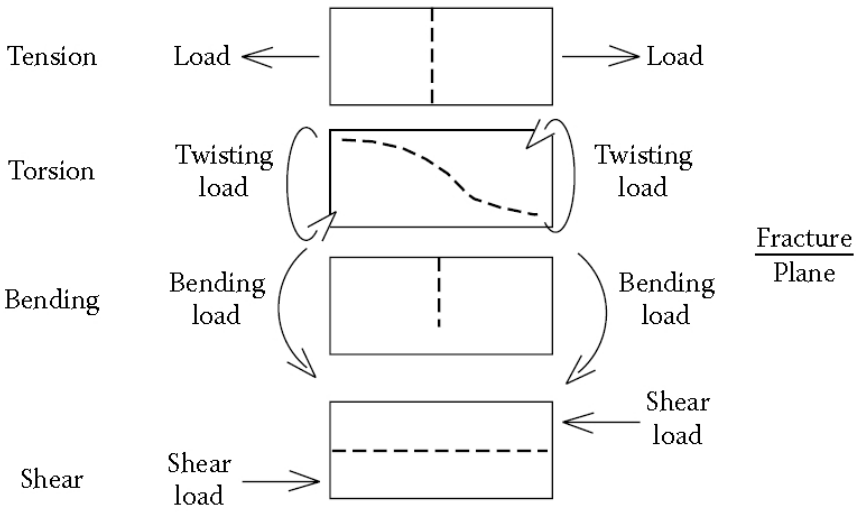


**Figure 2.26:** The four basic loads (forces) and the fracture planes that result from them [135].

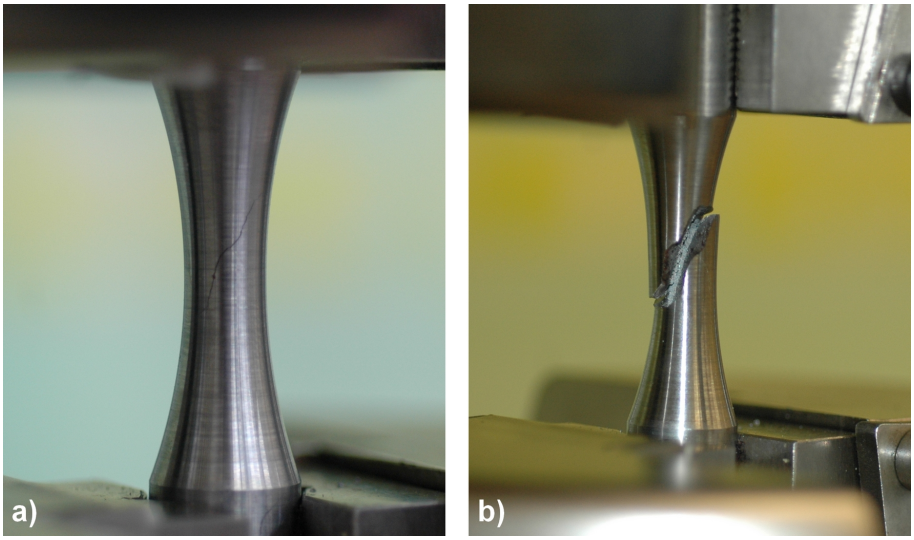


**Figure 2.27:** Fatigue crack under pure shear loading, 42CrMo4 material.

Figure 2.28 shows two different fracture surfaces of two proportional loadings obtained with hourglass samples. In Figure 2.28 a) the specimen test was loaded with a stress amplitude ratio equal to 30º, where the normal stress amplitude is higher that the shear one, in this case the normal stress fatigue damage has a higher contribution to the overall damage. Figure 2.28 b) shows the fracture surface resulted from a 60º stress amplitude ratio, where the shear damage has a higher contribution to the overall damage. Both fracture surfaces were obtained under proportional loading conditions, with the same equivalent stress amplitude, but the fracture surface is quite different in both cases.

The fracture topography is a important record of the crack initiation and growth processes where it is registered the fatigue crack stages. Figure 2.29 depicts an example of these fatigue crack stages under pure bending loading conditions. Mainly two major zones can be identified, the fatigue zone (FZ) in which it is included the crack nucleation spot (origin),

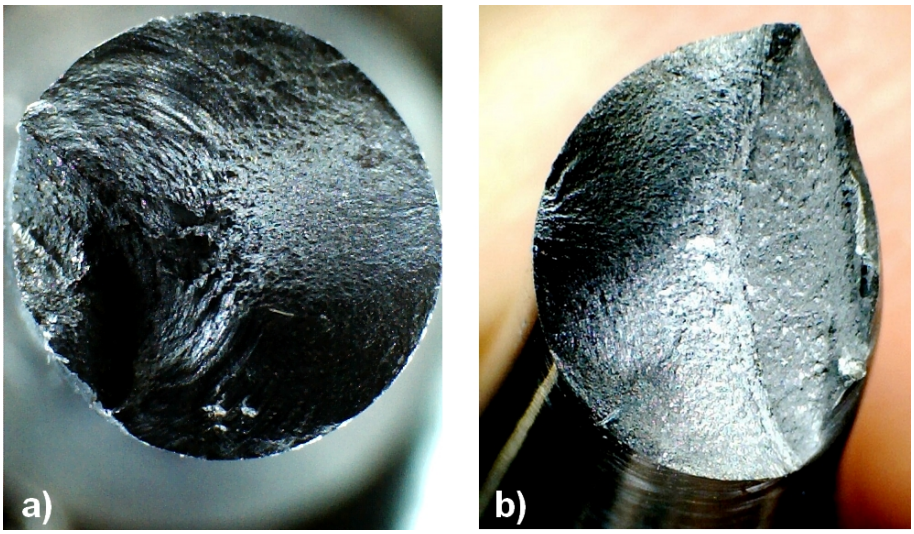


**Figure 2.28:** 42CrMo4 fracture surfaces under a) proportional loading with SAR=30°, and b) proportional loading with SAR=60°.

and the instantaneous zone where the specimen separation occurs instantaneously. One typical characteristic of the fatigue zone is the presence of progression marks, commonly referred as beach marks, in some materials and loading conditions it is possible to correlate the beach marks progression with the number of cycles performed before rupture. However, in some other materials like high strength steels, the beach marks cannot be found and is quite difficult to make such type of analysis. This brings some difficulties to differentiate between fractures obtained under high and low stress levels, but in the field fatigue cracks with rust is a good indicator of a slow crack grow.

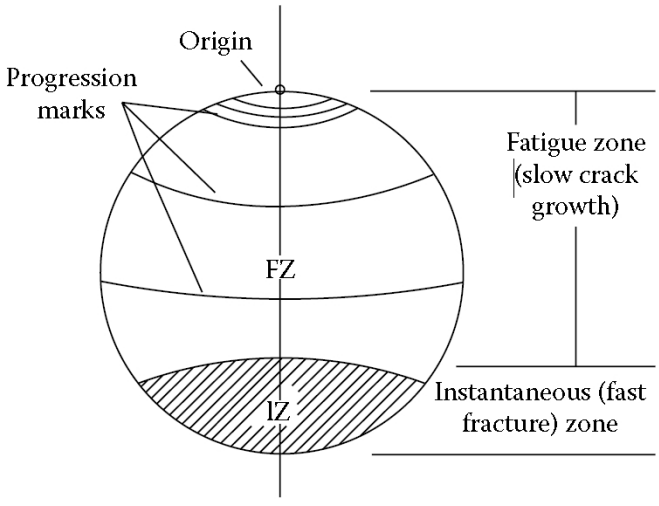


**Figure 2.29:** A view of a basic plane bending fatigue failure [135].

One example of fatigue crack in the field is depicted in Figure 2.30, here the fatigue crack propagates accordingly to the number of flying hours. In this cases it is possible to make some crack traps to detain the crack propagation, this traps are holes performed in the crack front in order to reduce the local stress intensity factor.

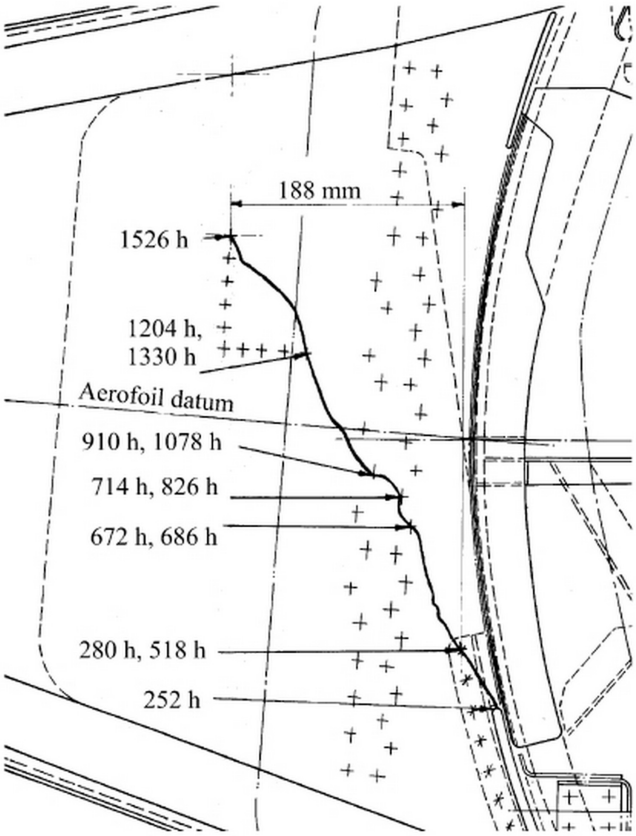


**Figure 2.30:** Fatigue crack path in a fighter aircraft centre section. In this case, the damage unit is flying hours instead of loading cycles [136].

### 2.7.2 Critical plane estimates

There are very few types of criteria to estimate the direction of the crack initiation planes. Typically, estimates for crack initiation planes are made using critical plane models. These models projects the stress or strain tensor in each plane and evaluate their damage parameter on these planes, as already presented in section 2.4.4. In these approaches, the critical plane is the one that has the maximum damage parameter and it is expected that the fatigue crack initiates and starts to growth on this plane. No special features or concepts were added to the critical plane methodology to obtain these estimates, therefore the critical plane direction estimates is a natural consequence of the critical plane criteria. Therefore, for each critical plane damage parameter presented in section 2.4.4. it is possible to estimate the direction of the crack initiation plane by inspecting the damage parameter evolution within the range of $0^o$ to $180^o$ degrees.

Figure 2.31 shows the damage parameter amplitude evolution for the LIU1 criterion. As it can be seen, the maximum amplitude value occurs at $+25^o$, thus based in the LIU1 estimate, the fatigue crack will initiate on this plane.

Critical plane criteria have a straightforward way to estimate crack initiation planes, which can be very useful in finite element simulations. However, commercial finite element

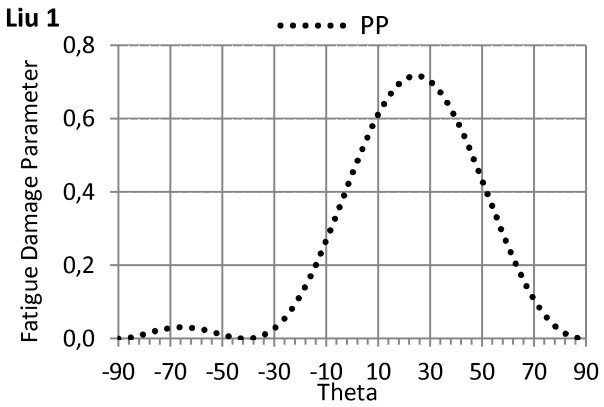


**Figure 2.31:** Critical plane estimate of the Liu criterion for a proportional loading.

packages do not have this type of models by default, thus, it is required external routines to implement these models within a FEM modulation. Also, they do not have cyclic elastic-plastic models to account with the cyclic variation of the material properties, which is a drawback to the critical plane calculations in finite element analysis. Although, FEM packages may have into account the material stress strain curve determined under monotonic loading conditions, the critical planes estimates requires cyclic stress-strain curves, which are obtained at stress levels much lower than the ones used in monotonic plasticity. Moreover, the plasticity models incorporated in FEM packages do not have into account special cyclic plasticity behaviours like the ones found in magnesium alloys or even in smart materials such as the nitinol, for instance.

# Chapter 3

# Contributions to Level 1

## 3.1 Introduction

This chapter presents the thesis contribution to level 1. It is developed a new cyclic elastic-plastic model under a phenomenological approach to capture the cyclic behaviour of magnesium alloys, which have a *non-standard* mechanical behaviour. This cyclic elastic-plastic model can be used to update stress-strain variations due to multiaxial cyclic loadings in design stages or in the field fatigue damage evaluation. Moreover, it is developed a new concept to characterize the materials non-proportional behaviour. Figure 3.1 shows the position of level 1 regarding the sequential work developed in this research.

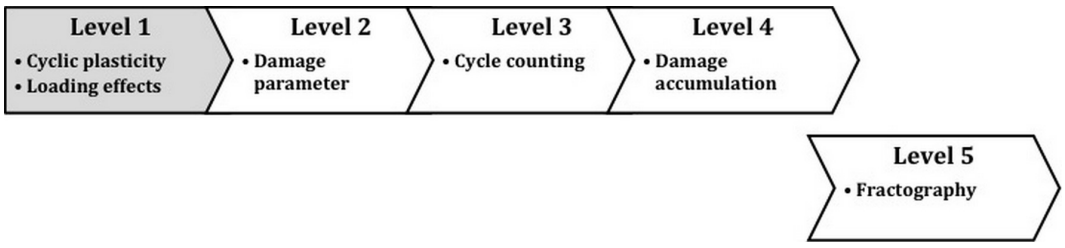


**Figure 3.1:** Multiaxial fatigue level 1.

## 3.2 Cyclic plasticity

### 3.2.1 Introduction

Nowadays, industry in general is following with great attention the scientific research in magnesium alloys. The positive results achieved by the scientific community have created expectations to improve existing magnesium (Mg) products and create new ones. From the 1950s until now, the auto industry has been one of the greatest players in the Mg alloys' research field. Materials with high strength and low density combination are very

appreciated in the transportation industry, however the search of the optimal material with these qualities remains a paramount goal that continues under pursuit. Until now, magnesium alloys are the structural metallic materials that better fulfil this goal. Despite the improvements in fuel consumption and vehicle performance be an economic approach and a driving force from the customer side, the reduction of fuel consumption is also motivated by legislative rules to reduce primary energy consumption, and environmental impact. Thus, approaches to reduce fuel consumption such as aerodynamics drag reduction, engine efficiency, and structural weight reduction are of prime importance in the transportation industry. The weight reduction requires a balance between the material properties and the geometry of mechanical components, under this equilibrium a fully understanding of cyclic, monotonic, and elastic-plastic properties are needed, as well as, the materials fatigue behaviour understanding in all loading regimens.

Cyclic plasticity is quite different from the quasi-static one, the material subjected to cyclic loads tends to change their mechanical properties, and due to that, stress states in the field can be different from the ones used in design stages [137]. Therefore, reliable cyclic elastic-plastic models are required in mechanical design. In the field, components and structures are subjected to multiaxial loadings, and in some cases, they are subjected to variable amplitude loadings or even random loadings [138]. Under multiaxial loading conditions, the stress-strain relation is very different from the uniaxial monotonic curve, which is usually used in constitutive plasticity models [139, 140]. Moreover, cyclic properties of structural materials are much more complex than the monotonic ones and they vary across the loading period. For instance, cyclic yield stress may change cyclically and is usually different from the monotonic yield stress, their variation depends on the material lattice, their constituents, and heat treatment. Some materials can cyclic softening, cyclic hardening, or even have a mixed cyclic behaviour (hardening and softening), which depends on the load level [141, 142]. Cyclic softening occurs when the cyclic yield stress decreases with the increase number of the loading cycles. In contrast, a material hardening occurs when cyclic loadings leads to the cyclic yield stress increase. Magnesium alloys tend to have a cyclic hardening behaviour, i.e. it is required a escalating stress level to cyclically maintain a constant strain amplitude. This cyclic behaviour is highly dependent on the material properties such as grain refinement, purity, microstructure, intrinsic deformation properties like twinning, de-twinning, and slipping or even mechanical transformation processes like lamination, extrusion or forging [23, 139, 143–147]. Thus, the cyclic behaviour modulation in magnesium alloys is of prime importance to estimate accurately their local stress states under cyclic loading conditions. To underline the importance of this need, it is scrutinized in the following, two types of inaccurate results usually obtained when the monotonic curve is used as stress-strain reference in cyclic numeric simulations or to perform fatigue experiments. First, the softening cyclic process under strain control leads to local stress levels lower than the ones

predicted by the monotonic curve. On the other hand, the strain amplitude increases under a stress control approach, which means that the strain amplitude predictions based in the material monotonic curve are smaller than they should be. Second, the cyclic hardening process is a mechanical behaviour opposite to the one found in the material softening, where the local stress amplitudes under strain control are greater than the ones predicted by the material monotonic curve, and the strain amplitudes under a stress control are lower due to the material hardening.

Figure 3.2 shows the monotonic and cyclic behaviour of the AZ31B-F magnesium alloy under uniaxial loading conditions, as one can see, the beginning of the cyclic hardening starts at 0.6% of axial total strain under strain control. Also, the AZ31B-F magnesium cyclic response shows different yield stresses in tension and compression for different total strain amplitudes. The yield stresses in compression have a value near the monotonic value, however, in the tensile branch, the cyclic yield stress is about 26% greater than the monotonic yield stress.

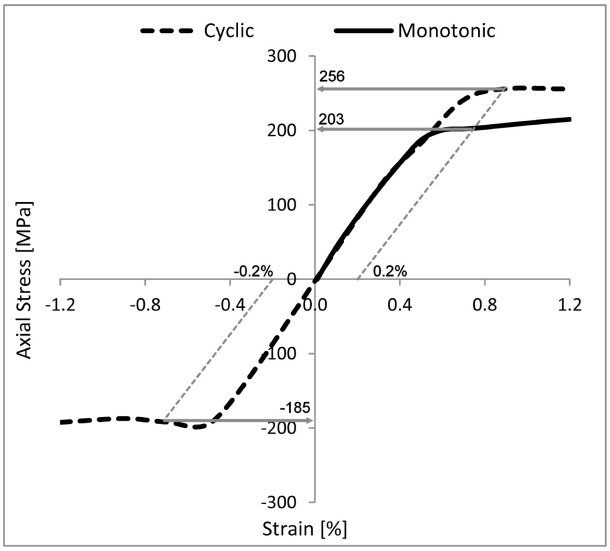


**Figure 3.2:** AZ31B-F monotonic and cyclic behaviour.

The monotonic curve depicted in Figure 3.2 is usually used in commercial finite element software as input to their plasticity codes. The cyclic curve can also be used as input, but it is not possible to enter with the relation between the degree of cyclic plasticity and the number of loaded cycles. Moreover, these two curves represent the material cyclic behaviour under uniaxial loading conditions, which is one loading case among many others - such as multiaxial loadings - that cause different stress-strain states. Thus, elastic-plastic models tuned with these curves to modulate multiaxial cyclic plasticity yield inaccurate estimates. This is so, because in these models, it is used an equivalent stress to transform a multiaxial stress state into a yield parameter - usually it is used the von Mises equivalent stress - in which the axial stress is transformed into a shear stress or vice versa by using a constant, in the von Mises equivalent stress this constant is $\sqrt{3}$. Although, this constant

yields good estimates in quasi-static plasticity assessment, in which the material plasticity level is high, for cyclic plasticity the *constant approach* do not capture the directional cyclic plasticity resulted from multiaxial loadings and the material cyclic anisotropy that is dependent on the material lattice and other mechanical properties.

Plasticity models have intrinsic functions to estimate the stress-strain relation for any kind of quasi-static loading type. These tools are set-up based in one reference loading case, which is the monotonic stress-strain curve. Thus, their yield function, hardening and flow rules are set-up based in the material uniaxial response, which means that their stress-strain estimates for multiaxial loading conditions are not experimentally based. Also, materials with non-standard mechanical behaviour such as magnesium alloys, are not well modulated with conventional plasticity models (standard models found in commercial finite element software) because they were formulated to estimate plasticity under quasi-static loading conditions.

Albinmusa [138, 148, 149] stated that it is need anisotropic plasticity models to cover the cyclic behaviour of magnesium alloys, under that statement a question can be raised up: it will be possible characterize the material anisotropy based only in one loading reference as found in typical constitutive models? From experiments, it was found out that magnesium alloys have a non-linear cyclic behaviour, which is dependent of many factors such as strain rate, micro-structure deformation mechanisms and loading type [137]. Thus, instead of using an uniaxial stress-strain curve in numerical simulations, why not using a function that set up a dynamic stress-strain curve accordingly to the material anisotropic response, load level, and load type? In this way, it becomes possible to enter with the material elastic-plastic cyclic behaviour in numerical simulations.

There are few works in literature regarding the subject of multiaxial stress-strain cyclic behaviour in magnesium alloys [28, 145, 146, 149, 150], but all of them report the peculiarity of the magnesium alloys cyclic behaviour, which is quite different from the one found in steels or even in aluminium alloys, in these studies it is also underlined the needed to go further in this subject. One reason that supports this suggestion is based in the hysteresis loop asymmetry found in magnesium alloys, where the yield stress in compression is quite different from the one in tension, also their rate of change is different in both hysteresis loop branches (tension and compression)[147, 151]. Therefore, it is quite inaccurate account these experimental evidences using only the monotonic stress-strain curve.

Commercial finite element packages such as Ansys or Abaqus do not have mechanisms to modulate unsymmetrical stress-strain curves. In these packages, the yield stress in tension and compression are assumed to be equal in absolute value, which is true for steels and aluminium alloys but not for magnesium alloys, also it is assumed that the plastic strains in tension and compression are equal, which is also not true in magnesium alloys. All these

assumptions are based in the well-known mechanical behaviour of steels and aluminium alloys, thus the tensile monotonic stress-strain curve is enough to modulate the tension and compression behaviour of these materials under a quasi-static loading condition. However, all these assumptions fail in magnesium alloys [138]. Moreover, the magnesium tensile and compressive back stresses are also different, thus it is required a new approach to modulate the mechanical behaviour of these alloys [151]. The problem complexity increases under multiaxial loading conditions, where yield stresses, hardening and flow rules vary accordingly to the loading type (proportional, non-proportional, sequential, etc.) and load level [149].

One way do deal with multiaxial stress states is to use an equivalent stress, which in turn is used in the yield functions formulations. However, in literature, it can be found studies reporting that equivalent stress approaches lose the loading direction dependence, therefore it is possible to obtain the same equivalent stress in all loading directions. Thus, the yield function "will not know" if the equivalent stress is from tension or compression and assumes an isotropic yielding [146], which can be found in steels but not in magnesium alloys. Cyclic elastic-plastic models must have a yield function, hardening and flow rules that capture the material anisotropy in order to be able to model the magnesium alloys cyclic behaviour. One way to do that, is performing an experimental mapping of the material cyclic response.

### 3.2.2 HYS phenomenological elastic-plastic model

#### 3.2.2.1 Introduction

In this section, it is proposed and discussed a phenomenological cyclic elastic-plastic model to estimate cyclic plasticity found in magnesium alloys. This model is deeply based in the hysteresis loop concept, due to that it was named as HYS, which comes from hysteresis. Phenomenological approaches are suitable to model cyclic behaviour of complex materials such as magnesium alloys. These materials exhibits a peculiar mechanical behaviour which has several cyclic effects already discussed in the previous section, thus phenomenological approaches are the most suitable option to modulate complex cyclic behaviours in materials. This model is based in stress-strain measurements (hysteresis loops) under a wide range of cyclic total strain amplitudes and loading conditions found in uniaxial and multiaxial loadings. The objective is to obtain a function/model that estimates the several physical mechanisms found in the magnesium elastic-plastic behaviour under uniaxial and multiaxial loading conditions. In order to validate the cyclic elastic-plastic model proposed here, it is performed a correlation between its estimates and the experimental data. Moreover, it is performed a comparison between the developed model and the Jiang & Sehitoglu plasticity model, already presented in Chapter 2, in order to evaluate the performance of the proposed model.

Typically, there are two ways to modelling cyclic plasticity, one way is the constitutive approach, and the other one is the phenomenological approach. Constitutive models are based in solid mechanics theories and do not require any especial experimental tests, the standard material mechanical properties are enough to set-up this kind of models [148]. Due to that, these models cover a wide range of materials, but regarding anisotropic materials they fail to capture their cyclic behaviour, for these materials the phenomenological cyclic models are advised. Phenomenological models are mainly based in experimental results, and cover the basic premises of constitutive models such as yield function, hardening and flow rules. Both approaches try to estimate the same cyclic behaviour, but following different paths. A phenomenological model like the one developed here, can be implemented in an external routine linked to a finite element package, in this way, this external routine can cyclic update the material cyclic behaviour across the numerical simulation. In order to develop the phenomenological model presented here (HYS model), it was adopted two strategies, the first one was to set-up the HYS model based in uniaxial hysteresis loops (axial and shear), and the second one considers axial and shear hysteresis loops resulted from proportional loadings.

#### 3.2.2.2 HYS model based in uniaxial hysteresis loops

In order to cover all cyclic phenomena discussed in previous sections, it is used here the AZ31B-F uniaxial hysteresis loops (axial and shear) performed under cyclic strain control in order to map the material cyclic behaviour. In this section, the objective is to implement a numeric model, based in uniaxial hysteresis loops, capable to estimate the stress-strain relation in uniaxial and multiaxial loading conditions under a predefined strain amplitude range.

Phenomenological models are deeply dependent on experiments, therefore their estimates reliability for strain amplitudes outside of the experimental envelope is not guaranteed, thus the HYS numeric model will be tested with strain amplitudes within the experimental envelope. Nevertheless, the total strain amplitude used in experiments ranges from elastic strains to total strains amplitude with high plasticity resulting in the specimen collapse at very few loading cycles. Thus, the total strain amplitude range used in experiments covers a cyclic stress-strain relation that is normally used in standard design stages.

From experiments, it was found that the magnesium alloy hysteresis loop branches (upper and lower branches) can be fairly approximated by a third degree polynomial function for any value of total strain, please see Figure 3.3. The constants of these polynomials are obtained based in the six points (P points) of the hysteresis loop depicted in Figure 3.3. Moreover, these P points are dependent of the total strain amplitudes and can be estimated by using functions obtained by regression analysis of the experimental P points, these functions were named as P functions. The upper hysteresis branch is defined by the

P points 4, 5, 6 and 1, and the lower hysteresis branch is defined by the P points 1, 2, 3, 4. This definition was used in both axial and shear hysteresis loops.

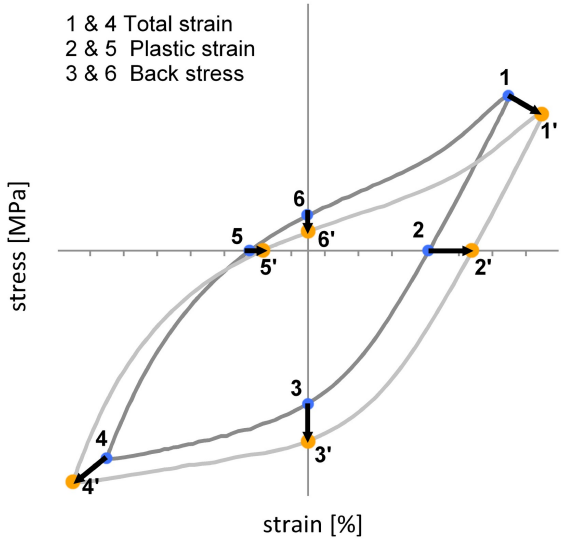


**Figure 3.3:** Third degree polynomial interpolation reference points, in tension and compression loading directions for two consecutive hysteresis loops.

Figure 3.4 depicts the reasoning steps behind the HYS model regarding the lower branch of a hysteresis loop, for the upper branch the reasoning is similar thus this explanation is only focused in one hysteresis branch. First, for a given total strain amplitude, it is obtained the P points at positions 1 to 4 through the P functions, these values are the input of the polyfit Matlab function. Second, the polyfit output $(a_{\varepsilon t}, b_{\varepsilon t}, c_{\varepsilon t}, d_{\varepsilon t})$ are the constants of the third degree polynomial for a given total strain amplitude. Third, the third degree polynomial is set up for the given total strain amplitude. Fourth, the stress-strain relation can be obtained within the range $-\varepsilon_{total} \leq \varepsilon \leq \varepsilon_{total}$.

$$\mathbf{1} \Downarrow$$

$$\overset{Matlab}{polyfit}\left(P_1(\varepsilon_{total}), P_2(\varepsilon_{total}), P_3(\varepsilon_{total}), P_4(\varepsilon_{total})\right)$$

$$\mathbf{2} \Downarrow$$

$$a_{\varepsilon_t}, b_{\varepsilon_t}, c_{\varepsilon_t}, d_{\varepsilon_t}$$

$$\mathbf{3} \Downarrow$$

$$\sigma(\varepsilon)_{right} = a_{\varepsilon_t}\varepsilon^3 + b_{\varepsilon_t}\varepsilon^2 + c_{\varepsilon_t}\varepsilon + d_{\varepsilon_t}$$

$$\mathbf{4} \Uparrow$$

**Figure 3.4:** Reasoning description of the HYS phenomenological model developed in this work.

Points 1 and 4, shown in Figure 3.3, can be considered as values of an experimental yield function, where point 1 belongs to the upper hysteresis branch and point 4 belong to the lower. Moreover, points 2 and 5 are the plastic strains, which can be directly related

to the typical isotropic/kinematic hardening models found in constitutive plastic models. Points 3 and 6 can be related to the back-stress concept which is the stress needed to reduce plastic strains to zero. Thus, if it is known the variation of these points (1 to 6) in respect to the total strain amplitude variation, it is possible to obtain the hysteresis loop shape for any total strain amplitude. With these hysteresis loops it is possible to capture the magnesium elastic-plastic mechanisms such as twinning, de-twinning, and slip effects at each total strain amplitude. The hysteresis loop equations at each total strain amplitude, within the experimental strain amplitude envelope, is given by Eq.(s) 3.1 and 3.2 regarding the lower and upper side of the hysteresis loop.

$$\sigma(\varepsilon)_{lower} = a_{\varepsilon_t}\varepsilon^3 + b_{\varepsilon_t}\varepsilon^2 + c_{\varepsilon_t}\varepsilon + d_{\varepsilon_t} \tag{3.1}$$

$$\sigma(\varepsilon)_{upper} = e_{\varepsilon_t}\varepsilon^3 + f_{\varepsilon_t}\varepsilon^2 + g_{\varepsilon_t}\varepsilon + h_{\varepsilon_t} \tag{3.2}$$

The values $a_{\varepsilon_t}$ to $h_{\varepsilon_t}$ of Eq.(s) 3.1 and 3.2 are dependent of the total strain amplitude of a hysteresis loop and are obtained as depicted in Figure 3.4. From here, the problem is reduced to the search of the polynomial constants ($a_{\varepsilon_t}$ to $h_{\varepsilon_t}$) in respect to the total strain amplitudes of the experimental range envelope. In order to do that, the polyfit Matlab routine is used to obtain these values. This routine has as input the stress-strain values found at points 1, 2, 3 and 4 for the lower branch of the hysteresis loop, and points 4, 5, 6 and 1 for the upper branch, as shown in Figure 3.3. Eq.(s) 3.3 and 3.4 shows the input and output variables of the polyfit Matlab function for the lower and upper branches of the hysteresis loop, respectively.

$$[a_{\varepsilon_t}, b_{\varepsilon_t}, c_{\varepsilon_t}, d_{\varepsilon_t}] = polyfit\left(P_{1`}\left(\varepsilon_t\right), P_{2`}\left(\varepsilon_t\right), P_{3`}\left(\varepsilon_t\right), P_4\left(\varepsilon_t\right)\right) \tag{3.3}$$

$$[e_{\varepsilon_t}, f_{\varepsilon_t}, g_{\varepsilon_t}, h_{\varepsilon_t}] = polyfit\left(P_4\left(\varepsilon_t\right), P_{5`}\left(\varepsilon_t\right), P_{6`}\left(\varepsilon_t\right), P_1\left(\varepsilon_t\right)\right) \tag{3.4}$$

Where the P functions have the following coordinates as output:

$$(\sigma_1, \varepsilon_{total}) = P_1\left(\varepsilon_{total}\right) \tag{3.5}$$

$$(0, \varepsilon_{plastic}) = P_2\left(\varepsilon_{total}\right) \tag{3.6}$$

$$(\sigma_3, 0) = P_3\left(\varepsilon_{total}\right) \tag{3.7}$$

$$(\sigma_4, -\varepsilon_{total}) = P_4(\varepsilon_{total}) \tag{3.8}$$

$$(0, -\varepsilon_{total}) = P_5(\varepsilon_{total}) \tag{3.9}$$

$$(\sigma_6, 0) = P_6(\varepsilon_{total}) \tag{3.10}$$

The P functions are obtained by interpolation of the experimental P points, these functions allow to estimate P points for any total strain amplitude even for the ones not considered in experiments. The functions $P_1(\varepsilon_{total})$ and $P_4(\varepsilon_{total})$ estimate the stresses of maximum total strain. The functions $P_2(\varepsilon_{total})$ and $P_5(\varepsilon_{total})$ estimate the plastic strains inherent to the maximum total strain, and functions $P_3(\varepsilon_{total})$ and $P_6(\varepsilon_{total})$ estimate the back stresses.

The methodology described in this section can be used in both axial and shear hysteresis loops of uniaxial loadings. Thus, the cyclic elastic-plastic behaviour of a biaxial loading can be roughly estimated with this approach by considering each load component of the biaxial loading (axial and shear) as a uniaxial loading without accounting with the combined effect from axial and shear loadings. Likewise to the Jiang & Sehitoglu plasticity model, the proposed elastic-plastic model is also related to an elemental cube; therefore, all conclusions made here are related to an infinitesimal material point.

#### 3.2.2.3 HYS multiaxial cyclic elastic-plastic model

In the previous section, the developed model estimate the biaxial elastic-plastic behaviour by considering separately the biaxial loading components (axial and shear strains), which it is a simplification of reality, however in the absence of biaxial stress-strain experiments it can be an useful model. With this simplification, it is assumed that the axial stress and shear stresses do not contribute to each other in terms of cyclic plasticity, which is not true.

In this section,it is performed an upgrade to the conceptual idea of the developed elastic-plastic model presented in the previous section in order to cover the combined effect of multiaxial loading components in the material elastic-plastic cyclic behaviour. To do that, the functions $P_1$ to $P_6$ were modified in order to have into account the SAR (strain amplitude ratio $\lambda$ ) variation and loading level. Thus, the upgraded P functions have here two inputs instead of one, the total strain amplitude is replaced by the loading SAR and by a new identity defined in this study: the Hypo-strain. Thus, the P functions have the following inputs:

$$P_{1to6}(\varepsilon_{hs}, \lambda) \tag{3.11}$$

The Hypo-strain is an equivalent strain that was developed in this work and is obtained based in the hypotenuse concept, being directly calculated with axial and shear strain components of a biaxial loading. In this concept neither the axial strain neither the shear strain is corrected with any factor such as the $\sqrt{3}$ used in the von Mises equivalent strain, for instance. The Hypo-strain aims to quantify the strain resulted from the contribution of two perpendicular strains, (axial and shear strains of an biaxial loading). This is an important concept, because geometrically the strain obtained in this way, is equal to the one found in the SAR direction.

In this study, the SAR ($\lambda$ ) nomenclature indicates the strain amplitude ratio, which is the same concept used under stress control experiments, usually named as stress amplitude ratio. SAR is a useful concept that establishes loading directions of loading paths and is defined by the ratio of shear strain to axial strain (SAR strain version). In this way, it is possible to get the loading direction, which is a loss information when it is used equivalent strain or equivalent stress concepts. Furthermore, SAR is also the angle between the Hypo-strain and the axial strain component, which is presented here in degrees.

Eq.(s) 3.12 and 3.13 presents the upgraded P functions for the axial and shear components of a biaxial loadings, this equations were obtained based in the best fit of axial and shear hysteresis loops of a biaxial loading in the AZ31B-F magnesium alloy. Also, here the upgraded P functions are only valid within the experimental strain amplitude used in experiments. The $i$ and $j$ indices vary between 1 and 6 where the hysteresis lower branch is cover by indices 1 to 4, and the upper hysteresis branch is cover by indices 4, 5, 6, and 1.

$$P_{axial,i}\left(\varepsilon_{hs},\lambda\right)=a_i+b_i\varepsilon_{hs}+c_i\lambda+d_i\varepsilon_{hs}^2+e_i\lambda^2+f_i\varepsilon_{hs}\lambda+g_i\varepsilon_{hs}^3+h_i\lambda^3+i_i\varepsilon_{hs}\lambda^2+j_i\varepsilon_{hs}^2\lambda \quad (3.12)$$

$$P_{shear,j}\left(\varepsilon_{hs},\lambda\right)=a_j+b_j\varepsilon_{hs}+c_j\lambda+d_j\varepsilon_{hs}^2+e_j\lambda^2+f_j\varepsilon_{hs}\lambda+g_j\varepsilon_{hs}^3+h_j\lambda^3+i_j\varepsilon_{hs}\lambda^2+j_j\varepsilon_{hs}^2\lambda \quad (3.13)$$

The input of Eq.(s) 3.3 and 3.4 is update with Eq.(s) 3.12 and 3.13 as follows in Eq.(s) 3.14 and 3.15.

$$\left[a_{\varepsilon_t},b_{\varepsilon_t},c_{\varepsilon_t},d_{\varepsilon_t}\right]=polyfit\left(P_1\left(\varepsilon_{hs},\lambda\right),P_2\left(\varepsilon_{hs},\lambda\right),P_3\left(\varepsilon_{hs},\lambda\right),P_4\left(\varepsilon_{hs},\lambda\right)\right) \quad (3.14)$$

$$\left[e_{\varepsilon_t},f_{\varepsilon_t},g_{\varepsilon_t},h_{\varepsilon_t}\right]=polyfit\left(P_4\left(\varepsilon_{hs},\lambda\right),P_5\left(\varepsilon_{hs},\lambda\right),P_6\left(\varepsilon_{hs},\lambda\right),P_1\left(\varepsilon_{hs},\lambda\right)\right) \quad (3.15)$$

#### 3.2.2.4 Experimental data

The AZ31B-F cyclic elastic-plastic behaviour was mapped with the 6 biaxial loading paths depicted in Figure 3.5. Figure 3.6 shows the sample used in this experiments (geometry and its dimensions). The first loading case, Case 1, is a pure uniaxial tension test, Case PT. The second one, Case 2, is a pure shear loading, named as Case PS (pure torsion). Cases 3, 4, and 5 are proportional loadings with SAR equal to 30°, 45°, and 60°, respectively. Finally, Case 6 is a non-proportional loading case, with a SAR equal to 45° and a phase shift equal to 90°.

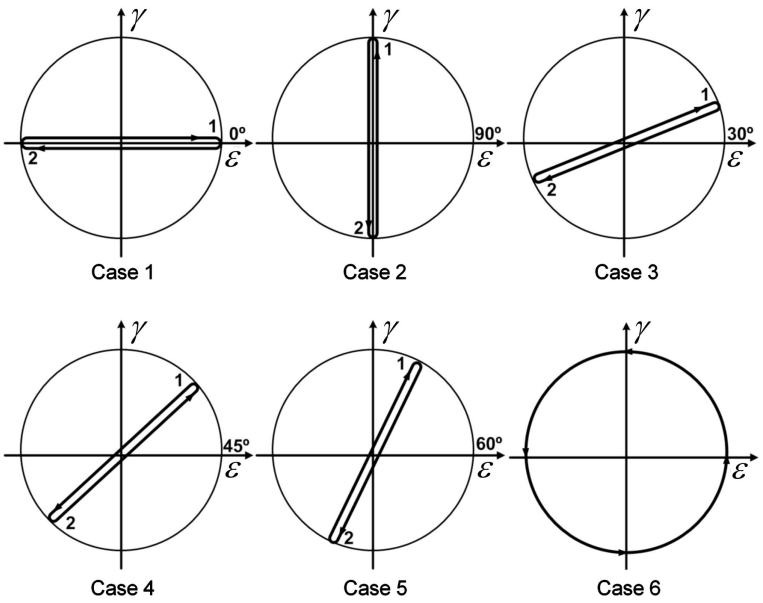


**Figure 3.5:** Loading paths under strain control: a) Case 1 PT, b) Case 2, PS, c) Case 3, PP30, d) Case 4, PP45, e) Case 5, PP60 and, f) Case 6, OP45.

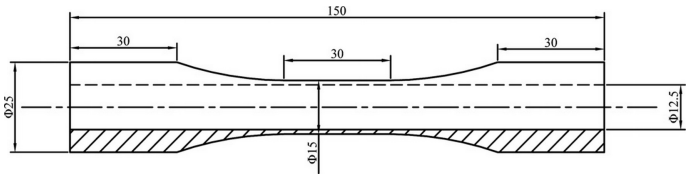


**Figure 3.6:** Sample geometry and its dimensions used in the strain control experiments performed in this study.

For each loading case several strain amplitudes were considered to obtain the experimental P points of the axial and shear hysteresis loops, which are used to obtain the axial and shear P functions. These functions will allow to estimate the hysteresis loops shape for strain amplitudes different from the ones used in experiments to map the magnesium alloy cyclic behaviour. All these loading paths, Cases 1 to 6, were carried out in experiments and implemented in numerical analysis. The experimental tests were performed at room temperature and ended up at 50% of load drop under strain control.

Figure 3.7 presents the uniaxial results for the hysteresis loops in pure axial and pure

shear loading conditions, i.e. Case 1 (PT) and Case 2 (PS). Figure 3.7 a) depicts the experimental results of Case 1, where unsymmetrical hysteresis loops with different plastic strains in tension and compression were found. Moreover, in these loops can be found different stress amplitudes in tension and compression for a given absolute total strain amplitude. Also, the plastic strains and stresses in tension and compression vary in a non-linear way. The experimental hysteresis loops show that the six P points inherent to the hysteresis loops are independent from each other, being required six P functions to estimate the P points dependence of the Hypo-strain variation.

Figure 3.7 b) shows the experimental hysteresis loops for the AZ31B-F magnesium alloy in pure torsion, being quite symmetric, which is a cyclic behaviour very different from the one found in the axial loadings, i.e. the shear stresses (right and left) have the same absolute value for a given shear strain amplitude (under strain control loading conditions). Moreover, the shear plastic strains are also very similar in both loading directions (lower and upper), the slight difference that can be seen in Figure 3.7 b) resulted from the loading direction of the first loading cycle.

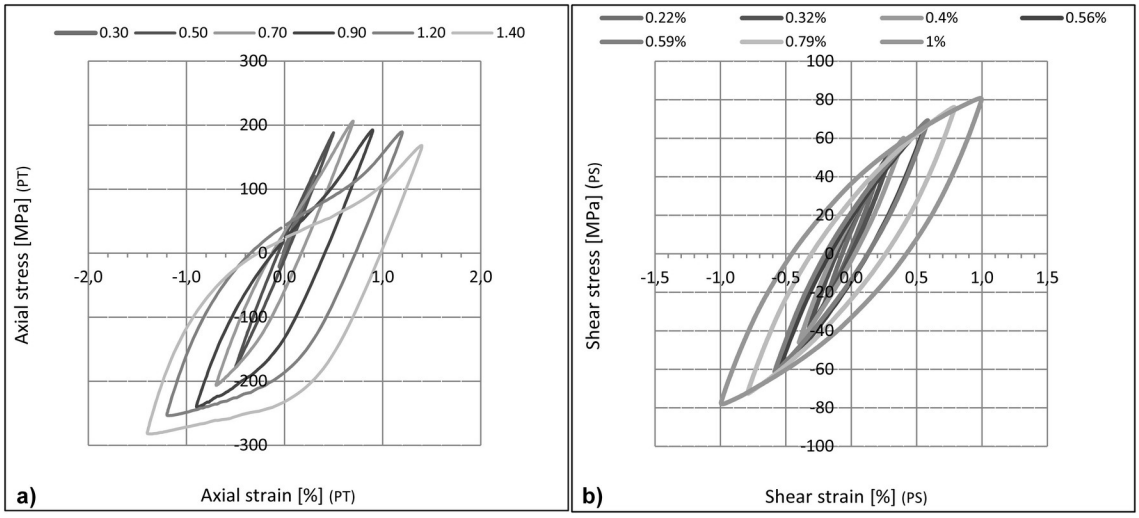


**Figure 3.7:** Experimental hysteresis loops for: a) Case 1 and b) Case 2.

Figure 3.8 presents the experimental hysteresis loops obtained in Cases 3 and 4. Figure 3.8 a), and 3.8 b) depict the axial and shear hysteresis loops of Case 3 where the proportional loading has a SAR equal to 30º (axial strain component higher than the shear one). In Case 3, the axial total strains and inherent plastic strains governs the deformation behaviour.

Fig.(s) 3.8 c) and 3.8 d) depict the experimental results of Case 4. Here, the biaxial loading has a SAR equal to 45º, which indicates that the maximum amplitude of the axial and shear strains are equal. Despite the shear and axial strains amplitudes be equal their stresses are quite different. For instance, a shear strain of 0.5% yields a 50 [MPa], but the axial strain with the same strain value yields 160 [MPa], please see Figure 3.8 c) and 3.8 d). Moreover, the axial stress is quite different in compression and tension, even for the

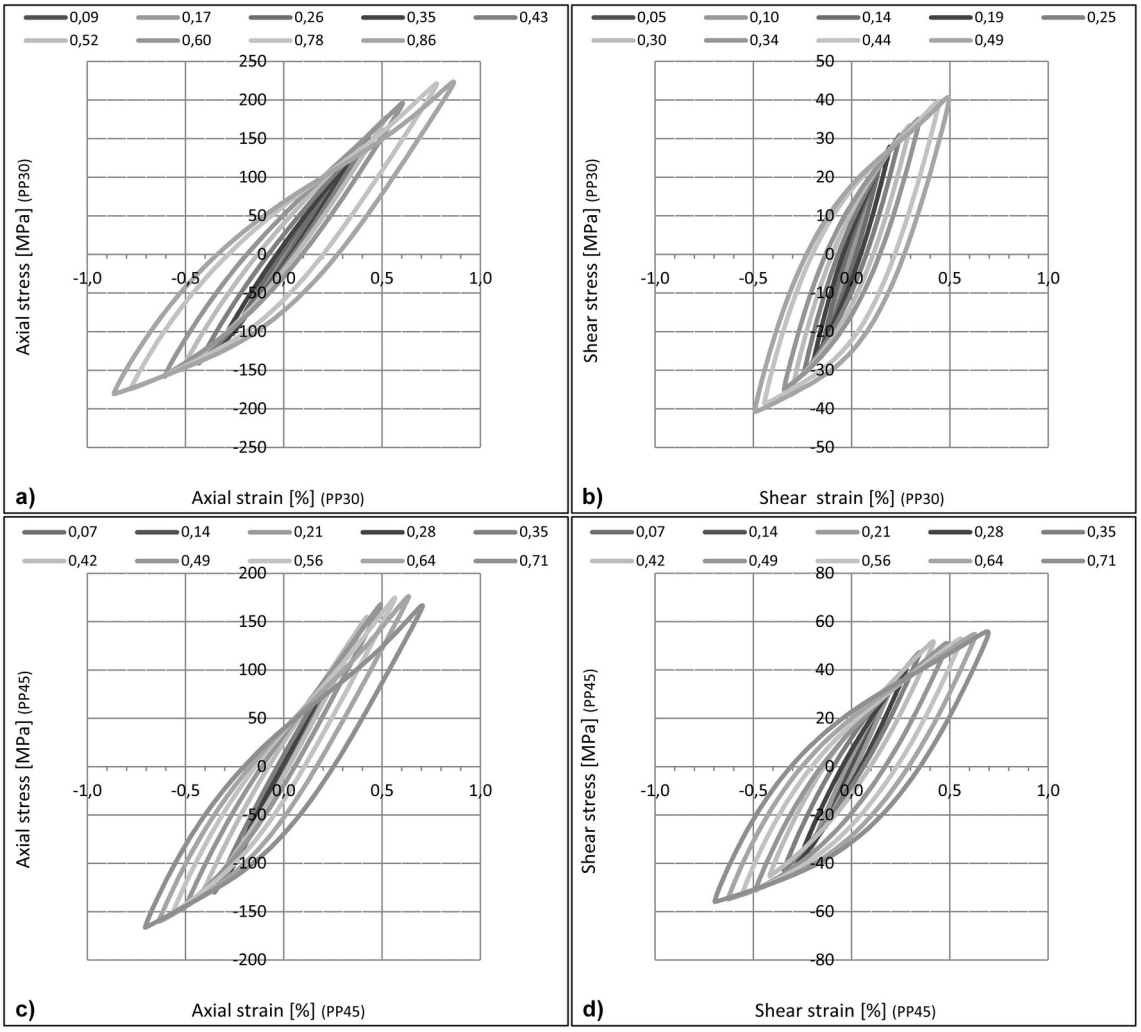


**Figure 3.8:** Experimental hysteresis loops for loading Cases 3 and 4: a) Case 3 axial stress-strain, b) Case 3 shear stress-strain, c) Case 4 axial stress-strain, and d) Case 4 shear stress-strain.

same axial strain amplitude in tension and compression. The shear strain hysteresis loops depicted in Figure 3.8 d), continues to show a symmetric pattern as seen in the pure shear loading case. This result shows that the hysteresis loop shape is not strongly affected by the biaxial loading condition, i.e. the presence of an axial strain amplitude do not affect the shear hysteresis symmetry. Regarding the results of Case 3 and 4 (proportional loadings with SAR equal to 30° and 45°) it can be concluded that the SAR increase leads to the reduction of the axial plastic strain and to the increase of the shear plastic strain, thus the SAR variation is a indicator of the axial/shear predominance effect in the material cyclic behaviour. Fig.(s) 3.9 a) and 3.9 b) present the experimental results for the proportional loading with SAR equal to 60° and named as Case 5. In this results, it is quite evident that the shear hysteresis loops have greater plastic strains than the axial ones, therefore, the deformation mechanisms and inherent stresses changes accordingly to each SAR. Thus, the typical equivalent stress concept, such as the von Mises equivalent stress/strain, is not suitable to capture this type of deformation effects, because they are

independent of the loading direction. For example, it can be obtained the same von Mises equivalent stress for all possible SARs (all loading directions), but each SAR has different deformation and cyclic behaviours as depicted in Fig(s) 3.7 to 3.9 as discussed in previous and proved here by experiments. Fig.(s) 3.9 c) and d) presents the Case 6 hysteresis loops (axial and shear), this loading case is a non-proportional loading path with SAR equal to 45°, the same used in Case 4. The cyclic results of Case 6 are different from the ones depicted in Fig.(s) 3.8 c) and d) regarding the Case 4 experimental results. Both loading cases have the same SAR (45°) but different cyclic behaviours were obtained regarding the axial and shear hysteresis loops. For instance, the shear plastic strain clearly increases with non-proportionality, also the back stresses changed their pattern by adding a phase angle to Case 4. These two parameters, cyclic plastic strains and back stresses, are an indicator of the loading type effect on the material cyclic behaviour. Thus, it can be concluded that non-proportional loadings create different cyclic patterns in the material cyclic behaviour comparatively to proportional loadings, even for the same SAR and load level.

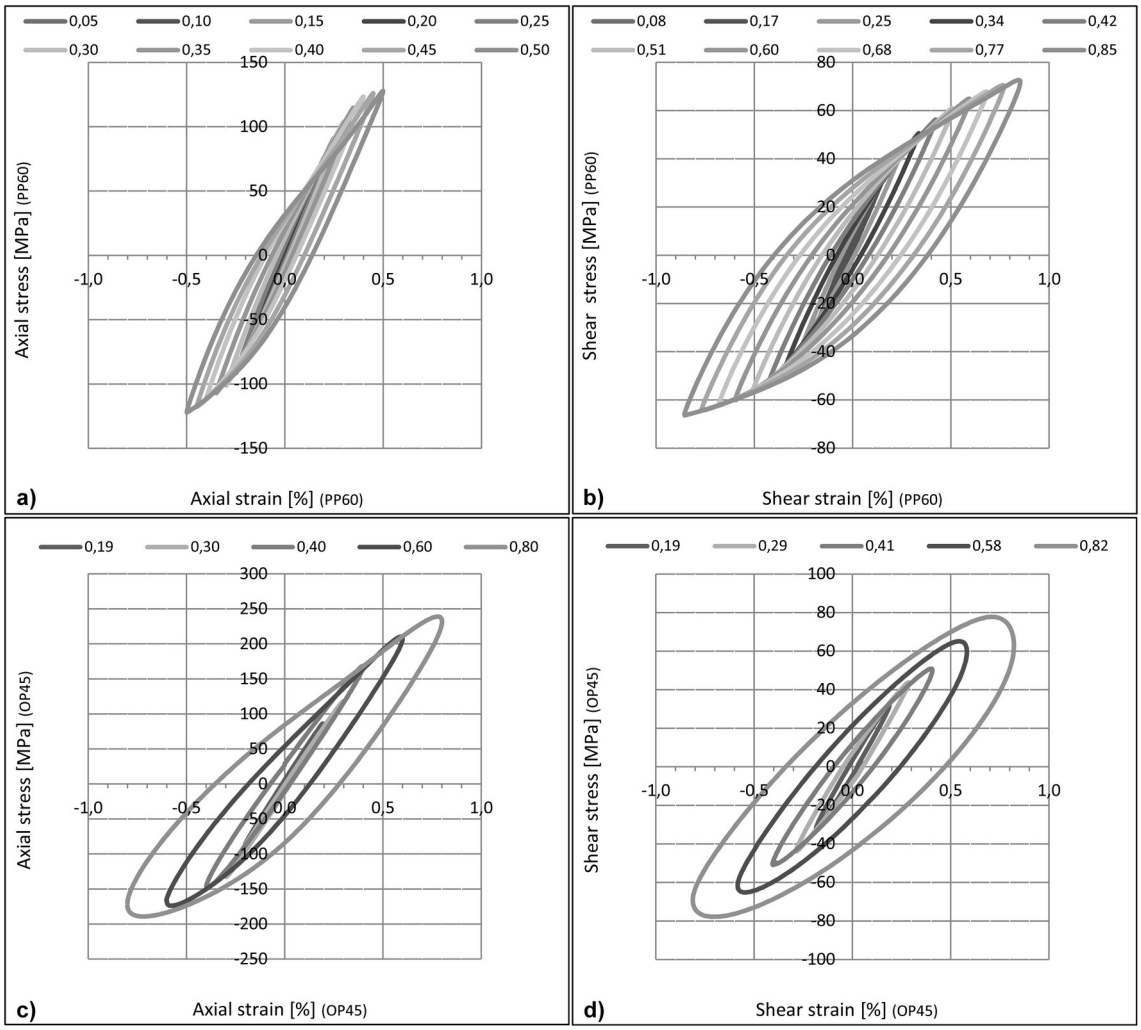


**Figure 3.9:** Experimental hysteresis loops for loading Cases 5 and 6: a) Case 5 axial stress-strain, b) Case 5 shear stress-strain, c) Case 6 axial stress-strain, and d) Case 6 shear stress-strain.

#### 3.2.2.5 Experimental P points

Figure 3.10 shows the P points dependence on the total strain amplitude in the pure axial loading case, Case 1. Figure 3.10 a) presents the maximum stress amplitudes inherent to each maximum strain amplitude. In graphs depicted in sub-figures 3.10 a) and b), the abscissa axis represents the axial strain amplitude of the cyclic loading, which in experiments takes negative and positive values. Therefore, tensile stresses have positive strains and compressive strains have negatives stresses. However, to better interpret and correlate the results of the compression and tension loads, it is considered here that the compressive strains and inherent stresses have positive values. In this way, it is facilitated the comparison between stress-strain relations in tension and compression. For instance, using this way to represent stress-strain data, it can be concluded that the axial stress-strain in tension and compression depicted in Figure 3.10 a) is almost equal in the interval below 0.4% of total strain, but, beyond that value, the physical elastic-plastic behaviour of the AZ31B-F magnesium alloy is quite different in tension and compression. Figure 3.10 b) shows that the plastic strains in compression and tension have similar values until bellow 0.4% of total strain, after this value, plastic strains in compression and tension have completely different values. Each curve depicted in Figures 3.10 to 3.17 represents the variation of the P points in respect to the total strain amplitude, the equations of these curves are the P functions obtained by regression procedures. With these functions it becomes possible to estimate any hysteresis loop of the axial and shear components of a biaxial loading in the AZ31B-F magnesium alloy.

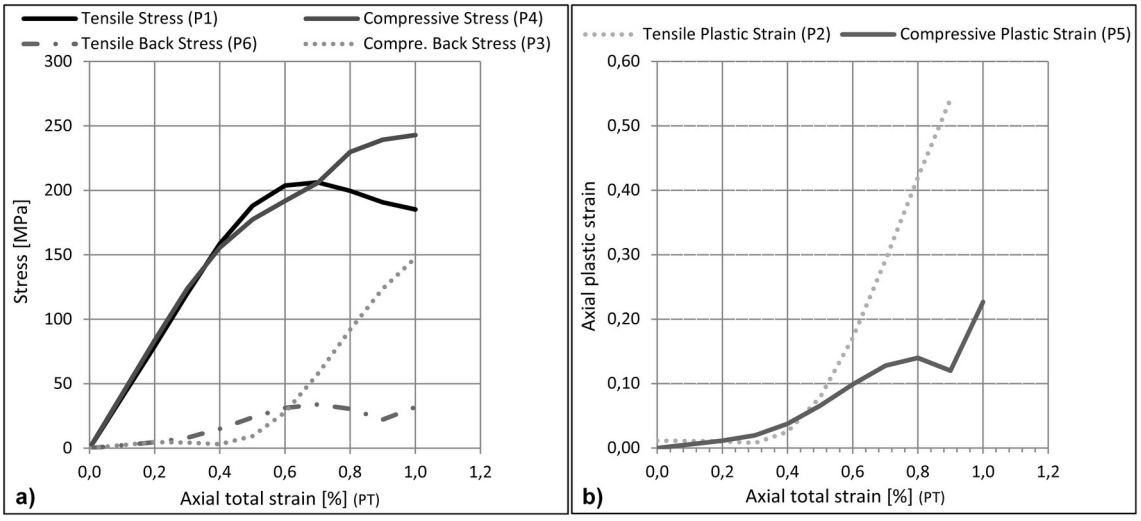


**Figure 3.10:** P points variation with axial total strain variation for Case 1

Figure 3.11 presents the P results obtained in Case 2, (the pure shear loading case), contrary to what is seen in Case 1 (the tension-compression loading case) where for low axial strain amplitudes the P1 and P2 functions are coincident, the shear stresses at points P1 and P4 are always different across the shear strain amplitude range, even for elastic shear strain amplitudes. The same pattern can be seen in the back stress evolution (P3 and

P6) as well as in the plastic strains evolution (P2 and P5). This results can be explained by the first loading direction of the total shear strain, where the first loading direction influences the overall elastic-plastic deformation pattern.

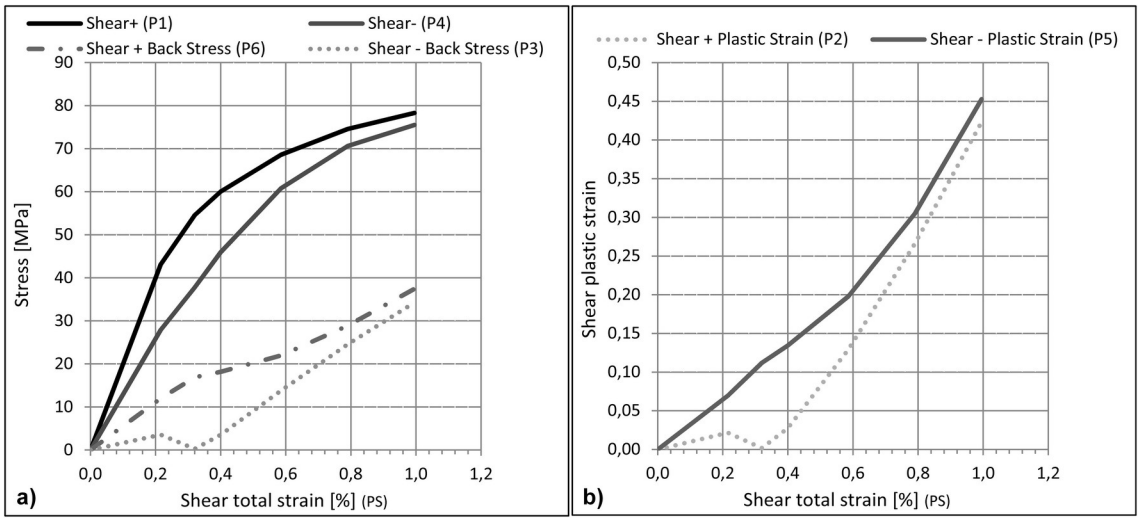


**Figure 3.11:** P points variation with total strain variation for Case 2.

Figure 3.12, presents the P results obtained for the loading Case 3 depicted in Figure 3.5, being a proportional loading path with SAR equal to 30º. Fig.(s) 3.12 a) and c) shows the P results in respect to the axial strain component of the proportional loading and Fig.(s) 3.12 b) and d) show the P results for the shear strain component. The axial elastic-plastic stresses of Case 3 (P1 and P4) are quite similar for total axial strains lower than 0.4%, as seen in Case 1. Surprisingly, the shear stresses evolution (P1 and P4) have the same stress values in both loading directions, the same can be said for the plastic strains, in this case the first loading direction (torque) did not affected the shear hysteresis position. Thus, it can be concluded that the hysteresis loops of the shear component of the proportional loading path, Case 3, are in fact symmetric for all total strain levels. This symmetry can be explained by the low cyclic plasticity resulted from the shear strain amplitude of Case 3, which is much lower than the axial one.

Figure 3.13 shows the magnesium alloy AZ3B-F cyclic behaviour under the proportional loading path with SAR equal to 45º, i.e. Case 4. The same cyclic pattern that was found in Case 3 can be seen in the results of Case 4, where the tension and compression stresses (P1 and P4) begin to have different values beyond 0.4% of total axial strain amplitude. The shear hysteresis loops also have a symmetric trend, as seen in Cases 2 and 3. In this loading path the axial and shear strains have the same amplitude, but the stresses inherent to these amplitudes are quite different. For instance, for 0.4% of axial and shear total strain, the axial yield stress is about 140 [MPa] (P1 in axial) and the shear yield stress is about 50 [MPa] (P1 in shear). Figure 3.14 shows the results obtained regarding Case 5, which is a proportional loading with SAR equal to 60º. In this case the shear strain component is greater than the axial one. The axial cyclic pattern in Case 5 is more

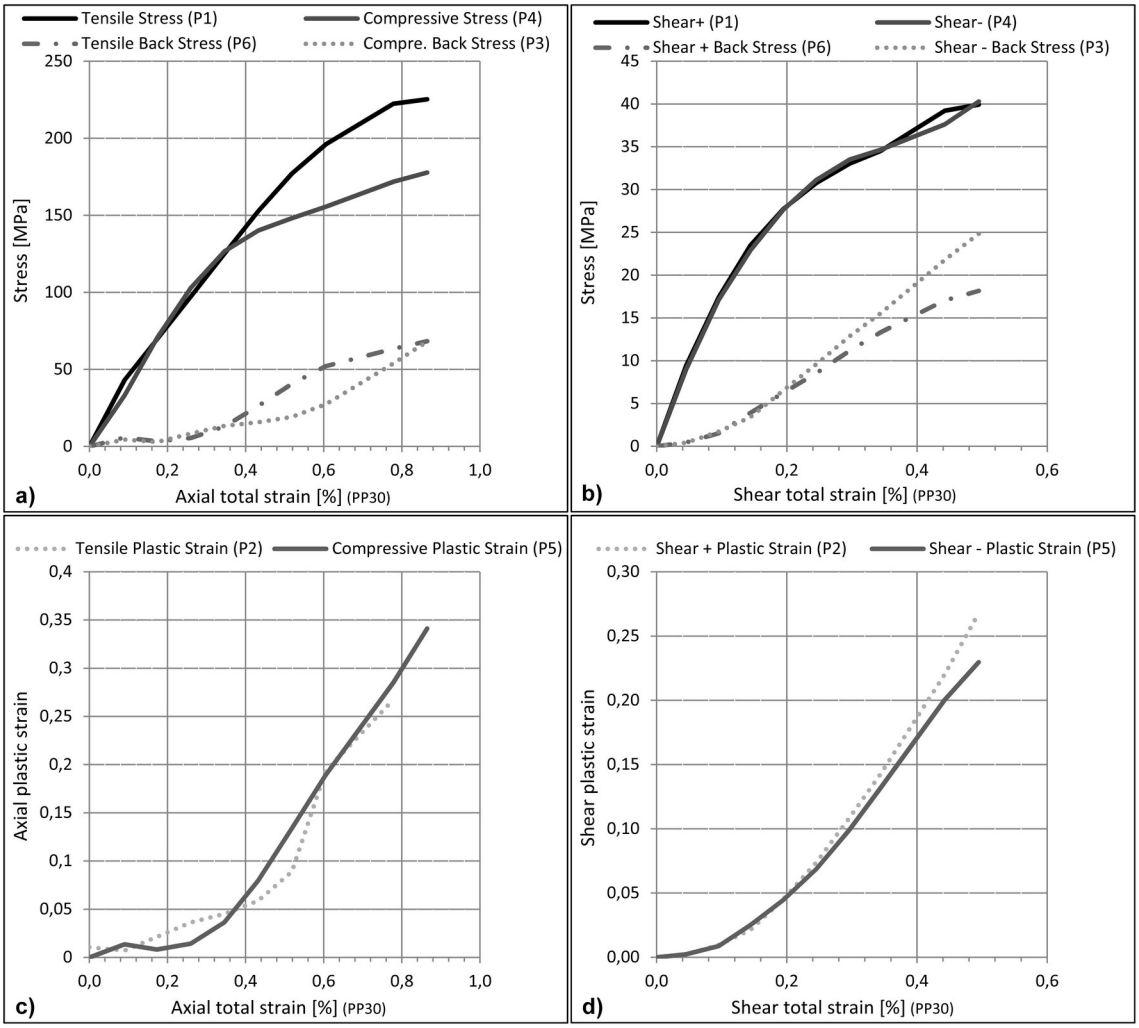


**Figure 3.12:** P points variation is respect to the strain amplitude variation obtained in Case 3.

or less similar to the ones found in Cases 1 to 4, but the shear cyclic pattern has a higher cyclic plasticity, which is an expected result because the shear strain amplitude is much higher than the axial one.

Figure 3.14 b) shows the same cyclic pattern obtained in Case 2, please see Figure 3.11, where the two strain-stress curves (P1 and P4) are not coincident, in this case the first loading direction (right or left) influences the position of the shear hysteresis loop creating a translation across the shear strain axis.

Figure 3.15 shows the results obtained in Case 6, these results are lightly different from the ones obtained in Case 4. Cases 4 and 6 have the same SAR, thus the difference between these two cases comes from the non-proportionality of Case 6. The non-proportional cyclic deformation has a huge influence in the hysteresis loop shape, but the differences found in the back stresses and plastic strains are not so evident.

Figure 3.16 shows the variation of P1 and P2 in respect to the axial and shear total strain amplitudes for all proportional loading cases considered here i.e. Cases 1 to 5, (P1 is the

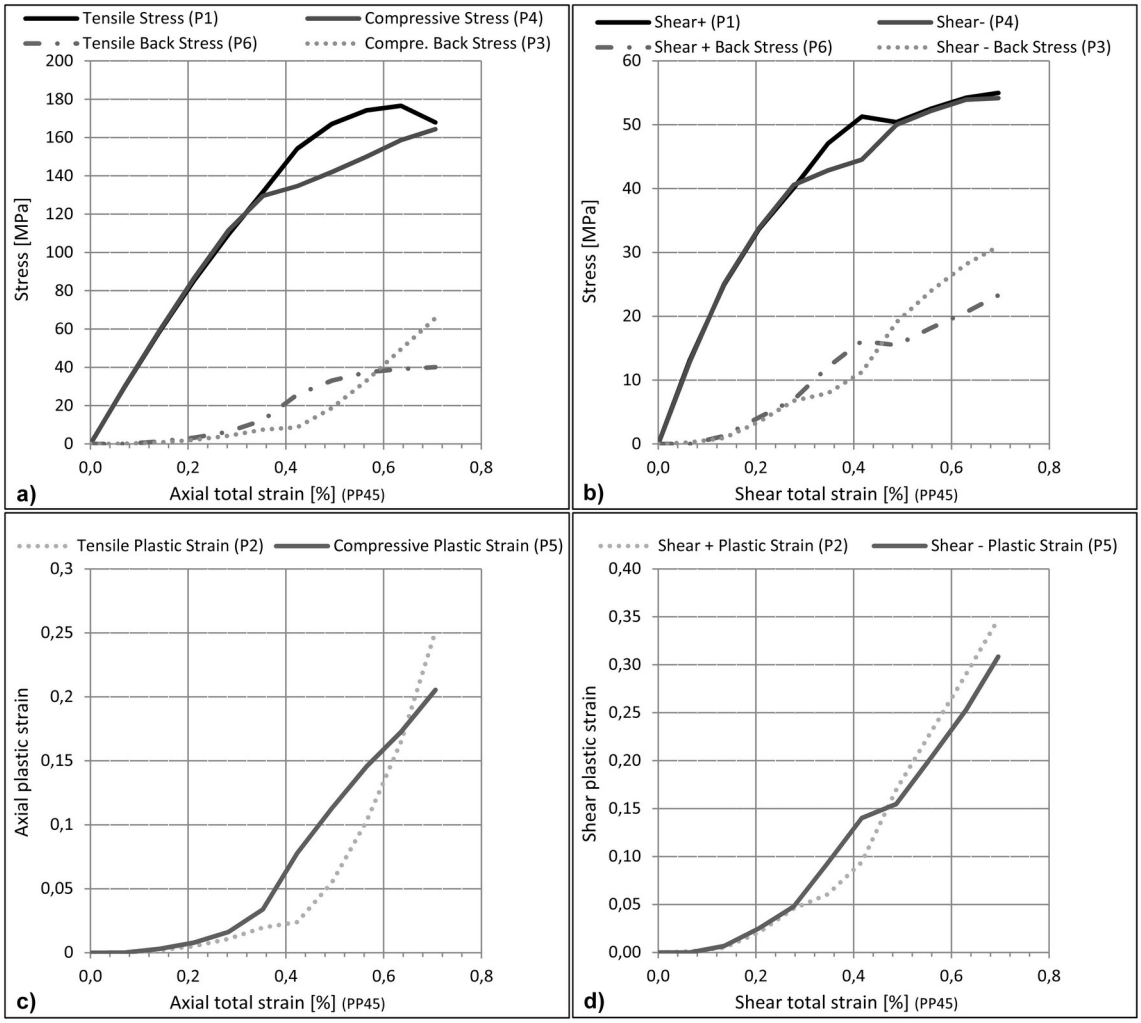


**Figure 3.13:** P points variation is respect to the strain amplitude variation obtained in Case 4.

maximum stress of the hysteresis lower branch and P2 is their plastic strain). The results show that the fitting curves of points P1 in all loading paths are not coincident across the strain amplitude range, thus it can be concluded that the SAR variation have influence in the hysteresis loops and in the inherent cyclic elastic-plastic behaviour. Moreover, the P1 curves are quite similar for total strains less than 0.4%, and the P2 curves are only similar for total strain amplitudes less than 0.2%.

Figure 3.17 shows the P3 and P4 variation in respect to total strain. The P3 curves of the shear component of a biaxial loading are different in all loading paths with no evident pattern, please see Figure 3.17 b). Regarding the P3 curves of the axial loading component, they have a similar pattern for total strain amplitudes lower than 0.4% has seen in the P1 curves. The P4 curves have also a similar pattern for total strains less than 0.4% in both axial and shear components of a biaxial loading, please see Figures 14 c) and d).

Figure 3.18 presents the experimental results obtained for points P5 and P6, which belong to the hysteresis upper branch, the P5 and P6 are the curves of the plastic strain and back stress, respectively. As seen in other curves, i.e. P1 to P4, these curves (P5 and

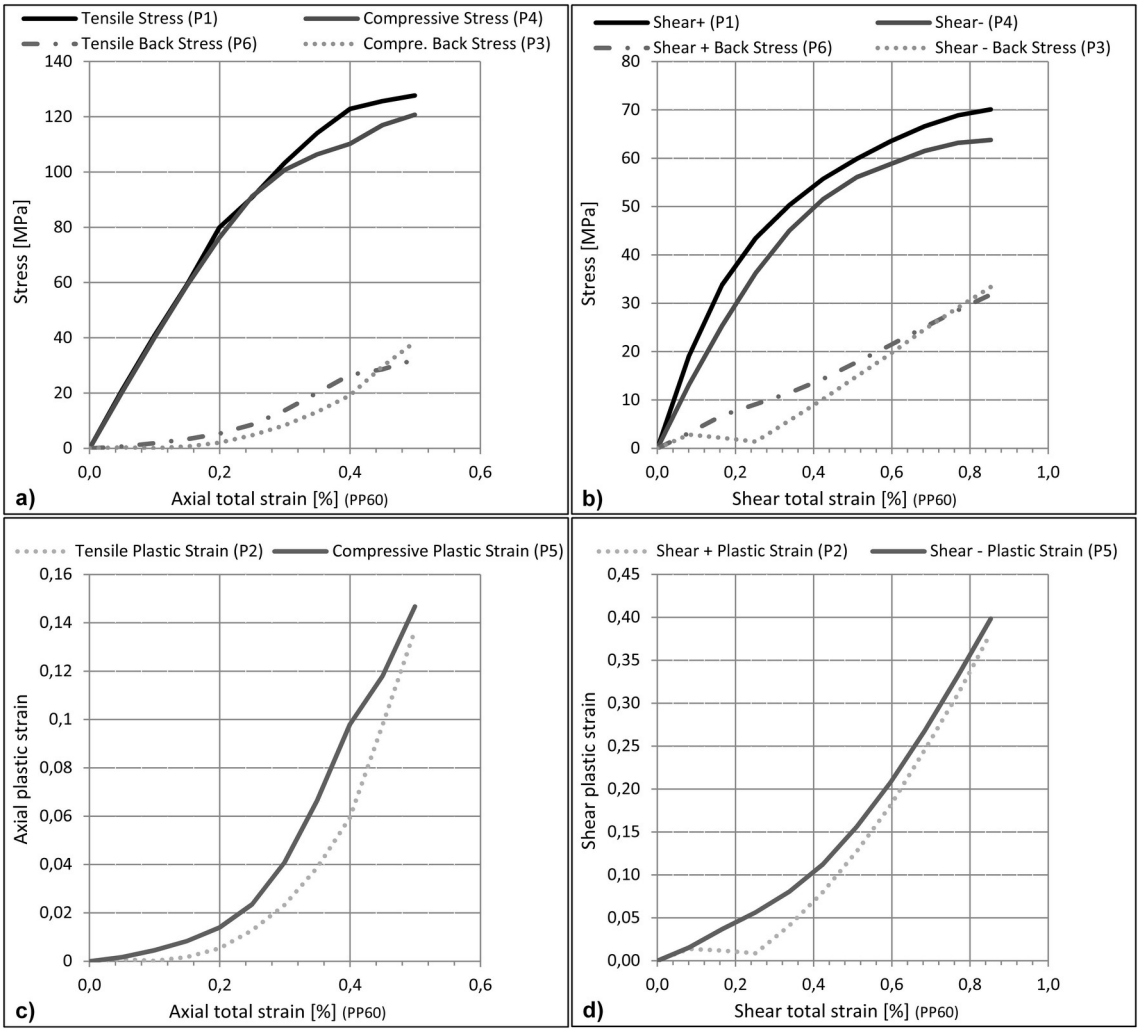


**Figure 3.14:** P points variation is respect to the strain amplitude variation obtained in Case 5.

P6) can be fairly merged in one curve for total strains lower than 0.4%, but beyond this value, they present patterns completely different, for each loading case. These results shown that the magnesium hysteresis loops can be fairly estimated using the uniaxial P functions as presented in section "HYS model based in uniaxial hysteresis loops" if the shear and axial total strain amplitudes are below the upper limit of 0.4%, for greater total strain amplitudes the model must be upgraded as presented in section 3.2.2.3. Figure 3.19 presents a comparison between proportional and non-proportional P curves of loading Cases 4 and 6. Both loading cases have a SAR equal to 45°, thus it is possible to compare the proportional and non-proportional P curves in respect to the same total strain amplitude. The P points of the shear loading components, have a pattern very similar in both loadings, however, the results of the axial loading components have great differences, especially in the curves P3, P4, P5, and P6. Therefore, based in the results depicted in Figure 3.19 it can be concluded that for the AZ31B-F magnesium alloy under non-proportional loading path, the SAR effect in the cyclic deformation only influences the axial component.

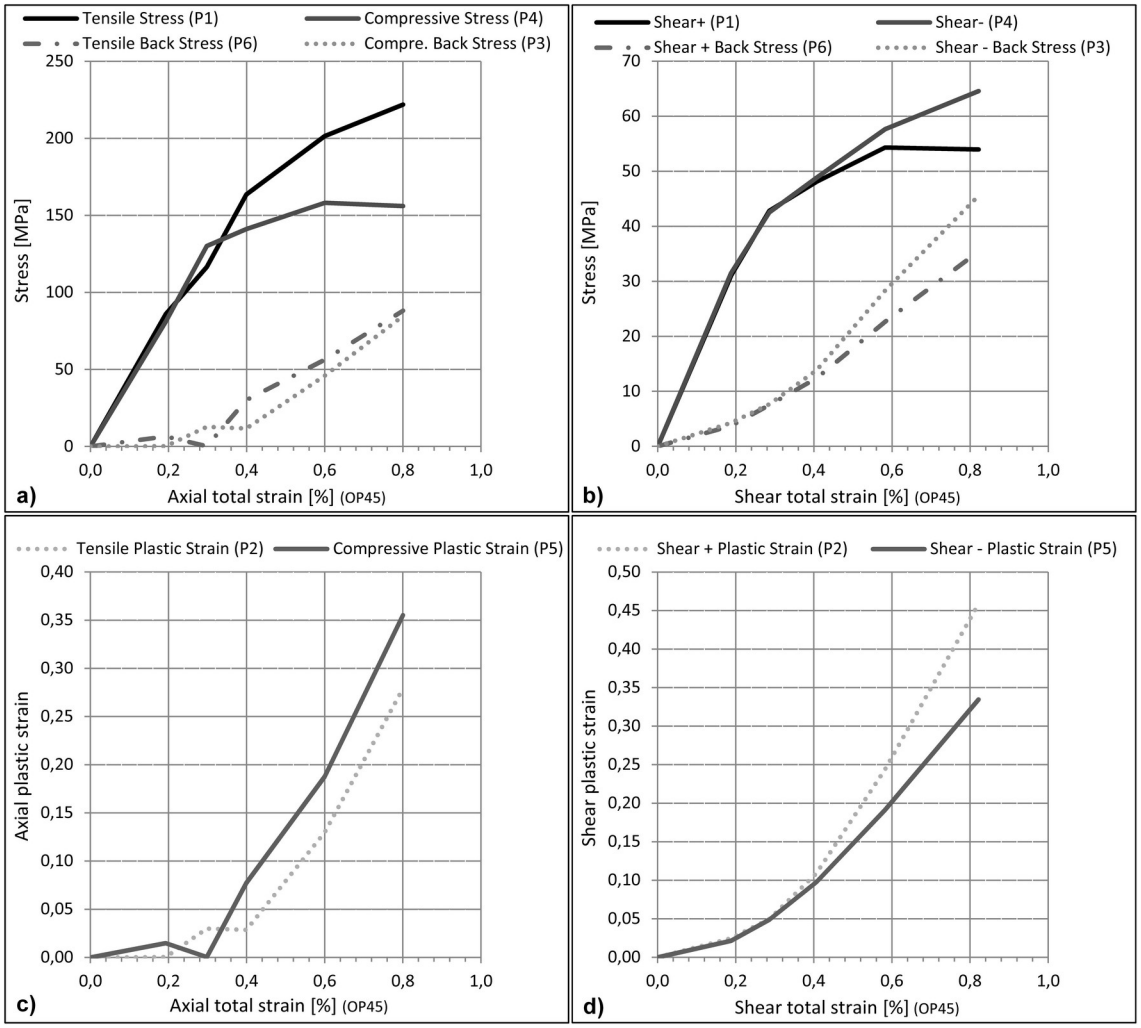


**Figure 3.15:** P points variation with strain variation for the Case 6.

Figure 3.20 presents de SAR (stress amplitude ratio) variation with the Hypo-strain variation, for the three proportional loading paths,i.e Cases 3 to 5. In the graph's abscissa it is presented the Hypo-strain and in ordinate is presented the SAR values (stress amplitude ratio version), which is the ratio of shear stress to axial stress obtained from the material response to the axial and shear strains. For each proportional loading path (Case 3 to 5), it is obtained different SAR values in tension and compression because the AZ31B-F magnesium alloy have different mechanical behaviours in tension and compression. Also, the shear component hysteresis loop is not always symmetric; therefore it will be obtained, in some cases, different stresses for each torsion direction, especially when the shear component is greater than the axial one. The results depicted in Figure 3.20 show that SAR depends on the strain amplitude level and also on the loading direction. This evidence enforces the idea that will be discussed and presented in Chapter 4, in which the SSF value is not constant and depends on the loading path type and stress level. Note that, the Hypo-strain in Figure 3.20 indicates the strain level, thus for each strain level and for a SAR (strain amplitude ratio), it is obtained different stress amplitude

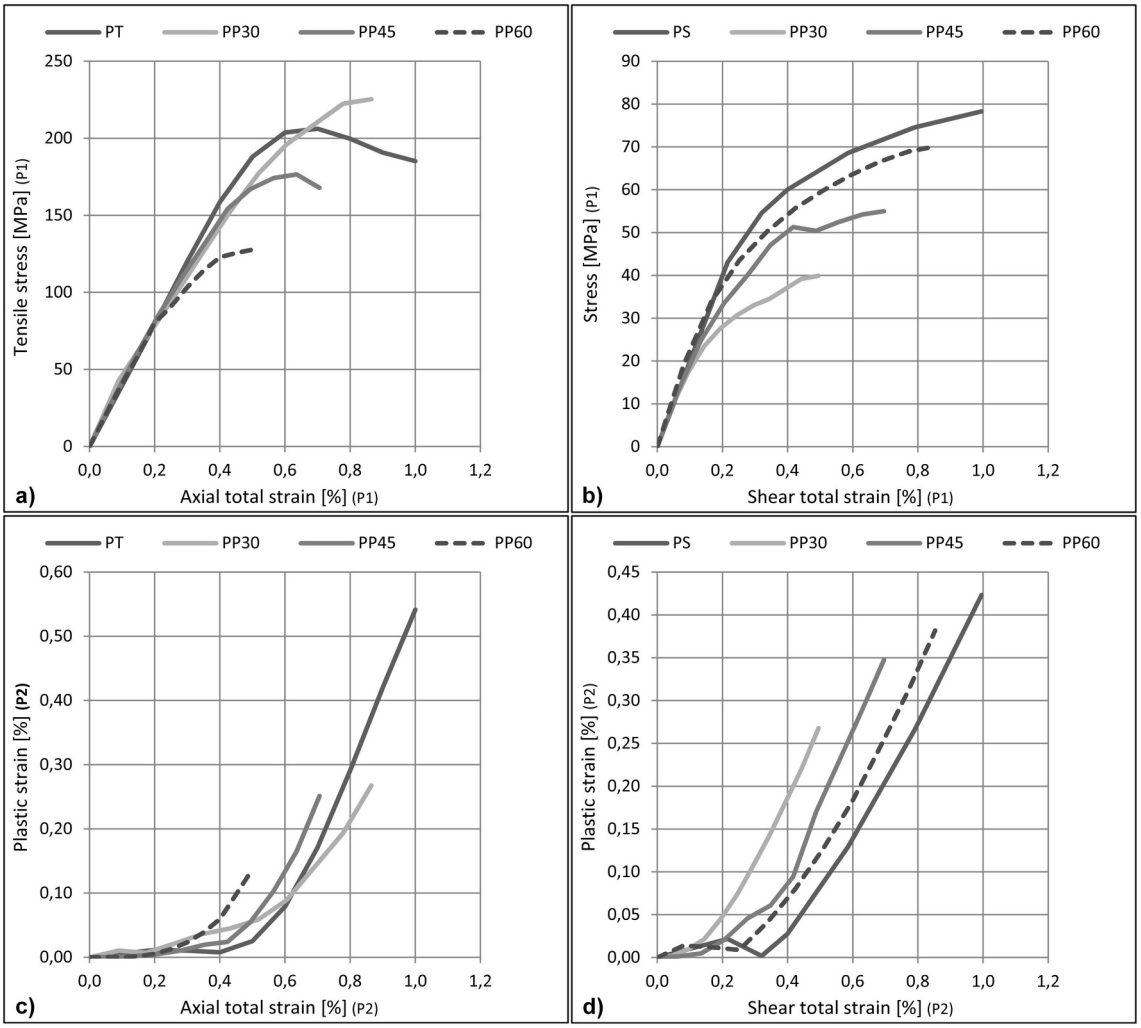


**Figure 3.16:** P1 and P2 variation with SAR and strain variation in all proportional loading paths.

ratios SAR (stress version) as seen in Figure 3.20. Tables 3.1 and 3.2 present the results for the polynomial constants introduced in Eq.(s) 3.12 and 3.13.

**Table 3.1:** Polynomial constants for the P functions for multiaxial loadings - Axial component.

| | **Axial** | | | | | |
|---|---|---|---|---|---|---|
| | **P1** | **P2** | **P3** | **P4** | **P5** | **P6** |
| **a** | -0.03408 | 0.003106 | -0.1717 | -2.35533 | 0.008663 | 0.932681 |
| **b** | 481.6159 | -0.12443 | -40.4912 | 523.3197 | -0.07452 | -8.05794 |
| **c** | -0.0783 | 0.000192 | 0.163393 | -1.38413 | 0.003737 | 1.102192 |
| **d** | -206.819 | 0.23118 | 134.2617 | -379.461 | 0.406281 | 155.8362 |
| **e** | -0.00448 | 1.86E-05 | 0.005408 | 0.0718 | -0.00021 | -0.05726 |
| **f** | -0.80869 | 0.001098 | -0.38309 | -3.55155 | 0.007819 | 1.267397 |
| **g** | -90.706 | 0.433687 | 57.93164 | 100.9811 | -0.13097 | -119.972 |
| **h** | 0.000124 | -4.6E-07 | -0.00016 | -0.00084 | 2.57E-06 | 0.000676 |
| **i** | -0.07011 | 6.69E-05 | 0.025193 | 0.003224 | -0.00016 | -0.03934 |
| **j** | 3.931702 | -0.01128 | -2.8987 | 1.435313 | 0.000804 | 1.018756 |

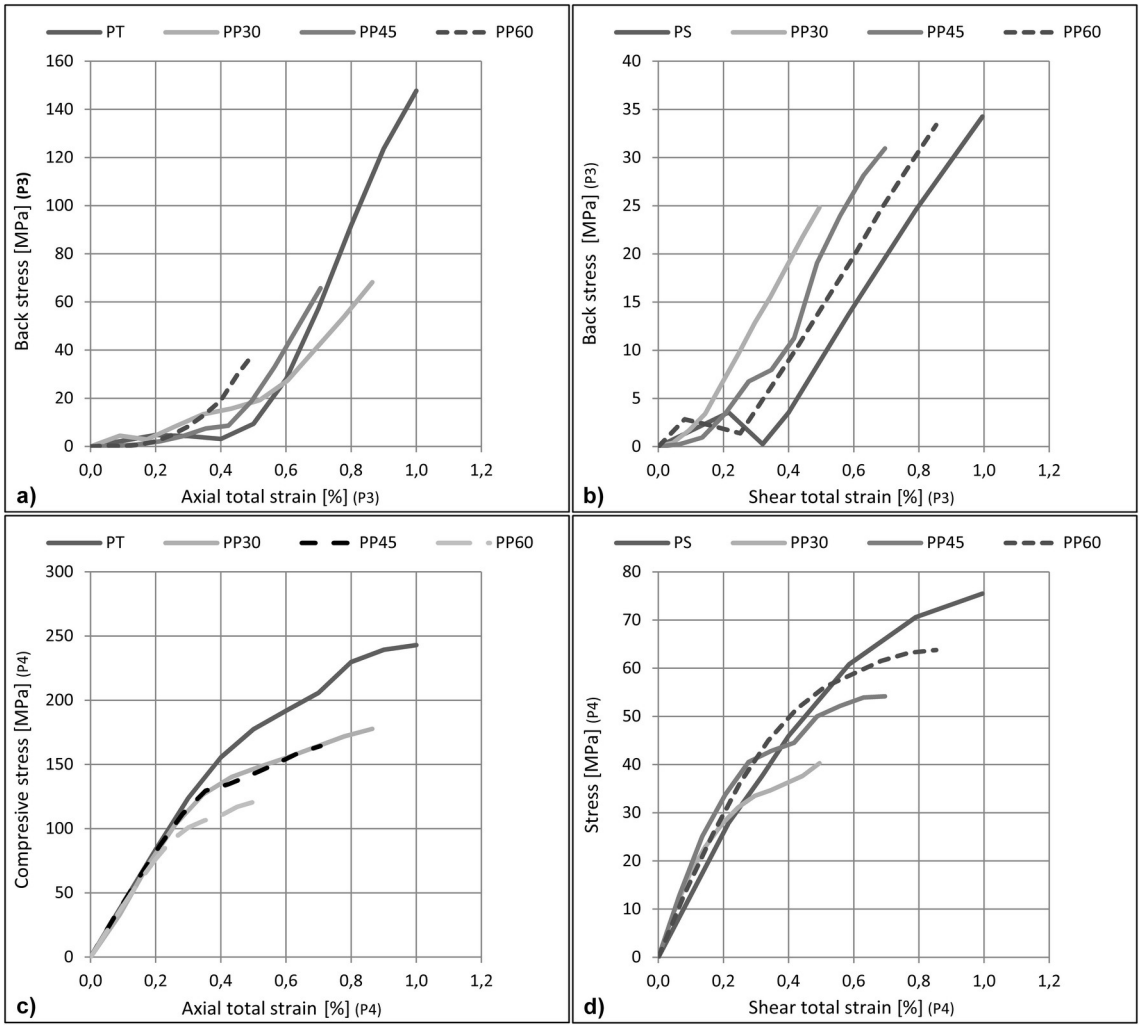


**Figure 3.17:** P3 and P4 variation with SAR and strain variation.

**Table 3.2:** Polynomial constants of the P functions for multiaxial loadings - Shear component.

| | **Shear** | | | | | |
|---|---|---|---|---|---|---|
| | **P1** | **P2** | **P3** | **P4** | **P5** | **P6** |
| **a** | 2.177984 | 0.038377 | 4.57375 | -25.3663 | 0.210432 | 25.51458 |
| **b** | 59.35201 | -0.17544 | -17.7933 | 70.0056 | -0.23946 | -10.164 |
| **c** | -0.4713 | -0.00154 | -0.2192 | 1.262069 | -0.01213 | -1.59249 |
| **d** | -147.976 | 0.374491 | 59.83082 | -106.496 | 0.200226 | 12.43844 |
| **e** | 0.013494 | 1.92E-05 | 0.00359 | -0.01797 | 0.000207 | 0.028779 |
| **f** | 2.867768 | 0.003991 | 0.417744 | 1.686582 | 0.010154 | 0.953978 |
| **g** | 86.14576 | -0.141 | -35.9188 | 40.76676 | 0.008696 | -1.96378 |
| **h** | -9.4E-05 | -6.1E-08 | -1.8E-05 | 7.46E-05 | -1.1E-06 | -0.00016 |
| **i** | -0.01049 | -5E-05 | -0.00508 | -0.00596 | -6.3E-05 | -0.00441 |
| **j** | -1.05301 | 0.004585 | 0.349309 | -0.32904 | 0.000738 | -0.1774 |

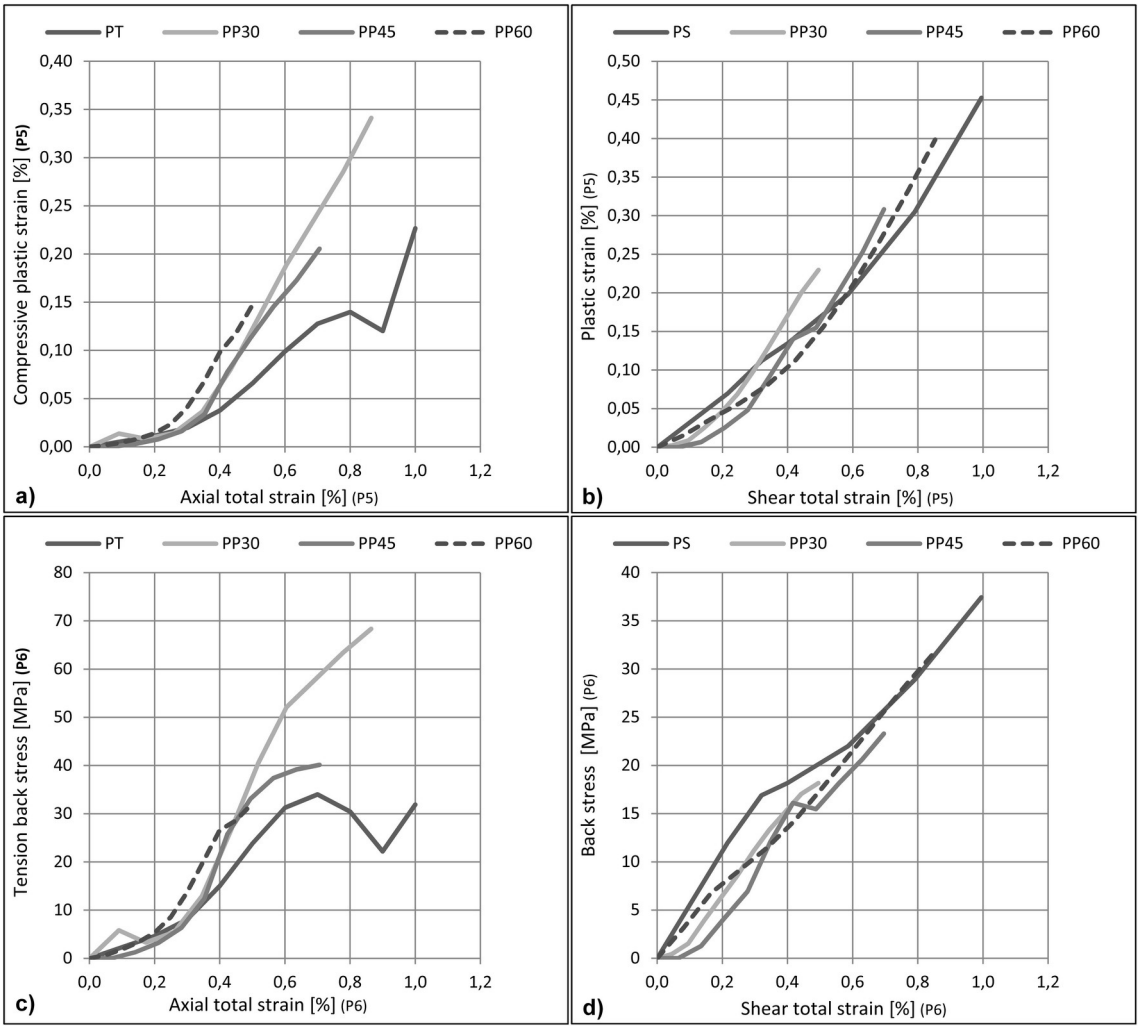


**Figure 3.18:** P5 and P6 variation with SAR in respect to total strain.

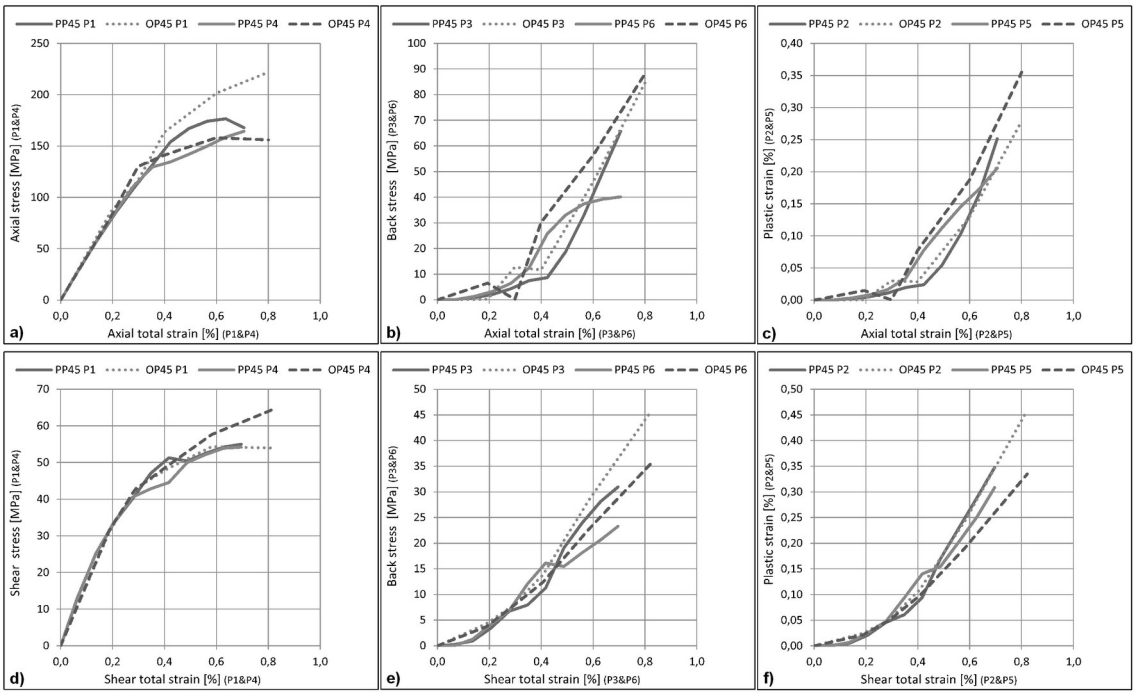


**Figure 3.19:** P points variation in Case 4, and Case 6.

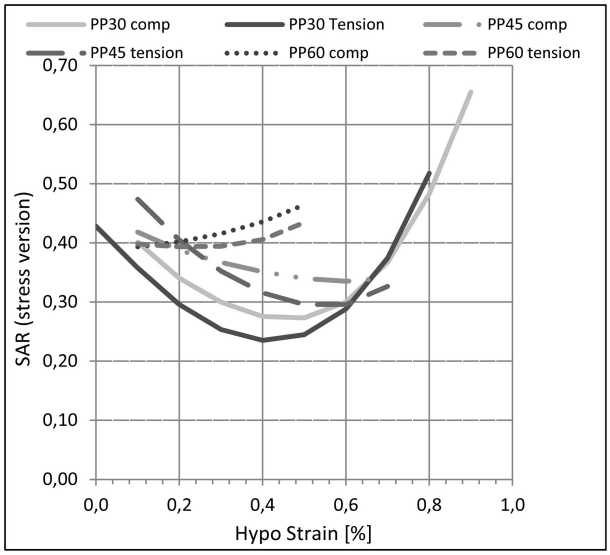


**Figure 3.20:** SAR (stress version) variations with Hypo-strain variation (strain level and load direction).

### 3.2.3 Correlation between HYS estimates and experimental data

#### 3.2.3.1 Introduction

In this section, it is validated the developed elastic-plastic model (HYS) by comparing their stress-strain estimates with the experimental data and with a well known cyclic elastic-plastic model, the Jiang & Sehitoglu model. Two approaches are used, first is is analysed the HYS estimates for multiaxial hysteresis loops by using the uniaxial P functions (P functions from Cases 1 and 2). In this approach, the cyclic behaviour of axial and shear components of a multiaxial loading are estimated without considering the combined effect of the axial and shear loading components. In the second approach, it is used the P functions obtained from the uniaxial and multiaxial loadings (Cases 1 to 5) to estimate the cyclic behaviour of proportional and non-proportional loadings in order to take into account the combined effect of the axial and shear components of a multiaxial loading.

#### 3.2.3.2 HYS estimates based in the uniaxial P functions

Figure 3.21 shows the experimental and numerical hysteresis loops estimated by the HYS model for the uniaxial loading cases i.e. Cases 1 and 2.

The pure axial results (Case 1) are depicted in Fig.(s) 3.21 a) and b) for several total strains, and the pure shear results (Case 2) are shown in Fig.(s) 3.21 c ) and d ). The total strain amplitudes selected to perform the numerical analyses were the same used in the experimental tests, in order to analyse the estimates accuracy yield by the HYS model. This numeric model was developed based on the experimental hysteresis loops, thus it is expected that the experimental and numeric results be quite similar, if the assumptions made on the numeric model definition are true. Nevertheless, the estimates shown in Figure 3.21 are quite acceptable for the uniaxial loading cases, which confirms the hypothesis in which the hysteresis loops in pure axial and pure shear loading conditions can be approximated by a third degree polynomial function.

In order to avoid any confusion regarding the graphs interpretation, it was only plotted numeric hysteresis loops with total strain amplitudes equal to the experimental ones. However, the numerical model can estimate any hysteresis loop within the range [0%, 1.4%] of total strain amplitude under uniaxial loading conditions. The hysteresis loops depicted in Figure 3.21 show asymmetry in the axial hysteresis loops, which results from the different mechanical behaviours found in tension and compression. Moreover, the shear hysteresis loops are quasi-symmetric. Figure 3.22 a) and b) shows the numeric results obtained with a total axial strain amplitude equal to 0.4% and a total shear strain amplitude equal to 0.23%.

Figure 3.22 a) shows the HYS and Jiang plasticity model estimates obtained in Case 1, (pure axial loading). Based on these results, it can be concluded that the Jiang hysteresis

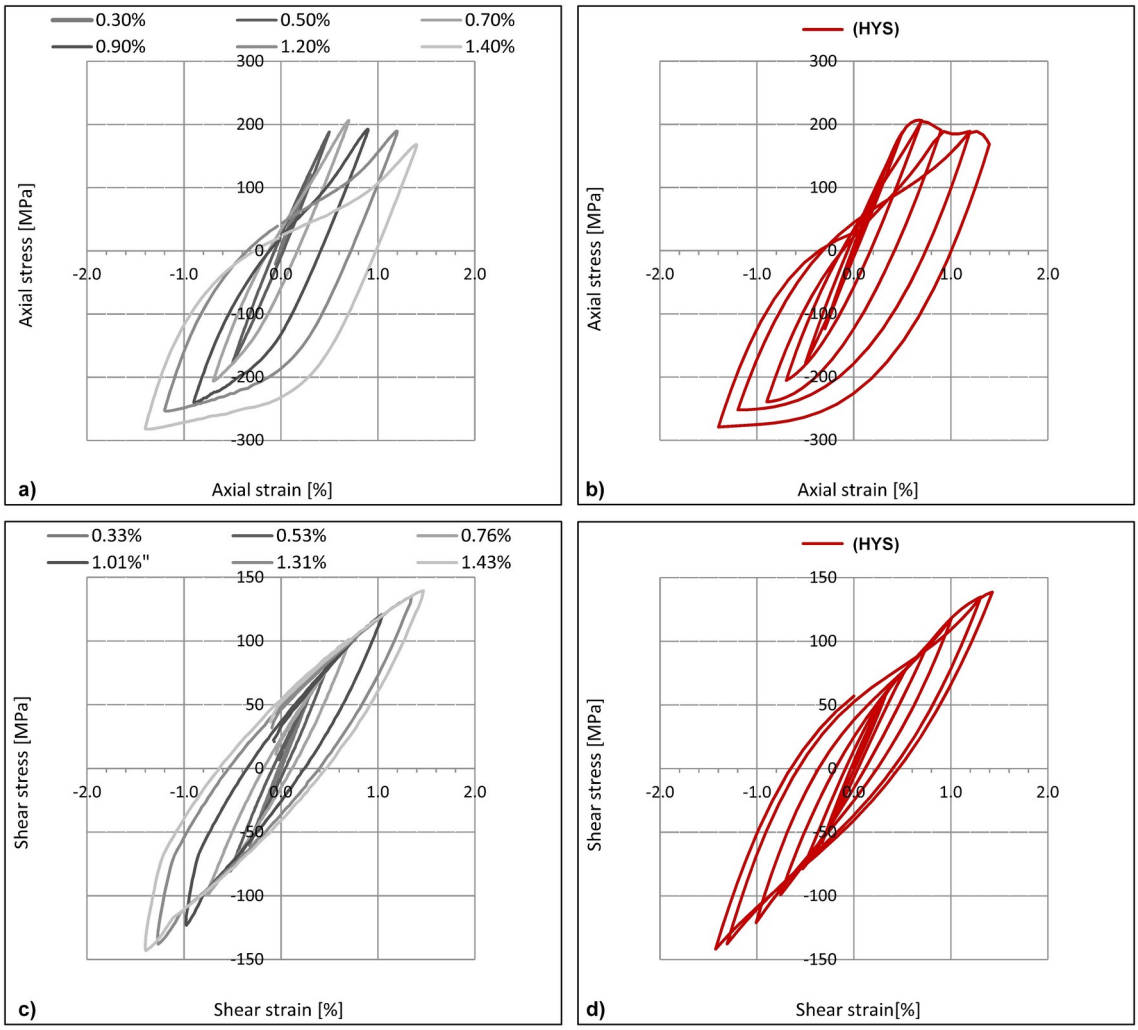


**Figure 3.21:** AZ31B-F experimental and numeric cyclic behaviour a) Axial experimental stress/strain evolution b) Numeric results for axial stress/strain hysteresis loops c) Shear experimental stress/strain evolution d) Numeric estimation for shear stress/strain hysteresis loops.

loop is more open than the experimental one, which indicates the existence of an additional plastic strain and back stresses that in reality does not exist. Moreover, the stresses estimated by the Jiang model, at the maximum total strain amplitude, please see Figure 3.22 b), are lower than the ones obtained with the numerical model. Regarding the pure shear results (Case 2), shown in Figure 3.22 b), it is observed that the Jiang model continues to estimate lower stresses than it should be at the maximum total shear strain amplitudes, as seen in Case 1. The estimates regarding the biaxial loading cases (Cases 4 and 6) are shown in Fig.(s) 3.22 c) and d). Based on the numeric estimates of Case 4, it can be concluded that the slope of the hysteresis loops (orientation) are different in both numeric models. This difference resulted from the scale factor used in the Jiang model to account the combined effect of axial and shear strains.

The HYS model based in the uniaxial P functions considers the axial and shear components of a biaxial loading as two independent loadings in order to estimate the multiaxial

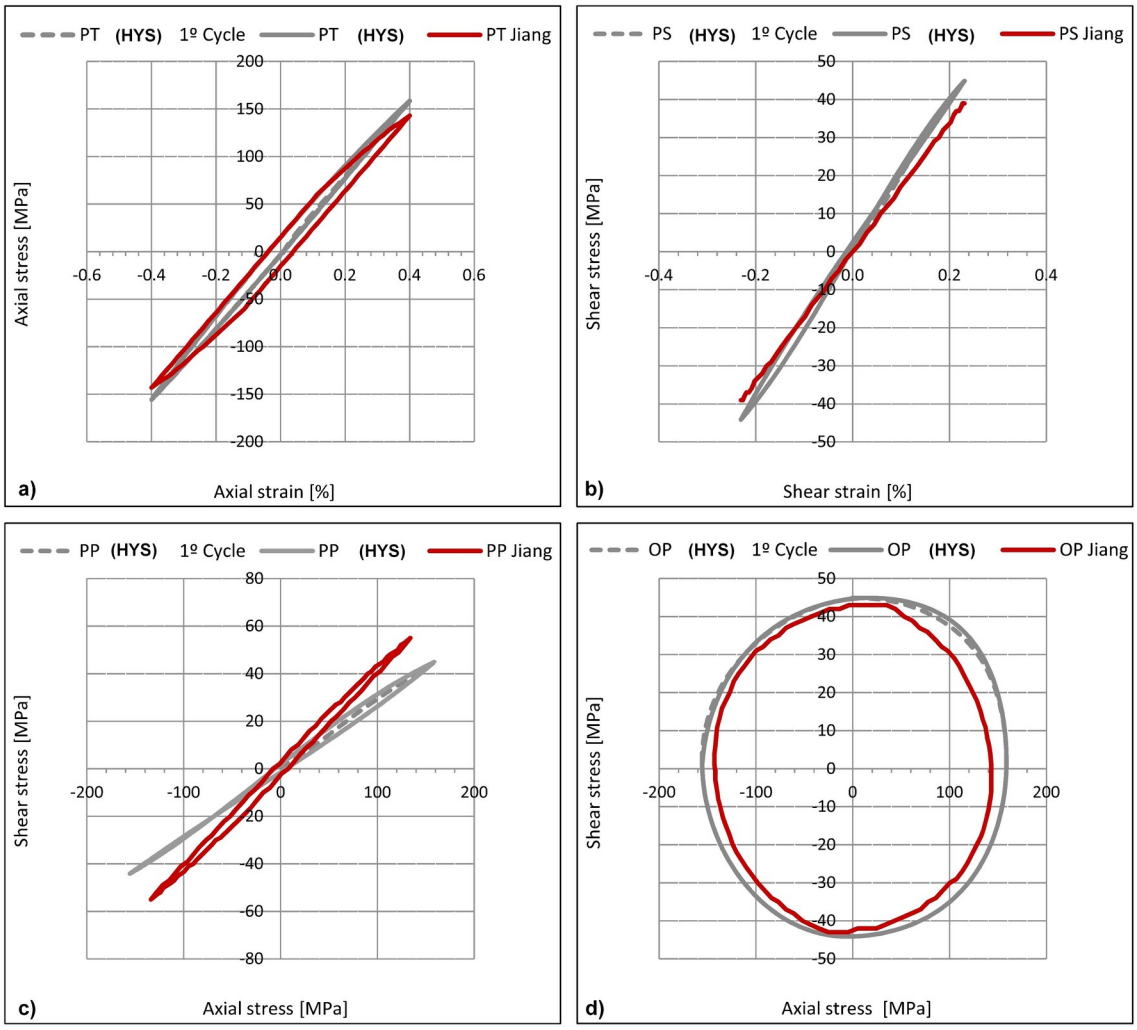


**Figure 3.22:** Numeric cyclic behaviour comparison between the numeric model developed and the Jiang & Sehitoglu plasticity model for 0.4% as axial strain reference a) Case 1, b) Case 2, c) Case 4 and d) Case 6.

mechanical behaviour, then the axial and shear results are joined as if the axial and shear components had been loaded together. This simplification leads to assume that a given strain amplitude has equal stress values under uniaxial and multiaxial loading conditions, for example in the HYS version discussed in this section, it is assumed that an axial strain amplitude has the same stress value in the uniaxial loading case and in the axial stress component of a multiaxial loading, which is not true because there is always a combined effect between axial and shear strains in a multiaxial loading. This combined effect can only be found by performing biaxial stress-strain tests under elastic-plastic loading conditions. Figure 3.22 d) shows the results for the fully out-of-phase loading case, Case 6; in this case, the estimates of both numerical models are quite similar in shape. The Jiang model estimates for the axial-shear stress loading path are within the HYS results, because the Jiang model yields lower stresses than the HYS model under the same total strain amplitude. Figure 3.23 shows the numeric results a total strain amplitude equal to 0.8%.

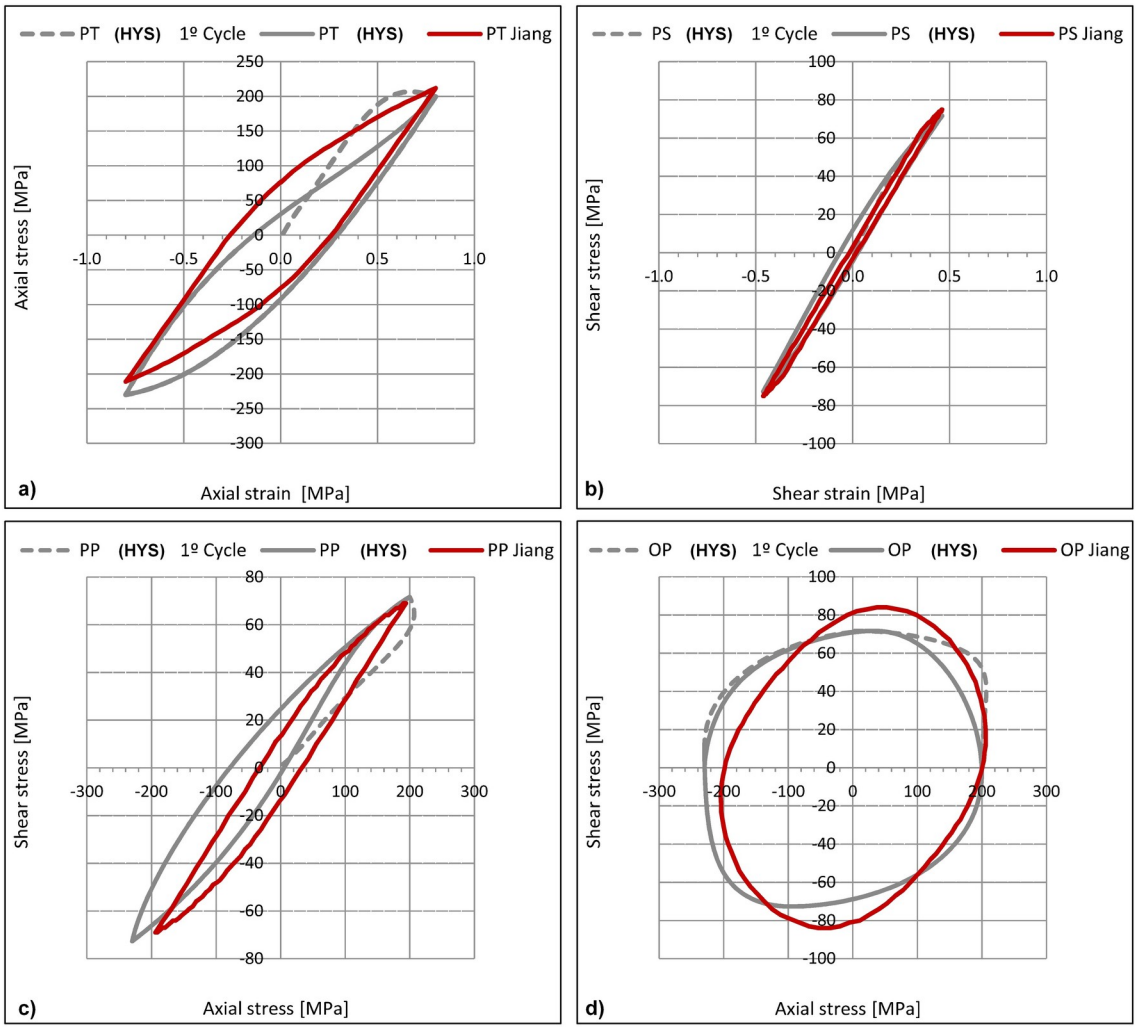


**Figure 3.23:** Numeric cyclic behaviour comparison between the numeric model developed and the Jiang & Sehitoglu plasticity model model for 0.8% as axial strain reference a) Case 1, b) Case 2, c) Case 4 and d) Case 6.

The uniaxial results presented in Fig.(s) 3.23 a) and b) show that the Jiang's model continues to estimate lower stresses at maximum total strain amplitudes in the compression region, but in tension, the inherent stresses are similar to the numerical model estimates. The dashed line depicted in Figure 3.23 shows the first hysteresis loop. The results of Case 1 show that the compressive plastic strain and back-stresses are quite similar in both models; however the plastic strains in the tension direction branch (upper hysteresis branch) are very different. Jiang's model gives values higher than the experimental results, please see Figure 3.23 a) and d). In Case 2, the Jiang's model has a hysteresis loop tighter than the experimental results, which were estimated here by the HYS results. The Jiang's model estimates regarding the shear stresses inherent to the shear total strains at the right and left loading directions (torque direction) are very similar to the HYS estimates. Moreover, the pure axial hysteresis loop is estimated as symmetric by the Jiang model, which is not true. In Case 4, please see Figure 3.23 c), the Jiang model also gives a symmetrical hysteresis loop.

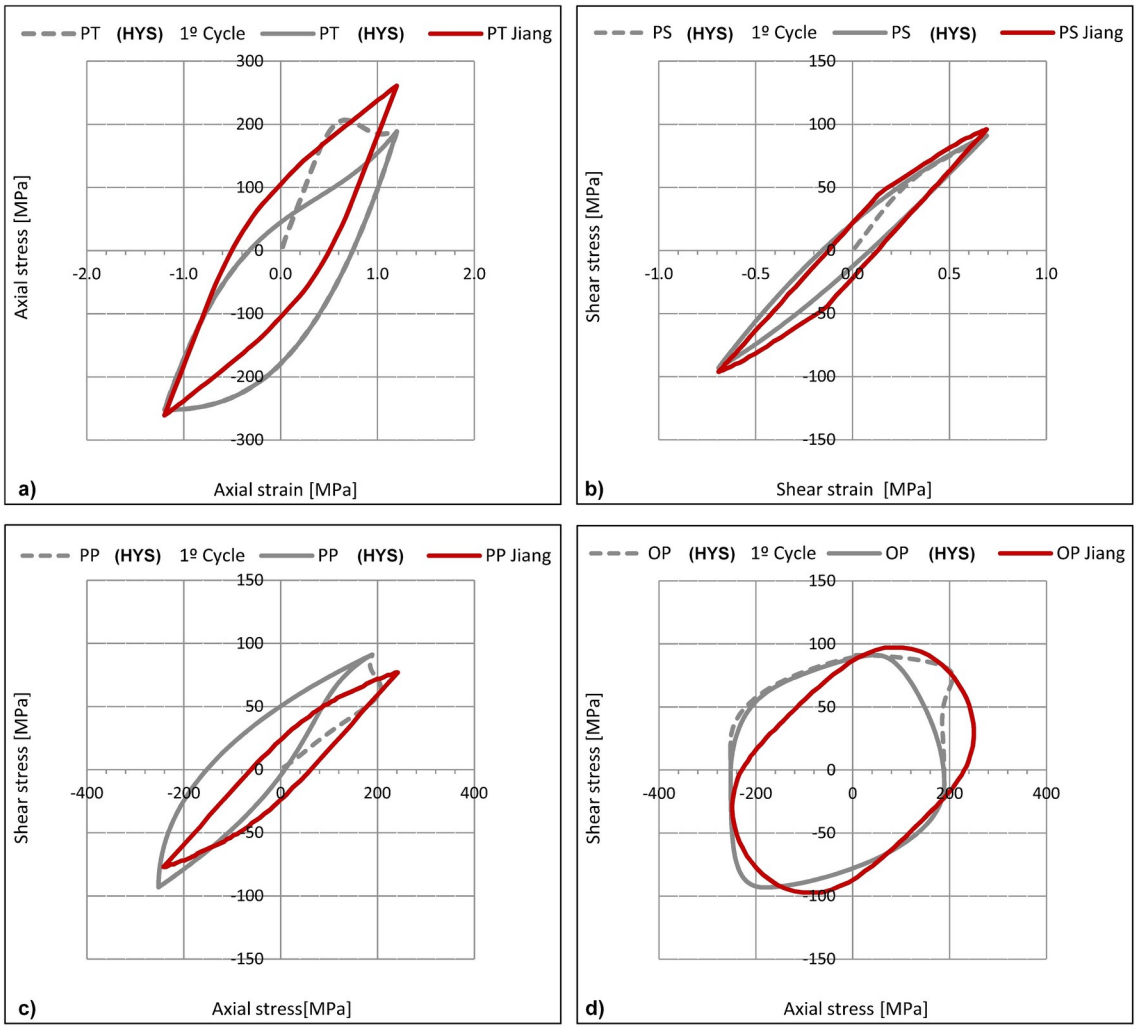


**Figure 3.24:** Numeric cyclic behaviour comparison between the numeric model developed and the Jiang & Sehitoglu plasticity model for 1.2% as axial strain reference: a) Case 1, b) Case 2, c) Case 4 and d) Case 6.

The numerical model displays asymmetrical hysteresis loop for the axial loading. The results of the out-of-phase loading case, Case 6, Figure 3.23 d), shows a distorted circle(loading path) in both models; however, the distortion pattern has different directions. Figure 3.24 shows the numerical estimates for 1.2% of total strain. Due to the high values of plastic strains involved in this simulation (total strain equal to 1.2%) it can be seen that the first hysteresis loop is quite different from the other ones (developed stress-strain hysteresis loops). This result indicates an adjustment of the material to the total strain level.

The Jiang model continues to estimate the hysteresis loops inherent to 1.2% of total strain as symmetric in all loading cases considered here, although the biaxial loading experiments have not been considered in this section, it is expected that the experimental biaxial hysteresis loops be asymmetric and not symmetric as reported by the Jiang's model, since the axial hysteresis loops under uniaxial loading conditions are always

asymmetrical. In the Jiang's model, the total strain amplitude increase leads always to the increase of their inherent maximum stresses. This indicates that the Jiang's model does not capture the total strain level effect in magnesium alloys, especially their cyclic softening. In this case, total strain equal to 1.2%, the two numerical estimates regarding Case 2 (the pure shear loading case) are very similar having plastic strains and back stress values much alike. The numeric results for Cases 4 and 6 depicted in Fig.(s) 3.24 c) and d), show the first loading cycle with similar results in both models, but diverging in the subsequent loading cycles. Figure 3.25 presents the HYS numeric results for a total strain amplitude equal to 1.4%, this is a very high strain level, which leads to the sample collapse in a few loading cycles. It can be seen that the Jiang's hysteresis loops remain symmetric in all loading cases. Under an extreme cyclic total strain amplitude, the Jiang's model presents equal plastic strain and back stress values in tension and compression. Which is a result very different from the experimental data where loads in compression direction (lower branch) induces high plastic strains and back stresses, moreover the plastic strain in tension is very small comparatively to the one found in compression.

Figure 3.25 b), depicts the experimental hysteresis loop of Case 2, results shows different values for back stresses and plastic strains, which is a pattern not seen in lower total shear strains. Figure 3.25 a), shows the results of Case 1, where it can be seen that the yield stress in compression is much higher than the one in tension, for the same total strain in tension and compression, which confirms the softening behaviour in tension and a little hardening in compression for this total strain level. Also, it can be concluded that the Jiang's model is able to estimate well the material hardening but unable to deal with its softening. From here, it can be reinforced the idea which suggests that an numerical model based in experiments is needed to establish the different physical phenomena encountered in materials with an hexagonal close packed micro-structure (HCP), such as the one found in magnesium alloys.

#### 3.2.3.3 HYS based in multiaxial stress-strain curves

Figures 3.26 and 3.27 show the correlation between the elastic-plastic models already presented (the Jiang & Sehitoglu and the HYS model) and the biaxial experimental results. It was selected three values for the Hypo-strain in order to compare the models performance under three levels of cyclic plasticity. To perform this correlation, it is presented the results using the stress space concept, where the axial stress vs shear stress are depicted, here neither the shear stress neither the axial stress are affected by any factor as seen in the von Mises stress space, for instance. Based on the results presented in Fig.(s) 3.26 and 3.27, it can be concluded that the developed model follows well the proportional loading paths obtained by experiments, only in Case 3 and 5 at 1% of Hypo-strain it was

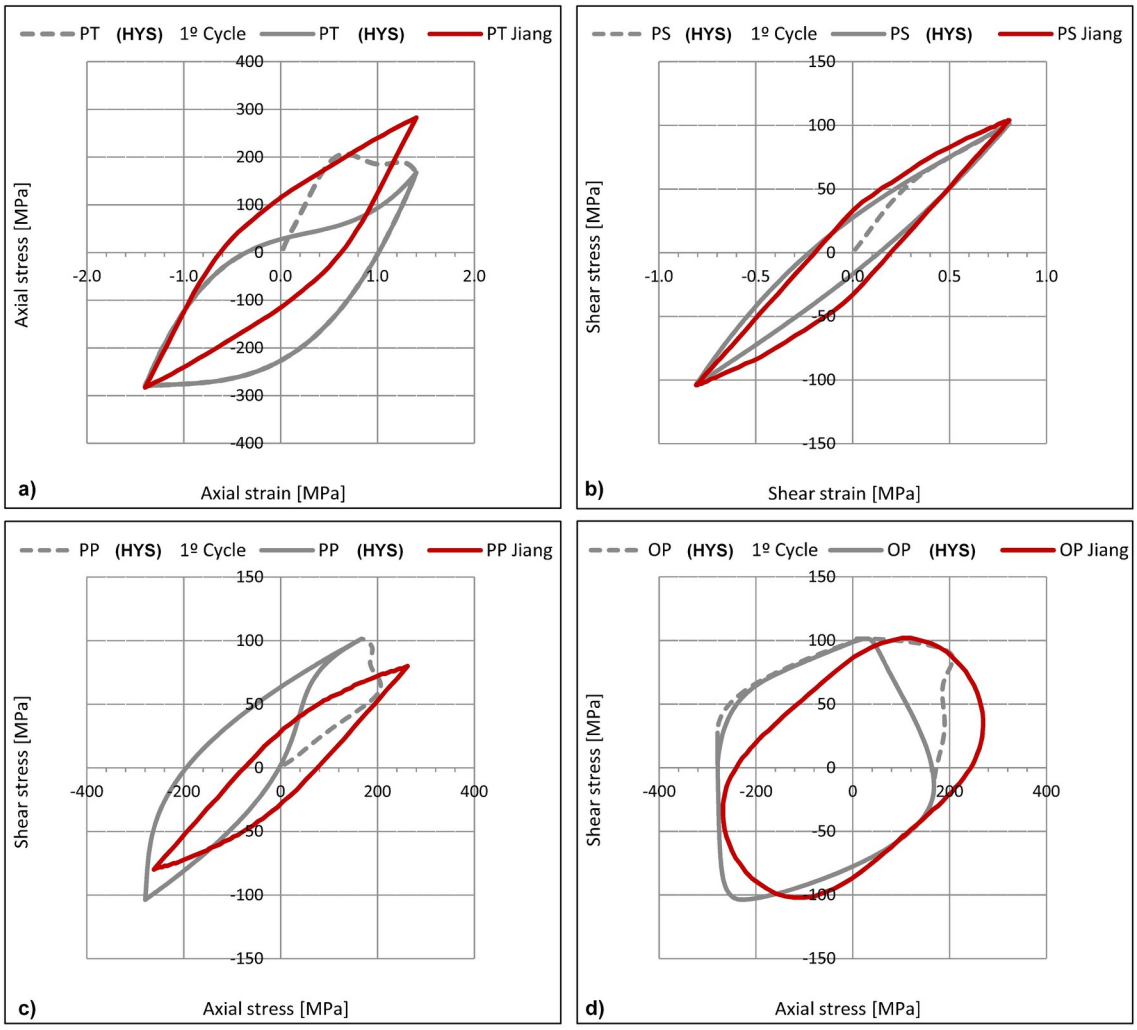


**Figure 3.25:** Numeric cyclic behaviour comparison between the numeric model developed and the Jiang & Sehitoglu plasticity model for 1.4% as axial strain reference: a) Case 1, b) Case 2, c) Case 4 and d) Case 6.

found a slight deviation from the experimental results, please see Figure 3.26 e) and 3.27 e). The advantage of the developed model comparatively to the Jiang & Sehitoglu model, is the possibility to simulate the SAR effect in the material cyclic behaviour, having into account cyclic effects such as twinning and de-twinning effects which are very relevant under higher Hypo-strain values. Regarding the Jiang & Sehitoglu model, it can be seen that their estimates fail to capture the shear stress limits, being higher than they should be. These results indicate that the yield function estimate higher equivalent stresses than it should, moreover the achieved stress amplitude ratios are quite different from the ones found in experiments. These results can be explained by the defective estimates yield by the hardening and flow rules, which indicates that the hardening rule embedded in the Jiang & Sehitoglu do not follows the magnesium hardening behaviour. Also this deviation of the experimental results may influence the estimates for crack initiation planes. The Jiang & Sehitoglu estimates for the axial stress limits are also different from the experimental results, however, this difference is not so pronounced as the one found in the shear stresses.

The highest deviation from experiments can be found in tension where magnesium has a particular hardening behaviour.

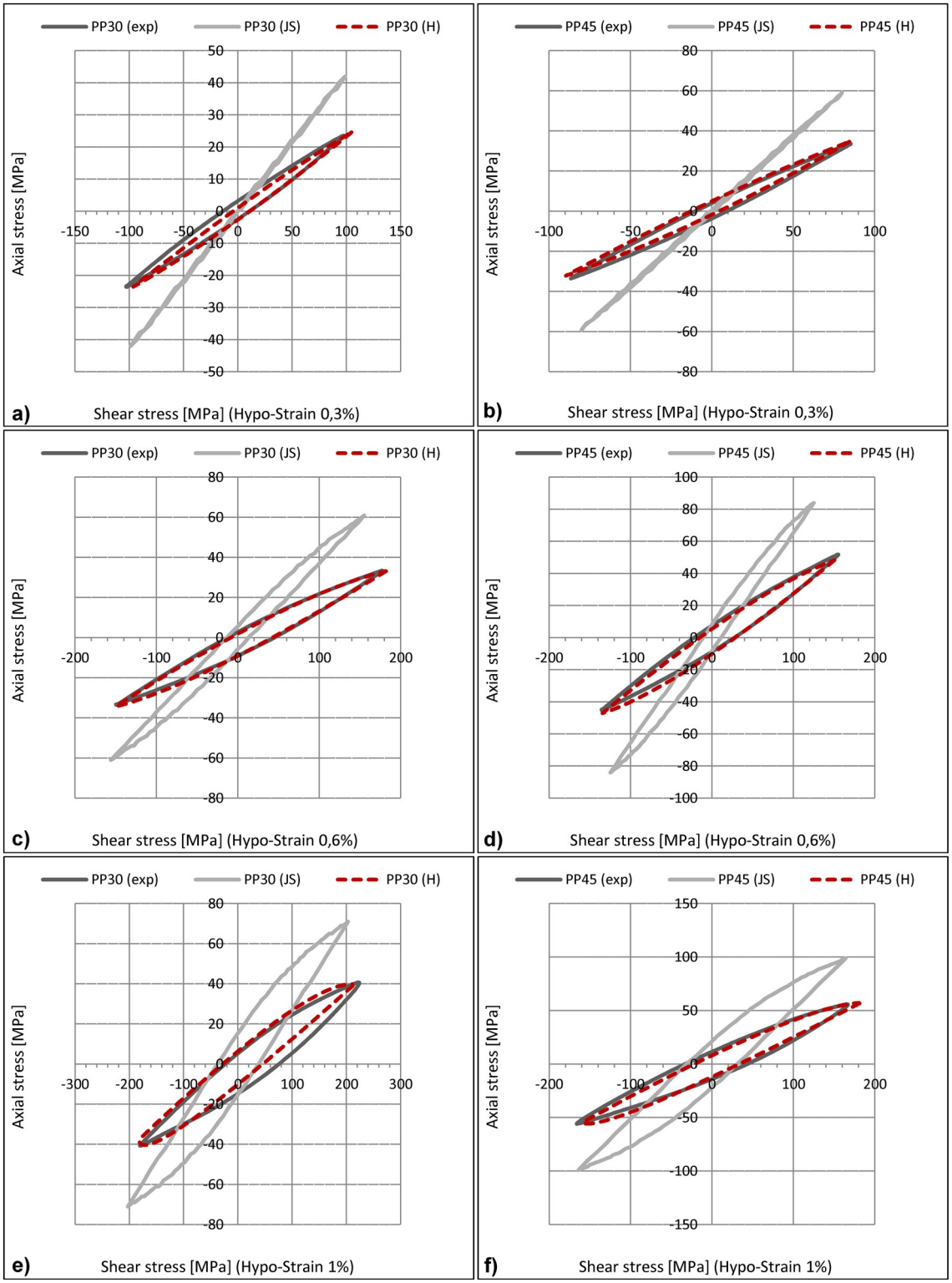


**Figure 3.26:** Correlation between estimations and experiments for cases: a) Case 3 - 0.3% Hypo-strain, c) Case 3 - 0.6% Hypo-strain, e) Case 3 - 1% Hypo-strain, and b) Case 4 - 0.3% Hypo-strain, d) Case 4 - 0.6% Hypo-strain, f) Case 4 - 1% Hypo-strain.

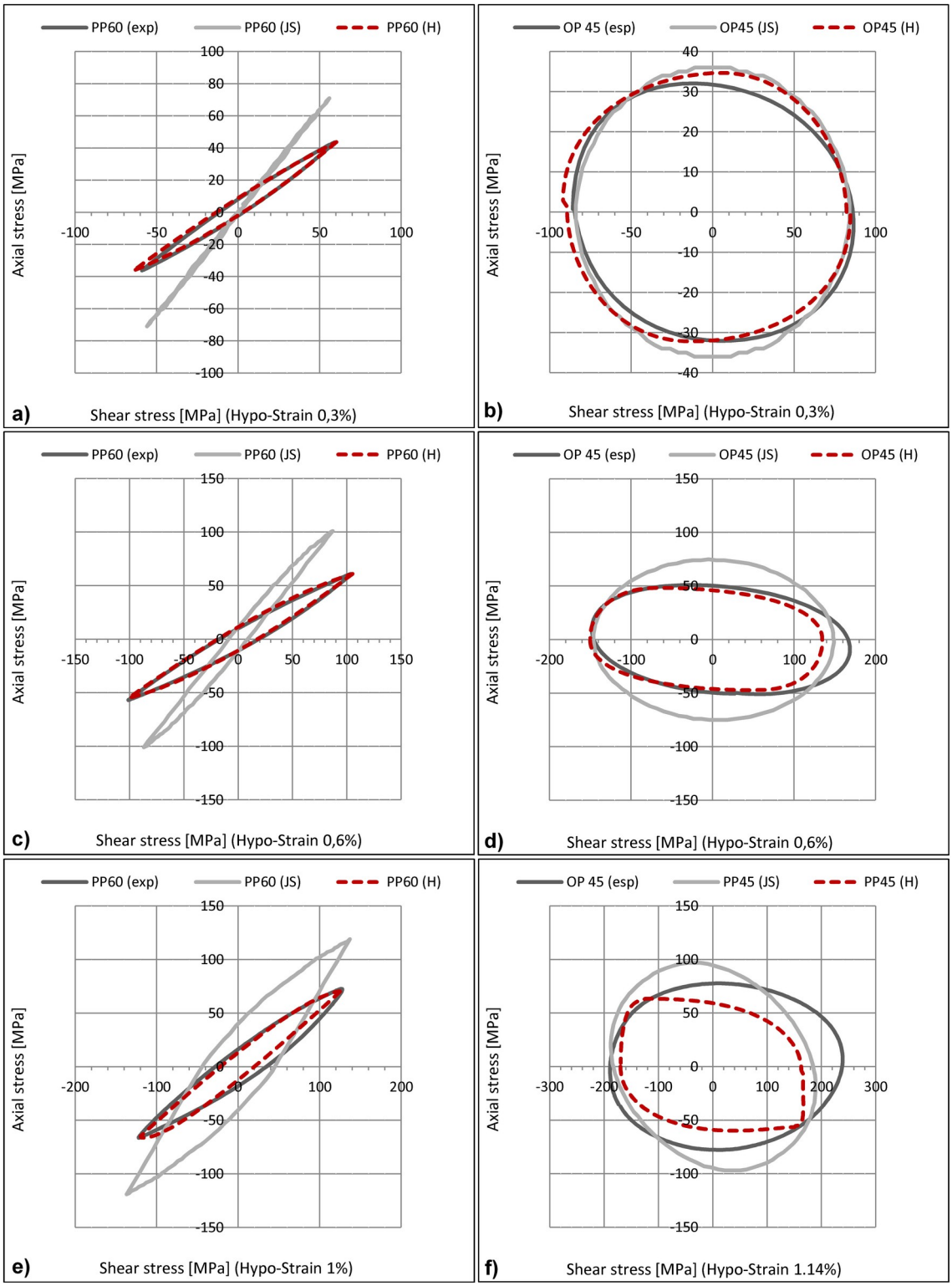


**Figure 3.27:** Correlation between estimations and experiments for cases: a) Case 5 - 0.3% Hypo-strain, c) Case 5 - 0.6% Hypo-strain, e) Case 5 - 1% Hypo-strain, and b) Case 6 - 0.3% Hypo-strain, d) Case 6 - 0.6% Hypo-strain, f) Case 6 - 1% Hypo-strain.

Under proportional loadings, the Jiang & Sehitoglu estimates for tension stresses are lower than they should, which indicates that the hardening rule do not captures the magnesium hardening in tension, however at compression the estimates are very similar to the experimental results. This is so because the magnesium hardening in compression is very low. It can be found in the Jiang & Sehitoglu results the loading path symmetry depicted in the stress space, i.e. shear and axial stresses amplitudes have the same absolute value in both loading directions. This result confirms the incapability of this constitutive model to estimate cyclic anisotropy. Figure 3.27 a), c), and e) presents the results for the Case 5, which have a SAR equal to 60°, in this case the shear strain amplitude is higher than the axial one. Also here the Jiang & Sehitoglu model over estimates the shear stress limits, surprisingly for 1% of total strain, the axial stress estimates are very similar to the experimental ones, please see Figure 3.27 e). At this Hypo-strain level, the developed model (HYS) also has a slight deviation as seen in Case 3. Regarding the non-proportional loading case, i.e. Case 6, both methods fail to follow the experimental results, only for a Hypo-strain equal to 0.3% it was obtained acceptable estimates, despite that, the developed model is the one that is closest to the experimental data, for instance in Figure 3.27 d) the HYS estimates almost follows the experimental results failing in the tensile region where it occurs a pronounced hardening. For 1.14% of total strain, Figure 3.27 f), the estimates of the developed model are within of the experimental results, in this case the stress values are lower than they should be indicating that the HYS model do not capture the magnesium non-proportional hardening, this evidence becomes more obvious greater Hypo-strain values.

### 3.2.4 Final comments

In this section, it was studied the elastic-plastic behaviour of a magnesium alloy under uniaxial and multiaxial loading conditions. Several proportional and non-proportional loading paths were carried out under strain control in order to acquire the relation between the biaxial stress components as well as the plastic strains and back stresses. The idea was to analyse the $SAR_{\varepsilon}$ effect in the elastic-plastic properties under proportional loadings and also analyse the non-proportional effect in these properties under a fixed $SAR_{\varepsilon}$. The experimental results were correlated with two elastic-plastic models, the well-known Jiang & Sehitoglu model and the HYS model, a numerical model developed here. The HYS Matlab code can be found in Appendix B at the end of this document. Results show that the experimental hysteresis loops are also asymmetric under multiaxial loading conditions, especially the ones from the axial loading components; the asymmetry found in the shear loading components came from the first loading direction, which is more pronounced at high strain amplitude levels. The Jiang & Sehitoglu model have poor estimates in proportional and non-proportional loadings, this poor performance can be explained by the inability to following the magnesium hardening behaviour, this conclusion

was corroborated by the symmetry found in the axial estimates. The model developed here have limitations that need to be overcome, i.e. it is required further investigations in order to incorporate the non-proportional hardening behaviour in the HYS model. Despite this limitation, the developed model shows good agreement with the experimental data under proportional loadings, the model captures very well the plastic strains, and back stresses for a wide range of total strains.

## 3.3 Cyclic non-proportionality

### 3.3.1 Non-proportional sensitivity parameter, Y

In this section, it is developed a new parameter that measures the material non-proportional sensitivity, the Y parameter. As seen in the previous sections, proportional and non-proportional loadings cause different cyclic effects, thus here it is performed a comparison between proportional and non-proportional loadings in order to evaluate the Y parameter in three different materials. The Y parameter aims to account the additional fatigue damage when it is added a phase shift to a proportional loading, thus in this study, proportional and non-proportional loadings have both a stress amplitude ratio equal to $1/\sqrt{3}$ . In order to evaluate the Y parameter, a new approach to represent S-N curves is adopted. In this approach, the axial and shear stress components of a multiaxial loading are depicted in the S-N chart as independent stresses instead of using a equivalent stress. Thus, here the S-N chart of a multiaxial loading has two curves, one for the axial stress component and other for the shear one.

Based on experiments, it was found out that the axial and shear S-N curves of proportional and non-proportional loadings are almost parallel to each other in the case of a stress amplitude ratio equal to $1/\sqrt{3}$ . This result lead to the conclusion that the relative position between axial and shear S-N curves of both proportional and non-proportional loadings is a outcome of the non-proportional contribution to the overall fatigue damage. Moreover, the relative damage between proportional and non-proportional loadings can be considered constant and independent from fatigue life-time, because both proportional and non-proportional S-N curves are parallel to each other. The reasoning that supports the physical meaning of the relative damage between proportional and non-proportional loadings histories is as follows: If the S-N curves of the axial and shear components of a non-proportional loading are above of their homologous proportional curves, then for a given fatigue life-time, it is necessary to increase the stress amplitude level of the non-proportional axial and shear stress components to obtain the same fatigue life-time. Therefore in this scenario, the non-proportional loading will have a greater fatigue life-time compared to the proportional loading case, for the same axial and shear stress amplitudes in both proportional and non-proportional loadings. In this scenario, the non-proportional loading is less damaging than the proportional one, indicating that

the material is less sensitive to non-proportionality. On the other hand, if the axial and shear S-N curves of a non-proportional loading are bellow of their homologous proportional curves, thus for a given fatigue life-time, the energy to be spent on the fatigue damage process is less in non-proportional than in proportional loading conditions. In this case, the non-proportional loading is more damaging than the proportional one, indicating that the material is more sensitive to non-proportionality. To quantify the materials non-proportional sensitivity, it was conceived here a new factor concept for non-proportionality, the Y parameter, which correlates proportional and non-proportional loading amplitudes, where the non-proportional S-N curves (axial and shear) can be estimated based in the proportional ones. Figure 3.28 shows in which way the Y parameter is defined in order to quantify the material sensitivity to non-proportionality.

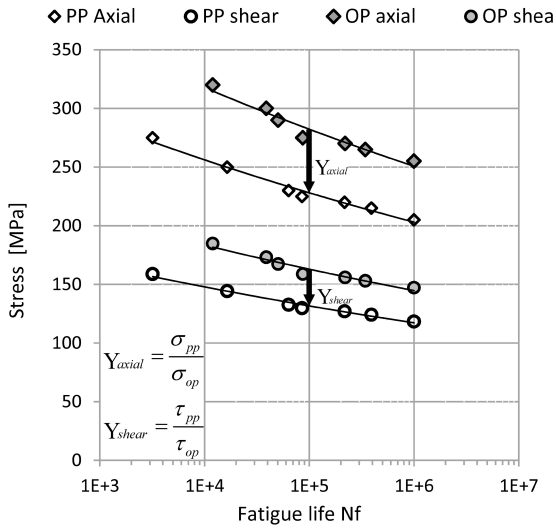


**Figure 3.28:** Non-proportional sensitive parameter definition, Y parameter.

The Y parameter interpretation is as follows: If the Y parameter has a value less than 1, thus the material is less sensitive to non-proportionality than it is to proportionality. If the Y parameter is equal to 1, thus proportional and non-proportional loadings have the same influence on the material fatigue strength. If the Y parameter is greater than 1, it can be considered that the material is very sensitive to the non-proportional loading conditions. In this case, for a given fatigue life-time, non-proportional loadings have lower stress amplitudes than the proportional ones.

### 3.3.2 Y parameter experimental evaluation

To evaluate the methodology of getting the material sensitivity to non-proportional loadings it was selected from literature non-proportional fatigue data of three materials [3], namely the high strength steel 42CrMo4, the Ck45, and the stainless steel AISI 303. Further information regarding the mechanical properties and industrial applications of these materials is given in Appendix A. Table 3.3 shows the fatigue data for these materials

and loading paths depicted in Figure 3.29. These experiments were made under stress control with a loading frequency between 5 Hz to 6 Hz at room temperature. The samples geometry and dimensions is shown in Figure 3.30.

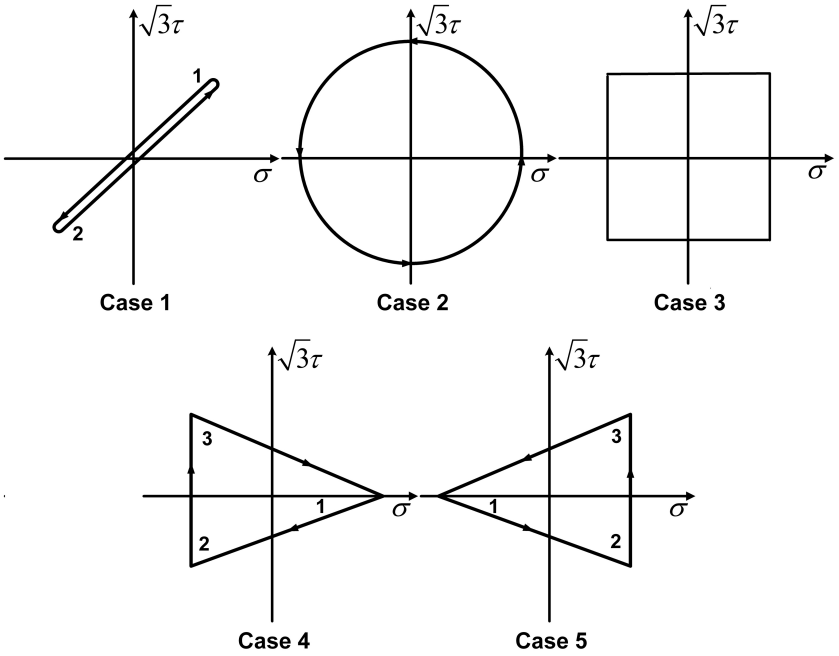


**Figure 3.29:** Proportional and non-proportional loading paths used to evaluate non-proportional sensitivity.

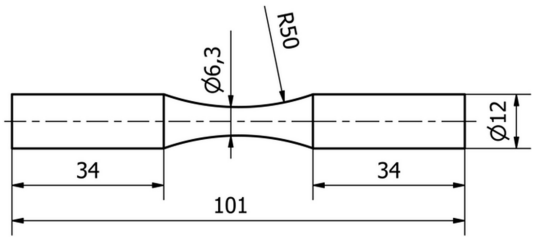


**Figure 3.30:** Sample geometry and its dimensions.

Figure 3.29 shows the loading paths considered in this section. Case 1 is a proportional loading path, the other loading cases, Cases 2 to 5, are non-proportional loadings with different non-proportional effects.

Fig.(s) 3.31 and 3.32 show the Ck45 experimental data for the selected multiaxial loading paths. For each non-proportional loading case, it was made a comparison between the proportional loading case, Case 1 depicted in Figure 3.29, and the other non-proportional loading cases (Cases 2 to 5 depicted in Figure 3.29). This comparison was made by representing in the same graph the axial and shear S-N curves of both the reference case (proportional) and non-proportional loading case, in order to inspect the relative damage between proportional and non-proportional curves.

**Table 3.3:** Multiaxial fatigue data for materials 42CrMo4, Ck45, and AISI303 [3].

| Case 1 | | | | | | | | | Case 2 | | | | | | | | |
|---|---|---|---|---|---|---|---|---|---|---|---|---|---|---|---|---|---|
| **Ck45** | | | **AISI 303** | | | **42CrMo4** | | | **Ck45** | | | **AISI 303** | | | **42CrMo4** | | |
| Sigma | Shear | Nf | Sigma | Shear | Nf | Sigma | Shear | Nf | Sigma | Shear | Nf | Sigma | Shear | Nf | Sigma | Shear | Nf |
| 190 | 109.7 | (ro) | 205 | 118.4 | (ro) | 425 | 245.4 | (ro) | 240 | 138.6 | (ro) | 255 | 147.2 | (ro) | 450 | 259.8 | (ro) |
| 200 | 115.5 | 466470 | 215 | 124.1 | 392005 | 435 | 251.1 | 564088 | 255 | 147.2 | 201751 | 265 | 153 | 342890 | 465 | 268.5 | 618128 |
| 205 | 118.4 | 383721 | 220 | 127 | 217075 | 440 | 254 | 311401 | 260 | 150.1 | 130640 | 270 | 155.9 | 219540 | 475 | 274.2 | 316712 |
| 210 | 121.2 | 184541 | 225 | 129.9 | 85376 | 445 | 256.9 | 239600 | 270 | 155.9 | 120704 | 275 | 158.8 | 86926 | 485 | 280 | 197548 |
| 220 | 127 | 116036 | 230 | 132.8 | 63540 | 465 | 268.5 | 109087 | 280 | 161.7 | 62780 | 290 | 167.4 | 50412 | 490 | 282.9 | 107374 |
| 235 | 135.7 | 73383 | 250 | 144.3 | 16405 | 470 | 271.4 | 97366 | 285 | 164.5 | 43932 | 300 | 173.2 | 38787 | 495 | 285.8 | 97548 |
| 245 | 141.5 | 39757 | 275 | 158.8 | 3194 | 495 | 285.8 | 48740 | 305 | 176.1 | 34719 | 320 | 184.8 | 11950 | 510 | 294.4 | 56411 |
| 260 | 150.1 | 19480 | | | | 520 | 300.2 | 27204 | 315 | 181.9 | 21308 | | | | | | |
| 280 | 161.7 | 11650 | | | | 610 | 352.2 | 4114 | 330 | 190.5 | 15502 | | | | | | |
| 285 | 164.5 | 8572 | | | | | | | 360 | 207.8 | 7922 | | | | | | |

| Case 3 | | | | | | | | | Case 4 | | | | | | | | |
|---|---|---|---|---|---|---|---|---|---|---|---|---|---|---|---|---|---|
| **Ck45** | | | **AISI 303** | | | **42CrMo4** | | | **Ck45** | | | **AISI 303** | | | **42CrMo4** | | |
| Sigma | Shear | Nf | Sigma | Shear | Nf | Sigma | Shear | Nf | Sigma | Shear | Nf | Sigma | Shear | Nf | Sigma | Shear | Nf |
| 200 | 115.5 | (ro) | 200 | 115.5 | (ro) | 360 | 207.8 | (ro) | 225 | 129.9 | (ro) | 225 | 129.9 | (ro) | 365 | 210.7 | (ro) |
| 215 | 124.1 | 401067 | 215 | 124.1 | 401067 | 375 | 216.5 | 756303 | 245 | 141.5 | 373421 | 245 | 141.5 | 373421 | 370 | 213.6 | 540305 |
| 220 | 127 | 210162 | 220 | 127 | 210162 | 380 | 219.4 | 127154 | 260 | 150.1 | 128408 | 260 | 150.1 | 128408 | 390 | 225.2 | 276100 |
| 225 | 129.9 | 190346 | 225 | 129.9 | 190346 | 385 | 222.3 | 97935 | 265 | 153 | 99702 | 265 | 153 | 99702 | 420 | 242.5 | 222393 |
| 235 | 135 | 82135 | 235 | 135 | 82135 | 400 | 230.9 | 76200 | 280 | 161.7 | 73980 | 280 | 161.7 | 73980 | 440 | 254 | 175442 |
| 245 | 141.5 | 46960 | 245 | 141.5 | 46960 | 410 | 236.7 | 65192 | 315 | 181.9 | 27678 | 315 | 181.9 | 27678 | 445 | 256.9 | 164508 |
| 270 | 155.9 | 32842 | 270 | 155.9 | 32842 | 430 | 248.3 | 38216 | | | | | | | 520 | 300.2 | 46129 |
| 285 | 164.5 | 8879 | 285 | 164.5 | 8879 | 445 | 256.9 | 26816 | | | | | | | | | |

| Case 5 | | | | | | | | |
|---|---|---|---|---|---|---|---|---|
| **Ck45** | | | **AISI 303** | | | **42CrMo4** | | |
| Sigma | Shear | Nf | Sigma | Shear | Nf | Sigma | Shear | Nf |
| 220 | 127 | (ro) | 220 | 127 | (ro) | 390 | 225.2 | (ro) |
| 225 | 129.9 | 855427 | 225 | 129.9 | 855427 | 400 | 230.9 | 790234 |
| 235 | 135.7 | 151380 | 235 | 135.7 | 151380 | 415 | 239.6 | 461134 |
| 245 | 141.5 | 1000847 | 245 | 141.5 | 1000847 | 445 | 256.9 | 359019 |
| 260 | 150.1 | 27592 | 260 | 150.1 | 27592 | 465 | 268.5 | 278889 |
| 270 | 155.9 | 24699 | 270 | 155.9 | 24699 | 495 | 285.8 | 123225 |
| 300 | 173.2 | 7283 | 300 | 173.2 | 7283 | 520 | 300.2 | 68465 |
| | | | | | | 525 | 303.1 | 60388 |

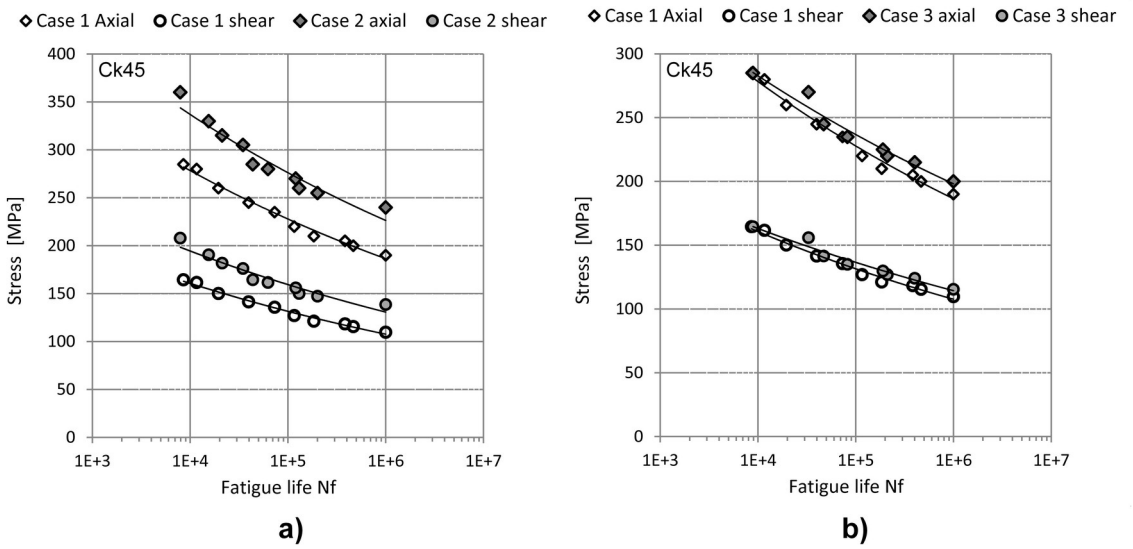


**Figure 3.31:** Ck45 fatigue life results and relative damage between Case 1 (reference case) and: a) Case 2, b) Case 3.

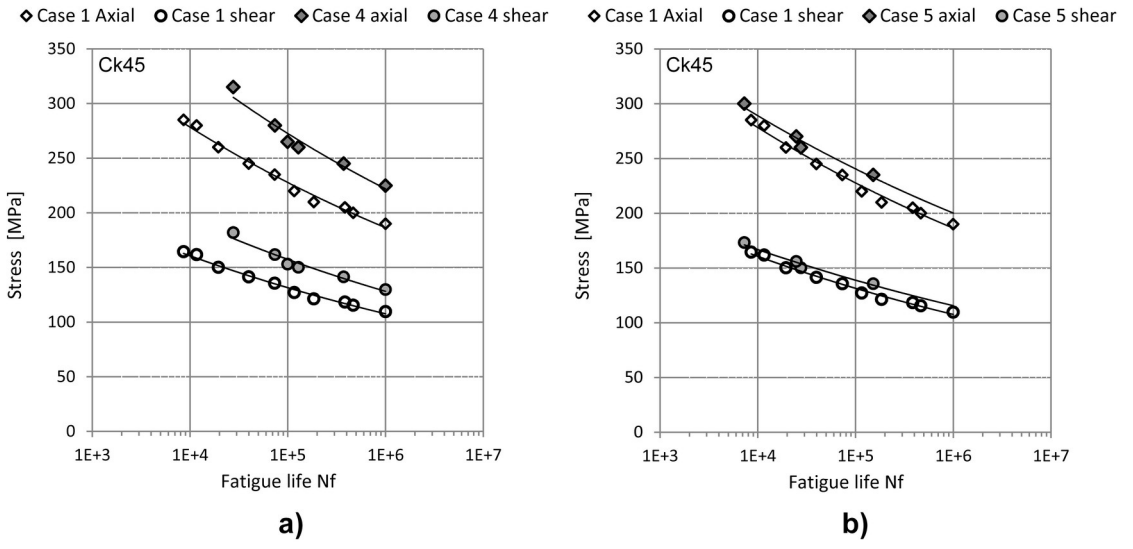


**Figure 3.32:** Ck45 fatigue life results and relative damage between the reference case, Case 1, and a) Case 4, b) Case 5.

Table 3.4 shows the Ck45 results regarding the Y values for each non-proportional loading considered here, these Y values match the axial and shear non-proportional curves with the proportional ones (multiplying the axial and shear S-N curves by Y it is obtained the proportional curves). Based on experimental results, it was found that the Y parameters that relates proportional and non-proportional shear S-N curves and Y parameters that relates proportional and non-proportional axial S-N curves are similar, thus the Y parameter mentioned hereinafter refers to both axial and shear S-N curves of a non-proportional loading.

**Table 3.4:** Ck45 Y values for Cases 2 to 5.

| Y | Case 2 | Case 3 | Case 4 | Case 5 |
|---|---|---|---|---|
| Ck45 | 0.83 | 0.96 | 0.84 | 0.96 |

Figure 3.31 a) shows the Ck45 relative damage between Case 1 and Case 2, where the axial and shear non-proportional S-N curves are above of the proportional ones. This result indicates that the Ck45 is less sensitive to non-proportional loading conditions than it is to proportional ones, i.e. the Y parameter is less than 1 for Ck45. Thus, to obtain the same fatigue life-time in both loading types it is required higher stress amplitudes in the non-proportional loading case, this pattern is observed more or less in the Ck45 fatigue behaviour regarding the other loading cases, Cases 3 to 5. Based on this results, it can be concluded that non-proportional loading paths don't aggravate the damage process comparatively to the proportional loadings in this material, if it is used the same stress level in both loading types (proportional and non-proportional). However, comparing the Y values obtained in Cases 3 and 5 and depicted in Figures 3.31 b) and 3.32 b) respectively, it can be concluded that steady stress increases the Y value which means that the non-proportionality in this cases is more damaging than the one verified in Case 2. In Case 4, Figure 3.32 a), the steady stress in compression do not affect significantly the Y values comparatively to the Y values obtained in Case 2, also the Y values in Cases 3 and 5 are equal, which indicates that steady stress in compression do not contribute significantly to the damage process, but steady stresses in tension increases the non-proportional damage. In this case, the additional damage from steady stresses almost equals non-proportional damage to the proportional one, i.e. Y parameter close to 1. Table 3.5, and Fig.(s) 3.33, 3.34 show the experimental results for the stainless steel AISI 303.

**Table 3.5:** AISI 303 Y values

| Y | Case 2 | Case 3 | Case 4 | Case 5 |
|---|---|---|---|---|
| AISI 303 | 0.81 | 0.83 | 0.77 | 0.85 |

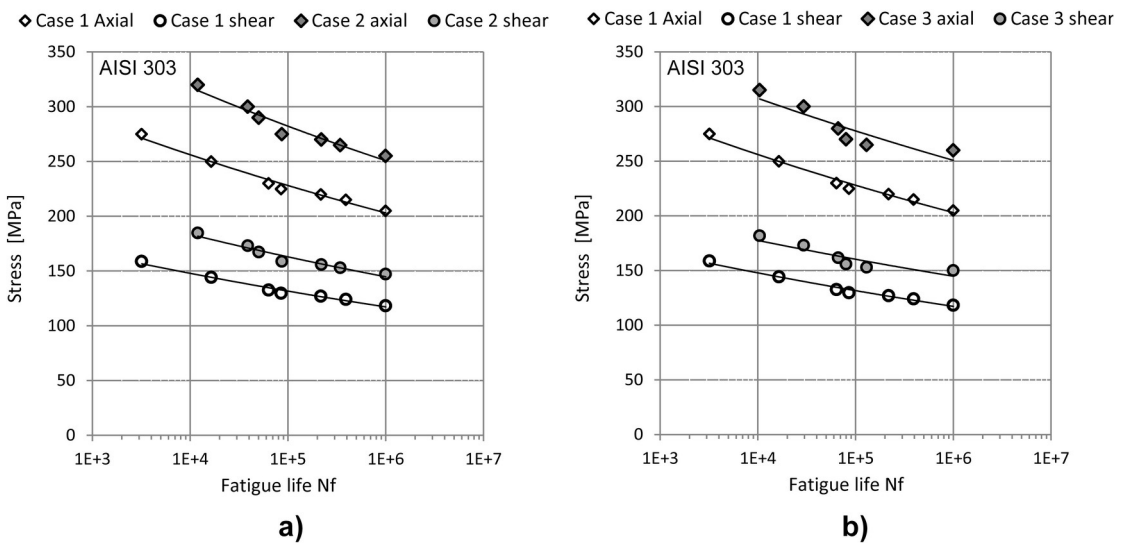


**Figure 3.33:** AISI 303 fatigue life results and relative damage between the reference case, Case 1, and a) Case 2, b) Case 3.

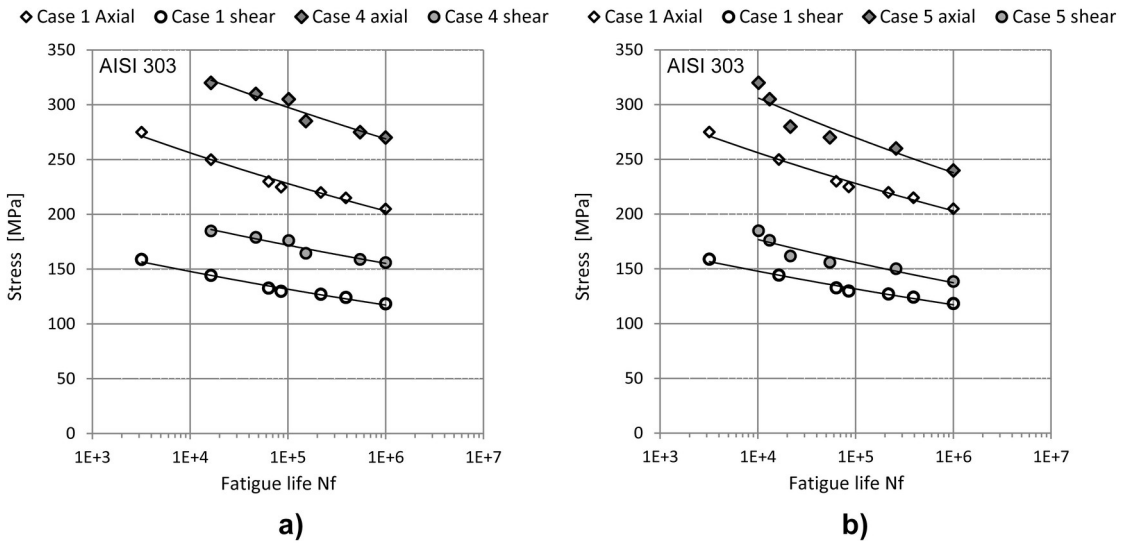


**Figure 3.34:** AISI 303 fatigue life results and relative damage between the reference case, Case 1, and a) Case 4, b) Case 5.

In the AISI 303 material, all non-proportional loading cases have Y values less than one, thus non-proportionality is less damaging than the proportional one regarding the same stress level. From Table 3.5 it can be concluded that Cases 2, 3 and 5 have a Y value very similar, however some conclusions can be draw. The Y parameter in Case 4, see Figure 3.29, is the lowest of all, i.e. the steady stress in compression some how decreases the non-proportional damage. The highest Y value was obtained in Case 5, being the non-proportional loading most damaging; this is explained by the steady stress in tension found in this case. Moreover, Case 3 has a Y value slightly lower than the one found in Case 5, this result indicates that the steady stress in compression compensates in some way the damage caused by the steady stress in tension, i.e. the steady stress in compression has

a mitigation action on the damage caused by the steady stress in compression. However, this damage reduction do not totally compensate the damage increment resulted from the steady stress in tension. The Y results in Case 4 corroborates the aforementioned conclusions, i.e. the Y value in Case 4 less than the one found in Case 2, which indicates that steady stress in compression reduces the non-proportional damage in this material.

The 42CrMo4 results are shown in Figures 3.35, 3.36, and Table 3.6. Regarding this material, the Y values for Cases 2, 4 and 5 are very close to 1, indicating that proportional and non-proportional fatigue strength is very alike regarding the same fatigue life. In this material, the most damaging loading path is the Case 3, please see Figure 3.35 b), where the fatigue damage increases, due to steady stress in tension and compression. This statement is corroborated with the fact that Y values for Cases 4 and 5, please see Figure 3.36 a) and b), are greater than the one obtained in the Case 2, Figure 3.35 a), indicating that both steady stress increases the non-proportional damage. Based on this results, it can be concluded that the 42CrMo4 material is slightly insensitive to non-proportional loadings, Y=0.95. However, it can be found higher Y values due to steady stresses in tension/compression, in this material the compression steady stress causes more damage than the tension one, this can be seen in Table 3.6 where the Y value calculated in loading Case 4 is greater than the one calculated in Case 5.

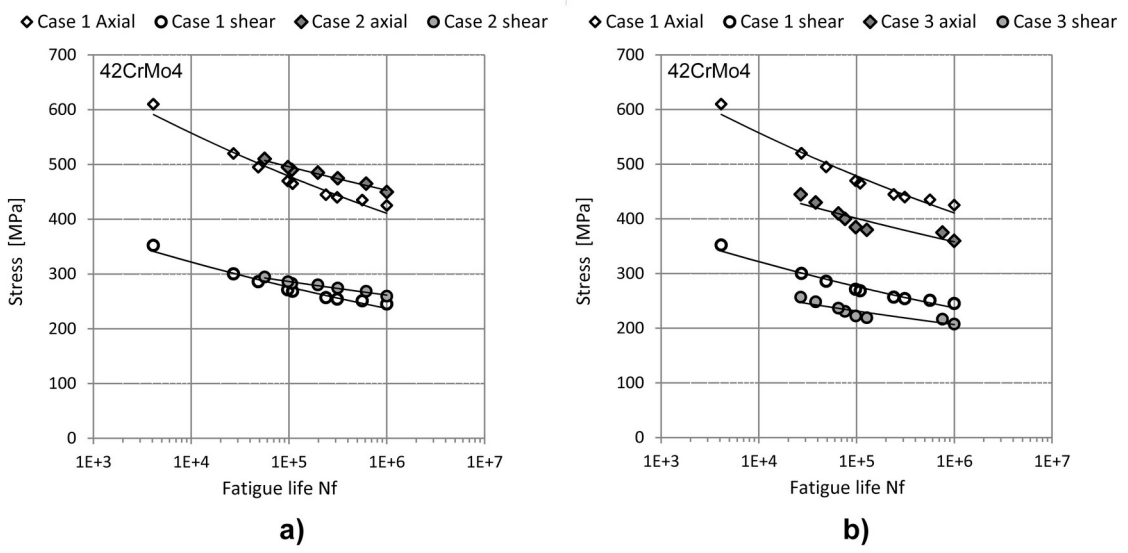


**Figure 3.35:** 42CrMo4 fatigue life results and relative damage between the reference case, Case 1, and a) Case 2, b) Case 3.

**Table 3.6:** 42CrMo4 Y values.

| Y | Case 2 | Case 3 | Case 4 | Case 5 |
|---|---|---|---|---|
| 42CrMo4 | 0.95 | 1.19 | 1.08 | 1 |

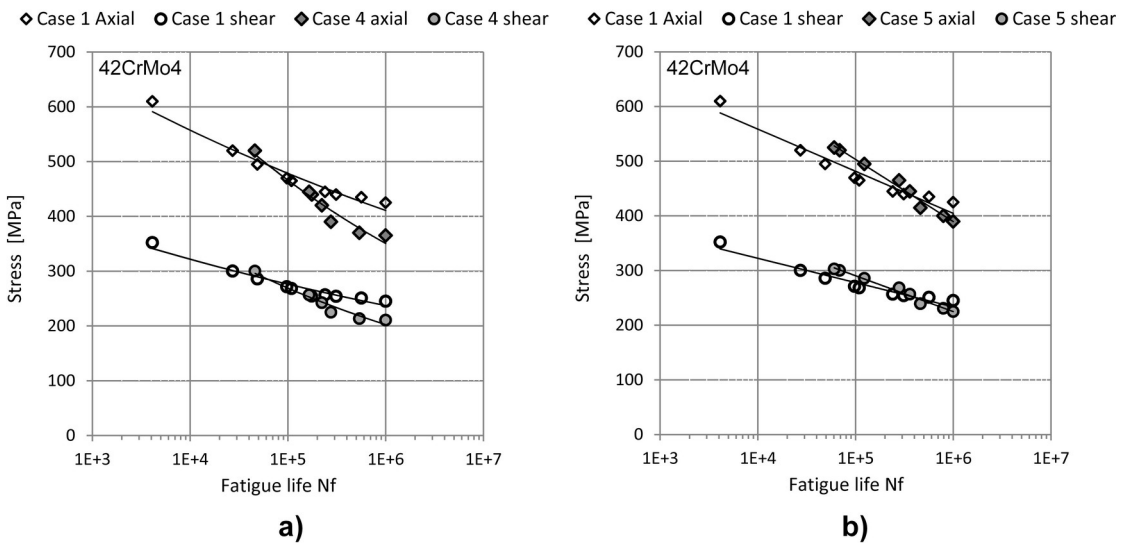


**Figure 3.36:** 42CrMo4 fatigue life results and relative damage between the reference case, Case 1, and a) Case 4, b) Case 5.

#### 3.3.2.1 Y comparison between materials

Table 3.7 summarizes the results regarding the three materials and the selected non-proportional loading cases.

**Table 3.7:** Y values comparison for the selected materials and loading paths.

| Y | Case 2 | Case 3 | Case 4 | Case 5 |
|---|---|---|---|---|
| Ck45 | 0.83 | 0.96 | 0.84 | 0.96 |
| AISI 303 | 0.81 | 0.83 | 0.77 | 0.85 |
| 42CrMo4 | 0.95 | 1.19 | 1.08 | 1 |

It can be concluded that for the same material the less damaging non-proportional loading path is the Case 2, i.e. the fully out of phase loading case, excepting on the AISI 303 material where the lowest Y value was obtained in the loading Case 4. The material most sensitive to non-proportionality among the three materials selected in this study was the 42CrMo4 for the experimental loading cases considered here, this statement is supported by the 42CrMo4 Y values which are the biggest ones among the selected materials. Comparing the Ck45 and AISI 303 results, all Y values are less than 1, however the Ck45 Y values are greater which indicates that Ck45 is more sensitive to non-proportionality than AISI 303, but less than 42CrMo4. Analysing the loading Case 4 in all materials, it was observed that the Y value of the loading Case 4 on AISI 303 is less than the one obtained in the Case 2, this behaviour do not occur in the Ck45 and 42CrMo4 materials, despite the AISI 303 microstructure (fcc) be different from the Ck45 and 42Crmo4 (bcc) in all other cases the AISI 303 follows the same pattern, i.e. the Y values in loading Cases

3 and 5 are greater than in loading Case 2. From here, it can be concluded that fatigue behaviour varies with material type and depend on the material response to the cyclic loading type. Moreover, equivalent stresses or damage parameters determined based on a fixed stress space, i.e. based on a constant value for the relation between the damage of the axial and shear stress components can lead to erroneous conclusions.

### 3.3.3 Final comments

The relative damage between non-proportional and proportional loading paths was analysed here for three different materials. In order to evaluate and quantify that damage it was proposed a Y parameter which relates the axial and shear S-N curves of a non-proportional loading to their homologous proportional curves. Regarding the Ck45 material, the non-proportionality parameters such as phase angle variation, shear and axial steady stress components do not lead to a greater damage than the proportional one, i.e. the average Y values are less than 1. The AISI 303 has a non-proportional damage behaviour very similar to the Ck45 material, however one difference was found in Case 4 regarding the steady stress in compression, where the Y non-proportional parameter is less than the one found in Case 2, this result was only observed in this material. Finally, the 42CrMo4 is the material most sensitive to non-proportional damage. Some remarks can be drawn from this analysis, three different materials were tested in multiaxial fatigue loading conditions; it was observed different non-proportional damage behaviours in the selected materials subject to loading paths with different degrees of non-proportionality. The non-proportionality influence is not equal for all materials, it changes accordingly to the material, and a constitutive parameter must be used to account with the additional non-proportional damage.

# Chapter 4

# Contributions to Level 2

## 4.1 Introduction

In this chapter, it is presented the thesis contribution to the state-of-the-art regarding the level 2 depicted in Figure 4.1.

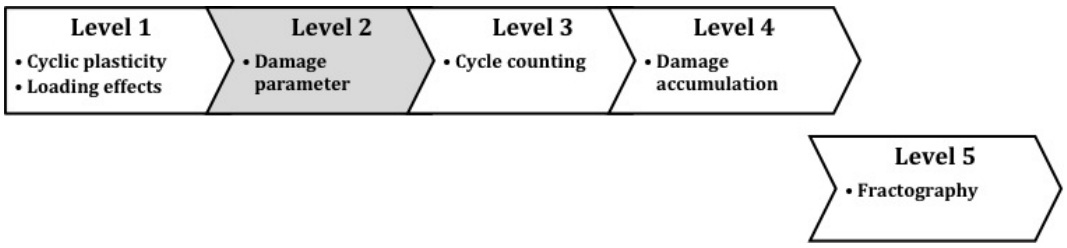


**Figure 4.1:** Multiaxial fatigue level focused in this chapter.

This contribution is a new equivalent shear stress for uniaxial and multiaxial loading conditions. The objective here, is to achieve a multiaxial fatigue criterion capable to deal with all types of loadings including multiaxial random loadings. In order to do that, it is developed a methodology to map a new multiaxial fatigue constitutive parameter that relates two physical quantities i.e. the fatigue damage from shear and normal stresses, which are always present under multiaxial loading conditions. This new constitutive parameter, the SSF damage map, is the cornerstone of the multiaxial fatigue criterion presented here, and later on used in the next two chapters.

## 4.2 Material constitutive behaviour

Material constitutive behaviour under the scope of fatigue damage assessment is the material physical response (loss of mechanical properties) to an external stimuli. This stimuli results from cyclic loadings that may be distributed or local forces. The idea behind the constitutive concept is to perform a correlation, using mathematical formulations, between the material physical behaviour and the physical variables involved in the fatigue

damage process. From this correlation it is obtained mathematical functions that can be used to estimate the material behaviour in the field, which is very useful in mechanical design procedures. For example, the Hook's law is a constitutive equation that estimate the physical relation between stresses and its inherent strains. In this case the constitutive parameter is the Young's modulus, which is a material property. In some cases constitutive parameters are not a constant value due to the non-linear material response, where the material physical behaviour is dependent of the external stimulus type. For instance, in anisotropic materials such as composites, the Young's modulus is a directional dependent constitutive parameter. In this case, the Young's modulus is a generalized tensor in order to capture the Young's modulus directional dependence that is typically found in composites.

In multiaxial fatigue, the material ability to resist to cyclic loadings can be also estimated using a constitutive relation. The external cyclic loadings and the inherent material fatigue response can be correlated using a cyclic constitutive parameter. This parameter must be capable to capture the fatigue damage process resulted from different multiaxial loading conditions and stress levels. From experiments it was proved the existence of different damage patterns resulted from different combinations of normal and shear stresses, even for the same stress level [16]. Despite that, this experimental evidence has been somehow overlooked in the multiaxial fatigue criteria found in literature. One example of this fact is the von Mises equivalent stress. In this equivalent stress the constant $\sqrt{3}$ is used to reduce the fatigue damage of shear stresses to the damage scale of normal stresses, however, this constant do not capture the different damages scales obtained under different combinations of normal and shear stresses. These damage scales are corroborated with different experimental deformation patterns found in pure axial, pure shear, and multiaxial loading conditions. These different patterns are illustrated in Figure 4.2 to clarify this matter.

Figure 4.2 a) depicts a grid at rest without any load. Now, consider Figure 4.2 b), in this case the grid is loaded with a normal loading with an elongation pattern in the axial direction. Figure 4.2 c) presents the same grid but now with a multiaxial shear loading causing a distortion deformation. As it can be seen, the deformation pattern is quite different in both loading conditions.

Now, consider the grain structure of a given material loaded with the conditions shown in Figure 4.2. Under these loading conditions, the grain structure will have different deformation patterns like the ones depicted in Figure 4.2 b), c) and d) for pure axial, pure shear, and biaxial loading conditions. Due to the different deformation patterns, the material strength (including fatigue strength) will be different for each load condition. Now, consider a biaxial loading having simultaneously two types of deformation patterns (normal and shear) as depicted in Figure 4.2 d).

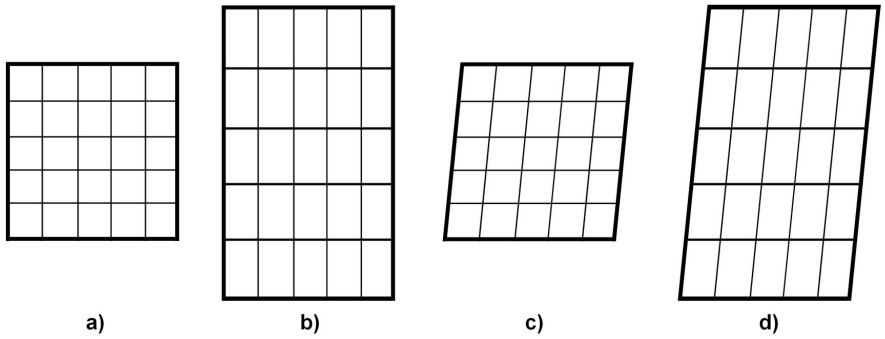


**Figure 4.2:** Illustration of different deformation patterns from different loading types: a) At rest, b) Uniaxial normal loading c) Uniaxial shear loading and d) Biaxial loading.

In this case, the deformation pattern is a mixture of normal deformation and shear distortion. To compute the fatigue damage of a biaxial loading it is required evaluate the contribution of each damage pattern (normal and shear) to the overall damage, to do that it is required evaluate both normal and shear damages in the same damage scale. Therefore, it is necessary reduce both normal and shear damages to the same damage scale because the normal and shear deformations cause different types of damage mechanisms in the material grain structure yielding different damage scales. However, in the von Mises equivalent stress criterion, in which the constant $\sqrt{3}$ is defined under uniaxial static loading conditions, it is not possible to capture the relation between normal and shear deformations under different stress amplitude ratios.

The assumption of a constant value to reduce both normal and shear damages has been widely used in multiaxial fatigue criteria. Nevertheless, from experiments it was found that the predominance of a normal damage over the shear one or vice versa causes different cyclic damage rates in the material cyclic response. Moreover, the aforementioned damage rates obtained under different stress amplitude ratios can be experimentally analysed by inspecting the material failure mode (crack separation mode), which is also dependent on the stress level and load type.

In order to scrutinize the fatigue damage behaviour under different multiaxial loading conditions and stress levels, it is performed in the following paragraphs a fatigue crack analysis over experimental results. The objective is to show the experimental evidence about the effect of the stress amplitude ratio in the fatigue damage process by focusing crack grow paths.

Fig.(s) 4.3 and 4.4 show for different loading paths the experimental crack growth as consequence of different damage mechanisms. This study was performed on a 2A12–T4 aluminum alloy [20] with two loading path variables, e.g. the stress amplitude ratio, which is the ratio between the multiaxial loading components, $\tau/\sigma$ , and the phase angle between the normal and shear loading components (non-proportional loading paths). It can be seen in Figure 4.3 that the stress amplitude ratio variation leads to different crack initiation

planes and crack growth patterns, which indicates different damage mechanisms. Figure 4.4 shows the phase angle effect on the fatigue crack initiation and growth, here the stress amplitude ratio is maintained fixed during the loading period. From these results, it can be concluded that the phase angle variation also induces different crack initiation planes and growth paths which in turn indicate different fatigue damage mechanisms.

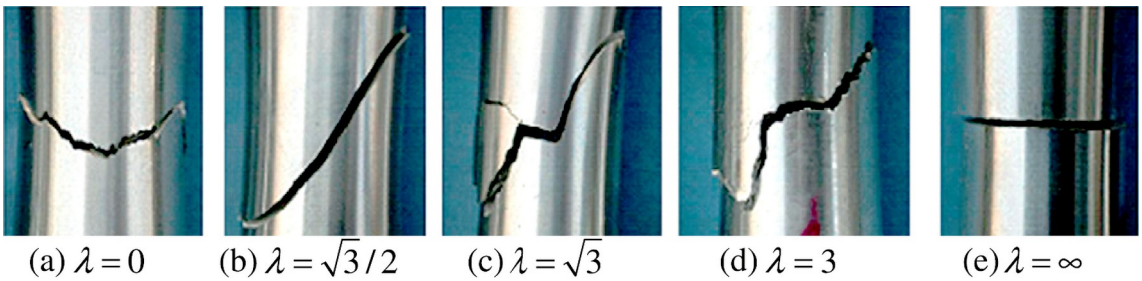


**Figure 4.3:** In-phase fatigue crack results under different stress amplitude ratios [20].

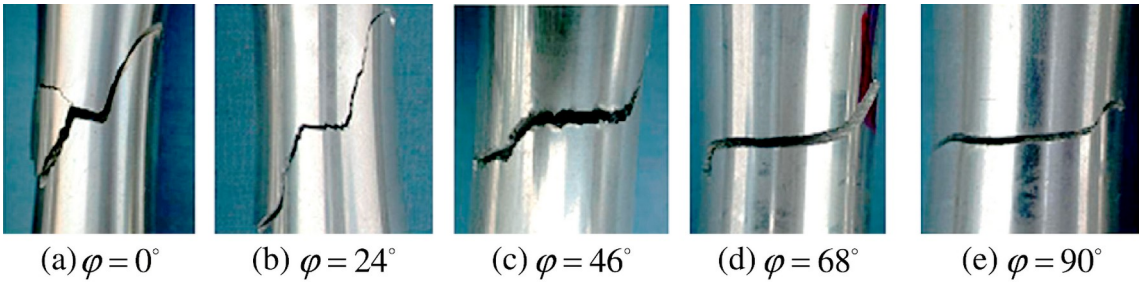


**Figure 4.4:** Out-of-phase fatigue crack results for a fixed stress amplitude ratio [20].

Furthermore, the fatigue damage mechanism is also dependent on the stress level. Figure 4.5 depicts different failure modes achieved under pure torsion loading conditions.

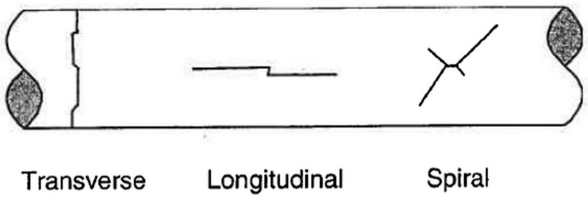


**Figure 4.5:** Failure modes in torsion [16].

For the uniaxial torsion loading case, different surface fractures can be achieved by changing the shear stress level involved in the damage process, please see Figure 4.6. In this case, for lower shear stress amplitudes it is achieved spiral cracks, for average shear stress amplitudes it is achieved longitudinal cracks and for higher shear stress levels it is achieved transverse cracks [16]. Thus, it can be concluded that for the same loading path it can be seen different crack initiation planes under different stress levels.

Based on the different fatigue crack behaviour discussed above, it can be concluded that the direction of the crack initiation plane varies according to the loading path type and

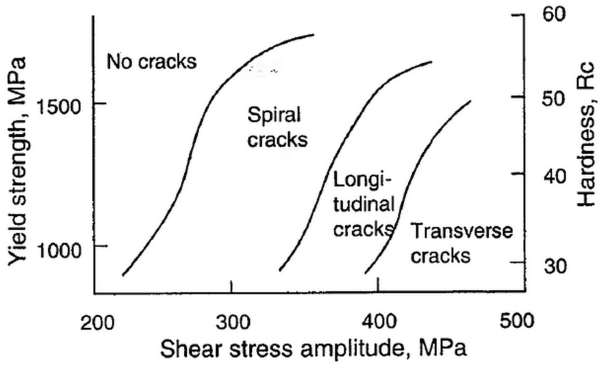


**Figure 4.6:** Map of macroscopic fracture mechanisms [16].

stress amplitude level. Therefore, the material ability to resist to multiaxial cyclic loadings has an anisotropic behaviour with non-linear patterns. Moreover, this ability to cyclic resist to external loads is therefore a material property and is strongly dependent on its micro-structure. It seems that the stress amplitude ratio ($\lambda$) and the stress level are two variables qualified to account the combined fatigue damage of multiaxial loading components. Thus, these variables are good candidates to be used in constitutive equations of multiaxial constitutive parameters, which must be representative of the loading path and stress level effects on the material fatigue strength.

## 4.3 Multiaxial fatigue constitutive parameter

The key to achieve the multiaxial fatigue constitutive parameter, described in previous sections, is on the interpretation of the combined fatigue damage from shear and normal stresses. Experimentally, it has been proven that the stress level needed to cause fatigue failure in pure shear is lower than the axial one for a wide range of materials. This fact has led to consider a stress scale factor (SSF) between shear and normal stresses in order to reduce different stresses in nature to the same stress space, i.e. to the same damage scale.

Most of the multiaxial fatigue models found in literature correctly consider the normal and shear stresses contribution to the material strength variation, and somehow a stress scale factor have been always defined. The stress scale factors of the multiaxial fatigue criteria presented and discussed in Chapter 2, are determined based on the materials fatigue strength under pure axial and pure shear loading conditions (uniaxial loading paths). Some of these criteria has been used to estimate fatigue strength in the finite life region under the assumption that the slopes of the pure shear and pure axial S-N curves are maintained equal in all fatigue life range. Due to this assumption, these criteria have been considered as an equivalent damage parameter, because their SSF formulation remains valid (according to their assumption) for finite and infinite fatigue life estimates. However, the slopes of the uniaxial S-N curves (axial and shear) varies across the fatigue

life range due to the stress level effect on each type of deformation (axial and shear), which results in the SSF variation with the stress level variation. Thus, in these criteria, the assumption of a constant SSF do not take into account the stress level effect in the fatigue damage process.

Considerable efforts were made to quantify the effective shear and normal stress amplitudes under three-dimensional stress states. However, the combined damage from these amplitudes have been estimated based in a constant value. In some criteria, mostly equivalent stress criteria, the constant value approach proved to be inadequate. For example, this approach has led to compute damage parameters with equal amplitude for different loading paths with different experimental fatigue lives.

### 4.3.1 The stress space damage paradigm

In continuum mechanics, the so called stress space or Haigh-Westergaard stress space is defined based in the principal stress directions of a generic stress tensor. These directions define the rotation and inherent direction of a Cartesian reference system (principal axes directions). In each principal axis, it is accordingly represented its principal stresses time evolution.

Principal stress functions can be also represented in this stress space, the von Mises yield function is one example of that. When a stress state has three principal stresses, this yield function becomes a cylindrical yield surface. However, when the stress tensor can be simplified into two principal stresses, the yield surface has circular shape in the $\pi$ plane (plane equally inclined to each principal axis). Under this reasoning, biaxial loading paths are usually represented in the $\pi$ plane with two principal axes. In one principal axis it is represented the normal stress amplitude and in the other one it is represented the shear stress amplitude multiplied by $\sqrt{3}$, which comes from the von Mises yield function.

Moreover, the von Mises equivalent stress is given by the vectorial norm of these principal stresses depicted in the $\pi$ plane. Based in this facts, it can be concluded that the von Mises stress space is a yield stress space that has been used to estimate multiaxial fatigue strength. For example, the ASME Boiler and Pressure Vessel code [3] evaluates its damage parameter in the von Mises stress space among others.

One characteristic of this stress space is the constant stress scale factor in the shear stress axis, which comes from the von Mises yield criterion. Therefore, the $\sqrt{3}$ constant results uniquely from a mathematical exercise and is not based on experimental evidences. Moreover, the von Mises damage scale is independent from the stress level, loading path, and material type. This is a crucial flaw, because fatigue damage is strongly dependent of the loading conditions and material type, thus the von Mises stress space paradigm is inappropriate to evaluate fatigue damage parameters. Despite that, the von Mises yield stress space has been used to estimate fatigue lives which is the cases of the invariant

criteria, for instance. In the following sections, it will be proved that the aforementioned fatigue damage scale (which has been represented by a constant) varies according to the material type and loading conditions. Therefore, if the fatigue damage scale varies due to the loading nature, thus the stress space damage scale must also vary, i.e. the stress space paradigm must be updated according to the material cyclic response.

## 4.4 Multiaxial SSF concept

In this section, a new stress scale factor concept (SSF) is proposed. The objective is to perform a experimental correlation between the material fatigue strength and the loading type to obtain a constitutive function i.e. the SSF function. The physical meaning of the proposed constitutive function is a multiaxial fatigue damage scale that adjusts its scale according to the multiaxial loading type and stress level. This new function will allow to add shear and normal damages having into account the loading type, stress level, and material type, which a feature that cannot be found in literature. In fact, the innovation in this approach is based on a paradigm change, where a constant damage scale is replaced by a two variable function. In this way, it becomes possible to capture the material fatigue damage anisotropy, which has been experientially verified under multiaxial loading conditions.

In order to obtain the SSF function, it was performed a series of specific experimental fatigue tests. In these tests, proportional loading paths with different stress amplitude ratios (SAR), and stress levels were used to characterize the fatigue damage anisotropy. The selected loading paths were chosen in order to avoid other type of influences on the experimental results, such as non-proportionality or mean stress effects in order to avoid biased interpretations. These effects can be later accounted trough dedicated parameters such as the Y parameter proposed in Chapter 3.

In the following, it is presented the reasoning behind the SSF function. For each stress amplitude ratio and stress level of the aforementioned proportional loadings used in experiments, the following reasoning is considered: In Figure 4.7 it can be found a S-N graph where it is represented the fatigue life-time evolution of two loadings. One is a proportional loading, which is represented by its two stress components (shear and normal) versus fatigue life, $N_f$.

This is a unconventional representation of a S-N curve, usually it is used a damage parameter computed with the two stress components of a loading path (shear and normal stresses) versus fatigue life. However, the aforementioned unconventional representation is adopted here to avoid any biased influence in the fatigue damage interpretation. The second load depicted on Figure 4.7 is the pure shear S-N curve that will be used as fatigue damage reference in order to correlate uniaxial and multiaxial loadings. The SSF function, as designed here, will reduce fatigue damage from normal stresses to the shear

damage scale. However, the reasoning behind this design can be also used to reduce shear damage from shear stresses to the damage scale of normal stresses, but in this case the S-N curve (reference damage curve) to be used in fatigue life estimates must be the axial one. Recalling Figure 4.7, the stress amplitude ratio of the multiaxial loading is calculated by dividing the shear stress amplitude $\overline{AB}$ by the normal stress amplitude $\overline{AD}$, i.e. $\overline{AB}/\overline{AD}$ ; which is maintained constant across all S-N graph.

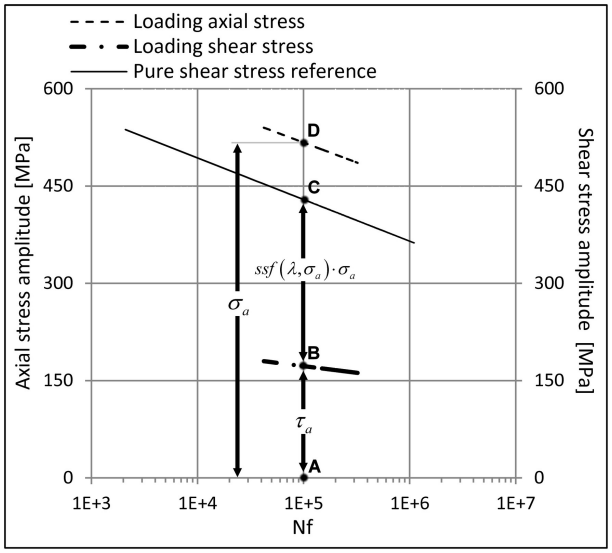


**Figure 4.7:** Illustrative case of a multiaxial and an uniaxial S-N curve.

Experimentally, it is observed that the slope of the lines represented in Figure 4.7 are not parallel to each other. This leads to the conclusion that the distance $\overline{BC}$ and $\overline{CD}$ does change with the fatigue life variation, indicating a non-linear effect on fatigue damage due to the stress level variation. Moreover, the stress amplitude ratio variation will also vary the distances $\overline{BC}$ and $\overline{CD}$, reflecting different fatigue strengths according to the combined effect of the normal and shear stresses. Now, the key concept behind the SSF damage map is the following:

Here, as an example, the SSF mapping concept is explained at $1E5$ cycles (fatigue life), however, to obtain the SSF damage function (based on the SSF damage mapping) the reasoning explained in the following is performed for the entire fatigue life range obtained in the experiments. Fatigue failure at $1E5$ can be achieved using the two loading paths depicted in Figure 4.7, for that it will be required the stress amplitude $\overline{AC}$ in pure shear, and the stress amplitudes $\overline{AB}$ (shear) plus $\overline{AD}$ (normal) in the proportional loading.

Since the fatigue failure occurs at the same fatigue life-time in both loading paths i.e. $1E5$ cycles, it can be considered that both fatigue damages ($\overline{AC}$ and $\overline{AB}$+$\overline{AD}$) are equivalent, because they cause the same final result. Now, imagine that, it is removed the normal component of the proportional loading, i.e. the stress amplitude $\overline{AD}$ is removed being left the shear stress component $\overline{AB}$. Under this circumstances, it is not possible to obtain a

fatigue failure at $1E5$ cycles, the $\overline{AB}$ amplitude must be increased with the increment $\overline{BC}$ to cause such a failure.

Therefore, the additional damage caused by the increment $\overline{BC}$ is equal to the one caused by the normal stress amplitude, depicted in Figure 4.7 by $\overline{AD}$. This is so because, the same life-time is obtained using the two following combinations: shear amplitude $\overline{AB}$ plus the shear increment $\overline{BC}$, or shear amplitude $\overline{AB}$ plus the normal stress amplitude $\overline{AD}$.

Thus, the $\overline{AD}$ normal stress amplitude has the $\overline{BC}$ amplitude in the shear damage scale. To reduce the fatigue damage of normal stresses to the shear damage scale, the $\overline{AD}$ normal stress amplitude must be multiplied by the respective SSF, which is given by $SSF = \overline{BC}/\overline{AD}$ . The SSF varies with the stress amplitude ratio and also with the stress level that is a dependent variable of the normal stress amplitude, thus the SSF damage map can be defined through a two variable function and used to obtain an shear equivalent stress as follows in Eq. 4.1.

$$ssf\left(\sigma_a, \lambda\right) = \frac{\mathrm{BC}\left(\sigma_a, \lambda\right)}{\mathrm{AD}\left(\sigma_a, \lambda\right)} \tag{4.1}$$

Where $\sigma_a$ is the normal stress of a given multiaxial loading and the $\lambda$ variable is its stress amplitude ratio, presented in Eq. 4.2.

$$\lambda = \frac{\tau_a}{\sigma_a} \tag{4.2}$$

### 4.4.1 Particular case of the uniaxial loading conditions

The SSF concept applied to the uniaxial loading cases, i.e. pure normal and pure shear loadings, is illustrated in Figure 4.8. The SSF concept applied to the uniaxial loading cases which transforms the normal and shear damages to the same damage scale, is given by the ratio between the shear stress amplitude and the normal stress amplitude for the same fatigue strength, as shown in Figure 4.8 and Eq. 4.3.

$$ssf = \left.\frac{\tau_{a\_uniaxial}}{\sigma_{a\_uniaxial}}\right|_{Nf} \tag{4.3}$$

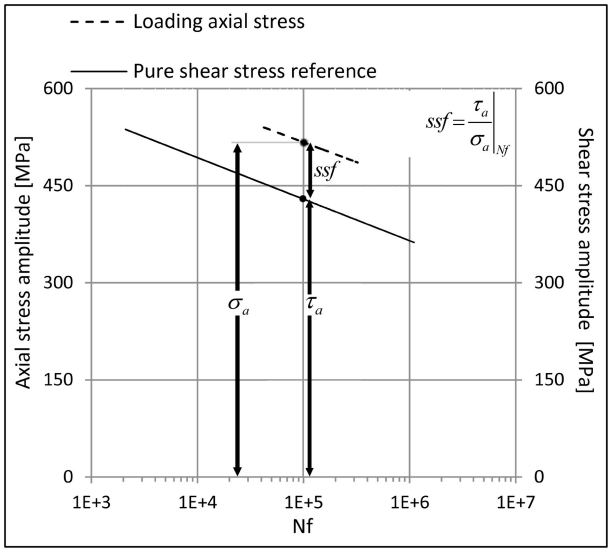


**Figure 4.8:** Illustrative case of uniaxial damage correlation using the SSF concept.

### 4.4.2 Additional non-proportional damage

Non-proportional loading cases are generally identified by the principal directions variation during the loading period. However, it is important to have in mind that the concept of the principal directions variation is insufficient to fully characterize the non-proportional damage of a given non-proportional loading. Non-proportionality may result from a wide range of loading types which creates also a variety of damage mechanisms. These mechanisms result essentially from the way in which the material micro-structure is loaded, which is very different from the one verified on proportional loading paths. Non-proportional loadings may activate all material slip systems which increase the loading effect on the material micro-structure (additional cyclic hardening or softening). In this way, non-proportionality is much more than a phase angle between normal and shear stresses or a variation of the principal directions. Figure 4.9 shows four non-proportional loading paths with different damage mechanisms. Although, these non-proportional loadings have their principal directions rotating during the loading period, they load the material micro-structure in different ways. Therefore, it can be concluded that the damage scale involved in each one of the presented loading paths are quite different.

In Figure 4.9, the out-of-phase loading path depicted in the upper left corner, have normal and shear strains with a sinusoidal shape and a phase shift equal to 90°. The diamond loading is similar to the out-of-phase loading case, the only difference is in the shape of the normal and shear strains time evolution, which have a sawtooth shape. The square loading path has a steady normal and shear strains during the loading period. Finally, the cross loading path is composed by two proportional loadings combined sequentially, here the non-proportionality occur by changing the loading direction. This type of non-proportionality, the one depicted in the cross case, is captured by the SSF damage map presented in the previous sections, however for the other ones, it is required

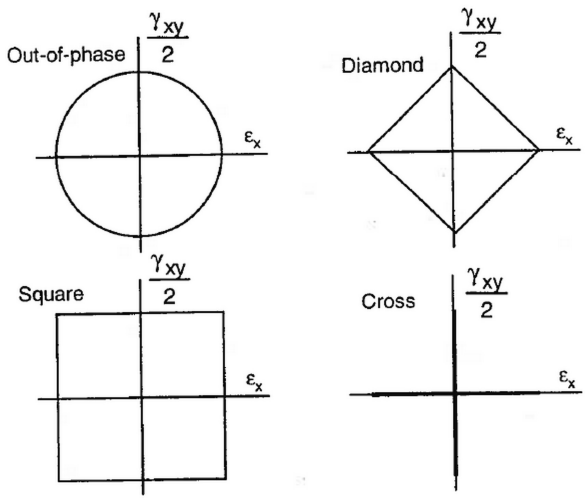


**Figure 4.9:** Out-of-phase, diamond, square and cross loading histories [16].

additional procedures. In Chapter 3, it was found that the steady stresses can increase or decrease the material fatigue strength, depending on the material and loading type. Moreover, the occurrence of simultaneous maximum stress amplitudes (normal and shear) during a non-proportional loading also creates a greater damage. Considering that, the principal directions variation can be associated with other fatigue phenomena such as steady stresses or mean stresses, this observation cannot be ignored when non-proportional damage is studied. In order to capture the non-proportional effect on the material's fatigue strength it was proposed in the previous chapter a non-proportional parameter, the non-proportional sensitivity factor Y, which translates the relative damage between proportional and non-proportional loading paths. The Y parameter will be used here to overcome the SSF limitations under non-proportional loadings.

### 4.4.3 Multiaxial fatigue damage criterion

All multiaxial fatigue criteria have the same purpose, which is to estimate the fatigue life under multiaxial loading conditions. Some of them have the additional possibility to estimate the orientation of the crack initiation plane, which is the case of the critical plane criteria. Surprisingly, the most used criteria are the easiest ones and not the most accurate. Typically, criteria that are the simple and easiest to implement are the ones chosen to correlate fatigue data. Complex criteria are hard to implement and difficult to understand which can turn them unpopular. However, there are some characteristics which every multiaxial fatigue criterion most have. A multiaxial fatigue criterion must be physically based in order to translate the real damage process in the material, which means, all criterion formulations must be physically justified. Also, a good multiaxial criterion must be robust and be able to capture all kinds of damage inherent to complex multiaxial loadings.

### 4.4.4 New equivalent shear stress proposal

In this section, it is proposed a shear equivalent stress based on the SSF concept presented in the previous sections. In Figure 4.10 it is sketched the S-N curve of the uniaxial shear stress for a given material. From Figure 4.10 it can be concluded that the shear stress amplitude (shear stress level) is directly related to the fatigue damage. The shear stress amplitudes in the points 1, 2, and 3 shown in Figure 4.10, are associated to different fatigue life times, i.e. different number of loading cycles at rupture time. Thus, the shear stress level is directly proportional to the material fatigue life. Considering, now a multiaxial loading with shear and normal loading components they can be added if they have the same damage scale.

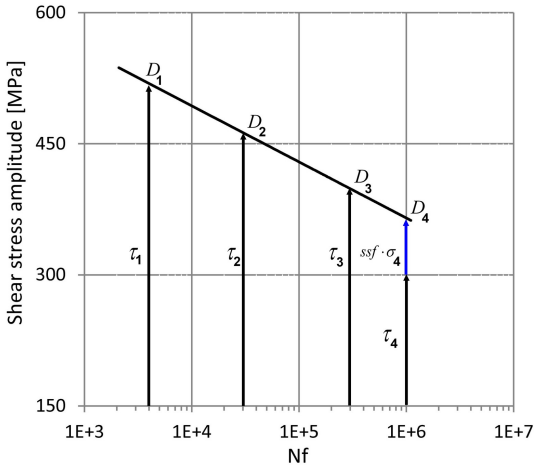


**Figure 4.10:** S-N curve of the uniaxial shear stress for a given material.

In Figure 4.10, the $D_4$ depicts a fatigue damage from a multiaxial loading where the shear stress amplitude $\tau_4$ have a magnitude insufficient to cause failure at $1E6$ cycles, the contribution that is needed to cause the failure comes from the normal stress component reduced to the shear damage scale. The normal stress contribution to the overall damage can be evaluated by $ssf \cdot \sigma$. In this way, it can be used a uniaxial S-N curve (in shear) to account the fatigue damage associated to a multiaxial loading. The damage parameter proposed here is an equivalent shear stress, named as SSF equivalent shear stress, that depends on the multiaxial loading components time evolution, which means that the equivalent shear stress damage scale and its amplitude will vary during a loading period. The uniaxial shear S-N curve (damage reference curve) is typically computed by experiments in respect to the maximum shear stress amplitude of a sinusoidal shear loading. Thus, the SSF equivalent shear stress, for fatigue life estimates, is also determined by its maximum value found during the loading period. Eq. 4.4 shows the expression for the SSF equivalent shear stress proposed here.

$$\tau_{eqv} = \max\left(\tau_a + ssf(\lambda, \sigma_a) \cdot \sigma_a\right) \tag{4.4}$$

### 4.4.5 Proposal of the damage sign time evolution

One drawback related to the equivalent stress criteria is the negative signal lost, which can lead to a misunderstood conclusions. As a matter of fact, one of the critical plane criteria advantages over the equivalent stress/strain criteria, is their preservation of the load sign. This advantage has been stressed by critical plane developers and users. The typical square root found in the equivalent stress/strain criteria must have positive arguments to yield real results (square root of negative numbers yields complex numbers), thus it is not possible to obtain negative values in a typical equivalent stress/strain criterion. Moreover, in the invariant type criteria, the load components (normal and shear) are all to the power of 2, therefore all load components become positive, thus the compression and tension stages can not be identified in this approach. Actually, this is a important subject because the load sign is experimentally associated to different fatigue damage mechanisms. Moreover, it is not possible to use cycle counting methods considering a equivalent stress time evolution in a direct way, the widely used Rainflow cycle counting method is one example of that. This is so because, typical equivalent stress/strain approaches do not capture the physical damage behaviour during its time evolution.

Other question regarding the load sign subject, occurs in equivalent stress criteria that do not use square roots in their formulation. For instance, equivalent stress criteria in which the instantaneous values of a load components (normal and shear) are directly added, it may occur that the normal and shear stresses have the same amplitudes but different load signs. In this case, the equivalent stress is zero which indicates no fatigue damage, which is not right. Thus, the load sign may affect erroneously the damage characterization. To illustrate this issue, please consider the following expression in Eq. 4.5, for a given multiaxial load instant.

$$-\tau + ssf \cdot \sigma \tag{4.5}$$

From Eq. 4.5 it can be concluded that, adding a negative shear stress and a positive normal stress, the resulting equivalent stress amplitude will be smaller than the one found in the negative shear stress. This result leads to the wrong conclusion where a multiaxial loading (with normal and shear components) causes less damage than the one obtained uniquely from their shear stress component. In order to overcome this drawback, here it is proposed a new concept to update the load sign accordingly to the physical damage time evolution.

The reasoning of this proposal is as follows: The sign of normal stresses indicate different damage mechanisms, i.e. positive (tension) and negative (compression) normal stresses cause two different types of damage. On the other hand, the shear stress sign is not related to different damage mechanisms, i.e. the fatigue damage from negative or positive shear stresses is equal, thus the load sign is independent of the damage mechanism in shear loadings. Based on these two experimental evidences, the sign of the shear stress component of a given multiaxial loading takes the sign of the normal stress component, thus the instantaneous value of the SSF equivalent stress is given as follows in Eq. 4.6

$$\tau_{eqv} = sign\left(\sigma\right) \cdot abs\left(\tau\right) + ssf \cdot \sigma \tag{4.6}$$

### 4.4.6 Capturing additional non-proportional damage

The SSF equivalent shear stress captures partially the non-proportional loading effect on the material fatigue damage. In this criterion, it is only covered the non-proportionality resulted from the SAR variation along proportional loading paths or proportional loading branches. Thus, in the SSF equivalent stress criterion it is missing the non-proportionality from out-of-phase loading conditions. The Y parameter concept presented in Chapter 3 aims to overcome this drawback in order to fulfil the SSF criterion capability to capture the non-proportional damage. The Y parameter captures the relative damage between proportional and non-proportional loading paths by updating the shear and normal stress levels. The SSF criterion under out-of-phase non-proportional loadings is given in Eq. 4.7.

$$\tau_{eqv} = \max_{block}\left(Y_{shear} \cdot \tau + ssf \cdot Y_{normal} \cdot \sigma\right) \tag{4.7}$$

Where $Y_{shear}$ gives the relation between proportional and non-proportional shear damages and the $Y_{normal}$ gives the relation between proportional and non-proportional normal stress damages. If Y parameter is equal in the shear and normal loading components, thus the Y is a constant value. In Eq. 4.8, it is presented the SSF equivalent shear stress updated to non-proportional conditions, where Y is the SSF non-proportional parameter and P indicates the loading period.

$$\tau_{eqv} = Y \cdot \max_{P}\left(\tau + ssf \cdot \sigma\right) \tag{4.8}$$

### 4.4.7 Multiaxial fatigue life estimation

In order to estimate multiaxial fatigue life-time using the SSF equivalent shear stress, it is used the uniaxial S-N curve obtained under pure torsion loading conditions. This S-N curve can be obtained by performing a curve fitting to the uniaxial fatigue data. Usually,

the best trend line for this type of fatigue data is a power law equation, in which the number of loading cycles is the trend-line argument and the output is the shear stress, please see Eq. 4.9.

$$\tau = A(N_f)^b \tag{4.9}$$

where $A$ and $b$ are the S-N trend-line parameters, $N_f$ is the fatigue life and $\tau$ is the inherent stress amplitude value. The SSF equivalent stress is a shear stress, thus the following Eq. 4.10 is valid.

$$\tau_{ssf} = \max_p \left(\tau + ssf \cdot \sigma\right) = A(N_f)^b \tag{4.10}$$

Thus, fatigue life estimates can be performed using the SSF equivalent stress by arranging Eq. 4.10 as follows in Eq. 4.11.

$$N_f = \left(\frac{\tau_{ssf}}{A}\right)^{\frac{1}{b}} \tag{4.11}$$

### 4.4.8 Generalization of the SSF damage map

To determine the SSF function it is required a considerable amount of fatigue tests, at least 25 successful tests, which can take a lot of time to perform and costs. Therefore, it makes sense to get some alternative ways to reduce the amount of these tests. Nevertheless, the present author wants to stress that it is advised to perform experimental tests to obtain the SSF damage map for each material in order to achieve better results.

However, within a structural steels family it can be assumed that the damage map (SSF funtion) has a similar pattern. Thus, by testing one material from a material family to obtain its SSF damage map it becomes possible to use that damage map within the same family. In order to use the SSF damage map in materials different from the tested one, the SSF can be corrected through the ultimate tensile strength of the untested material as presented in Eq. 4.12.

$$\tau_{eq} = \tau + \left(\frac{\sigma_{ut,untested}}{\sigma_{ut,tested}}\right) \cdot ssf(\sigma, \lambda) \cdot \sigma \tag{4.12}$$

where $\sigma_{ut,untested}/\sigma_{ut,tested}$ is the ratio between the ultimate tensile strength of the untested material (the one with unknown SSF function) and the ultimate tensile strength of the tested material (material with known SSF function).

### 4.4.9 SSF and stress gradient update

The SSF function must be also updated to account with stress gradient effects. This must be done in cases where the normal stress has a stress gradient different from the one used to obtain the SSF function. For instance, it is well known that under rotating bending the required stress level is higher than in tension-compression to obtain the same fatigue life-time in both loading conditions. For this reason, it is usual to adopt a constant to correlate both S-N curves, usually 0.8, that adapts the rotating bending S-N curve to the tension-compression loading conditions [68]. On the other hand, the S-N curve obtained in tension-compression can be also adapted to the rotating bending loading condition by using the constant 1.25 (which comes from 1/0.8). This approach assumes that axial bending stresses must be 20% higher than the normal stresses, for the same fatigue damage [68, 152].

Due to this assumptions, here it is assumed that the SSF damage function should be also updated according to the normal stress gradient. If the SSF equivalent stress has a SSF function obtained for normal stresses under tension-compression stress gradients, thus under bending conditions, the SSF equivalent stress must be computed as follows in Eq. 4.13.

$$\tau_{eq} = \tau + 0.8 \cdot \left( \frac{\sigma_{ut}}{\sigma_{ut,42CrMo4}} \right) .ssf(\sigma, \lambda) \cdot \sigma \tag{4.13}$$

where the constant 0.8 reduces the magnitude of the SSF damage map in about 20% and transforms the SSF damage map obtained under tension-compression to the rotating bending condition, however the SSF damage map pattern is maintained.

## 4.5 SSF damage map

In this section, it is presented the methodology designed to determine the SSF damage map, which is mapped from the experimental data shown in Table 4.1. Thus, the following results are totally based in fatigue life experiments performed using hourglass specimens, at room temperature with loading frequencies between 5-6 Hz, please see Figure 3.30.

Moreover, the experiments were carried out under stress control using the loading paths depicted in Figure 4.11, the failure criterion considered here was the specimen total separation. The experiments were performed using the high strength steel 42CrMo4, its monotonic, cyclic, and chemical properties are presented in Tables A.1 and A.2, respectively [3]. A brief description regarding the 42CrMo4 industrial applications is also performed in Appendix A. Figure 4.11 shows the loading paths considered to determine the SSF function. The loading Case 1 and 2 are the two multiaxial loading cases, in tension and torsion, respectively. Case 3, 4 and 5 are three proportional loading paths with

different stress amplitude ratios, namely 30°, 45°, and 60°. Case 6, is a non-proportional loading path with 90° phase shift. Table 4.1 presents the fatigue data for the loading paths depicted in Figure 4.11.

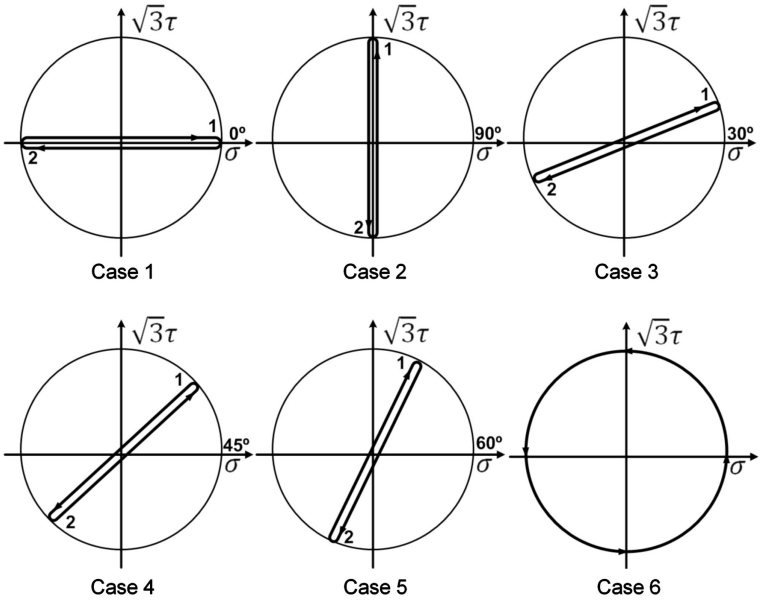


**Figure 4.11:** Loading paths considered in this section to determine the SSF map.

**Table 4.1:** 42CrMo4 fatigue data used in the SSF mapping.

| Case 1 | | | Case 2 | | | Case 3 | | |
|---|---|---|---|---|---|---|---|---|
| **Sigma** | **Tau** | **2Nf** | **Sigma** | **Tau** | **2Nf** | **Sigma** | **Tau** | **2Nf** |
| 700 | 0 | 6040 | 0 | 374 | 1100000 | 545 | 182 | 44610 |
| 600 | 0 | 19951 | 0 | 545 | 2088 | 533 | 178 | 42182 |
| 500 | 0 | 215910 | 0 | 484 | 11302 | 515 | 172 | 185465 |
| 485 | 0 | 269178 | 0 | 440 | 70610 | 507 | 169 | 154590 |
| 445 | 0 | 2368959 | 0 | 402 | 159854 | 494 | 165 | 172703 |
| 455 | 0 | 247953 | 0 | 395 | 315668 | 481 | 160 | 322588 |
| 560 | 0 | 53752 | | | | | | |
| 550 | 0 | 56929 | | | | | | |
| 450 | 0 | 3263000 | | | | | | |
| 470 | 0 | 338170 | | | | | | |
| 480 | 0 | 284348 | | | | | | |
| **Case 4** | | | **Case 5** | | | **Case 6** | | |
| **Sigma** | **Tau** | **2Nf** | **Sigma** | **Tau** | **2Nf** | **Sigma** | **Tau** | **2Nf** |
| 425 | 245 | 1000000 | 350 | 350 | 59784 | 450 | 260 | 1000000 |
| 435 | 251 | 564088 | 310 | 310 | 62809 | 465 | 269 | 618128 |
| 440 | 254 | 311401 | 300 | 300 | 130984 | 475 | 274 | 316712 |
| 445 | 257 | 239600 | 290 | 290 | 204933 | 485 | 280 | 197548 |
| 465 | 269 | 109087 | 261 | 261 | 246926 | 490 | 283 | 107374 |
| 470 | 271 | 97366 | 244 | 244 | 512872 | 495 | 286 | 97548 |
| 495 | 286 | 48740 | 292 | 292 | 105595 | 510 | 294 | 56411 |
| 520 | 300 | 27204 | | | | | | |
| 610 | 352 | 4114 | | | | | | |

### 4.5.1 Evaluating the stress scale factor

The SSF parameter discussed, for each criterion, in the state-of-the-art presented in Chapter 2, is generally obtained through the fatigue limits of the uniaxial loadings, usually in tension-compression and pure shear loading conditions [8]. This approach allows, in a easy way, to estimate fatigue lives using both tension-compression or torsion-torsion S-N curves accordingly to the criterion damage scale, which can be easily changed. Therefore, multiaxial fatigue life estimates can be obtained using the uniaxial S-N curves, in pure shear or pure axial loading conditions. One main requirement to a multiaxial model is to capture the fatigue damage under uniaxial loading conditions, many multiaxial criteria fail in this subject. To scrutinize this subject and others ones, several multiaxial criteria were selected from Chapter 2 to be analysed here, the objective is to evaluate the performance of the SSF constant approach in the 42CrMo4 material. Excepting the Sines, and the McDiarmid models, all the selected criteria can be considered as an equivalent stress, because their SSF is defined based in the ratio between shear and axial fatigue limits.

Table 4.2 shows the SSF constants for each selected criteria. The fatigue limits in tension-compression and pure shear (torsion-torsion) were obtained from the literature [8, 153]. In these criteria the SSF factor is defined in the shear domain, i.e. the SSF constant transforms the damage from normal stresses into the shear damage scale.

**Table 4.2:** Stress scale factors for the selected multiaxial fatigue criteria and 42CrMo4 material.

| Model | SSF | $f_{-1}(MPa) = 398$<br>$t_{-1}(MPa) = 260$<br>$\sigma_u(MPa) = 1025$ |
|---|---|---|
| von Mises | $\frac{1}{\sqrt{3}}$ | 0.577 |
| Crossland | $3\frac{t_{-1}}{f_{-1}} - \sqrt{3}$ | 0.228 |
| Sines | $\sqrt{3}\frac{f_{-1}}{\sigma_u}$ | 0.673 |
| Matake | $2\frac{t_{-1}}{f_{-1}} - 1$ | 0.307 |
| McDiarmid | $\frac{\tau_{A,B}}{2\cdot\sigma_u}$ | 0.127 |
| Dang Van | $3\left(\frac{\tau_{-1}}{f_{-1}} - \frac{1}{2}\right)$ | 0.46 |
| Papadopoulos | $3\frac{t_{-1}}{f_{-1}} - \sqrt{3}$ | 0.228 |
| Carpinteri-Spagnoli | $\frac{\tau_{af,-1}}{\sigma_{af,-1}}$ | 0.653 |

Results show that the Crossland and the Papadopoulos criteria have the same SSF, also the maximum SSF value was obtained in the Sines and Carpinteri & Spagnoli criteria, this means that, these two models give greater importance to the normal stress contribution to the overall damage than the other ones. In contrast, the Crossland, Papadopoulos and McDiarmid criteria have the lower SSF values, indicating that these models somehow give

low importance to the normal stress contribution to the overall damage process. The Dang Van criterion has a SSF in the middle range.

All SSF values are less than 1, being in concordance with the static results, where for the same damage result (material yield), the required shear stress is lower than the axial one. Another interesting observation is that, in the the Sines and Carpinteri & Spagnoli criteria, the obtained SSF constant is greater than the one found in the von Mises equivalent stress.

### 4.5.2 S-N results

Figure 4.12 shows the 42CrMo4 fatigue life results for the loading Cases 1 and 2, i.e the uniaxial loading cases (normal and shear). In order to analyse and compute the fatigue data, a trend-line approach was adopted to characterize the multiaxial and multiaxial stress components inherent to each loading case; the uniaxial shear trend line was depicted in the graphs as dashed lines. Despite the normal and shear fatigue stresses have different damage mechanisms, the uniaxial loading cases (normal and shear) can be directly compared. However, in biaxial loading conditions, in which the fatigue loading has two components (normal and shear stresses), the relation to the reference curve, i.e. uniaxial shear trend line, is not direct. In these loading cases that relation is entirely different from the one verified between Cases 1 and 2, please see Figure 4.12.

Fatigue data of these two loading cases are represented in the same graph, but it is known that the stress nature in both cases are quite different. With this in mind, Figure 4.12 depicts a fatigue failure condition for tensile-compression and pure shear loading conditions.

Observing Figure 4.12, one can conclude that different stress amplitudes in normal and shear loading conditions can lead to the same fatigue life-time. Thus, it is possible to achieve the same fatigue life-time under different stress natures, i.e. normal and shear, so they are in some way equivalent because the final result is the same (same number of cycles at failure). Determining that relation between stresses by establishing a stress scale factor to transform normal stress nature to shear one or vice versa allows to use a unique uni axial S-N curve to estimate multiaxial fatigue live.

Figures 4.13 to 4.15 show the fatigue data results for loading Cases 3, 4 and 5, respectively. In each loading case the biaxial loading is represented through two trend lines, one representing the normal stress component and the other the shear stress. In addition, it is considered the pure shear trend line, loading Case 2, as the reference case. In this study, the pure shear case (pure shear trend line) is considered as damage reference in order to quantify the stress scale factor between normal and shear stresses and also to perform fatigue life estimates, i.e. the equivalent damage parameter is the pure shear trend line argument.

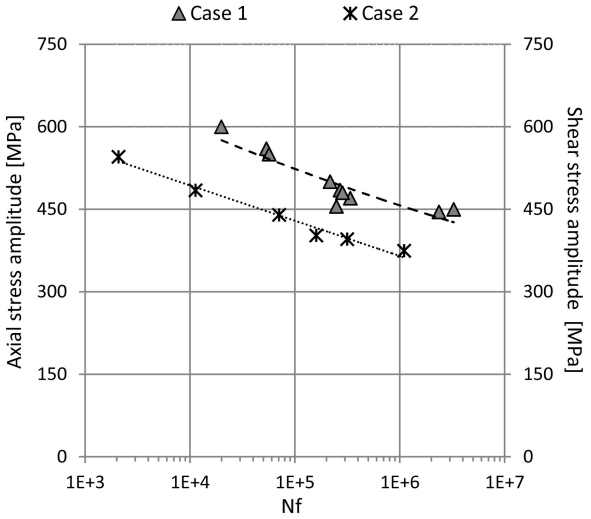


**Figure 4.12:** S-N results (42CrMo4) for Case 1 and Case 2.

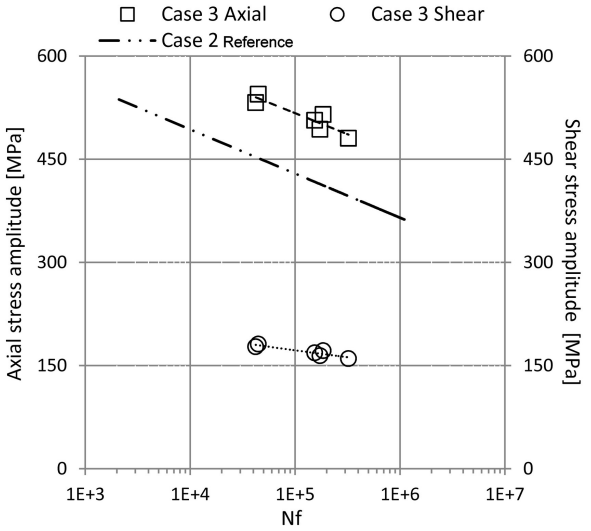


**Figure 4.13:** S-N results (42CrMo4) for loading Case 3.

From the plotted results in Figures 4.13 to 4.15, it can be seen that the shear stress amplitudes in each biaxial loading are clearly insufficient to create a fatigue failure because the trend lines of the shear component in Cases 3, 4 and 5 are clearly below the reference S-N curve, Case 2. Therefore, the missing damage contribution is carried out through the normal stress component. Also, the trend lines of the normal stress components in Cases 3 and 4, are above the Case, the reference S-N, thus using the same reasoning used for the shear components, the fatigue life estimates based only in the axial components, without any damage scale, will lead to fatigue life estimates shorter than the experimental results.

In Case 5, the opposite is observed, the axial trend line of the biaxial loading is below the reference case. In Cases 1 to 5, the amplitude of the axial stress component decreases, and the shear stress component increases, with the SAR increase, this stress amplitude relation

inherent to each loading case can be easily represented through the stress amplitude ratio variation.

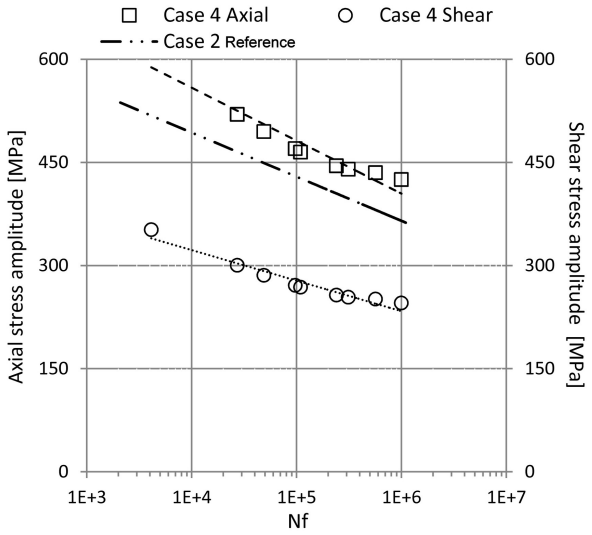


**Figure 4.14:** Loading Case 4, S-N experimental results (42CrMo4).

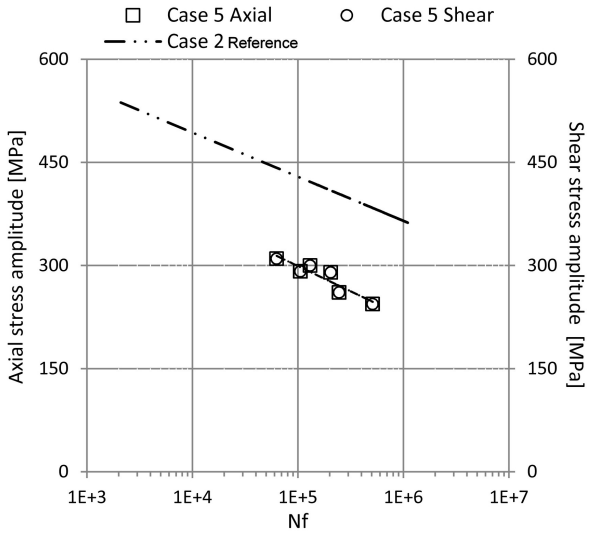


**Figure 4.15:** Loading Case 5, S-N experimental results (42CrMo4).

Table 4.3 shows the trend line equations of each multiaxial stress components (normal and shear) obtained from experiments for each loading case considered here and inherent fatigue life. For each loading case, it is correlated the normal and shear stress amplitudes with the experimental fatigue data by determining two trend lines per each multiaxial loading case. The trend lines have a power-law format, which typically fits well the material fatigue behaviour, with acceptable $R^2$.

**Table 4.3:** Axial and shear fatigue trend lines from S-N results for each loading case.

| Case | $\lambda = \frac{\tau}{\sigma}$ | Trend line | $R^2$ |
|---|---|---|---|
| 1 | 0 | $\sigma_a = 1034.4(N_f)^{-0.059}$<br>$\tau_a = 0$ | 0.83 |
| 2 | $\infty$ | $\sigma_a = 0$<br>$\tau_a = 864.78(N_f)^{-0.061}$ | 0.99 |
| 3 | 0.33 | $\sigma_a = 938.81(N_f)^{-0.052}$<br>$\tau_a = 312.94(N_f)^{-0.052}$ | 0.85 |
| 4 | 0.58 | $\sigma_a = 1025.7(N_f)^{-0.066}$<br>$\tau_a = 592.3(N_f)^{-0.066}$ | 0.96 |
| 5 | 1 | $\sigma_a = 1132.5(N_f)^{-0.116}$<br>$\tau_a = 1132.5(N_f)^{-0.116}$ | 0.86 |

### 4.5.3 Experimental stress scale factor (SSF)

In order to determine the experimental stress factor, it was used the S-N trend lines presented in Table 4.3. The results achieved for the selected proportional loading cases are shown in Tables 4.4 to 4.7. In these tables, the first column is filled with a specific fatigue life-time range, from 1E3 to 1E7, equally spaced in order to estimate the necessary stress amplitudes from loading Cases 1 to 5, through the use of the trend lines inherent to each case. In the second column, it was determined the pure shear amplitude for the selected fatigue life range; on the third and fourth column is computed the shear and axial stress amplitude from the multiaxial loading. In the fifth column, it is calculated the shear stress increment necessary to be added to the shear stress amplitude to cause fatigue failure, which will be related with the axial stress amplitude through the SSF value defined on the last column.

**Table 4.4:** Case 1, values in [MPa].

| $N_f$ | $\overline{AC}$ Pure Shear Amplitude | $\overline{AB}$ Shear Amplitude | $\overline{AD}$ Normal Amplitude | $\overline{BC}$ Shear Increment | $ssf = \frac{\tau}{\sigma}$ |
|---|---|---|---|---|---|
| 1.00E+03 | 567 | 0 | 688 | 0 | 0.82 |
| 1.00E+04 | 493 | 0 | 601 | 0 | 0.82 |
| 1.00E+05 | 428 | 0 | 524 | 0 | 0.82 |
| 1.00E+06 | 372 | 0 | 458 | 0 | 0.81 |
| 1.00E+07 | 324 | 0 | 400 | 0 | 0.81 |

**Table 4.5:** Case 3, values in [MPa].

| $N_f$ | $\overline{AC}$ Pure Shear Amplitude | $\overline{AB}$ Shear Amplitude | $\overline{AD}$ Normal Amplitude | $\overline{BC}$ Shear Increment | $ssf = \frac{\overline{BC}}{\overline{AD}}$ |
|---|---|---|---|---|---|
| 1.00E+03 | 567 | 219 | 656 | 349 | 0.53 |
| 1.00E+04 | 493 | 194 | 582 | 299 | 0.51 |
| 1.00E+05 | 428 | 172 | 516 | 256 | 0.5 |
| 1.00E+06 | 372 | 153 | 458 | 220 | 0.48 |
| 1.00E+07 | 324 | 135 | 406 | 188 | 0.46 |

**Table 4.6:** Case 4, values in [MPa].

| $N_f$ | $\overline{AC}$ Pure Shear Amplitude | $\overline{AB}$ Shear Amplitude | $\overline{AD}$ Axial Amplitude | $\overline{BC}$ Shear Increment | $ssf = \frac{\overline{BC}}{\overline{AD}}$ |
|---|---|---|---|---|---|
| 1.00E+04 | 493 | 323 | 558 | 171 | 0.31 |
| 1.00E+05 | 428 | 277 | 480 | 151 | 0.32 |
| 1.00E+06 | 372 | 238 | 412 | 134 | 0.33 |
| 1.00E+07 | 324 | 204 | 354 | 119 | 0.34 |

**Table 4.7:** Case 5, values in [MPa].

| $N_f$ | $\overline{AC}$ Pure Shear Amplitude | $\overline{AB}$ Shear Amplitude | $\overline{AD}$ Axial Amplitude | $\overline{BC}$ Shear Increment | $ssf = \frac{\overline{BC}}{\overline{AD}}$ |
|---|---|---|---|---|---|
| 1.00E+03 | 567 | 508 | 508 | 59 | 0.12 |
| 1.00E+04 | 493 | 389 | 389 | 104 | 0.27 |
| 1.00E+05 | 428 | 298 | 298 | 131 | 0.44 |
| 1.00E+06 | 372 | 228 | 228 | 144 | 0.63 |
| 1.00E+07 | 324 | 175 | 175 | 149 | 0.85 |

Figure 4.16 depicts for each loading case, the normal stress amplitude versus its shear stress equivalence, here it is represented the normal stress amplitude in the shear stress space accordingly to the methodology previously discussed in this chapter. Considering the results for loading Cases 1 and 3, the curve slopes for both cases are similar, which is acceptable because the amplitudes of the normal loading components are also very alike in these two cases. Moreover, the shear stress amplitude on Case 3 is much smaller than the normal one, which indicates a axial damage predominance in this loading path as seen in the loading Case 1.

In loading Case 4, the slope of the depicted data is much less steep than the one found in Cases 1 and 3, as a result, the normal stress represented in the shear stress space by an equivalent shear stress has a stress range lower than the ones observed in the Cases 1 and 3, indicating a shear stress dominance in the fatigue damage process.

In Case 5, the normal stress reduction to the shear stress space has a completely different behaviour, i.e. with the stress level increment, the normal stress increment in the shear stress space decreases, which is behaviour in opposition to the one verified in the other cases. The stress amplitude ratio is maintained equal for all stress levels, thus in loading Case 5, the shear stress component is much bigger than the normal one, where the shear damage contribution to the overall damage is greater, in this sense the normal stress contribution to the overall damage process strongly decreases with the stress level decrease. From here, it can be concluded that the normal stress reduction to shear stress space is strongly dependent on the loading path stress amplitude ratio.

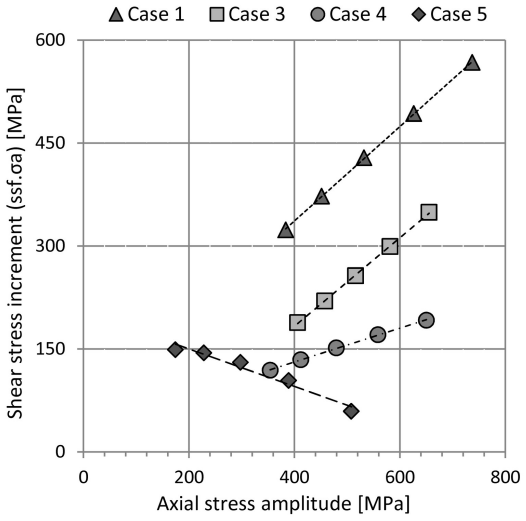


**Figure 4.16:** Normal stress reduction to the shear stress space for each loading case considered here and for the 42CrMo4 material.

Figure 4.17 shows the SSF parameter evolution for each loading case, this parameter is obtained by dividing the shear stress increment (required to cause fatigue failure) by the normal stress amplitude. In loading Cases 1 and 4, the SSF parameter decreases with a

SSF rate of change relatively similar. In Case 5, the SSF rate of change is much more pronounced but has always the same sign.

The Case 3 mapping has a opposite behaviour regarding the other cases, i.e. the SSF rate of change changed its sign; as the normal stress amplitude increases the corresponding SSF parameter also increases. For loading Cases 4 and 5, the SSF value increases as the normal stress amplitude decreases, which leads to conclude that the shear and normal stress amplitudes in HCF have different damage mechanisms comparatively to the ones verified in LCF, the same conclusion can be made in respect to loading Case 3. These results corroborates the premise in which the SSF damage scale cannot be a constant value.

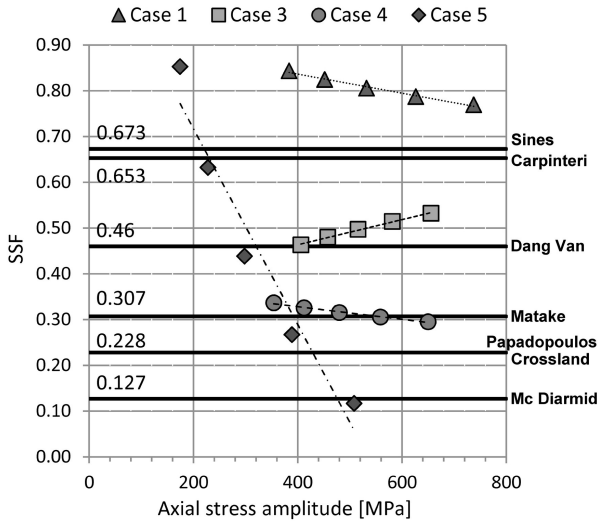


**Figure 4.17:** Experimental SSF for each loading case vs SSF from the state-of-the art criteria (horizontal lines).

Based on experimental results, it can be concluded that the concept of having a constant SSF for all kind of normal stress amplitudes levels and stress amplitude ratios do not reflect the physical damage behaviour that can be found in materials subjected to cyclic loadings. As one can see in Figure 4.17, the constant values determined for the selected multiaxial fatigue models are independent of the axial stress amplitude and insensitive to the loading path. Eventually, some models may have good results in some cases, which is the example of the Matake model, where in loading Case 4, the Matake's SSF constant parameter is very close to the SSF experimental results, however, the use of a constant SSF is not advised. In the McDiarmid criterion, the constant SSF is the lower one, as a consequence the inherit fatigue life estimates are very non-conservative because it is computed shorter equivalent stresses.

Considering the experimental SSF values of loading Case 5, which crosses all constant SSF values of the selected criteria, some models could be conservative in HCF and non conservative in LCF. Regarding the pure tension case, all models are non conservative

because their SSF constants are lower than the experimental SSF range. One may argue that these models were defined to establish fatigue strength for infinite life, because their constant SSF is determined based on the uniaxial fatigue limits. Moreover, one may also argue that if the S-N curves are well determined, thus the ratio of uniaxial stress amplitudes remains the same in the finite and infinite fatigue life regions. However, observing Figure 4.17 it can be easily detected that the SSF parameter is not constant on infinite fatigue life. The normal stress amplitude decrease will increase the fatigue life; with that in mind, the loading Cases 5, 1 and 4 have their SSF increasing as the normal stress amplitude decreases. Loading Case 3, has the opposite behaviour, the SSF is decreasing as the load decreases. This results lead to conclude that even in the infinite life region the SSF is not constant for all kinds of loading paths. Due to the material asymptotic fatigue life behaviour in the infinite region (more than $10^6$ cycles), a small variation of the equivalent stress amplitude may result in an unacceptable fatigue life estimate, thus a SSF function is essential to deal with loading path effects on the infinite life region.

The increase of fatigue life in Cases 1, 4 and 5, in which the normal stress contribution to the overall damage decreases from Cases 1 to 5, is linked to the SSF increase, because the shear stress amplitude on each case (Cases 1, 4, and 5) have trend lines with a slope different from the one verified in Case 2, i.e. the reference damage case. This slope variation is representative of the combined effect of the normal and shear stresses in the fatigue damage mechanism. If this effect does not exist it would be expected that these slopes would be equal to the slope of the S-N reference, and then the SSF would be independent from the stress amplitude level, which is not true.

This fact can be seen in Figures 4.13 to 4.15, where normal and shear trend lines are not parallel to the reference case, however, this difference also varies case to case. In loading Case 5, the trend line tends to approach the reference case at LCF region and tends to move away from it on the HCF region. For loading Cases 1, 3 and 4 occurs the opposite, the trend lines tend to converge with the reference case in the HCF region and diverge in the LCF region.

### 4.5.4 Stress scale factor damage function

Regarding the proportional loading cases considered in this study, the SSF experimental values were determined. However, it is not feasible to determine these values for all possible stress amplitude ratios and stress levels through experimental tests. The selected loading cases were chosen in order to be representative of the material fatigue strength under specific stress amplitude ratios in order to performing a SSF mapping. Table 4.8 shows the data collected to perform the SSF mapping by regression. In the first column is registered the normal stress amplitude for each case, at second column it is displayed the arc tangent of the stress amplitude ratio, and lastly in the third column, it is shown the SSF results for each loading case. Due to the stress amplitude ratio definition an infinite

value is obtained for the uniaxial tension-compression case. In order to avoid undefined values for the stress amplitude ratios and consequent information loss, it was performed a variable transformation using the arctangent function. This transformation does not affect the physical meaning of the stress amplitude ratio and helps in the regression procedures.

**Table 4.8:** Experimental data used in the regression methodology.

| $\sigma_a$ | $\lambda = \tan^{-1}(\tau/\sigma)$ | $ssf$ |
|---|---|---|
| 688 | 0 | 0.82 |
| 601 | 0 | 0.82 |
| 524 | 0 | 0.82 |
| 458 | 0 | 0.81 |
| 400 | 0 | 0.81 |
| 656 | 0.32 | 0.53 |
| 582 | 0.32 | 0.51 |
| 516 | 0.32 | 0.5 |
| 458 | 0.32 | 0.48 |
| 406 | 0.32 | 0.46 |
| 650 | 0.52 | 0.3 |
| 558 | 0.52 | 0.31 |
| 480 | 0.52 | 0.32 |
| 412 | 0.52 | 0.33 |
| 354 | 0.52 | 0.34 |
| 508 | 0.79 | 0.12 |
| 389 | 0.79 | 0.27 |
| 298 | 0.79 | 0.44 |
| 228 | 0.79 | 0.63 |
| 175 | 0.79 | 0.85 |
| 0 | 1.57 | 0.38 |
| 0 | 1.57 | 0.39 |
| 0 | 1.57 | 0.4 |
| 0 | 1.57 | 0.41 |
| 0 | 1.57 | 0.42 |

The regression result i.e. the SSF damage map, is shown in Eq. 4.14, from which it is possible to estimate the SSF values for the 42CrMo4 material under all stress amplitude ratios and allowed stress levels.

$$ssf(\sigma_a, \lambda) = a + b \cdot \sigma_a + c \cdot {\sigma_a}^2 + d \cdot {\sigma_a}^3 + f \cdot \lambda^2 + g \cdot \lambda^3 + h \cdot \lambda^4 + i \cdot \lambda^5 \tag{4.14}$$

This equation is a $5^{th}$ degree polynomials with two arguments. The goodness of the fit that lead to the $5^{th}$ polynomial is $R^2$ =0.98, which is acceptable since $R^2$ =1 is obtained when a regression fits utterly the experimental data. The experimental constants of Eq. 4.14 for the 42CrMo4 material are the following:

a=2.69; b=−9.90E−03; c=1.69E−05; d=−9.52E−09; f=−5.99; g=11.72; h=−8.04; i=1.63

The variable $\lambda$ from Eq. 4.14 is obtained as follows in Eq. 4.15.

$$\lambda = \tan^{-1}\left(\frac{\tau}{\sigma}\right) \tag{4.15}$$

Figure 4.18 depicts the SSF function plotting, where the SSF variation with the stress amplitude ratio and the normal stress amplitude is given by Eq. 4.14.

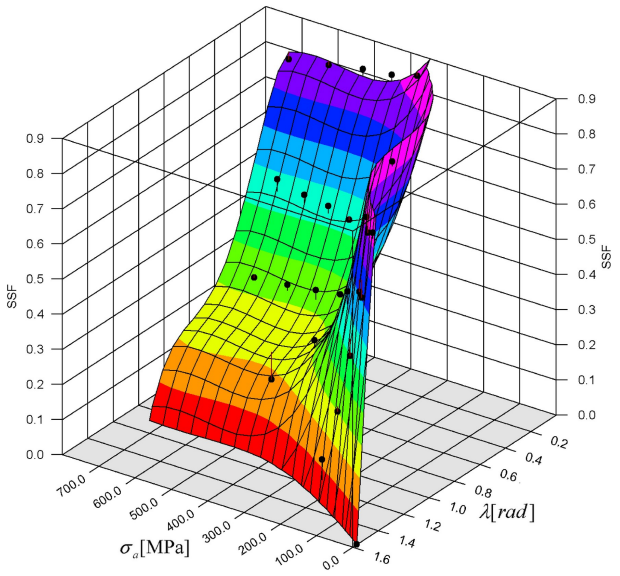


**Figure 4.18:** SSF surface regression (42CrMo4).

### 4.5.5 SSF under non-proportional loading conditions

Essentially, there are two kinds of loading paths, the proportional and non-proportional ones. An attribute commonly used to identify the loading type is the principal directions variation; which can be somewhat abstract and difficult to be interpreted. However, the stress amplitude ratio can be a successful parameter to easily identify the loading type (proportional and non-proportional) and also to distinguish the loading paths damage level between proportional ones (for example, loading Cases 3 to 5 in Figure 4.11).

As an example, the loading Cases 3, 4 and 5 are proportional loadings with steady principal directions, which is a characteristic of proportional loadings. In these loading

cases, the stress amplitude ratios are also constant during the loading period, being a straightforward procedure to mathematically distinguish between proportional and non-proportional loadings. Moreover, the stress amplitude ratio is different between proportional cases, being this variable very useful to differentiate proportional loading paths. The SSF concept is also applicable to non-proportional loading cases in which the stress amplitude ratio varies during the loading period. The SSF function allows to determine any kind of combinations between stress amplitude ratios and stress amplitude levels.

Figure 4.19 shows the variation of the SSF input variables under the selected non-proportional loading case, Case 6. For each time instant, the SSF is determined based in the instantaneous normal and shear stresses. Thus, the time evolution of the non-proportional stress components are computed in the SSF function as if they were proportional, which yields a instantaneous time variation for the SSF value.

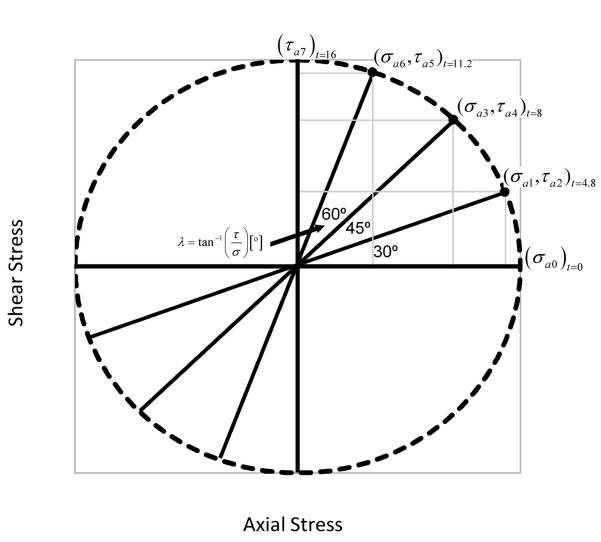


**Figure 4.19:** SSF input variable variation under non-proportional loading conditions, Case 6 (42CrMo4).

Figure 4.20 shows the stress amplitude ratio and the instantaneous SSF variation along the selected non-proportional loading period, Case 6. This time variation can be easily connected to the concept of the principal directions variation usually used to identify non-proportional loadings.

The SAR concept leads to improve the loading path characterization, mathematically it is possible to determine, in an easy way, the load nature and it fatigue damage regimen. Also, the SSF function has as argument the stress amplitude ratio; this turns the SSF sensitive to the loading path under proportional and non-proportional loading conditions. Figure 4.20 shows the SSF variation along the period time for loading Case 6, which is in conformity with the stress amplitude ratio variation discussed above. The multiaxial models selected in this study considers that the SSF parameter is always constant and

less than 1, also in Figure 4.20 the instantaneous and maximum values of the SSF under a non-proportional loading case, Case 6, are also less than 1. One of these SSF maximum values is related to the maximum SSF equivalent stress achieved within the loading period.

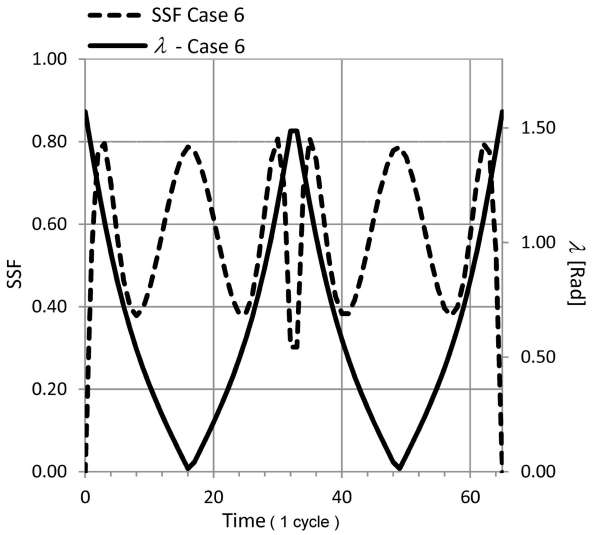


**Figure 4.20:** SSF and $\lambda = \tan^{-1}\left(\frac{\tau}{\sigma}\right)$ variation during the non-proportional loading period (42CrMo4).

Figure 4.21 shows the normal stress transformation to the shear stress space under non-proportional loading conditions with the following multiaxial stress components amplitudes: 510 [MPa] as normal stress, and 294 [MPa] as shear stress, the SSF equivalent stress computed was 434 [MPa].

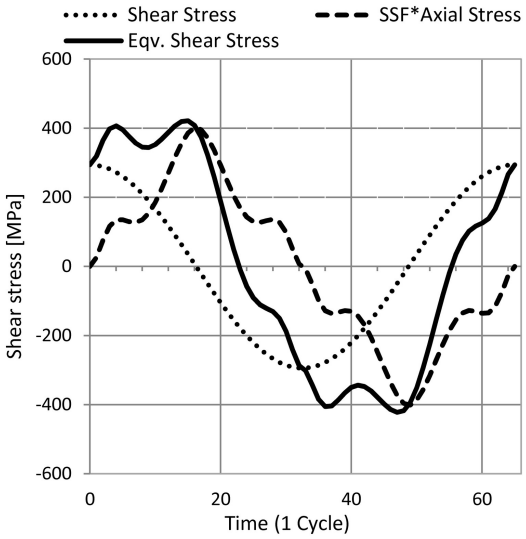


**Figure 4.21:** Corrected normal stress vs shear stress and equivalent shear stress (42CrMo4).

As one can see, the normal stress amplitude is modified during the loading period. The SSF function is a kind of experimental weight function, which corrects the instantaneous

normal stress amplitude according to the instantaneous and directional damage inherent to the loading path nature, thus the SSF equivalent stress time evolution ceases to be a perfect sinusoid (as verified in proportional loadings) to take an irregular cyclic shape. The SSF equivalent stress is given trough the maximum value found within the loading period, which is obtained from the summation between the instantaneous shear stress and the corrected instantaneous normal stress.

In the SSF equivalent stress time evolution depicted in Figure 4.20, the maximum value occurs through the instantaneous combination of both multiaxial stress components (normal and shear); in this way, the SSF equivalent stress has a multiaxial nature under non-proportional loading conditions, because the the SSF function is sensitive to the loading path type through the SAR variable.

The fatigue life results for Cases 1, 3, 4, and 5 using the SSF equivalent stress are shown in Figure 4.22, for each loading case the equivalent stress estimates are obtained based on the trend line of the uniaxial shear fatigue data (uniaxial S-N curve) i.e. they are based on the Case 2 trend line. Regarding the loading Cases 1, 3, 4 and 5 the results are good as expected, because the SSF damage map was determined based on the experimental values of these loading paths. The scatter found in this correlation is explained through the use of the trend line approach to compute fatigue life estimates in each loading path, and due to the residuals of the stress scale factor regression. In loading Case 6, the SSF values found within the loading period are completely independent from the data used to determine the SSF function, i.e. the experimental S-N results for loading Case 6 were not used in the SSF function assessment. Moreover, the fatigue life estimates of the SSF equivalent stress for the loading Case 6 yields a reasonable correlation with the experimental data, leading to conclude that the SSF equivalent stress is sensitive to proportional and non-proportional loading conditions. Another feature that should be underlined is the possibility to use the SSF equivalent stress to estimate uniaxial fatigue lives, which is a basic requirement in multiaxial fatigue criteria.

The correlation between fatigue life estimates and the experimental fatigue data was performed using the multiaxial shear trend line, Case2. Moreover, a fatigue life factor of 3 was considered to characterize the equivalent stress goodness, please see Figure 4.23. Most of the correlation results are within the fatigue life boundaries; only 1 point from Case 1 is outside of the boundary lines. The majority of the proportional results are on the non-conservative side, above the middle reference line. This result indicates that the SSF equivalence stress is smaller than it should be under proportional loading conditions. On the other hand, for loading Case 6, the results are near the middle line, despite the probabilistic effect always present in experimental fatigue data [154]; this is a positive result regarding non-proportional fatigue life estimates using the SSF equivalent stress. This means that the SSF function is sensitive to the normal stress contribution

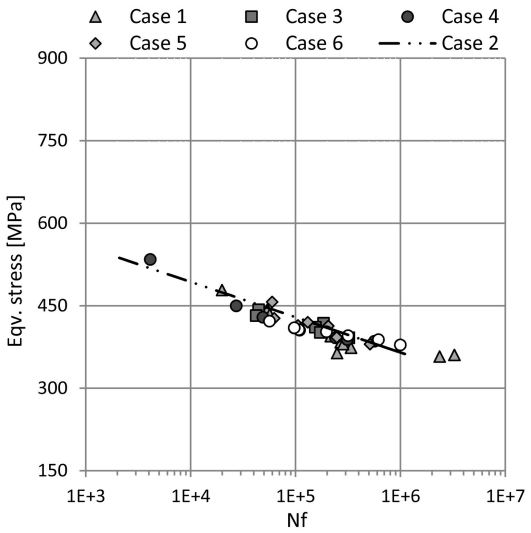


**Figure 4.22:** SSF equivalent shear stress for each loading path and stress level (42CrMo4).

to the overall damage under non-proportional loadings. However, it is necessary additional studies to apply the equivalent stress to other non-proportional loading paths in order to analyse in full the SSF equivalent stress sensitivity to non-proportional damage.

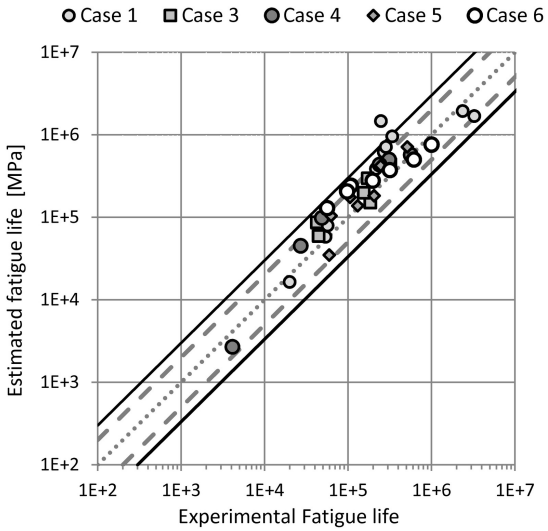


**Figure 4.23:** Estimated vs experimental fatigue life (42CrMo4).

## 4.6 SSF estimates and fatigue data

### 4.6.1 42CrMo4 fatigue life evaluation

In order to evaluate the performance of the SSF criterion it was correlated its estimates with experimental data and with the fatigue life estimates from other multiaxial fatigue criteria. In this correlation, it was considered the fatigue data of the hight strength

steel 42CrMo4 in respect to the loading paths shown in Figure 4.24. The fatigue data of these loading paths was already presented in Table 3.3. Only in the SSF criterion it was used a non-proportional factor correction. In the other multiaxial fatigue criteria, it was used their original formulations to estimate fatigue lives under non-proportional loading conditions. Figure 4.25 a) shows the von Mises equivalent stress correlation with experimental data for the loading cases presented in Figure 4.24, it can be seen a weak correlation as a result of a von Mises equivalent stress too high. These results supports the idea in which an equivalent stress based on stress space norms, such as von Mises, yields equivalent stresses higher than it should be.

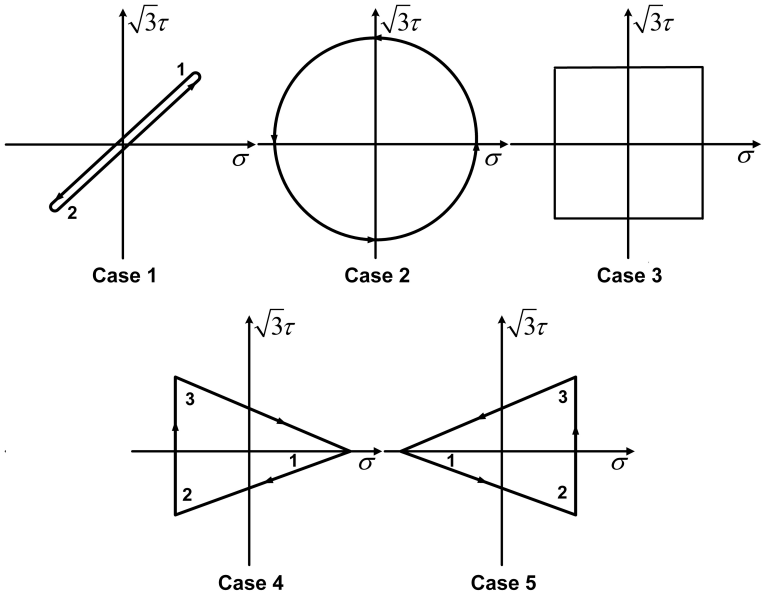


**Figure 4.24:** Non-proportional loading paths.

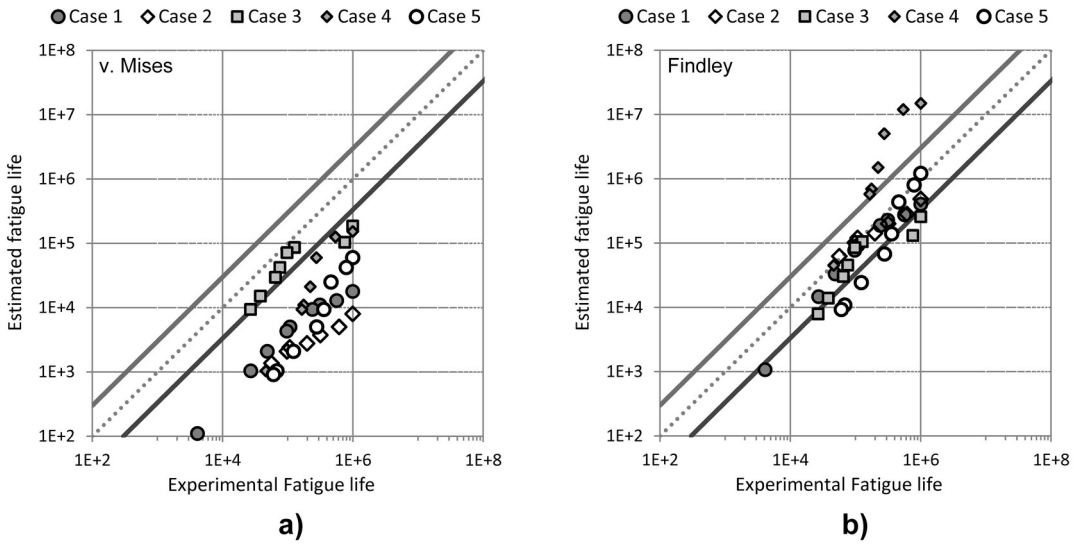


**Figure 4.25:** Fatigue life correlation a) von Mises criterion b) Findley criterion.

Figure 4.25 b) shows the fatigue life correlation for the Findley's criterion, which has very acceptable results; only the results of Case 4 are out of the fatigue life boundaries. However, the correlation between experiments and estimates remains not centred, being the Findley's parameter lightly higher than it should be. Figure 4.26 a) shows the fatigue life correlation for the Crossland criterion, as one can see the fatigue life correlation is very weak.

The Crossland's parameter tends to be smaller than it should be, leading to non-conservative fatigue life estimates. Only the results of the proportional loading case, Case 1, are inside of the fatigue life boundaries (scatter bands). Figure 4.26 b) shows the results for the Papadopoulos criterion; this criterion is the only one with an undefined trend on the fatigue life estimates. In some loading cases, the damage parameter is too high but in other ones is too low.

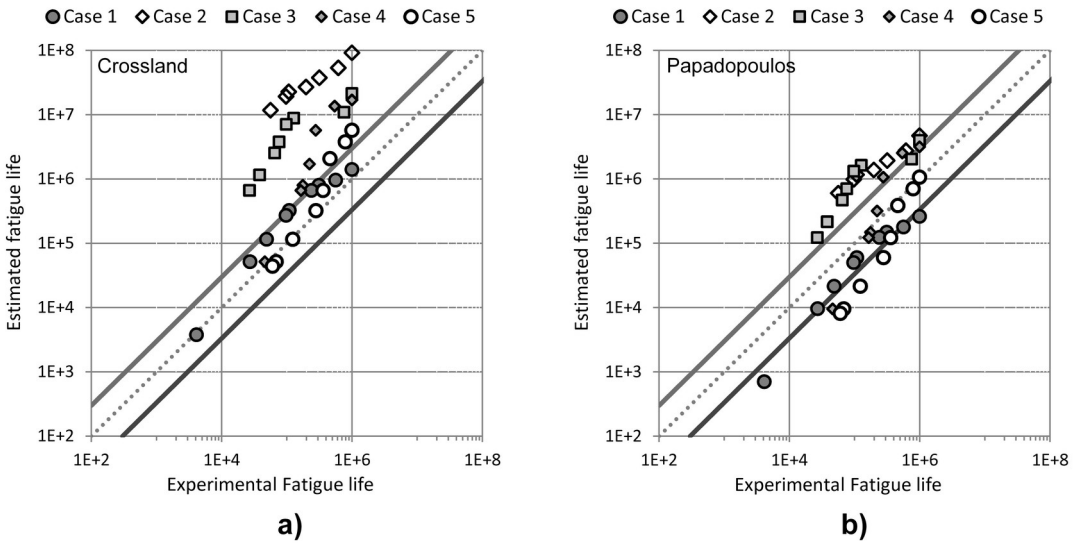


**Figure 4.26:** Fatigue life correlation a) Crossland's criterion b) Papadopoulos's criterion.

Figure 4.27 presents the results for the SSF criterion. Figure 4.27 a) shows the SSF fatigue life estimates without non-proportional correction (without using the Y parameter), in this correlation only Case 3 is out of the fatigue life boundaries. From here it can be concluded that the SSF criterion without an additional non-proportional correction can deal fairly well with non-proportionality.

In Figure 4.27 b) the SSF fatigue life correlation, with non-proportionality correction, is presented. It can be concluded from teh results depicted in Figure 4.27 that the overall fatigue life correlation was improved by using the Y parameter.

From the fatigue life correlation of the state-of-the-art fatigue life criteria, it can be concluded that a fixed damage scale, i.e. a damage scale independent from the loading path, stress level, and material, provides weak fatigue life correlations. In some cases, a

constant SSF value may eventually match the damage scale associated with the material and loading type, which was the case of the Findley criterion; however changing the loading conditions will lead to inconsistent results.

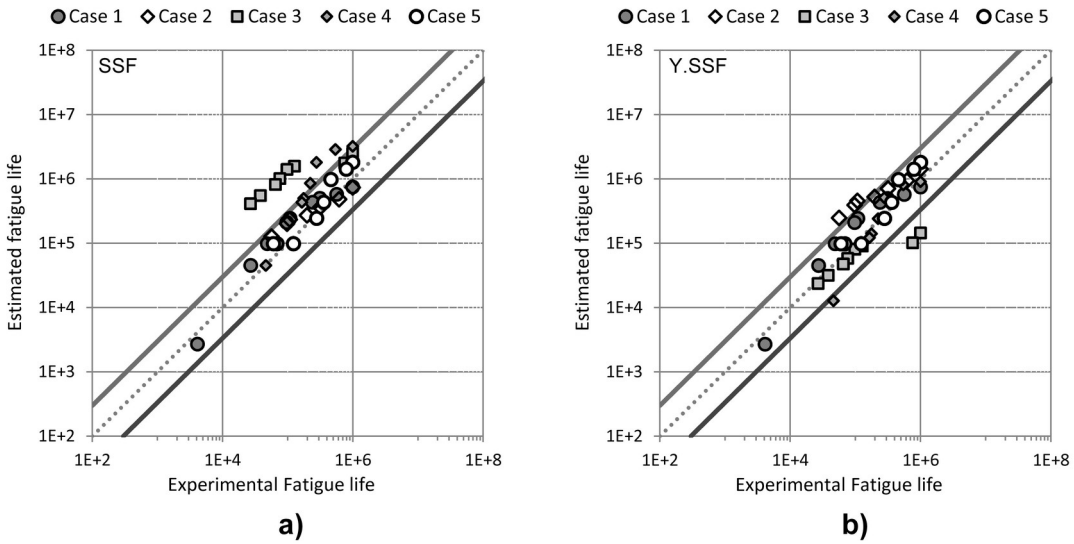


**Figure 4.27:** Fatigue life correlation a) SSF criterion b) SSF criterion updated with the Y parameter.

### 4.6.2 Ck45 & C40 fatigue life evaluation

In this section, it is analysed the SSF, and the MCE criteria regarding their (please see Chapter 2 for MCE deep detail) performance to predict fatigue lives for the Ck45, and the C40 materials [155]. The chemical composition, monotonic and cyclic properties for these two materials, the Ck45 and the C40, can be found in Table.(s) A.1 and A.2.

The sample geometry and its dimensions for the selected materials are shown in Fig.(s) 4.28, and 4.29. The loading paths of these experiments are depicted in Figure 4.30.

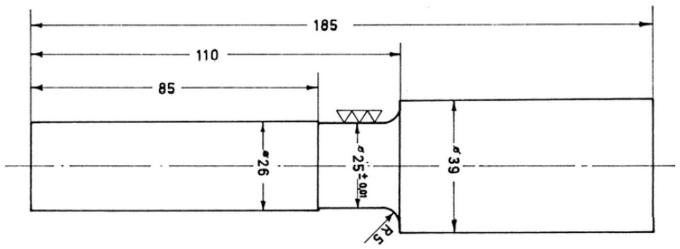


**Figure 4.28:** Ck45 specimen test used in experiments of Table 4.9, [155].

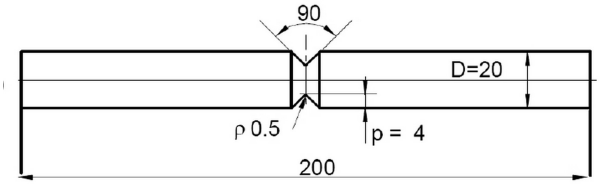


**Figure 4.29:** C40 specimen test used in experiments of Table 4.10.

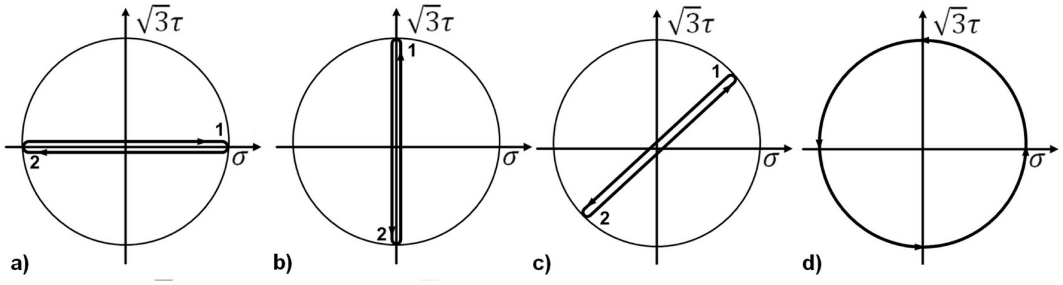


**Figure 4.30:** Loading paths performed in the Ck45 and C40 materials.

The two sets of fatigue data used in this section, were performed by two different research groups. The first set was carried out by Simburger [156] at Fraunhofer Institute for Structural Durability LBF in Darmstadt, Germany, and the second set was performed by Aztori et al. [157] in Berlin, Germany. In both experimental programs were used notched specimens. Simburger tested notched specimens with mild notch under bending/torsion and Aztori et al. tested specimens with a sharp notch under tension/torsion.

The Simburger's specimens were made of Ck45 steel and the Aztori's specimens were made of C40 steel, both steels were quenched and tempered. These fatigue data, have been widely used in the validation of some multiaxial fatigue criteria in literature.

Since both criteria, MCE and SSF, are equivalent shear stresses, it was used here the S-N equations from the uniaxial shear trend lines experientially obtained for each material, in order to estimate fatigue lives. Thus, to correlate the Simburger's experimental work (Ck45 steel) with the estimates of the equivalent stress criteria selected for this section, it was used the pure shear S-N curve obtained using bending/torsion specimens presented in Figure 4.28, whereas in the Atzori correlation, the pure shear S-N curve was obtained using the tension-compression/torsion specimens, please see Figure 4.29.

Here, the idea is to relate the multiaxial fatigue damage, obtained through loading Cases 3 and 4 (Cases c) and d) from Figure 4.30) with the uniaxial reference loading (Case 2 - Case b) from Figure 4.30) under the same geometric and loading conditions. The objective is to have a shear S-N curve that takes into account the notch effect in the fatigue damage process. The fatigue data for the Ck45 and C40 and loading paths depicted in Figure 4.30, is presented in Tables 4.9 and 4.10, respectively.

**Table 4.9:** Fatigue data obtained by Simburger for the Ck45 material [155, 156].

| **Case 1( Pure bending)** | | | **Case 2 (Pure shear)** | | |
|---|---|---|---|---|---|
| **Sigma** | **Shear** | **Nf** | **Sigma** | **Shear** | **Nf** |
| 490 | 0 | 46600 | 0 | 296 | 24900 |
| 490 | 0 | 51100 | 0 | 296 | 34300 |
| 490 | 0 | 54700 | 0 | 296 | 36500 |
| 490 | 0 | 60600 | 0 | 296 | 37700 |
| 490 | 0 | 66600 | 0 | 296 | 42300 |
| 490 | 0 | 71600 | 0 | 296 | 42900 |
| 490 | 0 | 79000 | 0 | 296 | 46500 |
| 490 | 0 | 86200 | 0 | 296 | 54500 |
| 442 | 0 | 95200 | 0 | 255 | 124000 |
| 442 | 0 | 117000 | 0 | 255 | 204000 |
| 442 | 0 | 132000 | 0 | 255 | 239000 |
| 442 | 0 | 136000 | 0 | 255 | 347000 |
| 442 | 0 | 145000 | 0 | 255 | 373000 |
| 442 | 0 | 148000 | 0 | 255 | 430000 |
| 442 | 0 | 161000 | 0 | 255 | 574000 |
| 442 | 0 | 190000 | | | |
| **Case 3 (Comb. in-phase)** | | | **Case 4 (Comb. out-phase)** | | |
| **Sigma** | **Shear** | **Nf** | **Sigma** | **Shear** | **Nf** |
| 442 | 254 | 7600 | 392 | 225 | 13200 |
| 442 | 254 | 11200 | 392 | 225 | 13900 |
| 442 | 254 | 11800 | 392 | 225 | 16000 |
| 442 | 254 | 13200 | 392 | 225 | 16900 |
| 442 | 254 | 16400 | 392 | 225 | 17400 |
| 442 | 254 | 17480 | 392 | 225 | 17800 |
| 442 | 254 | 21800 | 392 | 225 | 20200 |
| 442 | 254 | 25200 | 392 | 225 | 27500 |
| 343 | 197 | 94600 | 343 | 197 | 42700 |
| 343 | 197 | 138000 | 343 | 197 | 48300 |
| 343 | 197 | 144000 | 343 | 197 | 50900 |
| 343 | 197 | 179000 | 343 | 197 | 59800 |
| 343 | 197 | 186000 | 343 | 197 | 66000 |
| 343 | 197 | 204000 | 343 | 197 | 68100 |
| 343 | 197 | 229000 | 343 | 197 | 95700 |
| 343 | 197 | 258000 | 343 | 197 | 98800 |
| 285 | 164 | 926000 | 285 | 164 | 258000 |
| 285 | 164 | 1000000 | 285 | 164 | 271000 |
| 285 | 164 | 1580000 | 285 | 164 | 289000 |
| | | | 285 | 164 | 1080000 |

**Table 4.10:** Fatigue testing results obtained by Atzori et al. for the C40 material with local stresses with SAR=0.59, $K_{ta} = 3.68$ and $K_{tt} = 1.95$.

| **Case 1( Pure bending)** | | | **Case 2 (Pure shear)** | | |
|---|---|---|---|---|---|
| **Sigma** | **Shear** | **Nf** | **Sigma** | **Shear** | **Nf** |
| 1144 | 0 | 25220 | 0 | 474 | 26810 |
| 1144 | 0 | 35200 | 0 | 476 | 41070 |
| 953 | 0 | 48750 | 0 | 415 | 145420 |
| 957 | 0 | 58050 | 0 | 415 | 242230 |
| 762 | 0 | 94220 | 0 | 359 | 211200 |
| 762 | 0 | 100400 | 0 | 359 | 412820 |
| 666 | 0 | 164250 | 0 | 312 | 608770 |
| 666 | 0 | 325140 | 0 | 312 | 2239000 |
| 622 | 0 | 293250 | 0 | 312 | 2453280 |
| 570 | 0 | 566820 | 0 | 271 | 2607400 |
| 570 | 0 | 638520 | 0 | 273 | 2967800 |
| 526 | 0 | 1061360 | 0 | 291 | 5757000 |
| 526 | 0 | 1336200 | | | |
| **Case 3 (Comb. in-phase)** | | | **Case 4 (Comb. out-phase)** | | |
| **Sigma** | **Shear** | **Nf** | **Sigma** | **Shear** | **Nf** |
| 810 | 429 | 12530 | 736 | 390 | 11500 |
| 736 | 390 | 27280 | 662 | 351 | 14600 |
| 589 | 312 | 73040 | 662 | 351 | 18000 |
| 515 | 273 | 155500 | 515 | 273 | 19700 |
| 478 | 254 | 185300 | 589 | 312 | 42150 |
| 662 | 351 | 194000 | 589 | 312 | 47270 |
| 662 | 351 | 229500 | 478 | 254 | 118100 |
| 442 | 234 | 445800 | 515 | 273 | 286350 |
| 478 | 254 | 638200 | 478 | 254 | 699400 |
| 405 | 215 | 840100 | 442 | 234 | 942000 |
| 442 | 234 | 1682550 | 405 | 215 | 1114200 |
| 442 | 234 | 1802200 | 368 | 195 | 1433400 |

#### 4.6.2.1 Non-proportional sensitivity parameter

During a non-proportional loading, several slip plans are loaded with the maximum stress within the non-proportional loading path. Under proportional loading conditions only some of those slip planes are activated, thus the material response is different in each kind of loading path. However, it is possible to relate proportional and non-proportional damages using the Y parameter proposed in Chapter 3 where the relative damage between proportional and non-proportional loadings is taken into account.

Figure 4.31 presents the results for the non-proportional sensitivity parameter for the Ck45 and C40 materials, respectively. As one can see, Figure 4.31 a) shows parallelism between non-proportional and proportional S-N curves for the Ck45 results. However, the S-N curves are not parallel in the C40's results, please see Figure 4.31 b). The Ck45 results are in accordance with the premise adopted in the Y parameter definition, where the Y parameter is independent from the stress level, but in the C40's experimental results it is found a contrary behaviour. One reason that can explain this result is that the C40 results have insufficient number of experimental tests because it was only performed, for each stress level, one or two experiments (the good practices indicates at least 5 experiments for each stress level). Therefore, the trend lines shown in Figure 4.31 b) may be a biased S-N curves. Moreover, the C40 experiments have a higher level of plasticity due to local stress concentrations at notch root, the notch severity in the C40 samples is much higher than the one found in the Ck45. This may be a reason for the non-parallelism between proportional and non-proportional S-N curves found in the C40 material. To overcome this question and obtain the Y non-proportional sensitivity factor for the C40, it was considered here the determination of the Y parameter at $10^6$ cycles, where the stress level variation causes a slight effect on the Y parameter value. Figure 4.31 presents the Y parameter results for Ck45 (Y=1.09) and C40 (Y=1.07), both are higher than one, which suggests that the non-proportional loading causes a greater damage than the proportional ones.

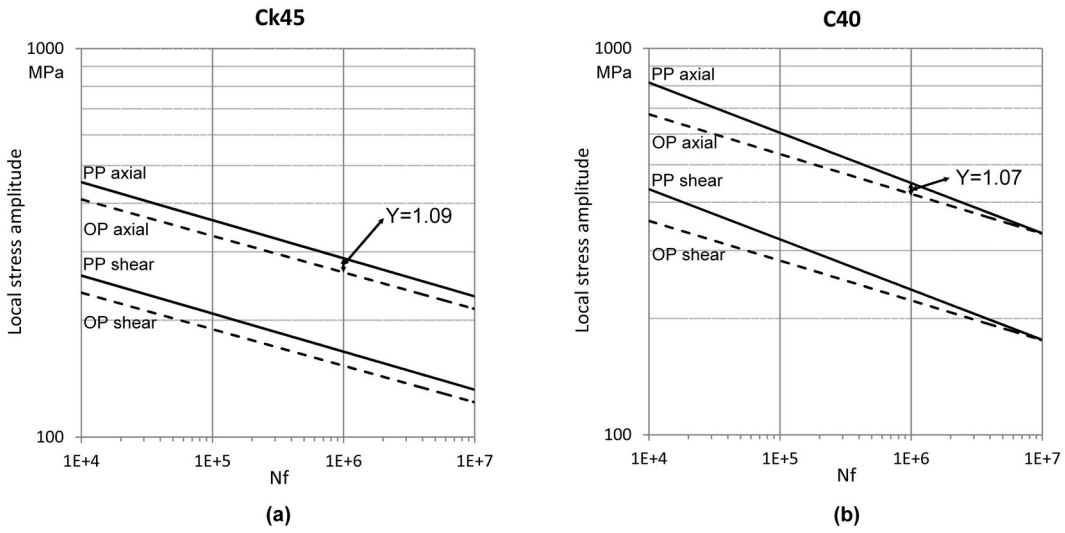


**Figure 4.31:** Y parameter for the: a) Ck45 steel, b) C40 steel.

#### 4.6.2.2 Procedures in fatigue life estimations

The Ck45 fatigue data was gathered from literature with local normal and shear strains measured with gauges glued at notch root, thus the local stresses were obtained directly without the use of any stress concentration factor. Afterwards, the 42CrMo4's SSF

damage map (obtained under tension-compression/torsion) was updated to the Ck45 loading conditions in order to take into account the stress gradient effect in the fatigue damage assessment, please see Eq. 4.13. In the out-of-phase loading case (Case 4), the SSF equivalent stress was corrected with the non-proportional sensitivity parameter, the Y parameter. Regarding the C40 results, the local stresses were computed by using nominal stresses and Kt values. Afterwards, the time evolution of these stresses were used to calculate the SSF equivalent stress, where the 42CrMo4 damage map was corrected for the C40 steel, using the C40's ultimate tensile strength and the 42CrMo4's ultimate tensile strength. Furthermore, the SSF equivalent stress is also corrected with the C40's Y parameter to evaluate the out of phase loading path. The S-N curves (trend lines) used to obtain fatigue life estimates in both materials, are the pure shear S-N curves based in local stresses (nominal transformed into local).

#### 4.6.2.3 Fatigue life estimates

Fig.(s) 4.32 a) and b) presents the S-N results for the Ck45 and C40 materials using the SSF and the MCE equivalent shear stresses, respectively. Scatter bands with appertaining ranges ($T_\sigma = 1 : 1.22$) based in the pure shear S-N curve are represented in the S-N graphs depicted in Figure 4.32. Thus, the upper scatter band considered here, has a survival probability of 10% and the lower one has 90%. In the present author opinion, the probability of these scatter bands to enclose all possible uniaxial shear stress trend lines is very high and it is adequate to these kind of steels (Ck45 and C40).

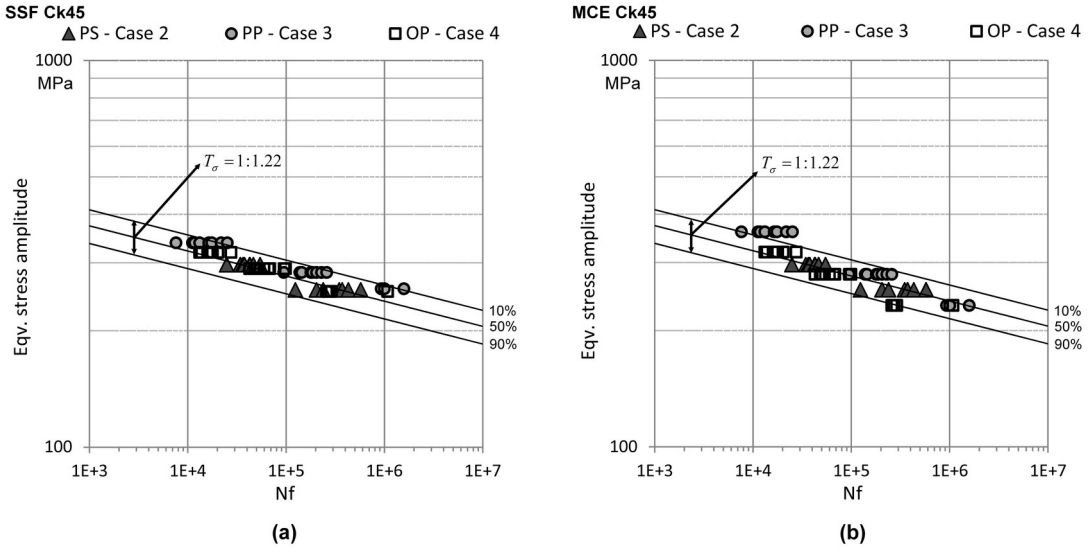


**Figure 4.32:** Ck45's S-N curves using the: a) SSF equivalent stress, b) MCE equivalent stress.

The S-N results obtained for the Ck45 material are best enclosed by the SSF equivalent stress approach, please see Figure 4.32 a), where only two proportional results (PP – loading Case 3) are outside of the upper scatter band. In the MCE approach, the results

of the out-of-phase loading path matches the reference damage curve (Ck45 uniaxial shear trend line), however the proportional results are above of the upper scatter band for high stress levels (low cycle fatigue region) indicating that the MCE equivalent stress is greater than it should be in this region.

Usually, the SSF equivalent stress estimates under non-proportional loadings tends to be near of the upper band, and under proportional loadings tends to match the damage reference curve (S-N pure shear curve), which is contrary to the results obtained in the MCE estimates. Under bending/torsion loading conditions the proportional and non-proportional S-N curves of the SSF equivalent stress are higher than they should be, as expected. This is so, because the SSF damage map is determined based on the axial tension-compression/torsion loading conditions, which has a normal stress gradient much more damaging than the one found in bending/torsion loadings. Thus, in order to account for the stress gradient effect in fatigue life estimates, the 42CrMo4 SSF damage map (SSF function) was multiplied by 0.8 [68].

Figure 4.33 presents the S-N results for the C40 material using the SSF equivalent stress and the MCE criterion; here the scatter band is also based in the same survive probability used in the S-N curves of the Ck45 , please see Figure 4.32. The SSF and MCE results are very similar being mostly within the scatter bands. Regarding the C40 results, there was no need to correct the SSF damage map as seen in the Ck45 because the fatigue tests were made in tension-compression/torsion loading conditions, therefore the only correction made in the SSF criterion it was the SSF damage map update to the C40 material, using the ratio between the C40 and 42CrMo4 ultimate tensile strengths.

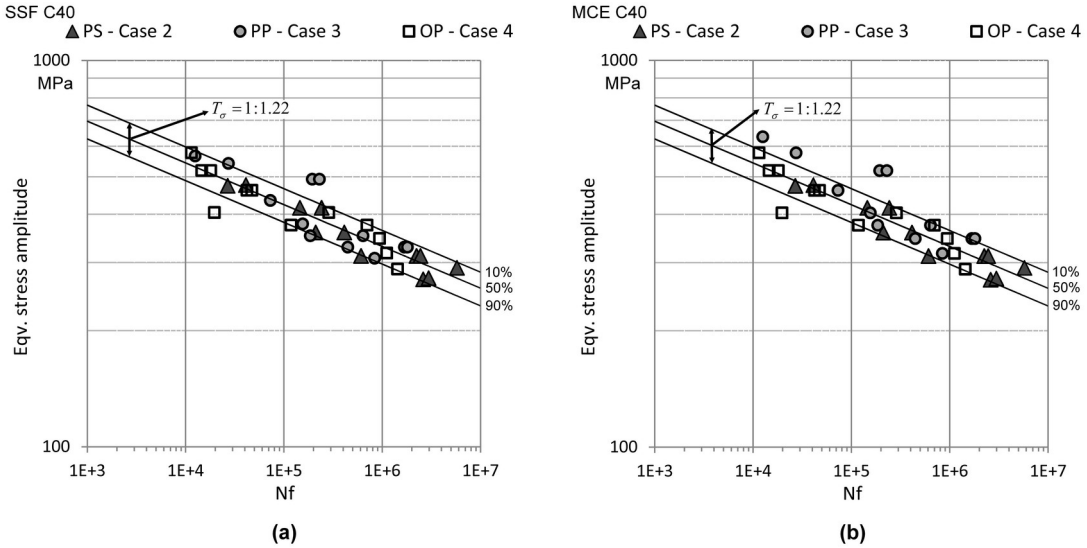


**Figure 4.33:** C40's S-N curves using: a) SSF equivalent stress, b) MCE equivalent stress.

Fig.(s) 4.34 and 4.35 show the fatigue life correlation between experiments and estimates performed by the SSF and MCE criteria, the fatigue life boundaries considered in correlations have a life factor of 3.

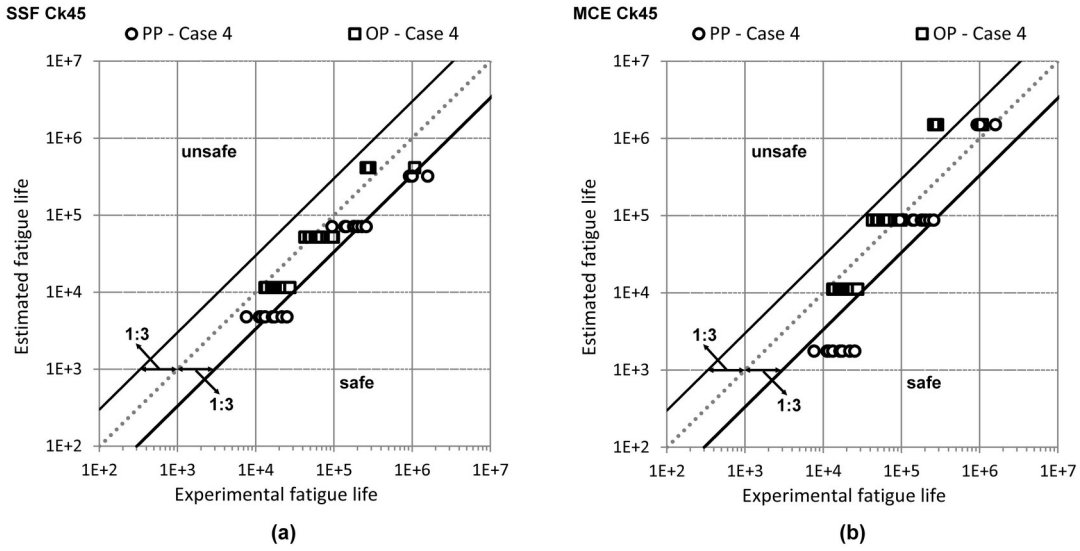


**Figure 4.34:** Ck45's fatigue life correlation using: a) SSF criterion, b) MCE criterion.

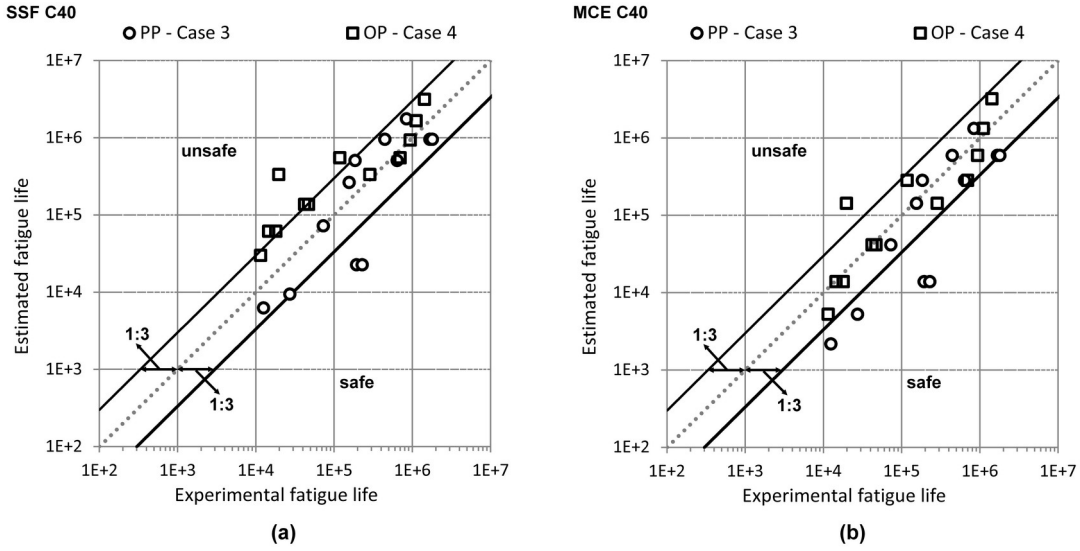


**Figure 4.35:** C40's fatigue life correlation using a) SSF criterion b) MCE criterion.

From the correlation results, it can be concluded that the SSF and MCE estimates are mostly within the boundaries in both materials. Regarding the Ck45 material, the SSF criterion shows a linearisation between estimates and experimental fatigue lives, i.e. the correlation trend line in both loading paths (Case 3 and 4) is parallel to the boundaries. However, in the MCE correlation such linearisation was not found, i.e. the correlation trend lines crosses the fatigue life boundaries. Regarding the C40 results, it can be also identified a linearisation between the experimental data experimental and the SSF criterion estimates.

In the MCE results, the trend line of the proportional correlation crosses the fatigue life boundaries without linearisation, though the non-proportional correlation trend line is

parallel to the correlation boundaries. The linearisation interpretation allows to analyse the criterion capability to capture the damage increase due to a stress level increment for a given loading path (sensitivity to the stress level variation)

## 4.7 Final comments

Under multiaxial fatigue loading conditions two type of stresses are involved in the fatigue damage process. These stresses, normal and shear stresses, perform on the material different damage mechanisms with different damage scales. To quantify the combined damage, it is necessary to have both stresses on the same stress space i.e. in the same damage scale. In order to do that, it is commonly used a stress scale factor (SSF). Generally, multiaxial fatigue models use a constant stress scale factor, however, in this chapter, it was shown that the SSF is not constant and varies according to the loading path an stress level. Moreover, it was also shown that the stress scale factor(SSF) is a function that must be experimentally determined to correctly establish the fatigue damage scale between normal and shear stresses to compute an effective multiaxial fatigue damage. An algorithm was designed to easily determine the SSF damage map for all kinds of materials by experiments. This algorithm is based on the S-N results of specific loading paths defined in this chapter. As a result, it was obtained a SSF function (a damage map) to reduce the fatigue damage of normal stresses to the damage scale of shear stresses. This function is a two variable function which has as arguments the normal stress and the stress amplitude ratio of a given loading path. Using the new SSF concept, a new equivalent stress was proposed:

$$\tau_{eqv} = \max\left(\tau + ssf(\lambda, \sigma) \cdot \sigma\right)$$

Non-proportional loading paths have as characteristic the stress amplitude ratio (SAR) variation within their loading period; in contrast, in proportional loadings their SAR is maintained constant. It was proved that the SSF equivalent stress is sensitive to the loading path nature (proportional or non-proportional) due to the SSF function dependence on the stress amplitude ratio and its stress level. The stress amplitude ratio is a loading variable which captures very well the loading path nature, and it can be used mathematically to identify proportional and non-proportional loading paths.

# Chapter 5

# Contributions to Level 3

## 5.1 Introduction

In this chapter, it is presented the thesis contribution to the state-of-the-art regarding the multiaxial cycle counting subject, which is depicted in Figure 5.1 as level 3. The main objective is to achieve a correct definition for a loading cycle under multiaxial loading conditions.

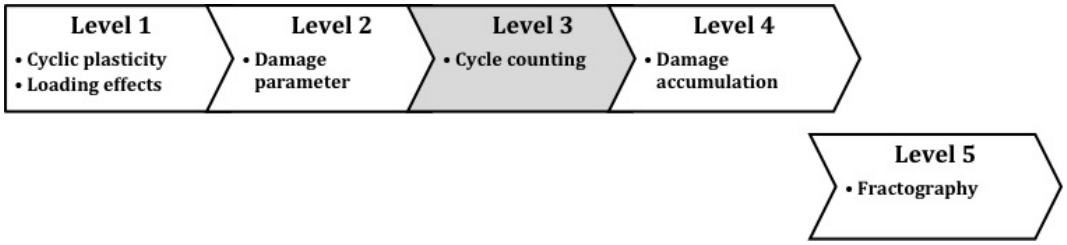


**Figure 5.1:** Multiaxial fatigue level focused in this chapter.

Multiaxial stress states under cyclic loading conditions are a key issue in several mechanical components. Their fatigue strength analysis is of utmost importance to avoid unexpected failures of equipments, vehicles or structures. Among several parameters, a correct definition of a loading cycle in multiaxial fatigue loading conditions appears to be crucial regarding fatigue life assessment for complex loadings, such as loading blocks or loading spectra. Under this context, here it is evaluated the performance of the state-of-the-art criteria regarding this subject, to do that it is studied 11 different loading blocks using two different cycle counting methods, the Bannantine and Socie [93] and the Wang and Brown [98]. Several loading blocks were considered taking into account different loading effects such as: the sequential loading effect, the proportional and non-proportional loading effects, and the effect of different frequencies between the axial and the torsional stress components (asynchronous loading paths). In this chapter, a new loading cycle concept, and a new cycle counting methodology (the SSF virtual cycle counting method) are proposed based on the SSF equivalent shear stress time evolution, previously presented

in Chapter 4. For each cycle counting method considered here, i.e. the proposed method and the selected ones from the state-of-the-art, it was performed a fatigue life correlation between their estimates and the 42CrMo4 experimental fatigue data presented in Table 5.3, in order to evaluate their performance.

## 5.2 Multiaxial cycle counting

As seen in the typical equivalent stress concept, the SSF equivalent stress only captures the fatigue damage inherent to its maximum value found within a loading period. However, in such procedure, the contribution of the intermediate SSF loading history to the overall damage is missing, i.e. the maximum value of the SSF equivalent stress found within a loading period do not account with the fatigue damage from local the SSF equivalent stress reversals that can be found within a loading block. Therefore, fatigue life estimates based only in the maximum equivalent stress found within a loading block are smaller than it should be, leading to non-conservative fatigue life results.

### 5.2.1 Loading spectra and loading block concept definitions

Usually, variable amplitude loadings are transformed into an equivalent spectrum where each loading block is identified based on the stress amplitude levels found within the variable amplitude time histories, please see Figure 5.2. Figure 5.2 a) shows a variable amplitude time history commonly found in the field, and Figure 5.2 b) shows its equivalent spectrum with constant amplitude steps. This equivalent spectrum approach is suitable to be used in the damage accumulation assessment under a Miner's rule type approach, but this spectrum transformation that transforms a loading time history into an equivalent load spectrum (Figure 5.2 b)) leads to lose information during the damage monitoring process. Thus, the stepped spectrum is a simplified way to account the instantaneous damage performed by the stress time history. In this way, the stepped stress or the stepped damage parameter approaches will hardly capture the fatigue damage inherent to the instantaneous normal and shear stresses, specially under multiaxial loading conditions.

The loading block concept can lead to wrong interpretations, because simply loadings only based in one sinusoidal loading, can be also interpreted as loading blocks too. Therefore, to avoid this misconception, here a loading path is considered as a loading block when its fatigue damage cannot be accounted using uniquely the maximum damage parameter approach. In other words, when a time evolution of a given damage parameter have reversals with peaks lower than the maximum peak, then that loading path is a loading block. Figure 5.3 shows two different loadings with the same loading time and maximum stress level. Though they have the same maximum stress during the load period, the fatigue damage inherent to each loading path is quite different. However, this is the approximation performed when it is used an equivalent stress spectrum in which the

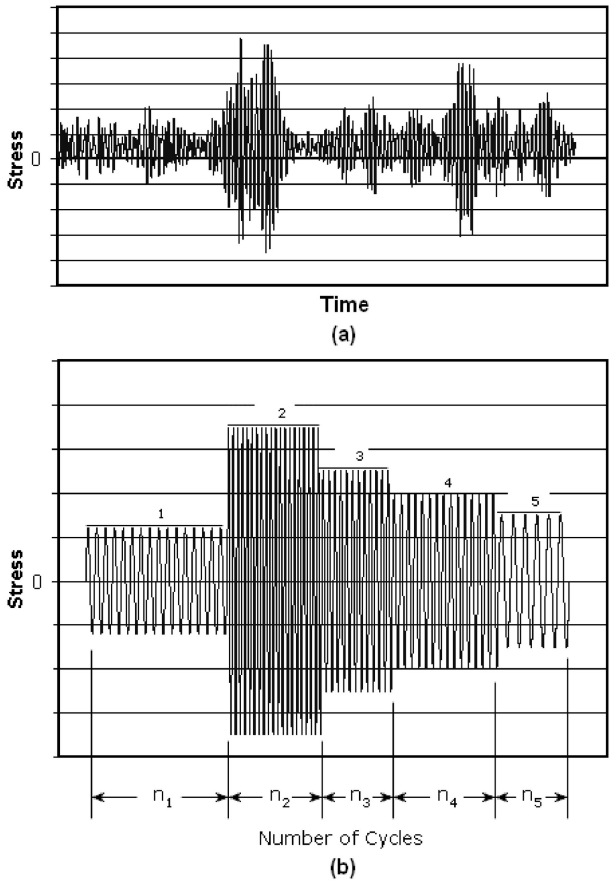


**Figure 5.2:** Loading spectrum: a) In the field, b) *Equivalent* loading spectrum.

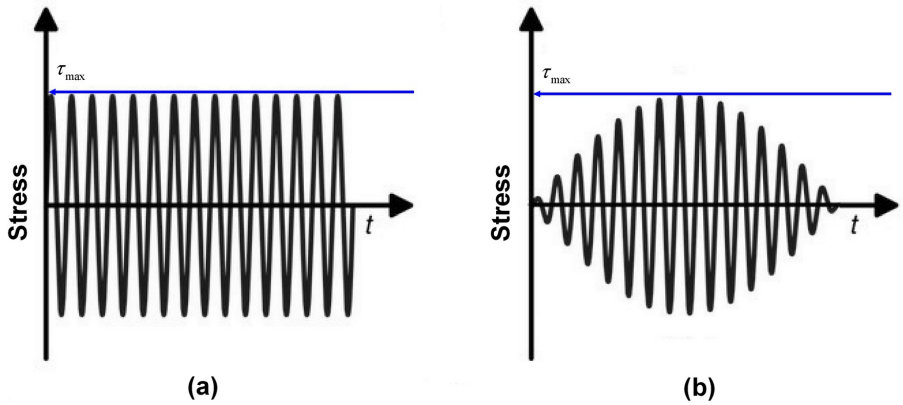


**Figure 5.3:** Two different loading paths with same maximum stress.

varying amplitude is reduced to loading steps with constant amplitude as already discussed and depicted in Figure 5.2. Regarding the block definition adopted here, the loading depicted in Figure 5.3 a) is not a loading block, because their damage can be directly related to the loading maximum amplitude. On the other hand, the loading depicted in Figure 5.3 b) can be treated has a loading block because their fatigue damage is related to all loading amplitudes performed during the loading period. None of these two loading paths causes the same fatigue damage, because they have different amplitudes and load

sequence (Hi-LO, LO-HI). Thus, in order to quantify an unitary damage of a loading block, to be used in damage accumulation procedures, it is necessary to account with all loading amplitudes (their reversals) within a loading block. Therefore, the load depicted in Figure 5.3 a) has the unitary damage based in its maximum amplitude, being possible estimate its fatigue damage based in the maximum stress amplitude found during the loading period. However, in the loading case depicted in Figure 5.3 b) that it is not possible, the maximum equivalent stress is only found in one loading peak, all others are below this value, which means that it is necessary to find the unitary damage inherent to this loading block, which is not trivial as is in the loading path depicted in Figure 5.3 a).

### 5.2.2 Unitary damage concept

Unitary damage is a new concept developed here to quantify the fatigue damage inherent to loading blocks with the objective of being used in damage accumulation rules. Therefore, the unitary damage concept allows the direct addition of fatigue damage from loading blocks as if they were simple sinusoidal loading cycles, like the ones used to obtain the uniaxial SN curves. The unitary damage can be determined by considering two damages quantities evaluated within a loading block. Firstly, must be computed the damage captured by the maximum damage parameter found within the loading block, and secondly, the block relative damage must determined, thus the unitary damage is computed based in these two damage quantities. As shown in the previous subsections, the most suitable way to evaluate fatigue damage of a loading path is the use of a maximum damage parameter found within a loading block. However, this approach does not captures the overall damage of a loading block, therefore it is required an update to the damage estimate, this upgrade is given by the relative damage quantity. The relative damage quantity can be evaluated by determining how many times the experimental block fatigue life is less than the one estimated by its maximum damage parameter as shown in Eq. 5.1, where the fatigue life estimate is compared with the experimental result.

$$\underset{Block}{RelativeDamage} = \frac{N_{f_{estimate}}}{N_{f_{\exp erimental}}} \tag{5.1}$$

Eq. 5.1 needs the experimental fatigue life of the loading block to determine the relative damage, which is a drawback. In order to estimate the relative damage without falling back on experimental tests it is proposed here the relative damage estimation by using a cycle counting method. Thus, with a cycle counting method, it is estimated how many times the fatigue life estimate (using the maximum damage parameter approach) must be reduced due to the block loading path, please see Eq. 5.2. In this way, it is accounted in the block damage evaluation (unitary damage assessment) the entire loading history and not only the maximum damage parameter found within the loading block.

$$\underset{block}{N_f} = \frac{N_{f_{estimate}}}{n_{cycles}} \tag{5.2}$$

Where, $n_{cycles}$ is the number of cycles found in the loading block using a cycle counting method, $N_{f_{estimated}}$ is the number of cycles computed using the maximum damage parameter, and $\underset{block}{N_f}$ is the block fatigue life estimate. Thus, the unitary damage is given by Eq. 5.3.

$$\frac{1}{N_{block}} = \frac{1}{\frac{N_{f_{estimated}}}{n_{cycles}}} = \frac{n_{cycles}}{N_{f_{estimated}}} \tag{5.3}$$

## 5.3 SSF virtual cycle counting (vcc)

Cycle counting methods are used in fatigue life evaluation because the maximum damage parameter within a loading block does not capture the fatigue damage of loading blocks as already discussed. Therefore, fatigue life estimates of loading blocks obtained solely with a maximum damage parameter yields poor results. In order to improve the fatigue damage assessment of loading bocks, it is proposed here a new way to estimate unitary fatigue damage inherit to loading blocks, the SSF virtual cycle counting method (vcc).This new cycle counting method is based in the SSF equivalent stress previously presented in Chapter 4. In this new approach, it is not analysed hysteresis loops, as seen in the Rainflow methodology, and due to that the new method presented here was named as virtual cycle counting. However, this new method is physically based, because it relates the maximum damage parameter (found within a loading block) with the total damage of a loading block. In the present author opinion the equivalent stress approaches are much more suitable than other approaches to account fatigue damage of loading blocks. Equivalent stress/strain criteria represent in one damage parameter the instantaneous values of normal and shear damages, avoiding the issue found in the critical plane approaches in which the stress/strain maximum values are always computed as taking place at the same time instant, however in some loading paths such as non-proportional loadings such assumption is not true. The concept and use of the virtual cycle approach is much easier to implement than other methods usually found in literature to evaluate fatigue damage of loading blocks and their damage accumulation. The paradigm behind this approach is as follows:

*"The experimental fatigue life of a loading block is less than the one estimated by its maximum damage parameter. Thus, the fatigue life of a loading block can be correctly estimated if it is known how many times the experimental fatigue life of a loading block is less than the estimated one."*

Under this paradigm, the key issue is to find how many times the fatigue damage of a loading block is greater than its damage reference. The damage reference is given by the maximum damage parameter of a given loading block, which in this study, is the

maximum SSF equivalent shear stress. The additional damage in respect to the damage reference is obtained by adding all equivalent stress absolute values at each peak and valley found between two consecutive zero stress points of the SSF equivalent shear stress time evolution of a loading block. Then, the summation result is divided by two times the maximum SSF equivalent stress, in this way it is achieved an estimate for the damage increase (comparatively to the reference damage) inherent to the loading block. Eq. 5.4 presents this concept. Figure 5.4 shows a graphical description of the SSF virtual cycle counting method, and how it is estimated the block fatigue life using the virtual cycle counting method.

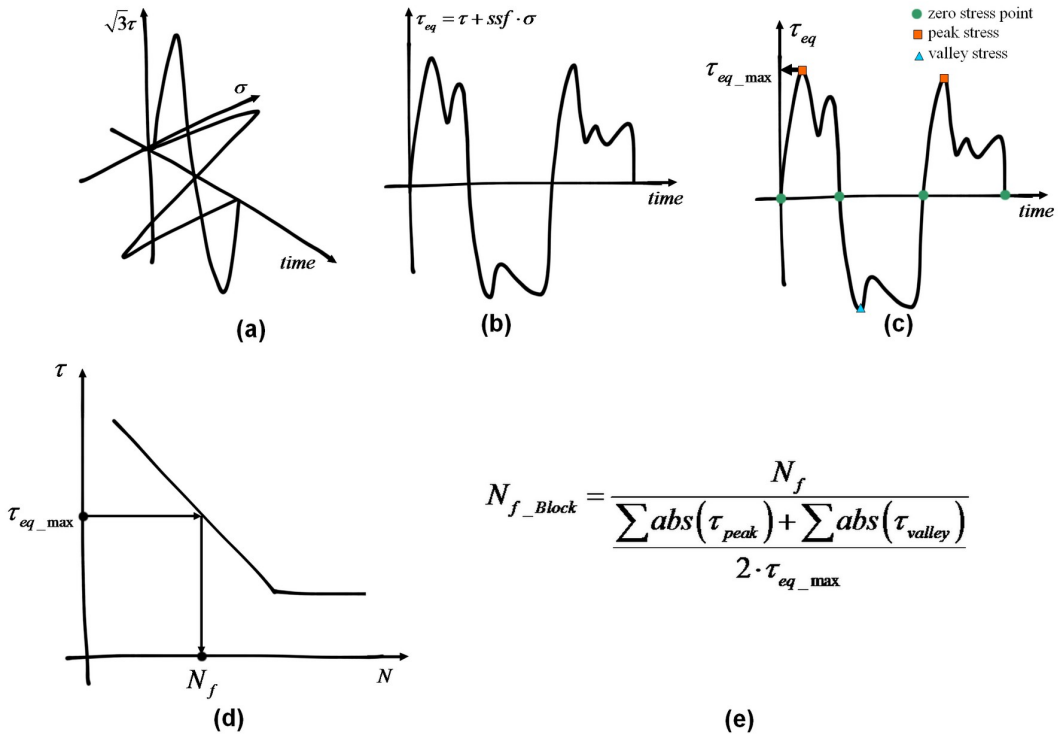


**Figure 5.4:** Virtual cycle counting methodology and procedure to estimate block fatigue lives.

Figure 5.4 a) presents the normal and shear stress components time variation of a multiaxial loading, which are computed to get the SSF time history depicted in Figure 5.4 b). Next up, in Figure 5.4 c), it is selected from the SSF time history the greatest SSF value (orange dot) and the SSF stress values at every peak and valley found between two consecutive SSF zero stress points, depicted in green dots. The greatest SSF value is the block damage reference to compute the block fatigue life, please see Figure 5.4 d) and e). Eq. 5.4 shows the virtual cycle counting expression, where the virtual cycle counting (vcc) is achieved by adding each SSF peak/valley absolute values and divide the result by the damage reference of the loading block.

$$vcc = \frac{\sum abs(\tau)_{peak,valley}}{2 \cdot \tau_{\max,Block}} \tag{5.4}$$

where *vcc* is the virtual cycle count inherent to a loading block and $\tau$ is the SSF equivalent shear stress at each peak/valley. In cases where the loading block is defined by two SSF reversals with the same amplitude, i.e. one peak and one valley, the *vcc* is equal to 1. Thus, it can be concluded that the SSF virtual cycle counting verifies 1 cycle loading cases that usually are the reference ones used in fatigue life experiments. The multiaxial cycle counting method, vcc, is much simpler and easier to implement than other cycle counting methods found in literature such as BS and WB discussed in Chapter 2.

### 5.3.1 Block fatigue life estimates

The block fatigue life estimate is achieved by using the block reference damage and the virtual cycle count as follows in Eq. 5.5.

$$N_{f\_block} = \frac{N_{f\_\tau\,\max}}{vcc} \tag{5.5}$$

where $N_{f\_block}$ is the block fatigue life and $N_{f\_taumax}$ is the block damage reference determined using Eq. 5.6

$$N_{f\_\tau\,\max} = \left(\frac{\tau_{\max,Block}}{A}\right)^{\frac{1}{b}} \tag{5.6}$$

where A and b, are the power law regression components obtained from pure torsion fatigue data.

### 5.3.2 Illustrative example

In this subsection, it is performed a illustrative example where it is used the virtual cycle counting methodology to estimate the fatigue life of a loading block. Now, consider the loading block with the shear and axial stress time evolution shown in Figure 5.5.

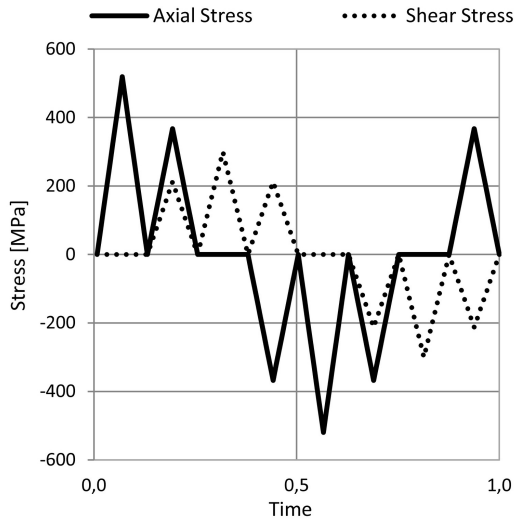


**Figure 5.5:** Multiaxial loading block.

The SSF equivalent stress time evolution for this loading block is depicted in Figure 5.6.

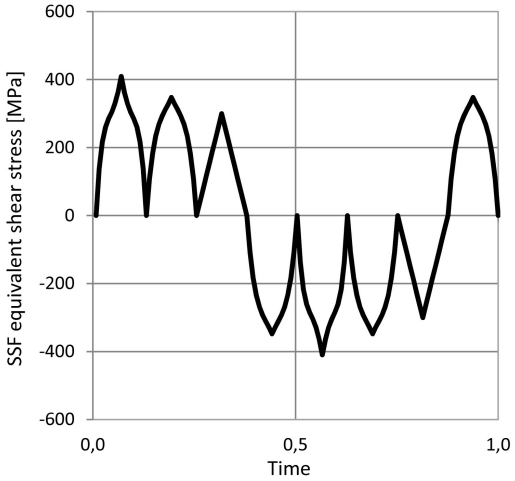


**Figure 5.6:** SSF equivalent shear stress time evolution for the selected loading block.

Here, the shear stress sign is established through the sign of the normal stress; this assumption is based on the fact that the fatigue damage of shear stresses is independent from the loading direction, i.e. negative shear stresses cause the same fatigue damage than the positive ones. However, the fatigue damage of normal stresses in tension is quite different from the compression one, thus the SSF approach considers that the shear stress sign is always equal to the sign of the normal stresses, as stated in Chapter 4. Thus, the SSF equivalent stress time evolution is divided into several loading branches defined between two consecutive zero stress points. This becomes possible due to the shear stress sign convention discussed in the previous lines. In Figure 5.7, one can identify the SSF loading branches and the location of their maximum stresses for this loading block. Note that the load branch concept used here is different from the reversal concept, the local SSF peak/valley value for each branch is found between two consecutive zero stress points of the SSF time evolution, and not in the points where the stress time evolution changes direction, as seen in some Rainflow based criteria. The loading block selected to perform this illustrative example (Figure 5.5) was tested in the high strength steel 42CrMo4. In one of these fatigue tests, the multiaxial loading components had the following stress level: 520 [MPa] in the normal stress amplitude, and 300 [MPa] in the shear stress amplitude. For this stress level, it was obtained for each loading branch, the SSF equivalent stress amplitudes shown in Table 5.1.

**Table 5.1:** Values for the SSF equivalent shear stress loading branches.

| | B1 | B2 | B3 | B4 | B5 | B6 | B7 | B8 |
|---|---|---|---|---|---|---|---|---|
| SSF [Mpa] | 428 | 340 | 300 | -352 | -422 | -354 | -330 | 369 |

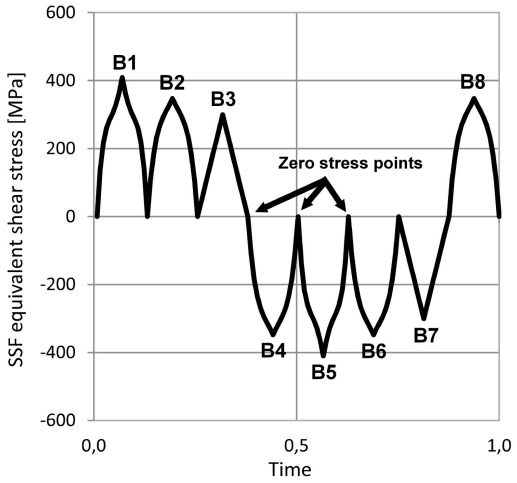


**Figure 5.7:** Loading branches identification in the SSF equivalent shear stress time evolution for the selected loading block.

The maximum equivalent stress, which occurs at loading branch B1, is used to estimate the block reference damage, which is obtained by applying the equivalent stress value (SSF equivalent stress at branch B1) into the uniaxial shear trend line equation previously obtained by experiments for the 42CrMo4 material. Thus, the computed fatigue life regarding the 428 [MPa] found in B1 was 103097 cycles, which is a fatigue life quite different from the 36102 cycles obtained in the experiments for this loading block and stress level.

In fact, this result indicates a block damage greater than the one obtained using a fully reversed proportional loading with a SSF equivalent shear stress amplitude equal to 428 [MPa]. So, this result confirms the hypothesis in which the experimental fatigue life of a loading block is less than the one estimated by the maximum SSF equivalent stress obtained within the loading block.

Considering that, it is necessary to find how much more damaging is the loading block comparatively to the reference damage given by the load branch that has the maximum equivalent shear stress. Thus, in order to clarify the virtual cycle counting already presented in this section the paradigm can be rephrased as follows:

*If the maximum equivalent shear stress amplitude verified in the loading block is the damage reference determined based in the uniaxial SN curve (shear), thus the number of virtual cycles inherent to the loading block can be determined by finding how many times that damage reference is reached during the accumulative damage process within the loading block.*

The paradigm formulation is given by adding all SSF stress amplitudes found in the SSF time evolution of a loading block, then divide that result by the double of the maximum

equivalent stress verified on the loading block. Recalling the illustrative example, the virtual cycle counting for this loading block is determined as follows in expression 5.7.

$$\frac{428{+}340 + 300 + 352{+}422{+}354{+}330 + 369}{2 \times 428} = 3.38 \tag{5.7}$$

Eq. 5.7 shows that this loading block has a fatigue damage 3.38 times greater than the reference one, which indicates a 3.38 virtual cycles. In this way, it is determined the relative damage in respect to the damage reference given throughout the maximum SSF equivalent stress. The fatigue life estimate of the loading block is determined by dividing the fatigue life estimate (obtained by the maximum SSF value i.e. the damage reference), by the achieved virtual cycle counting, as seen in expression 5.8.

$$N_{f\_block} = \frac{\left(\frac{428}{864.78}\right)^{\frac{1}{-0.061}}}{3.38} = 30463 \tag{5.8}$$

Thus, the fatigue life estimate for this loading block and stress level is 30463 cycles, which is a result very close to the 36102 cycles obtained in the experiments.

## 5.4 Fatigue life estimates correlation with fatigue data

### 5.4.1 Rainflow cycle counting results

The ASTM E-1049 Rainflow method, developed by Dr. Darrel Socie, and discussed in [158, 159] was selected here to evaluate the number cycles inherent to each loading block shown in Figure 5.8. The objective is to inspect its performance under multiaxial loading conditions and correlate the results with the virtual cycle counting methodology. Despite the ASTM E-1049 method have been developed based in the stress-strain relation for uniaxial loading conditions, here it is evaluated its performance by using the time evolution of the SSF and the von Mises equivalent stresses in respect to the loading blocks depicted in Figure 5.8. Fig.(s) 5.9, 5.10 and 5.11 show the equivalent stress evolution along each loading case for the von Mises and SSF approaches regarding the selected loading blocks present in Figure 5.8. The fatigue data of these loading blocks, i.e. Cases 1, 2, and 3, are presented in Table 5.3 through Cases 1, 3, and 6, respectively. As it can be seen, the von Mises equivalent stress time evolution is always positive, in contrast the time evolution of the SSF equivalent stress has positive and negative values.

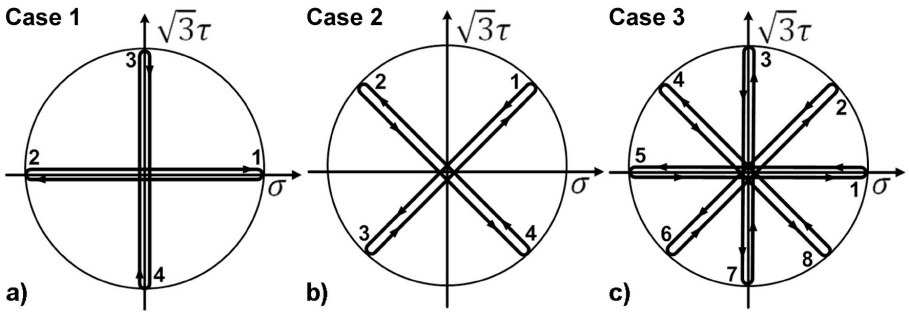


**Figure 5.8:** Multiaxial loading blocks.

Due to that, the Rainflow cycle counting method extracts from the von Mises stress evolution 1 cycle for each loading branch of the loading block, therefore to count the number of Rainflow cycles associated to each loading block, it is just need to count the number of branches on the von Mises loading path trajectory (stress space) please see Figure 5.8; however for the SSF equivalent stress time evolution the number of loading cycles cannot be directly extracted.

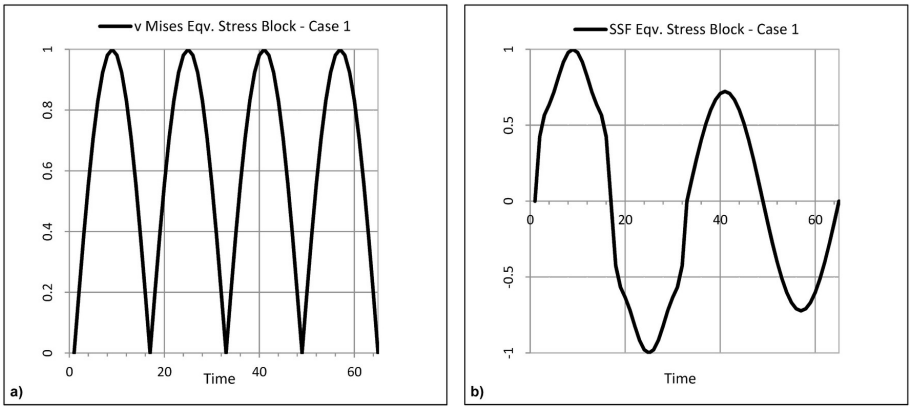


**Figure 5.9:** Equivalent stress time evolution for Case 1: a) von Mises equivalent stress, b) SSF equivalent stress.

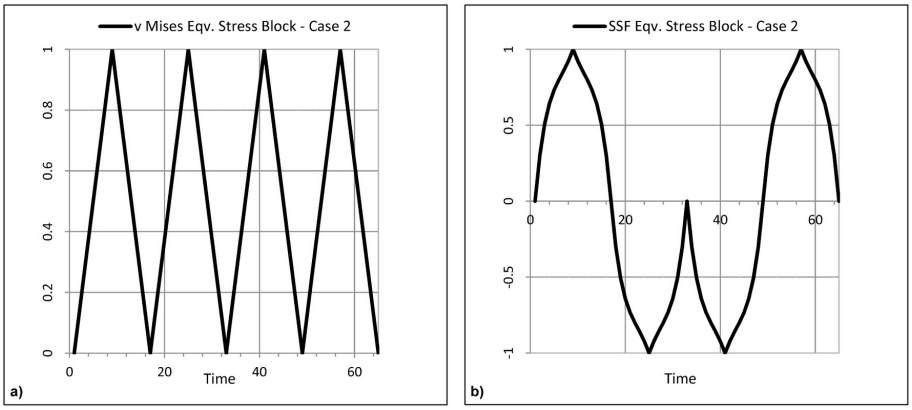


**Figure 5.10:** Equivalent stress time evolution for Case 2: a) von Mises equivalent stress, b) SSF equivalent stress.

Table 5.2 shows the results for the Rainflow cycle counting method in respect to each loading block selected here (columns 1 and 2) and for each equivalent stress criterion selected here, i.e. the von Mises and the SSF equivalent stresses. Columns 3 and 4 presents the relative damage calculated using the von Mises, and the SSF equivalent stress, respectively. These results were computed by dividing the reference damage (fatigue life estimate based in the maximum value found in the equivalent stress time evolution) by the experimental fatigue life obtained for each loading case.

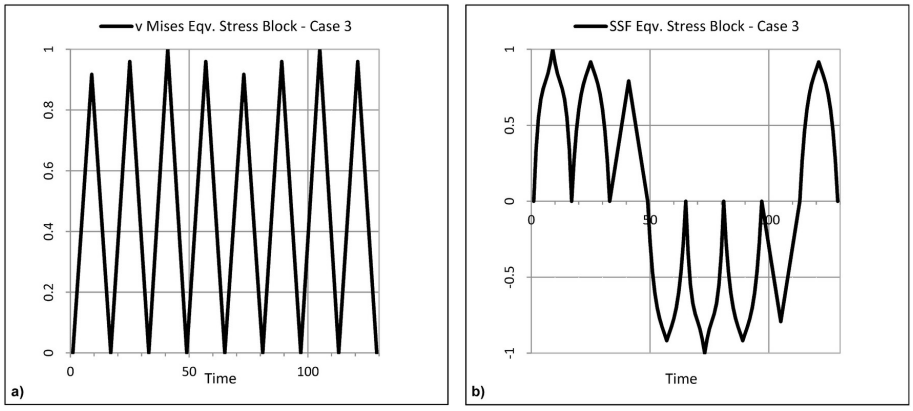


**Figure 5.11:** Equivalent stress time evolution for Case 3: a) von Mises equivalent stress, b) SSF equivalent stress.

**Table 5.2:** Rainflow cycle counting and block relative damage for each loading case.

| | Rainflow | | Block Damage | |
|---|---|---|---|---|
| | v Mises | ssf | v Mises | ssf |
| Case 1 | 4 | 2.5 | 1.2 | 1.9 |
| Case 2 | 4 | 3 | 0.1 | 4.5 |
| Case 3 | 8 | 7 | 1.9 | 9.1 |

As expected, the Rainflow results for the von Mises time evolution yields a cycle counting equal to the number of loading branches encountered on the loading path trajectory depicted in the stress space as shown in Fig.(s) 5.9 to 5.11. However, for the SSF equivalent stress time evolution the Rainflow results are different from the number of branches, as it can be seen in the second column of Table 5.2. In the third and fourth columns of Table 5.2, it is shown for each loading case and equivalent stress approach the block relative damage in average (several samples were tested for each loading block).

Regarding the von Mises results, the relative block damage in Cases 1, and 3 is greater than 1 which means that the damage caused by the loading block is greater than the one estimated by the reference damage. However, in Case 2, the block relative damage is much smaller than 1, about 0.1, which is in contradiction to the premise in which the damage caused by a loading block is greater than the one estimated by its maximum equivalent

stress verified on that same loading block. Therefore, the von Mises equivalent stress is not suitable to capture block unitary damages because its fatigue life estimates based in the maximum value approach is much greater than the block experimental fatigue life. On the other hand, the block relative damage computed using the SSF equivalent stress is greater than 1 for all loading blocks, being consistent with the premise described above. Regarding the SSF relative damage results, the loading blocks 1, 2 and 3 are 1.9, 4.5 and 9.1 times more damaging than the respective reference damage.

Now, the relative damage results and the Rainflow counting results obtained for the SSF equivalent stress can be compared in order to evaluate the performance of the Rainflow method in respect to the capability to capture the unitary damage inherent to each loading block selected here. Thus, for the SSF equivalent stress, the Rainflow cycle counting results are very similar to the computed relative damages, i.e. 2.5 cycles for 1.9 in Case 1, 3 cycles for 4.5 in Case 2, and 7 cycles for 9.1 in Case 3.

Therefore, the block relative damage can be fairly estimated using the Rainflow cycle counting technique in association with the SSF equivalent stress, avoiding in such way the need of experimental fatigue data to compute relative damages. In the von Mises approach, the Rainflow results yields a number of cycles very different from the relative block damage results, thus the relative damage cannot be estimated using the von Mises and the Rainflow method being unsuitable to capture unitary damages from complex loading paths.

### 5.4.2 Rainflow fatigue life correlation

Fig.(s) 5.12, 5.13 and 5.14 show the fatigue life correlation for the selected loading cases and equivalent stress criteria. In each graph a square symbol is used to identify the results of the fatigue life correlation performed with the maximum equivalent stress (von Mises and SSF) found within the selected loading blocks. Moreover, the circle symbol was used to represent the fatigue life correlation in which the fatigue life estimates of the equivalent stress criteria were updated by the Rainflow results. This update was performed by dividing the aforementioned estimates by the inherent Rainflow cycle counting values. The loading block fatigue life correlations using the SSF approach and the Rainflow methodology have a satisfactory results with few data points outside the fatigue life boundaries with a life factor equal to 3. However, the results for the the von Mises fatigue life correlation in Case 2 are totally outside of fatigue life boundaries, please see Figure 5.13 a). Moreover, the von Mises estimates without a cycle counting update gave the same damage level in Cases 1 and 3, because it is computed the same maximum equivalent stress value in these two loading blocks.

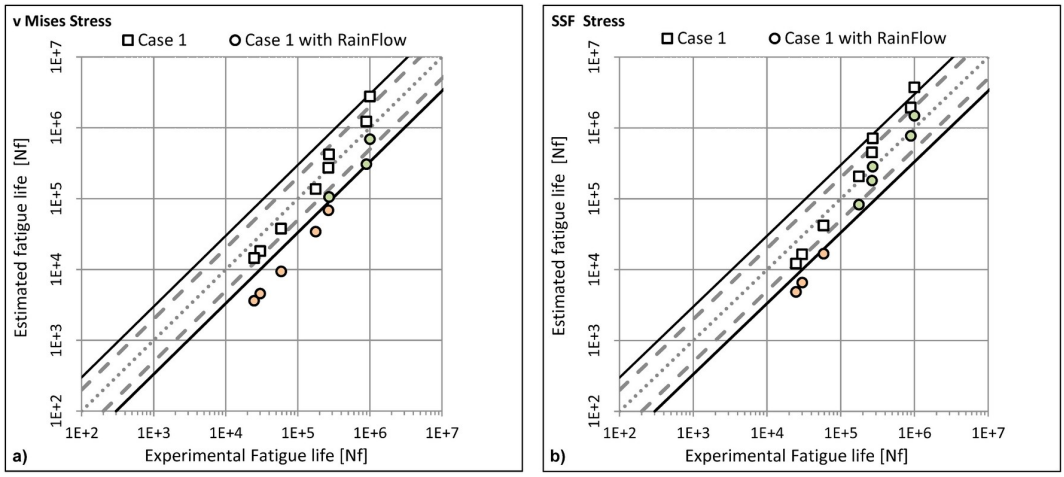


**Figure 5.12:** Fatigue life correlation for Case: 1 a) von Mises approach, b) SSF equivalent stress approach.

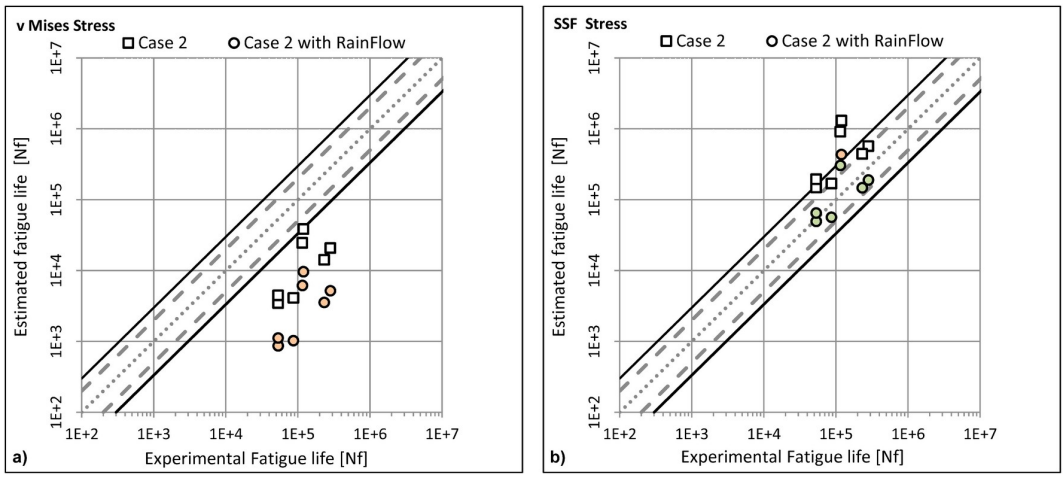


**Figure 5.13:** Fatigue life correlation for Case 2: a) von Mises approach, b) SSF equivalent stress approach.

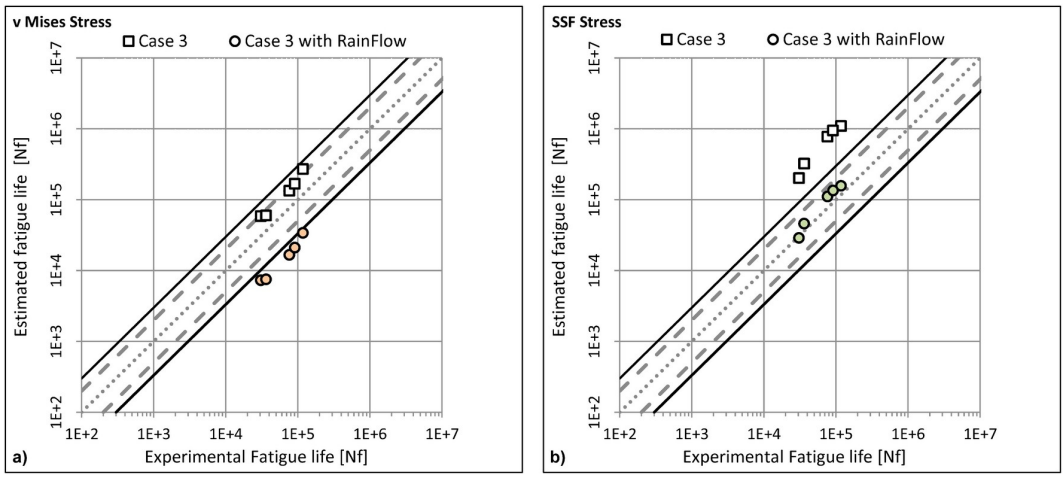


**Figure 5.14:** Fatigue life correlation for Case 3: a) von Mises approach, b) SSF equivalent stress approach.

### 5.4.3 Multiaxial cycle counting analysis

In this sub-section it is performed a deep analysis of eleven loading blocks (please see Figure 5.15) using the developed multiaxial cycle counting method (vcc, virtual cycle counting method) and the selected ones from literature, i.e. the Wang and Brown (WB), and the Bannantine and Socie (BS) methods.

The theoretical results to analyse the vcc, WB, and BS multiaxial cycle counting methods are presented in Fig.(s) 5.16 to 5.26. For each loading block, it is presented in the same Figure the WB and BS cycle counting results in order to turn easier the comparative exercise between results.

Table 5.3 present the fatigue life results for the loading blocks depicted in Figure 5.15. These results were obtained under in experiments stress control with loading frequencies between 5-6 Hz at room temperature. The failure criterion was the sample total separation. The test sample geometry and its dimensions are depicted in Figure 3.30.

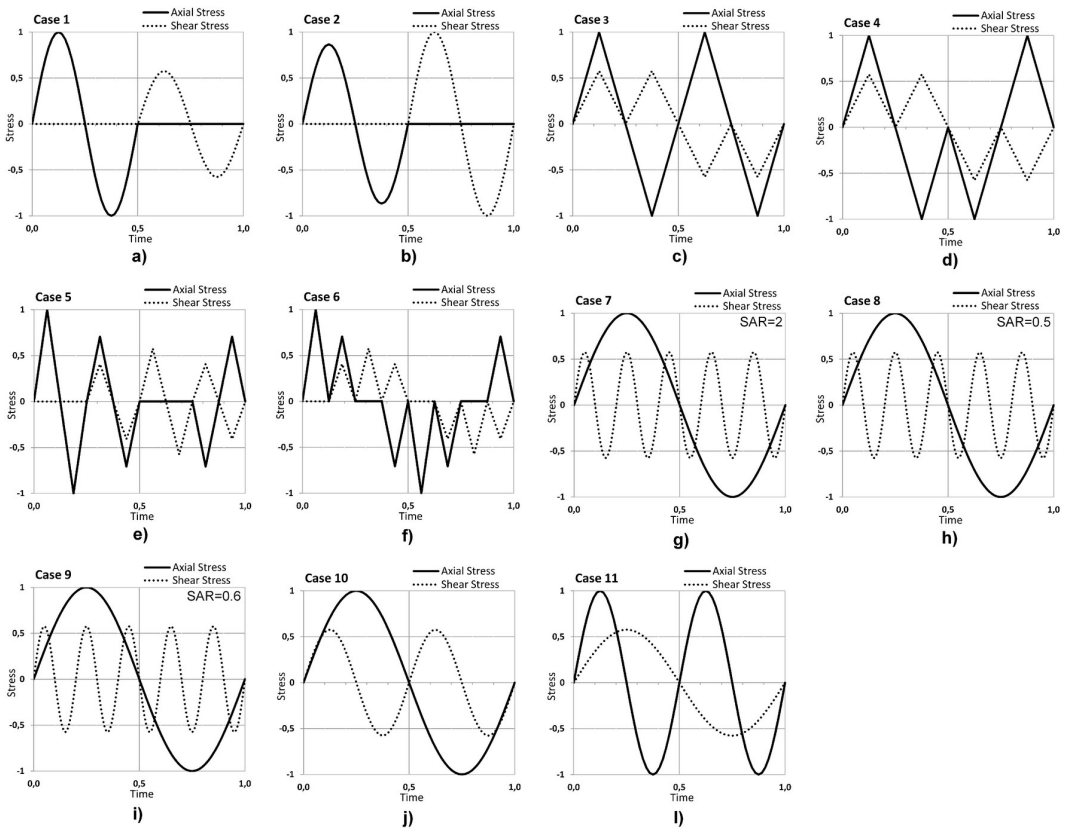


**Figure 5.15:** Multiaxial loading blocks considered in this sub-section.

**Table 5.3:** 42CrMo4 fatigue life results for the loading blocks depicted in Figure 5.15 [3, 9, 160–162].

| Case | Axial | Shear | Nf | Case | Sigma | Shear | Nf |
|---|---|---|---|---|---|---|---|
| **Case 1** | 610 | 352 | 24722 | **Case 7** | 194 | 388 | 35003 |
| | 600 | 346 | 30058 | | 184 | 368 | 47934 |
| | 570 | 329 | 58703 | | 175 | 350 | 79496 |
| | 520 | 300 | 176793 | | 160 | 321 | 133058 |
| | 495 | 286 | 265955 | | 143 | 287 | 1000000 (ro) |
| | 480 | 277 | 271243 | **Case 8** | 520 | 300 | 36102 |
| | 445 | 257 | 892629 | | 493 | 285 | 76297 |
| | 420 | 243 | 1000000 (ro) | | 487 | 281 | 90993 |
| **Case 2** | 360 | 416 | 337186 | | 466 | 270 | 117530 |
| | 345 | 398 | 518622 | | 441 | 255 | 464214 |
| | 375 | 433 | 121014 | **Case 9** | 470 | 271 | 38487 |
| | 305 | 352 | 1000000 (ro) | | 465 | 269 | 52836 |
| **Case 3** | 450 | 260 | 21485 | | 455 | 263 | 86000 |
| | 440 | 254 | 32374 | | 440 | 254 | 127693 |
| | 435 | 251 | 41060 | | 430 | 248 | 265312 |
| | 415 | 240 | 128000 | | 420 | 248 | 803827 |
| | 405 | 234 | 181991 | **Case 10** | 510 | 294 | 12116 |
| | 395 | 228 | 427877 | | 480 | 277 | 41466 |
| Case 4 | 420 | 243 | 34807 | | 460 | 266 | 93247 |
| | 415 | 240 | 53246 | | 440 | 254 | 200489 |
| | 410 | 237 | 86669 | | 435 | 251 | 421814 |
| | 400 | 231 | 115474 | | 430 | 248 | 692953 |
| | 395 | 228 | 119252 | **Case 11** | 440 | 254 | 32350 |
| | 380 | 219 | 231943 | | 425 | 245 | 53116 |
| | 370 | 214 | 282332 | | 415 | 240 | 96837 |
| **Case 5** | 520 | 300 | 26009 | | 410 | 237 | 123305 |
| | 552 | 318 | 26509 | | 405 | 234 | 158375 |
| | 540 | 312 | 82293 | | 400 | 231 | 342411 |
| | 520 | 300 | 461232 | | | | |
| | 490 | 283 | 733273 | | | | |
| **Case 6** | 479 | 240 | 4088 | | | | |
| | 463 | 232 | 10719 | | | | |
| | 434 | 217 | 37031 | | | | |
| | 399 | 200 | 99052 | | | | |
| | 347 | 173 | 558219 | | | | |

#### 5.4.3.1 How to read the results

The multiaxial cycle counting methods Wang and Brown, and Bannantine and Socie have different approaches to evaluate multiaxial cycle counting, therefore their results are presented in two different ways. However, they have a common variable, which is the number of cycles found for each loading block. This variable will be used to compare their performance to capture the unitary damage for each loading block considered here. In the following, Figure 5.16 will be used to describe the reading process regarding the results

achieved for the WB and BS methods as well as the SSF equivalent stress time evolution for each loading block. Sub-figures 5.16 a), b) and c) depicts the results of the Bannantine and Socie methodology.

The loading path (loading block) is depicted in Figure 5.16 a) using the von Mises stress space, from where it can be correlated the critical plane orientation identified in Figures 5.16 b) and c) with the loading path shape. In Figure 5.16 a), the $\sigma$ axis is aligned with the specimen test longitudinal direction, and the $0^o$ plane orientation is parallel to the $\tau$ axis.

In sub-Figures 5.16 b) and c) it is presented the pattern of the SWT and Fatemi-Socie fatigue damage parameters at each plane by a full line, the maximum value found in this line is used to estimate the loading block fatigue life as shown in Chapter 2. Moreover, it is also depicted a dotted line which presents the number of reversals extracted from the damage parameter time evolution (SWT and Fatemi-Socie) at each plane.

In addition, the sub-figures 5.16 d) and e) are also related, here the number of reversals and damage parameter time evolution is shown for the Wang and Brown method. The WB reversals are time dependent, thus it can be identified the time instant of the most damaging reversal. Moreover, the most damaging reversal can be identified in the stress time evolution depicted in sub-figure 5.16 d) through the time instant of the most damaging reversal. The same reasoning can be made to the SSF equivalent stress time evolution by comparing sub-figures 5.16 d) and f).

Furthermore, the reversals number in the Bannantine and Socie, and in the Wang ad Brown methods have different paradigms associated. Thus, the reversals in Bannantine and Socie results, shown in sub-figures 5.16 b) and c), are the number of the accumulated reversals on each plane. On the other hand, the reversals of the Wang and Brown method indicates the reversal number and their time window within the loading block period.

### 5.4.4 Cycle counting results

Figure 5.16 presents the results for the loading block Case 1, this is a sequential loading block where a sinusoidal normal load is followed by a sinusoidal shear load, which has an amplitude $\sqrt{3}$ times lower than the normal one. Regarding the BS results, the SWT and F-Socie criteria estimate the critical plane at $0^o$ with 4 and 3 reversals, respectively. The number of reversals must be always kept up with the inherent damage parameter value in order to conclude about the loading block damage. For instance, in Figure 5.16 b) at $-45^o$ it was found the highest number of reversals, about 6, however the damage parameter associated with it is near zero, moreover the maximum damage parameter was found at $0^o$ plane where the reversals number is lower, i.e. 4 reversals. Regarding the WB results, it can be found 4 reversals for this loading block, and the $2^{nd}$ one is the most loaded. The second reversal is divided into two time periods within the load period, please

see Figure 5.16 e). From the WB results, it can be identified the most damaging region of the block stress-time history depicted in Figure 5.16 d), where the time period of the most damaging load is in the range of 16 to 33 seconds and 57 to 65 seconds. Thus, based in the WB methodology, the greatest contribution to the block unitary damage results from the compressive normal stress and from the last shear loading branch. The SSF equivalent stress time evolution shown in Figure 5.16 f) is very similar to the stress time evolution shown in Figure 5.16 d), where the zero stress points occur at same time in both graphs, the SSF virtual cycle counting methodology extracts 3.4 reversals for this loading block, and the Rainflow methodology extracts from the SSF time evolution about 5 reversals.

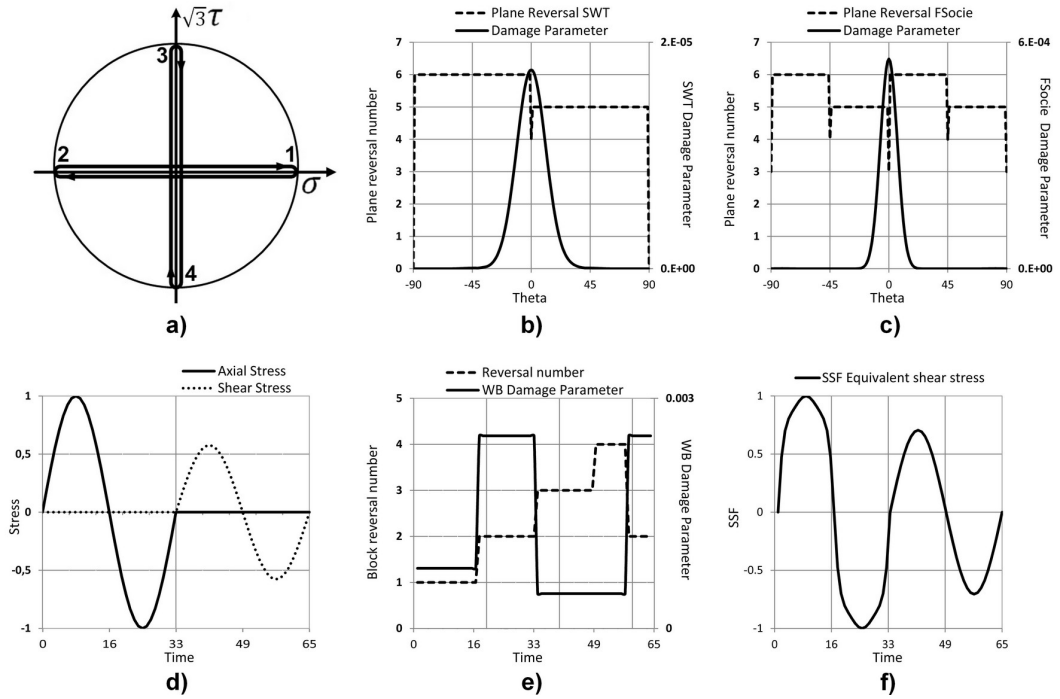


**Figure 5.16:** Case 1: a) von Mises stress space, b) BS results with SWT, c) BS results with FSocie, d) Block stress time evolution e) WB results, and f) SSF time evolution.

Figure 5.17 presents the theoretical results for Case 2, this loading block is a sequential loading similar to the loading Case 1, where the shear stress amplitude is now $\sqrt{3}$ times greater than the normal one. Within the BS method, the SWT estimates for the critical plane orientation is $\pm 45^{o}$ where the BS criterion yields 6 and 5 reversals, respectively. Here, it is reached the same accumulated damage parameter for different number of reversals, also the estimate of the F-Socie criterion regarding the critical plane is $0^{o}$, where the BS method yields 3 reversals. The WB results are very alike to the ones verified in Case 1, where the maximum damage occurs at the $2^{nd}$ reversal. The SSF equivalent stress time evolution and the multiaxial loading components time evolution have in common the same zero stress points. The SSF criterion extracts about 3.6 reversals and the Rainflow criterion applied to the SSF time evolution extracts 5 reversals.

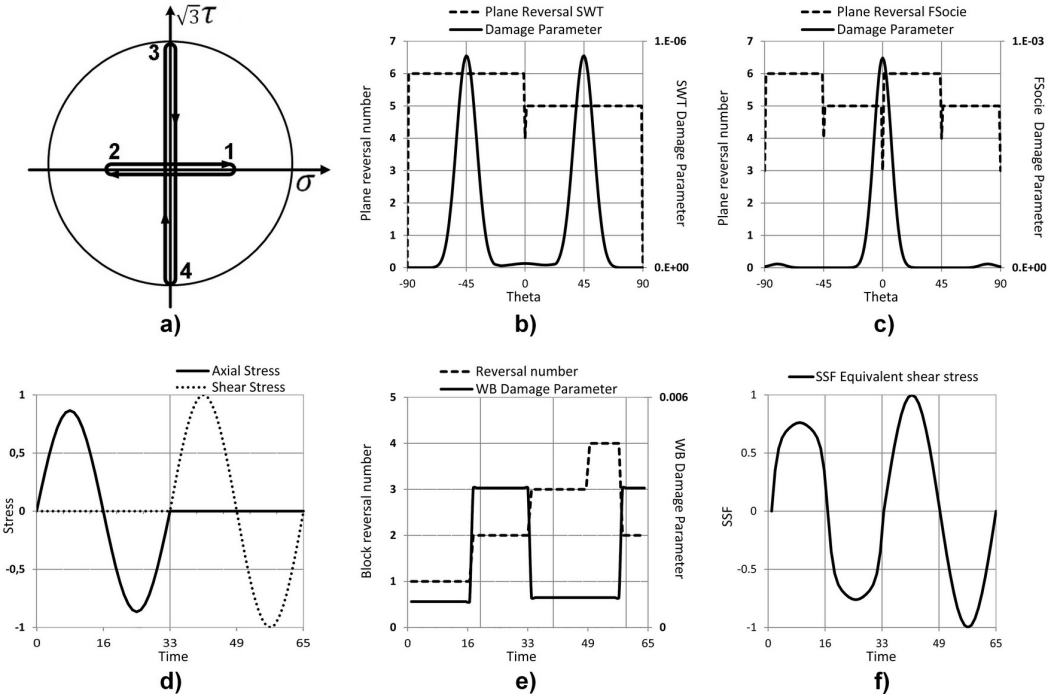


**Figure 5.17:** Case 2: a) von Mises stress space, b) BS results with SWT, c) BS results with FSocie, d) Block stress time evolution, e) WB results, and f) SSF time evolution.

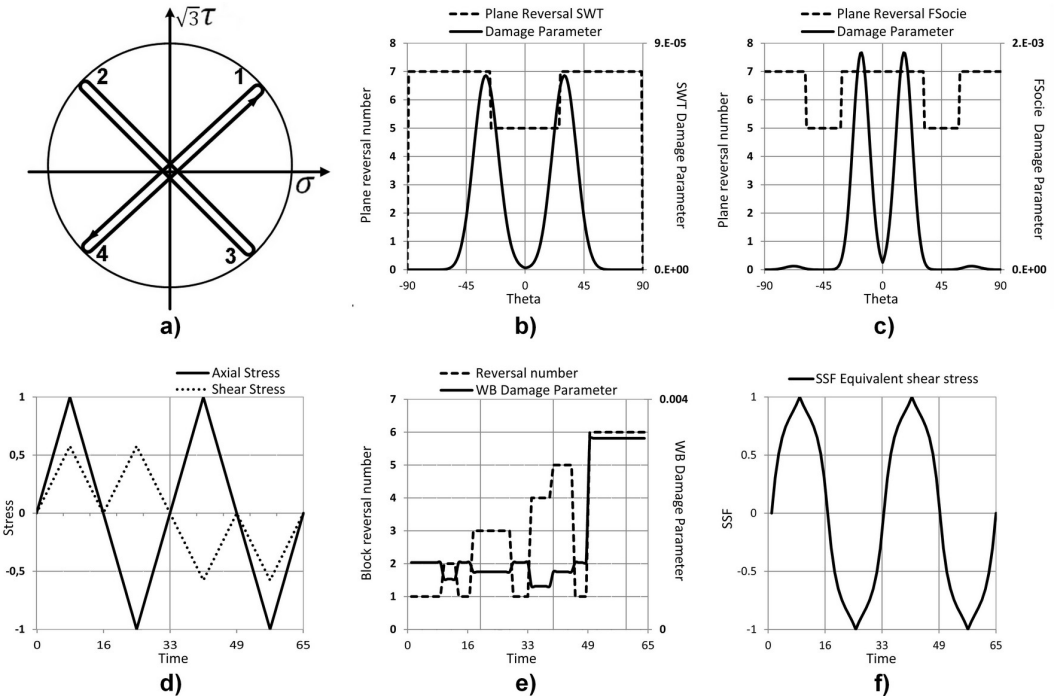


**Figure 5.18:** Case 3: a) von Mises stress space, b) BS results with SWT c) BS results with FSocie d) Block stress time evolution e) WB results and f) SSF time evolution.

Figure 5.18 shows the results regarding loading Case 3, which is a multiaxial loading path with four proportional loading branches similar to Case 4, but with a different loading sequence, please see Figure 5.19 a). The BS method extracts 7 reversals in this loading

block in both critical plane criteria (SWT and FS). Regarding the BS-SWT approach, the maximum value of the accumulated damage parameter occurs at $\pm 30^{o}$ and the F-Socie estimate for the critical plane was $\pm 16^{o}$. In this loading block the experimental crack initiation plane was about $29^{o}$ [161].

The SWT and F-Socie critical plane estimates, computed without using the Bannantine and Socie cycle counting method, were $\pm 25$ and $\pm 21; \pm 69$, respectively.

In the WB method, the most damaging reversal occurs in the last loading branch and extracts about 6 reversals for this loading block.

The SSF virtual cycle counting method extracts from this loading block 4.2 reversals, also here the zero stress points of the SSF equivalent stress, and the stress-time loading history occurs at same time. Moreover, the Rainflow method extracts 5 reversals from this SSF equivalent stress time evolution.

Figure 5.19 presents the results for loading Case 4, this loading block is very similar to Case 3, the difference between them is the loading sequence given by the sequential numbering depicted in the stress space. In this loading case, there is no fully reversed stress time evolutions as seen in Case 3, please see Figure 5.18 a). The experimental crack initiation plane for this loading block was $31^{o}$ [161].

The Bannantine and Socie results are presented in sub-figures 5.19 b) and c). From these results, the SWT and F-Socie critical plane estimates for the critical plane orientation are $\pm 29^{o}$ and $\pm 17$, respectively. Moreover, the BS method yields the same number of reversals in both critical plane criteria. The critical plane estimates obtained without the accumulated damage approach (BS), were $\pm 25$ for SWT and $\pm 21^{\circ}; \pm 69^{\circ}$ for F-Socie, respectively.

In sub-figure 5.19 d) it is shown the block multiaxial stress components time variation, moreover in sub-figure 5.19 e), it is presented the WB results, here the WB methodology yields 6 reversals, which is the same value extracted with the BS method. Also here, the WB method identifies the last reversal as the most damaging one, as seen in Case 3.

In sub-figure 5.19 f) it is presented the SSF time variation for this loading block. The SSF vitual cycle counting methodology extracts 4 reversals and the Rainflow method extracts 6 reversals from the SSF equivalent stress time evolution depicted in sub-figure 5.19 f). The loading sequence variation between Case 3 and Case 4 do not affect substantially the critical plane estimates and the experimental crack initiation plane, as it can be seen by comparing the theoretical and experimental results from both loading cases.

The loading Case 5 is presented in Figure 5.20 a), this is a loading block composed by several proportional loading branches with different stress amplitude ratios (SAR), the loading sequence is given by the number sequence depicted in Figure 5.20 a).

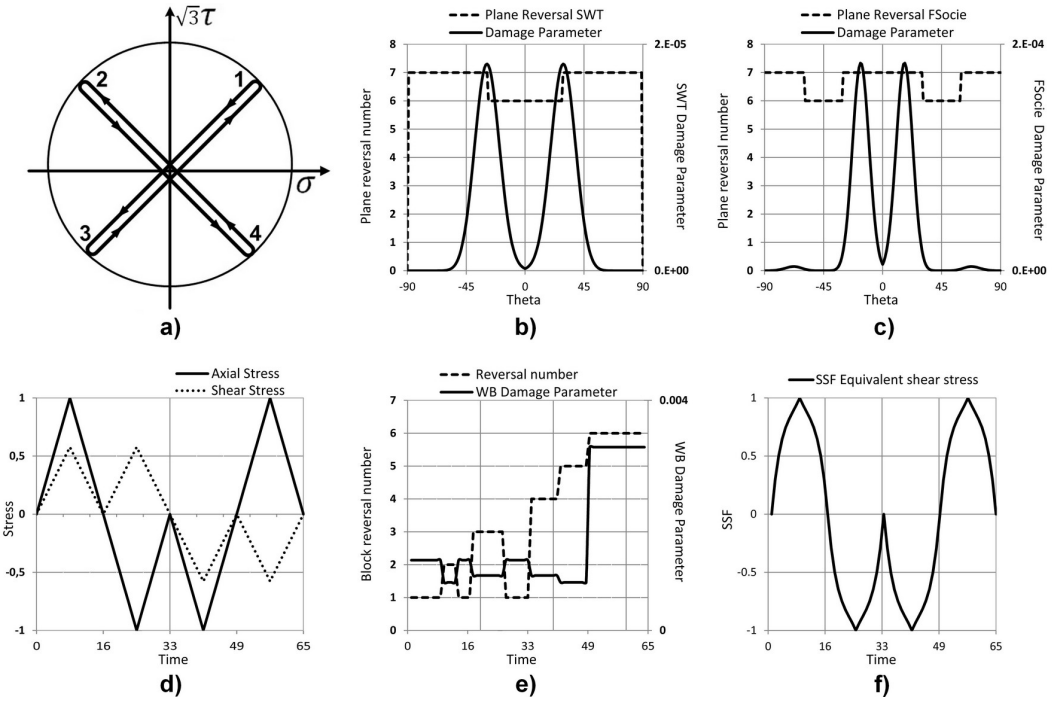


**Figure 5.19:** Case 4: a) von Mises stress space, b) BS results with SWT c) BS results with FSocie d) Block stress time evolution e) WB results and f) SSF time evolution.

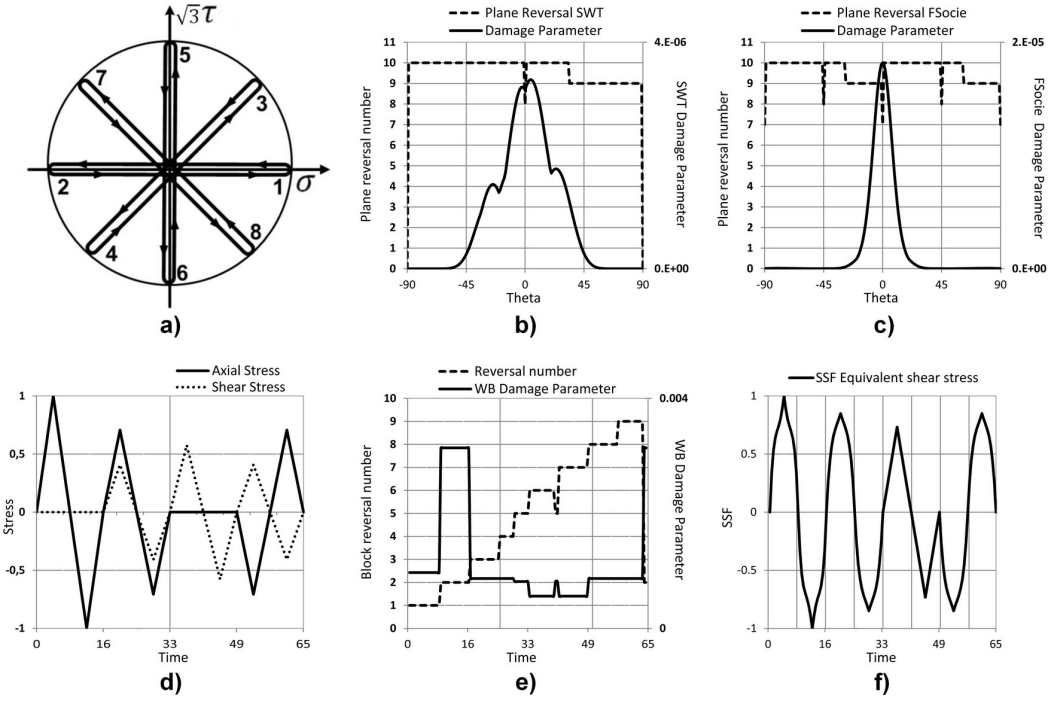


**Figure 5.20:** Case 5: a) von Mises stress space, b) BS results with SWT, c) BS results with FSocie, d) Block stress time evolution, e) WB results, and f) SSF time evolution.

The experimental crack initiation plane for this loading block was 0° [161]. The Bannantine and Socie method yields 10 reversals for this loading block under the SWT and F-Socie damage criteria. The critical plane estimates under the BS accumulated damage approach were 4° for SWT and 0° for F-Socie. The critical plane estimates obtained without

using the BS damage accumulation approach was 0° in both SWT and F-Socie criteria. Regarding the results of the WB methodology, it was extracted 9 reversals from this loading block, minus 1 reversal than the ones obtained by the critical plane approach in association with the BS method. The SSF virtual cycle counting method extracts 6.8 reversals from the SSF equivalent stress time evolution, and the Rainflow methodology extracts 10 reversals.

Figure 5.21 a) shows the loading Case 6, which is similar to Case 5. These two loading blocks have different loading sequences, which is given by the numeric sequence depicted in the von Mises stress space, please see Figure 5.21 a) and Figure 5.20 a). The experimental critical plane was measured at 6° [3].

In this loading block the BS yields 10 reversals in the SWT criterion and 11 reversals in the F-Socie on the most loaded plane. The BS critical plane estimates were 2° for the SWT criterion and 0° for F-Socie, respectively. The critical plane estimates without the BS damage accumulation approach was 0° for both SWT and F-Socie criteria.

The WB methodology extracts 14 reversals from this loading block and the most loaded reversal was the number 8. The SSF virtual cycle counting methodology extracts 6.8 reversals, and the Rainflow methodology extracts from the SSF equivalent stress time evolution 14 reversals.

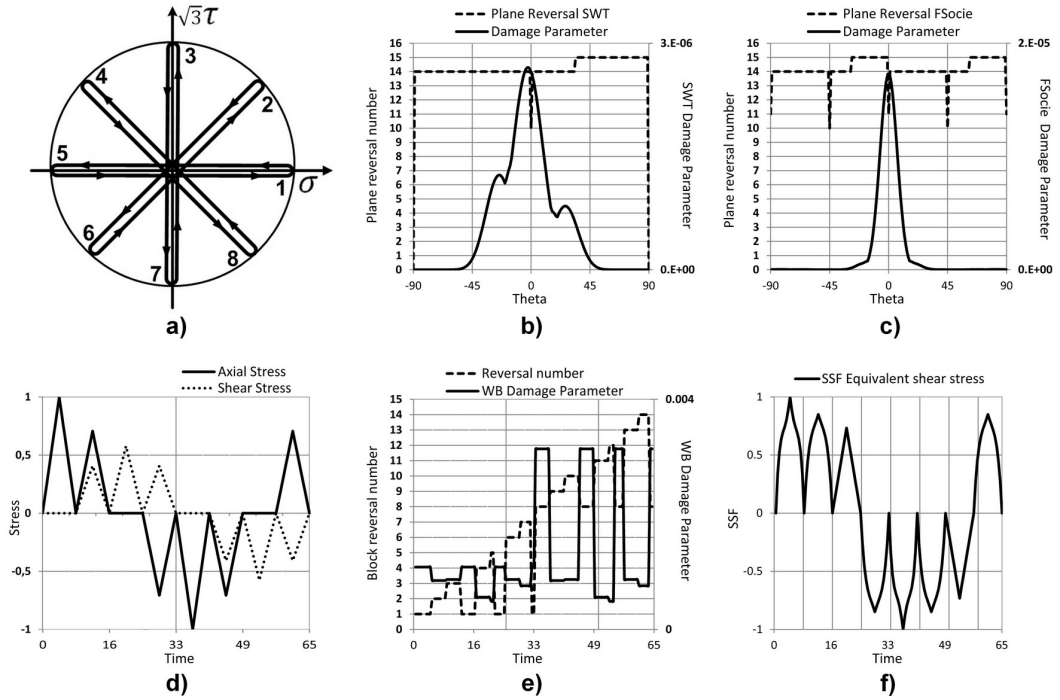


**Figure 5.21:** Case 6: a) von Mises stress space, b) BS results with SWT, c) BS results with F-Socie, d) Block stress time evolution, e) WB results and, f) SSF time evolution.

Fig.(s) 5.22 to 5.24 show the results for loading Cases 7, 8 and 9, respectively. These loading blocks are asynchronous loadings where the shear stress loading frequency is five

times greater than the normal stress amplitude. The difference between these loading blocks is based in the variation of their stress amplitude ratios having 2, 0.5 and 0.6 as SAR, respectively. In loading Cases 8 and 9 the normal stress amplitude is greater than the shear stress amplitude, in Case 7 the opposite occurs, the shear stress amplitude is twice the normal stress amplitude. The results obtained for loading Cases 8 and 9 are very similar, thus a slight SAR variation has little influence in the computed number of reversals and accumulated fatigue damage.

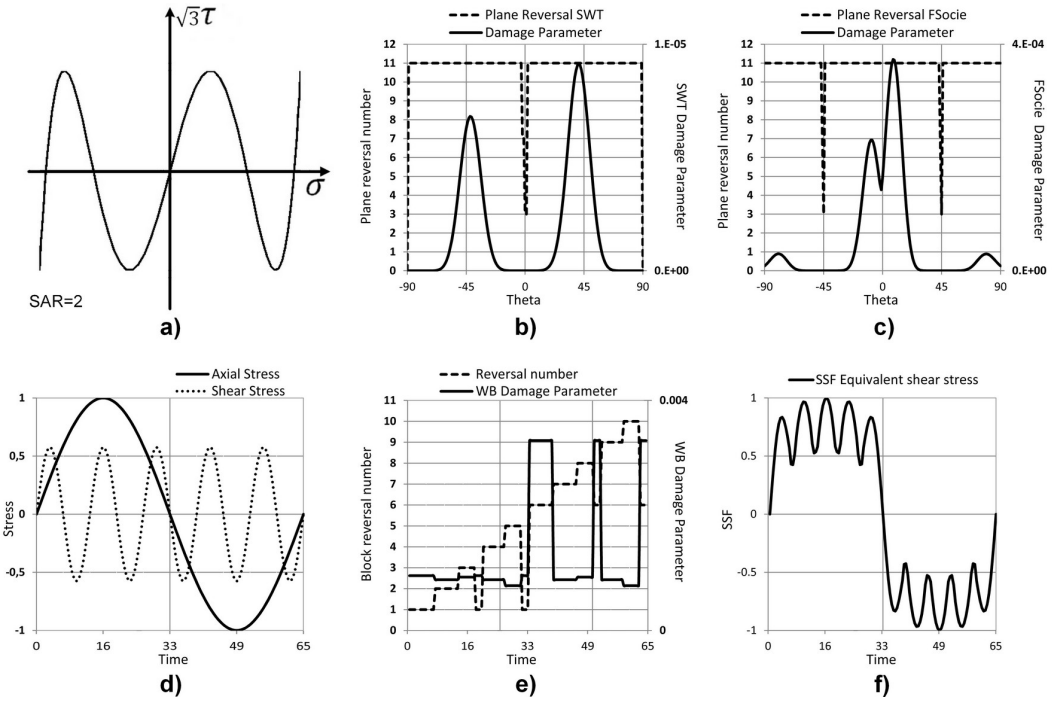


**Figure 5.22:** Case 7: a) von Mises stress space, b) BS results with SWT, c) BS results with F-Socie d) Block stress time evolution, e) WB results, and f) SSF time evolution.

Regarding the results of loading Case 7, please see Figure 5.22, it can be seen a strong influence of the SAR increase in the accumulated damage variation in respect to $\theta$, comparatively to the results obtained in loading Cases 8 and 9.

In loading Cases 8 and 9, the Bannantine and Socie method extracts 11 reversals in both critical plane criteria. The BS critical plane estimates, in Cases 8 and 9, were 24° and 26° based in the SWT criterion, and based in the F-Socie criterion were −20° and −19°. In Case 8, the critical plane estimates without a damage accumulation criteria were −25° and 23° based in the SWT criterion, and based in the F-Socie they were −39° and 38°. Moreover, in Case 9 the critical plane estimates were −23° and 25° in the SWT criterion, and in the F-Socie criterion they were −20° and 70°. The critical plane estimates in loading Case 7 were 41° for SWT, and 8° for F-Socie. The experimental results for the crack initiation plane in loading Cases 7, 8 and 9 were −19°, −22° and −19° [9, 162], respectively. The critical plane estimates without the accumulative damage approach (BS method) were −39°; 38° in the SWT criterion, and −13°; 12° in the F-Socie criterion.

Regarding the results for the SSF virtual cycle counting method in loading Cases 7, 8 and 9, it was computed 2, 1.8 and 1.8 cycles, respectively. The Rainflow results based in the SSF equivalent stress time evolution yields 19, 27 and 27 reversals in Cases 7, 8 and 9, respectively.

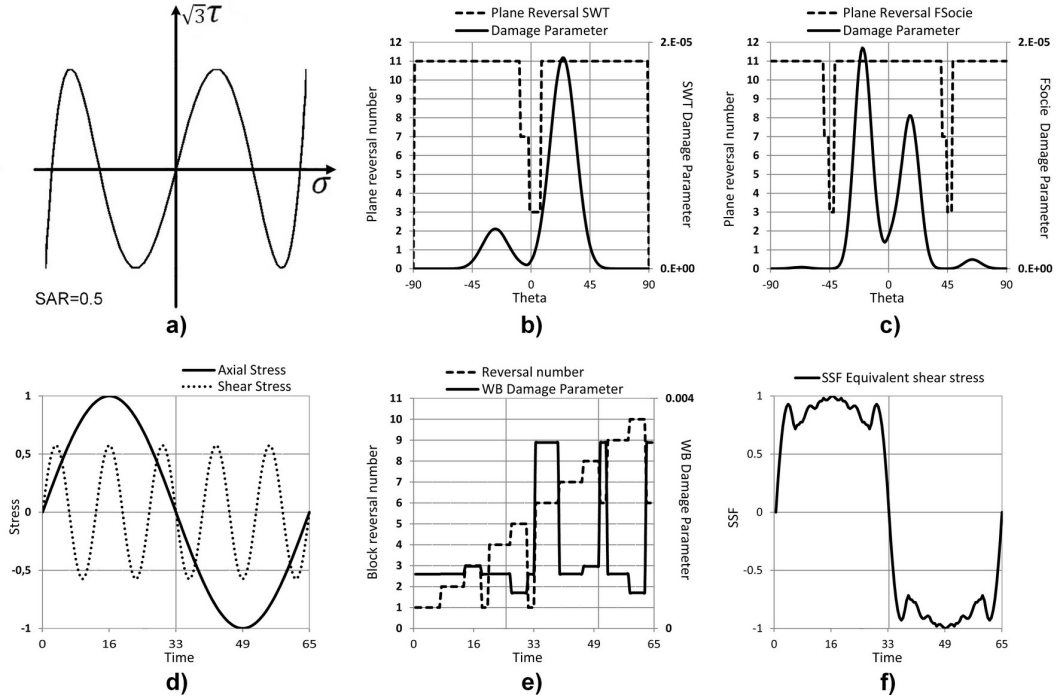


**Figure 5.23:** Case 8: a) von Mises stress space, b) BS results with SWT, c) BS results with F-Socie, d) Block stress time evolution, e) WB results, and f) SSF time evolution.

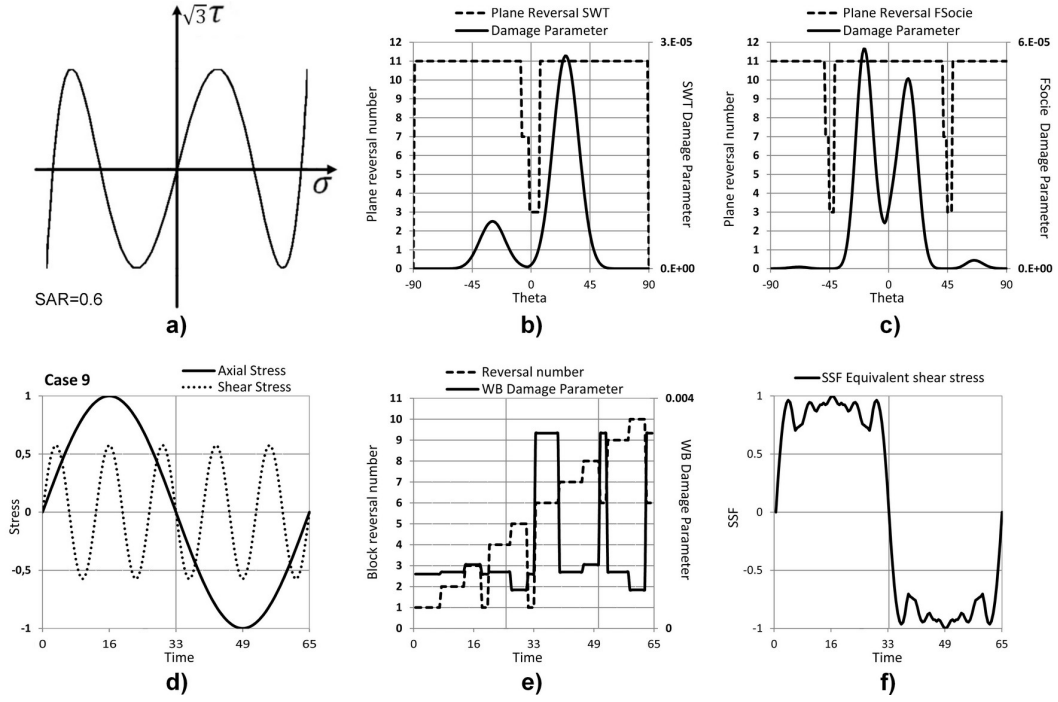


**Figure 5.24:** Case 9: a) von Mises stress space, b) BS results with SWT, c) BS results with F-Socie, d) Block stress time evolution, e) WB results, and f) SSF time evolution.

The results of loading Cases 10 and 11 are presented in Fig.(s) 5.25 and 5.26. These loading blocks are asynchronous loadings where the shear stress loading frequency is twice the normal stress frequency in Case 10, and in Case 11 the normal stress loading frequency is twice the shear one.

In loading Case 10, the BS method extracts from the loading block time evolution the same number of reversals in the SWT and F-Socie criteria on the most loaded plane (plane with higher accumulated damage parameter). The BS critical plane estimates were $-28^{o}$ for the SWT criterion, and $15^{o}$ for the F-Socie criterion. In this case the experimental crack initiation plane was $-18^{o}$ [162]. The critical plane estimates, without an accumulate damage approach, were $\pm 25°$ for the SWT criterion, and $\pm 17°$; $\pm 73°$ for the F-Socie. The WB yields 4 reversals for this loading block (Case 10) where the most damaging reversal occurs at the last quarter of the loading period.

Regarding the results of loading Case 11, the BS method yields the same number of reversals achieved for loading Case 10, i.e. 5 reversals at most loaded plane. The critical plane estimates under the BS accumulative approach was $-22^{o}$ for the SWT and $\pm 17^{o}$ for the F-Socie criterion, the experimental crack initiation orientation was $-23^{o}$ [162]. The critical plane estimates without the BS accumulative approach were $\pm 21^{o}$ for the SWT criterion, and $\pm 23^{o}$; $\pm 67^{o}$ for the F-Socie criterion. The WB extracted 4 reversals from the loading block 11, where the most damaging reversal occurs in the last quarter of the loading period.

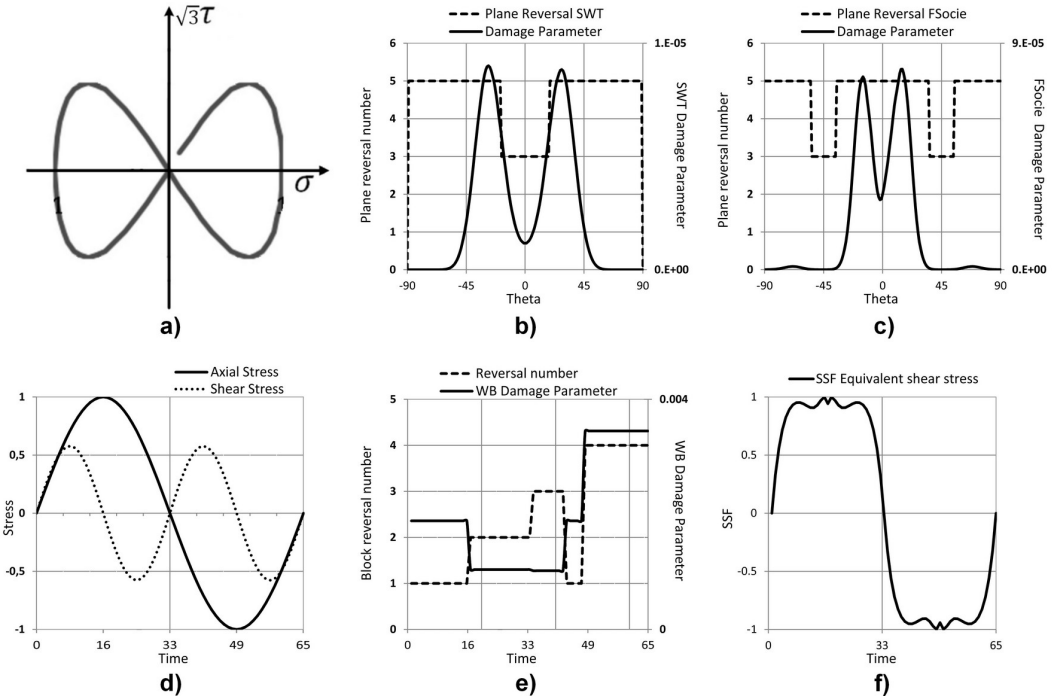


**Figure 5.25:** Case 10: a) von Mises stress space, b) BS results with SWT, c) BS results with F-Socie, d) Block stress time evolution, e) WB results, and f) SSF time evolution.

Regarding the results of the SSF virtual cycle counting method for loading Cases 10 and

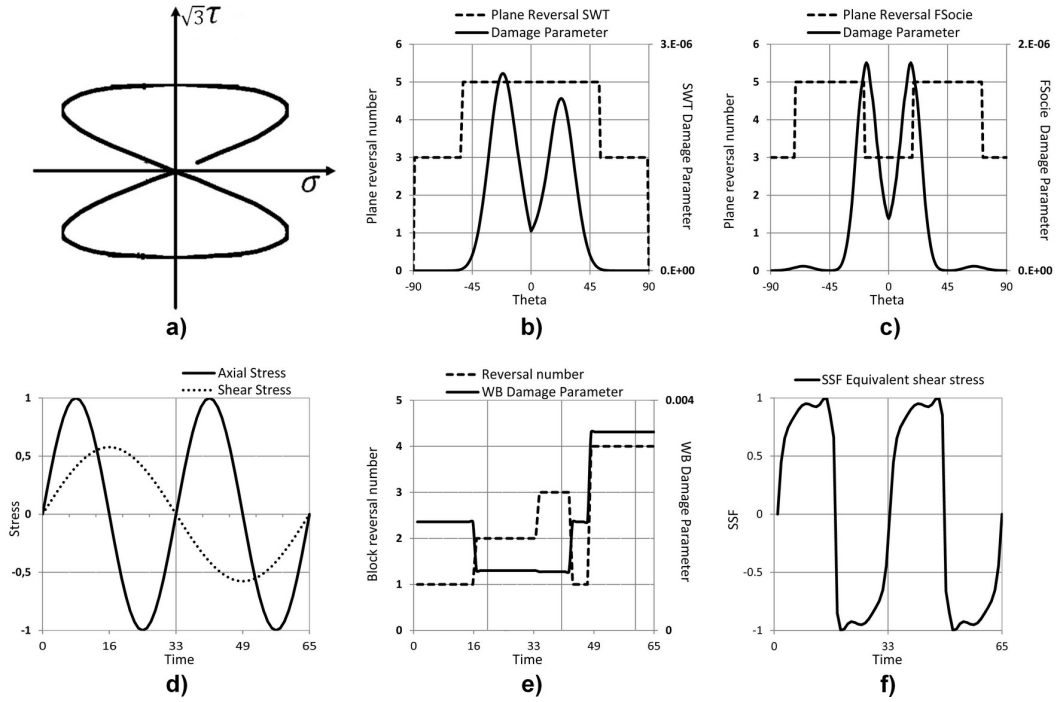


**Figure 5.26:** Case 11: a) von Mises stress space, b) BS results with SWT, c) BS results with F-Socie, d) Block stress time evolution, e) WB results, and f) SSF time evolution.

11, the extracted loading cycles were 1.8, and 1.4, respectively. The Rainflow results based in the SSF equivalent stress time evolution yields 14 and 23 reversals for loading Cases 10 and 11, respectively.

Table 5.4 presents a summary of the critical plane estimates under the BS accumulative approach. Based on these results it can be concluded that the SWT and the F-Socie criteria in association with the Bannantine and Socie cycle counting methodology have a similar accuracy regarding the estimates of the crack initiation plane. Moreover, it can be concluded that the critical plane estimates without an accumulating damage approach are very alike to the ones obtained with the accumulated Bannantine and Socie methodology.

Table 5.5 summarizes the results of the cycle counting methods used to evaluate each loading block considered in this section.

The results gathered in Table 5.5 show that the critical plane estimates are not improved with the Bannantine and Socie cycle counting methodology neither with its damage accumulation approach i.e. the critical plane estimates with the BS accumulative damage approach and without it are very similar. However, the BS accumulative damage approach yields different fatigue life estimates comparatively to the ones achieved without an accumulative damage approach. The Bannantine and Socie cycle counting methodology is based in a physical behaviour by using the Rainflow methodology to account the loading block reversals at each plane.

In contrast, the Wang and Brown methodology identifies damaging reversals within the

**Table 5.4:** Critical plane results for the selected loading blocks under the BS criterion.

| Case | SWT | F-Socie | Experiment |
|---|---|---|---|
| 1 | 0° | 0° | −5° |
| 2 | ±45° | 0° | 0° |
| 3 | ±30° | ±16° | 29° |
| 4 | ±29° | ±17° | 31° |
| 5 | 4° | 0° | 0° |
| 6 | −2° | 0° | −6° |
| 7 | 41° | 8° | −19° |
| 8 | 24° | −20° | −22° |
| 9 | 26° | −19° | −20° |
| 10 | −28° | 15° | −18° |
| 11 | −22° | ±17° | −23° |

**Table 5.5:** Cycle counting results for the Bannantine and Socie, Wang and Brown, and the SSF approaches obtained with the vcc and the Rainflow methods.

| Case | BS - SWT block cycles at most loaded plan | BS-FS block cycles at most loaded plan | WB block cycles | SSF virtual block cycles | SSF Rainflow cycles |
|---|---|---|---|---|---|
| 1 | 2 | 1.5 | 2 | 1.7 | 2.5 |
| 2 | 2.5 | 1.5 | 2 | 1.8 | 2.5 |
| 3 | 3.5 | 3.5 | 3 | 2.1 | 2.5 |
| 4 | 3 | 3.5 | 3 | 2.0 | 3 |
| 5 | 5 | 3.5 | 4.5 | 3.4 | 5 |
| 6 | 7 | 5.5 | 7 | 3.4 | 7 |
| 7 | 5.5 | 5.5 | 5 | 1.0 | 9.5 |
| 8 | 5.5 | 5.5 | 5 | 0.9 | 13.5 |
| 9 | 5.5 | 5.5 | 5 | 0.9 | 13.5 |
| 10 | 2.5 | 2.5 | 2 | 0.9 | 7.5 |
| 11 | 2.5 | 1.5 | 1.5 | 0.7 | 6.5 |

loading block without any logical connectivity to the physical damage process, thus it is not clear in this method why certain reversals are more damaging than others. Despite that, both methods have a very similar results regarding the block reversals extraction, in some loading cases no significant differences were found. The maximum difference between the results computed for these two methods was 2 reversals in loading Cases 5 and 11. In the other loading cases considered here, the difference found between cycle counting methods was 1 reversal or less.

The SSF virtual cycle counting methodology in some loading cases yields a number of reversals less than one, please check the results regarding loading Case 11 presented in Table 5.5 where the SSF virtual cycle counting extracts 1.4 reversals, which is one reversal plus 40% from other one. These results can be explained by recalling the SSF virtual cycle paradigm which is based on the SSF equivalent stress time evolution. In this paradigm the number of cycles within a loading block are calculated by the summation of the peaks and valleys divided by the maximum peak values, in this way, it is determined the block unitary damage under the SSF approach. Therefore, the results of the SSF virtual cycle counting method can not be round-up or round-down as seen in the Rainflow based cycle counting methods. The values of the SSF virtual cycle counting method were inferior to the ones obtained with the Bannantine and Socie, and Wang and Brown methods, however the Rainflow results based in the SSF equivalent stress time evolution were in most cases similar to the BS and WB results, but there were cases where the results were greater.

### 5.4.5 Vcc, WB, and BS fatigue life correlation

In order to estimate the loading blocks fatigue lives, it is necessary to take a multidisciplinary approach in fatigue life characterization, because multiaxial loading blocks have much more complex loading histories than the reference loadings where the loading cycle identification is a straightforward procedure. Therefore, under complex loading histories it is usually used three main multiaxial fatigue methods to estimate fatigue life for complex loading histories, namely, a damage parameter criterion, a cycle counting method,and a damage accumulation rule. The inner issue related to this fatigue life paradigm (criterion, method, and rule) is based on the damage parameter definition; this parameter must translate the physical fatigue damage mechanism in order to allow the use of a cycle counting method and an damage accumulation rule.

Usually, the maximum damage parameter obtained on a specific reversal is insufficient to capture the total fatigue damage of a loading block, and it yields unsatisfactory estimates under complex loading histories. Thus, it is necessary to discriminate the loading block into reversals using a cycle counting methodology in order to compute the loading block unitary damage. After that, it is necessary to compute the contribution of each loading block to the overall damage by using a damage accumulation rule. The reversals extraction from complex loading paths must be always associated to the value of the damage parameter in

order to account the stress level effect on the block unitary damage. Figure 5.27 presents the fatigue life correlation between the theoretical estimates and experimental results for the Bannantine and Socie cycle counting method. Fig.(s) 5.27 a) and b) show the BS correlation based in the SWT criterion and Fig.(s) 5.27 c) and d) show BS correlation based in the F-Socie criterion.

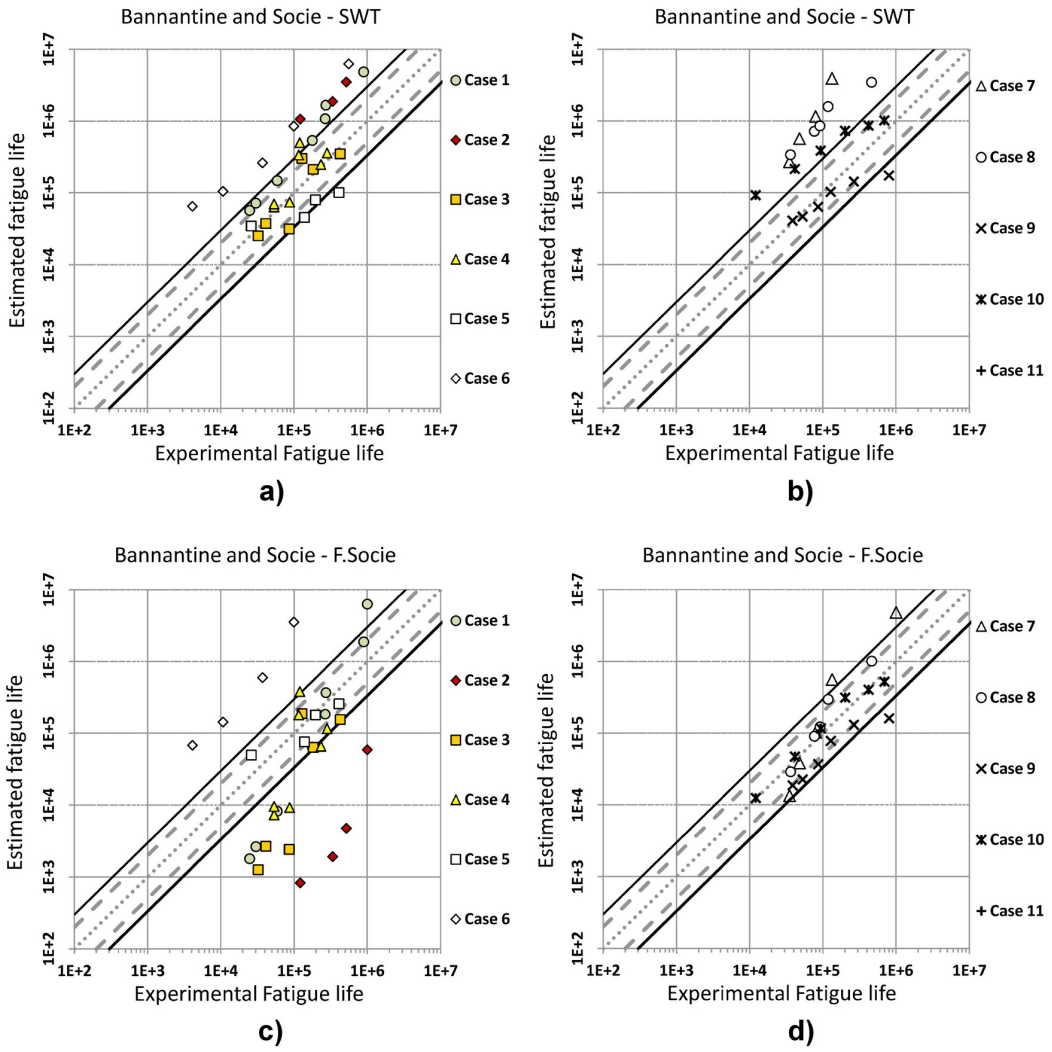


**Figure 5.27:** Fatigue life correlation for BS in association with SWT: a) and b) and c), d) with F-Socie damage parameter.

Based on the results depicted in Figure 5.27, it can be seen that the SWT criterion yields an accumulative damage parameter too low, because the results of the fatigue life correlation tends to be above of the upper boundary line. Regarding the BS fatigue life results based in the F-Socie criterion, it can be seen that the correlation yields an inconclusive trend in the Cases 1 to 6 where a big scatter can be found. In contrast, in the Cases 7 to 11, the fatigue life correlation is very acceptable, where only two results were found outside of the boundary lines. The Wang and Brown fatigue life correlation is shown in Figure 5.28. In sub-figures 5.28 a) and b) it is presented the WB results for $S = 0.3$ which sets

up the Wang and Brown damage parameter to the infinite fatigue life (1E6 cycles). In sub-figures 5.28 c) and d), it is shown the fatigue life correlation for $S = 0.7$ that sets up the Wang and Brown method to half fatigue life. The fatigue life correlation in Cases 1 to 6 have also a big scatter, as seen in the Bannantine and Socie method, for both $S = 0.3$ and $S = 0.7$.

However, in this scatter it can be seen a accumulative damage parameter too high in Cases 1 to 6, where the correlation results tends to be under the lower bond of the fatigue life limits (life factor equal to 3). Nevertheless, the results for Cases 7 to 11 show an improved fatigue life correlation, where it can be found very acceptable results for $S = 0.7$, likewise to the observed in the Bannantine and Socie method.

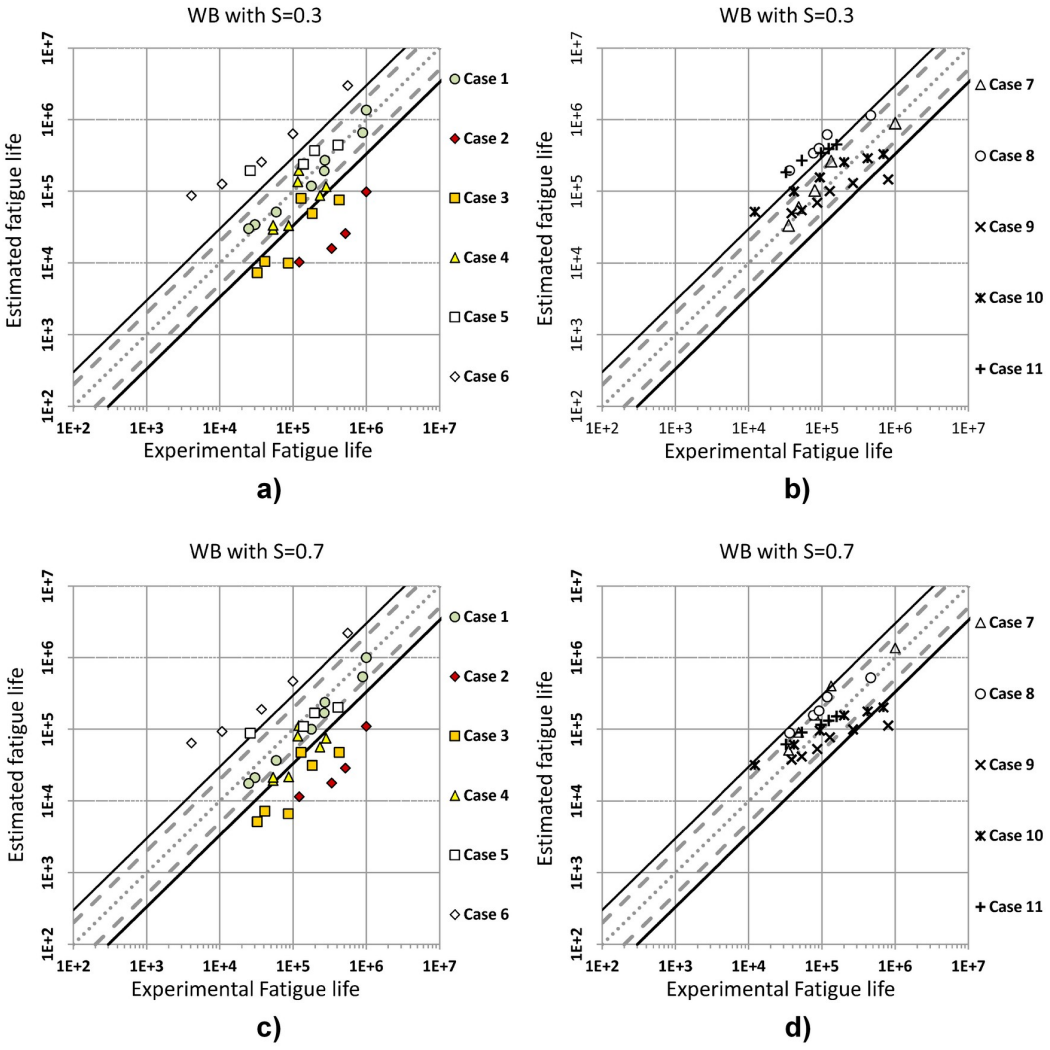


**Figure 5.28:** Fatigue life correlation for WB with S=0.3: a), b), and with S=0.7: c), d)

Figure 5.29 shows the SSF fatigue life correlation with experimental results, as it can be seen the fatigue life correlation has very acceptable results. The scatter found in Cases 1 to 6 shown in the Bannantine and Socie and Wang and Brown methods is reduced here

with the SSF virtual cycle counting methodology. Also the results for loading Cases 7 to 11 are within the fatigue life boundaries where only 2 points are outside of the limits. The SSF's scatter in these loading blocks is more reduced comparatively to the results obtained in the Bannatine-Socie and Wang-Brown cycle counting methods.

Based on the SSF fatigue life correlation results, it can be generalized the idea in which the SSF virtual cycle counting method associated to the SSF equivalent stress is at the same level of the Bannatine-Socie or Wang-Brown methods, but with the advantage to be a simpler cycle counting method and a quicker methodology to estimate fatigue lives for loading blocks. The complexity of the reversals extraction found in the Bannantine-Socie and Wang-Brown cycle counting methodologies makes these methods prone to errors being not practical to implement manually or even within a numeric code.

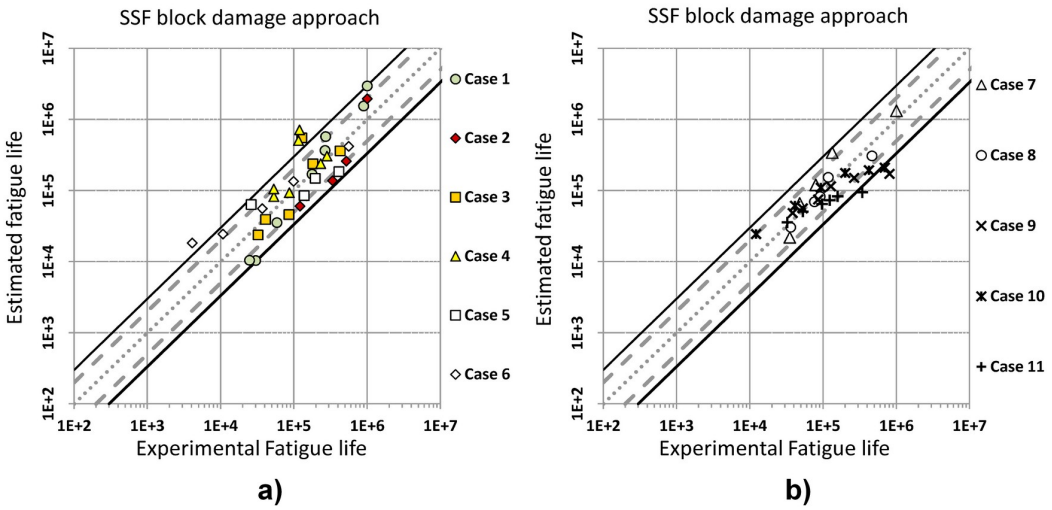


**Figure 5.29:** Fatigue life correlation for the SSF virtual cycle counting in association with the SSF equivalent shear stress: a) Cases 1 to 6, and b) Cases 7 to 11.

## 5.5 Final comments

In this chapter, it was proposed a new cycle counting methodology based on the SSF equivalent shear stress time evolution to estimate fatigue life of complex loading blocks under multiaxial loading conditions. The capability of the SSF virtual cycle counting method to successfully estimate fatigue lives of loading blocks was analysed based in experimental fatigue data from 11 multiaxial loading blocks in order to be validated as a new cycle counting method.

Moreover, it was evaluated two state-of-the-art multiaxial cycle counting methods, the Bannatine-Socie and the Wang-Brown methods, in order to make a comparison between their capability to deal with the fatigue damage characterization of loading blocks. The SSF estimates were successfully correlated with the experimental fatigue life data, having a slight advantage over the estimates yield by the Bannatine-Socie and the Wang-Brown

methods. Also, it can be concluded that the simplicity to implement the SSF virtual cycle counting method, comparatively to the other methods considered here, is a strong point in favour of the new proposal.

# Chapter 6

# Contributions to Level 4

## 6.1 Introduction

In this chapter, it is used the tools developed in the previous chapters to evaluate multiaxial damage accumulation under random loading conditions in order to inspected the SSF equivalent stress performance under random loading conditions using a linear damage accumulation approach. The nature of the method present here is quite different from the conventional or traditional multiaxial fatigue damage evaluation which is traditionally addressed to mechanical design routines in mechanical design. The idea is to take several tools such as damage parameters, multiaxial cycle counting methods, multiaxial fatigue loading effects characterization, and use these tools in the structures damage monitoring for instantaneous damage evaluation. This concept will allow to monitor the structural health of structures in a instantaneous way which can be very useful in replace/repair decisions as well as prevent more demanding regimes in the field. Figure 6.1 shows the fatigue level inherent to this chapter.

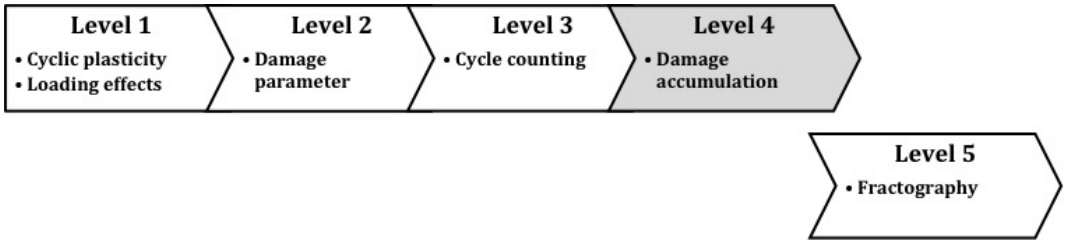


**Figure 6.1:** Multiaxial fatigue level focused in this chapter.

One important decision to make about maintenance occurs when a part or component should be replaced due to fatigue damage. For instance, in aeronautics some parts of aircraft have a kind of fly hours stock that can be expended with a rate defined by the fly manoeuvre regime. When the stock of flight hours is totally expended, the part or structure of the aircraft must be substituted. In some cases, replacing an aircraft's part can be quite costly and time-consuming. Therefore, the replacing decisions based on fatigue damage

assessment by local stress/strain measurements performed by wire or wireless could be a way to optimize resources. The critical parts monitoring allows to compute local stresses and their inherent local fatigue damages at the structures most loaded regions. Therefore, in this way, the decisions of replacing parts would be based in the local stress/strain time histories and not based on projections of damage accumulation. This is an important subject, because local measurements will allow to interpret loading path features and their effect on fatigue damage during the loading period, which is an important information in the fatigue damage assessment of random loadings.

It is well-known that the loading path type has a huge influence in the fatigue strength. Damage effects like non-proportionality, proportionality, sequential, asynchronous, mean stresses, among others, lead to different rates of fatigue damage [16, 52, 63].

Under multiaxial random loading conditions, some of the aforementioned loading effects may be activated individually or simultaneously. Thus, fatigue damage assessment under such loading conditions (random loadings) must have into account the fatigue damage inherent to each loading type found in each loading block extracted from a loading spectra. Furthermore, those effects may have different damage levels according to the load level and may differ from material to material.

In some cases, the loading path effect could be more damaging in one material than in other one, because of that, and in cases of major importance, it is recommended to have for each material a damage map, like the SSF damage map presented in Chapter 4, which is obtained by experiments. Therefore, an universal procedure to capture all kind of damages found within a loading spectrum without having into account the material cyclic properties, such as the g-counts of the aircraft's flight history, can lead to a very conservative replacement decisions, waste of money, and cut of incomings.

The random fatigue approach aims to characterize fatigue damage from loadings with unknown time histories, i.e. in the field a given mechanical part will be subjected to unknown loadings, which is a loading conditions quite different from the ones usually performed in the lab. Therefore, these kind of loadings are quite difficult to simulate in the lab, because the most common fatigue testing machines needs an input file to operate, which is read in a closed loop in order to load the sample according to a predetermined loading path, and due to that, the aleatory nature always present in random loadings is loss.

One way to overcome this issue is to record the stress/strain time variation obtained in the field to be used as machine input. Nevertheless, in the field nothing is totally random, for instance when car suspension travels the same path every day, the random forces in the car suspension will have a similar pattern every day, but not the same pattern. Another example of a structure subjected to complex loadings is the wind towers used in energy harvest. In this case, the tower structure is subjected to wind patterns

which can be quite random and damaging, ranging from laminar to turbulent flows [163, 164]. These structures are positioned in strategic places to be subjected to the highest wind forces to optimize the energy harvest. Other examples are the ship and offshore structures where the waves with random pattern induce random loadings in the structures. These cases are examples of multiaxial random loadings in harsh environments which have features that influences and increases fatigue damage, such as corrosion, for instance [165]. Anodic corrosion that results from electric polarization between metal and sea water creates micro-notches that locally, creates stress raisers. It is well-known, that the loading path effect on fatigue damage is strongly influenced by micro-notches [166–168]. Thus, the loading effects under corrosive environments must be treated with extra care.

As aforementioned, random loadings are very different from the ones traditionally made in lab. However, there are some cases where the loading pattern in the field can be successfully modulated in lab, for instance the loadings found in power shafts is one example of that. Despite the huge amount of random loading patterns found in the field, in literature it can be found very few works related to the damage assessment of random loadings.

Many multiaxial fatigue models were designed to be used under lab loading conditions, which can be quite different from the ones found in the field. One reason that can explain such evidence is the necessity of a multidisciplinary approach, that covers all fatigue fields, to characterize multiaxial fatigue damage from a loading spectra [167, 168]. To characterize random multiaxial fatigue it is necessary to have a damage parameter such as an equivalent stress, a robust cycle counting method and an accumulative damage rule. Multiaxial random fatigue is the ultimate stage in fatigue life assessment because it takes into account several multiaxial fields that usually are tackled separately. Moreover, the available cycle counting methods in literature are very few especially for multiaxial loading conditions. Most of them are very complex to carry out and takes a huge amount of computational resources, which can be a shortcoming for the on-line damage assessment approach such as the ones used in structural health monitoring. Also, the wide used multiaxial cycle counting methods based on the Rainflow method do not show, so far, good correlations with experimental lab data even for well-defined loading paths.

In mechanical design, structures can be designed for multiaxial complex loading regimes under an assumption that the loading spectrum used in design is representative of the damage found in the field. However, despite being a valid approach, such procedure only indicates a fatigue life estimate if the loading history in the field is equal to the spectrum used in design stages. Therefore, if the structure or mechanical part is loaded outside of the design-loading spectrum the estimates obtained in design stages are meaningless. Thus, it is important to have a reliable loading spectra based in the field patterns to estimate structural damage under random loading conditions. Health monitoring is commonly

made using mechanical vibration techniques and stiffness variation analysis among other techniques. However, in terms of vibration, fatigue damage is only detectable when a fatigue crack begins to growth (nowadays it is not possible to monitor crack initiation using mechanical vibration techniques). In some materials, usually high strength steels, the time spent in crack growth is very short (most of the time is spent in crack nucleation), i.e. the remaining time until failure after the crack starts to grow is very short. Therefore, fatigue damage monitoring based on crack growth can be quite dangerous in some cases.

## 6.2 SSF and the linear damage accumulation

In this section, it is not proposed a damage accumulation rule, as a matter of fact the present author uses the linear damage rule proposed by Palmgren and Miner as a valid tool to be used in damage accumulation assessment. Some shortcomings were pointed out in literature regarding this damage accumulation rule, which are based in erroneously perceived interpretations. In the present author point of view, the shortcomings pointed out result mainly from the incapacity of their damage parameter to capture the material constitutive behaviour under certain loading conditions. For instance, the Hi-Lo or Lo-Hi sequence effects on the material damage cannot be captured by a Palmgren-Miner type rule, because it only computes the fraction of damage consumed and does not have mechanisms to account with the material cyclic behaviour. Thus, the load features must be captured by the damage parameter and constitutive models and not by a damage accumulation rule.

In the aforementioned loading cases (the Hi-Lo or Lo-Hi sequences), a damage parameter is obtained by local stress-strains measurements, which must be updated by an elastic-plastic model, such as the one proposed in Chapter 3 (the HYS model), in order to account with the material cyclic properties variation due to the stress level variation. Thus, it makes sense that the Palmgren-Miner rule cannot capture the material hardening or softening due to the stress level or loading type. However, if the damage parameter captures these effects then the Palmgren-Miner rule will give acceptable results.

It is stated in literature that the Palmgren-Miner rule estimates erroneously the overall damage at the collapse instant, i.e. in some cases failure occurs for an accumulated damage greater than one and in other cases occurs for an accumulated damage less than one. These results are expected and there is nothing wrong with the Palmgren-Miner rule concept, because in multiaxial fatigue damage characterization it is always present the statistical behaviour typically found in fatigue life experiments. It is not possible or it is very unlikely to get the same fatigue life in different samples for the same testing conditions. Therefore the S-N curve is a type of statistical curve which for a certain stress load gives the most probable fatigue life. The Palmgren-Miner linear damage rule will be used in association with the SSF equivalent shear stress in order to account accumulated fatigue damage under

random loading conditions. Eq. 6.1 presents the Palmgren-Miner damage rule where $N_i$ is the maximum number of loading cycles before failure at certain stress level of the SSF equivalent stress, and $n_i$ is the number of cycles performed at the SSF equivalent stress level mentioned above. In this damage accumulation rule, failure is expected when the damage summation reaches or overcome the value 1.

$$\sum_{i=1}^{I} \frac{n_i}{N_i} \geq 1 \tag{6.1}$$

As illustration, consider a constant amplitude loading at certain stress level, the maximum number of loading cycles before failure is estimated based on that stress level in association with the material S-N curve, which gives the $N_i$ value. Now, if the number of loaded cycles $n_i$ equals the value $N_i$ thus the damage summation equals 1 with only one stress level. Thus, the S-N curve has embedded a linear damage summation, where each loading cycle is added until reach the collapse, this is another reason why it is chosen in this study a linear damage accumulation rule instead a non-linear one.

## 6.3 Multiaxial random fatigue damage characterization

The ultimate goal under multiaxial fatigue characterization is to find a way to deal with random multiaxial fatigue, this is an unsolved and complex problem that is dependent of several cornerstones related to the damage parameter formulation, cycle counting methods, block damage assessment and block extraction from random loading spectra. Also, multiaxial random fatigue is an unpopular subject due to the complexity involved and lack of knowledge in some pillars of multiaxial damage accumulation. However, mechanical components and structures are mainly subjected to multiaxial random stress states with variable amplitude, moreover, at design stages, it continues to be used simply fatigue loading paths as a reference in design of mechanical components and structures against fatigue. Moreover, at the present author knowledge, does not exist any methodology that deals effectively with accumulative damage under random loadings, especially under the loading conditions that can be found in the field.

### 6.3.1 Block extraction proposal

In this section, it is proposed a new method to evaluate, in real time, the accumulated damage that can be found in a loading spectra, where the multiaxial fatigue damage estimates are obtained using the SSF equivalent shear stress time evolution and the SSF virtual cycle counting method. The main idea behind this new method is to extract loading blocks from the loading spectrum recorded in the field in real time during service, and then evaluate their unitary damages and compute the overall damage with a linear damage accumulation rule.

Random damage characterization is mainly a block extraction issue, i.e. in order to evaluate multiaxial random damage it is necessary to identify the loading blocks within a recorded loading history (loading spectra), and for each loading block it is necessary to compute the inherent number of loading cycles as discussed in the previous Chapter 5. Thus, in the proposed method the normal and shear loading components of a loading spectrum are computed to obtain the SSF equivalent stress time evolution, from where it is extracted loading blocks to estimate multiaxial random accumulative damage. Afterwards, the fatigue damage of each extracted loading block, and their amplitude variation effect (sequential effect) is accounted using the Palmgren-Miner's rule. The paradigm proposed here to extract loading blocks from the SSF equivalent stress time evolution is depicted in Figure 6.2, where it is shown the block extraction methodology from a multiaxial random loading reduced to the SSF equivalent shear stress time evolution.

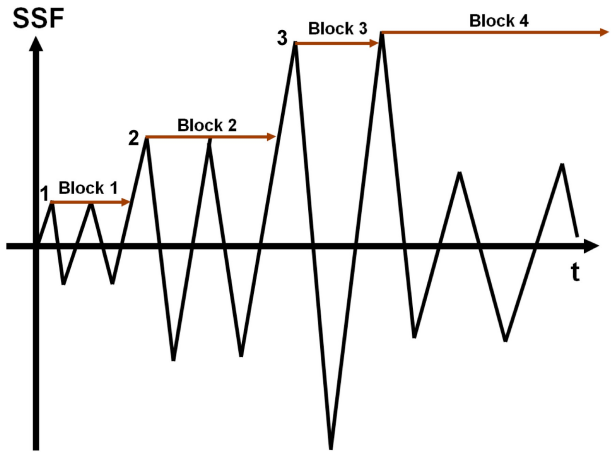


**Figure 6.2:** Loading blocks extraction from a random SSF equivalent shear stress time evolution.

The block extraction methodology is based on the SSF maximum peak found within the instantaneous SSF equivalent stress, the first maximum peak is set as damage reference to be used in the SSF virtual cycle procedures, please see point 1 in Figure 6.2. The damage reference is maintained until the SSF maximum peak is exceeded, as seen in point 2 of Figure 6.2, at point 2 the first block ends and starts the second block region with a new damage reference given by the SSF new peak at point 3 depicted in Figure 6.2. The same methodology is used to extract all other blocks from the loading spectrum. During the block extraction can be computed the inherent block damage, as follows in expression 6.2, and discussed in the previous Chapter 5.

$$D_{block} = \frac{1}{\frac{N_{block.peak}}{vcc_{block}}} \tag{6.2}$$

In Eq. 6.2, the number 1 is related to the number of extracted blocks which in this context is 1, in dominator it is represented the material fatigue strength estimated by the maximum SSF peak and updated with the virtual cycle counting found in the extracted

loading block. In order to estimate the instantaneous accumulated fatigue damage, the Palmgren-Miner's rule is used as follows in Eq. 6.3.

$$D_{SSF_{random}} = \sum_{1}^{i} \frac{1}{\left[\frac{N_{block.peak}}{vcc_{block}}\right]_i} \tag{6.3}$$

Eq. 6.3 can be used to compute the instantaneous accumulated damage, which is updated block by block until $D_{SSF_{random}}$ reaches the value 1, which is the damage accumulation trigger most used to estimate a high probability of fatigue failure.

## 6.4 Random fatigue life correlation

In this section, the SSF criterion capability to capture fatigue damage is scrutinized in order to validate its use in damage accumulation rules, such as the Palmgren-Miner's rule or the Morrows' rule. The main objective is to inspect the SSF performance to successfully estimate fatigue failure under complex accumulative loading conditions [88, 169]. To validate the aforementioned hypothesis, it was gathered from literature multiaxial random fatigue data obtained for the aluminium alloy 2024-T4 [134], in order to evaluate the performance of the SSF method for this type of aluminium alloys under random loadings. These data were obtained in the lab with loading spectra build with 16 loading paths (considered as loading blocks) randomly ordered, which is a clever way to simulate random loadings in the lab. The experimental results used here were obtained by Xia et al. in [134], however the experiments and methodologies used in their work are briefly explained in the following: The experiments were performed using a biaxial loading machine under stress control, and using tubular samples. The failure criterion was the specimen total separation. The main idea documented in [134] is to simulate random loadings based in 16 different loading paths, in which the loading paths random combination covers different loading effects as well has different load levels. The random loading condition was achieved by combining aleatory the loading sequence of the 16 loading paths and changing aleatory their stress level, thus the loading sequence is previously defined before testing. Moreover, each loading path in the predetermined loading block sequence, is loaded until reach 3% of its fatigue life. At the fatigue failure instant, the position of the loading sequence (actual loading path) and the number of cycles performed with the actual loading path is registered. Figure 6.3 presents the loading paths used in [134] to define the aforementioned random loading sequences. These loading paths were divided in three loading types, i.e. uniaxial, proportional, and non-proportional, and also by stress levels. The uniaxial loading conditions were covered by the pure axial (PT) and pure shear (PS) loadings, the proportional loading paths (PP) have a stress amplitude ratio (SAR) equal to 0.577 and 0.77, and the non-proportional loadings (NP) have a SAR ranging from 0.5 to 0.88 with phase shift equal to $30^0$, $45^0$, $60^0$, and $90^0$. Figure 6.4 shows the SAR variation

effect in the loading path shape. Figure 6.4 a) shows this effect in the proportional loadings considered in this study, and Figure 6.4 b) shows the same effect in the non-proportional loadings. Essentially, under proportional loadings, the SAR variation changes the slope of the loading path (depicted in the von Mises stress space), and in non-proportional loading cases it changes the shape of the loading path, i.e. the loading path changes from circular shape to an elliptical one as the SAR increases. The experimental fatigue data of each loading path are presented in Table 6.1.

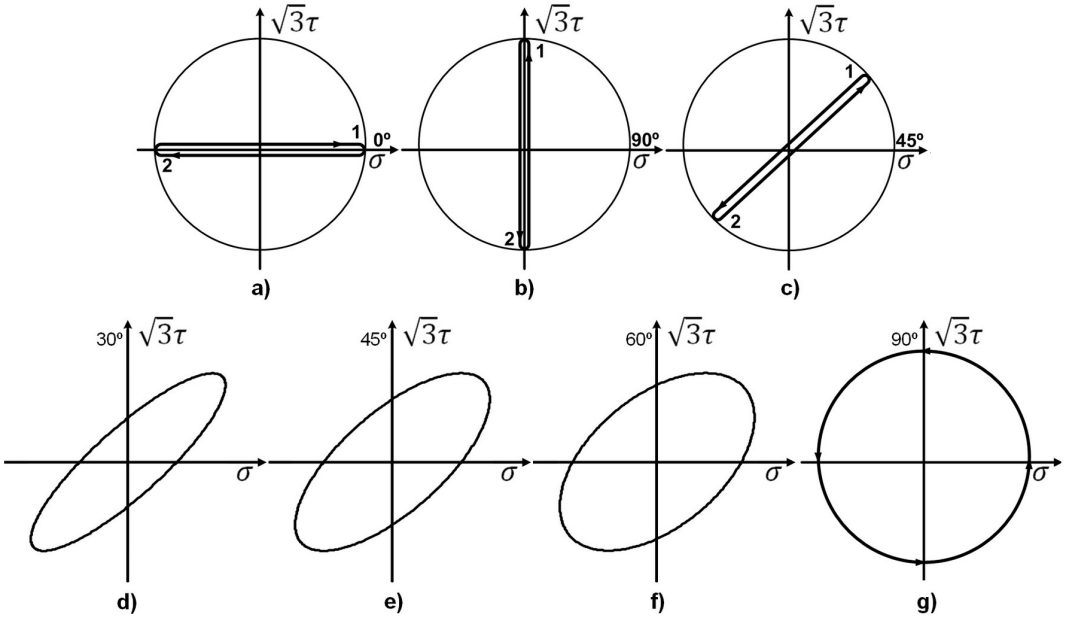


**Figure 6.3:** Multiaxial loading paths, (a) Pure axial (PT); (b) Pure shear (PS), (c) PP with SAR equal to 0.577 (PP45), (d) NP with phase shift equal to $30^0$ and SAR equal to 0.577 (30OP45), (e) OP with phase shift equal to $45^0$ and SAR equal to 0.577 (45OP45), (f) OP with phase shift equal to $60^0$ and SAR equal to 0.577 (60OP45), (g) OP with phase shift equal to $90^0$ and SAR equal to 0.577 (90OP45).

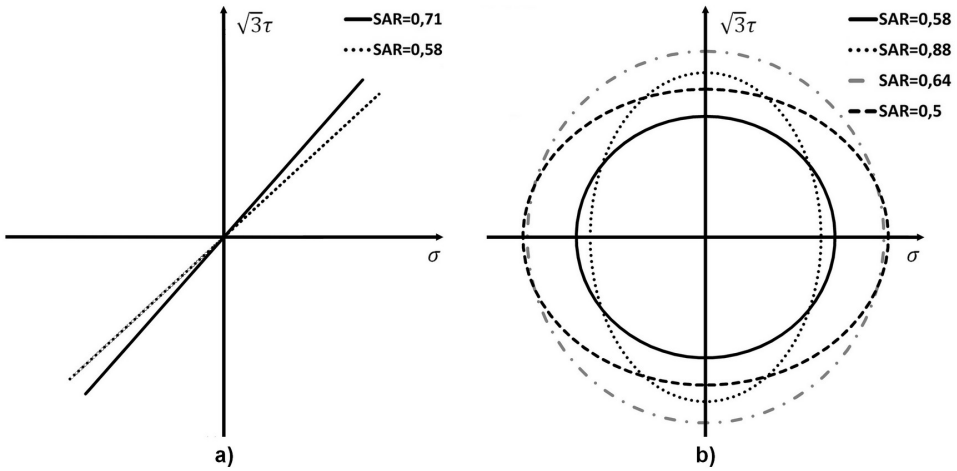


**Figure 6.4:** SAR effect in the loading path shape. a) Proportional loading paths b) Non-proportional loading paths with $90^0$ of phase shift.

**Table 6.1:** 2024-T4 experimental fatigue data [134].

| Block | Path | $\sigma_a$ [MPa] | $\tau_a$ [MPa] | $\tau_a/\sigma_a$ | $N_f$ |
|---|---|---|---|---|---|
| A | Uniaxial tension and compression | 250 | 0 | 0 | 56316 |
| B | Uniaxial tension and compression | 350 | 0 | 0 | 6167 |
| C | Pure torsion | 0 | 144 | - | 63795 |
| D | Pure torsion | 0 | 167 | - | 49912 |
| E | Proportional | 158 | 112 | 0.709 | 76451 |
| F | Proportional | 177 | 102 | 0.576 | 80107 |
| G | Proportional | 248 | 143 | 0.577 | 6488 |
| H | 30 Non-proportional | 158 | 120 | 0.759 | 63584 |
| I | 45 Non-proportional | 158 | 125 | 0.791 | 57004 |
| J | 45 Non –proportional | 248 | 143 | 0.577 | 7363 |
| K | 60 Non –proportional | 158 | 132 | 0.835 | 30893 |
| L | 90 Non-proportional | 177 | 102 | 0.576 | 49292 |
| M | 90 Non-proportional | 158 | 139 | 0.880 | 15459 |
| N | 90 Non-proportional | 244 | 157 | 0.643 | 3453 |
| O | 90 Non-proportional | 250 | 144 | 0.576 | 4634 |
| P | 90 Non-proportional | 250 | 125 | 0.500 | 6811 |

Table 6.2 presents the random sequence of the loading paths used in experiments and their inherent fatigue lives. For each loading sequence, two experiments (two runs) with two different samples were performed. The results gathered in Table 6.2 (third column) are read as follows: the first number indicates the number of loading paths completely loaded before failure; the letter indicates the last running path at failure instant, and the last number indicate the number of cycles performed during the last loading path.

The SSF validation for random loading conditions will be carried out in two steps:

First, the constant amplitude multiaxial fatigue data of the wide range of loading paths described in Figure 6.3 and Table 6.1 are used in the SSF estimates. Second, the aleatory combination of the loading paths described in Table 6.2, which were considered as random loadings (runs), are used in order to evaluate fatigue damage accumulation using the SSF criterion. The SSF packaged (SSF equivalent stress, Y parameter, and virtual cycle counting method) in association with two accumulation damage rules described in Eq.(s) 6.4 and 6.5, were used to evaluate the fatigue damage accumulation under random loading conditions.

The Palmgren-Miner's rule, please see Eq. 6.4, states that the ratio between the number of loaded cycles and the fatigue life estimate must be less than 1 to have a low probability of fatigue failure [88].

**Table 6.2:** 2024-T4 aluminium alloy fatigue data under random loading conditions [134].

| Loading spectrum | Aleatory loading paths sequence | | Results |
|---|---|---|---|
| Run 1 | O-D-G-M-H-F-G-H-O-H-M-J-M-N-J-E-K-F G-G-K-A-F-N-B-B-B-B-B-I F-J-P-O-A-B B-B-B-B-B-B-B-B-B-N-O-B-B-B | 26-B-113 | 31-J-57 |
| Run 2 | L-C-A-C-I-G-C-D-B-N-D-P-B-B-G-O-L-I-P B-D-C-M-P-D-K-L-I-A-L-C-H-M-P-D-A-H C-I-J-K-H-D-E-F-D-L-O-G-I | 25-K-349 | 22-M-437 |
| Run 3 | O-M-B-B-B-B-B-F-G-E-L-A-M-I-I-B-B-B B-B-I-H-A-P-H-G-P-I-B-B-B-B-B-J-D-O P-P-H-O-M-A-H-G-D-K-J-O-L-A | 28-B-182 | 38-H-669 |
| Run 4 | E-B-B-B-B-B-E-P-B-B-B-B-B-G-D-K-N-N F-L-O-G-M-A-P-O-L-E-F-G-I-D-B-B-B-B B-H-L-J-O-H-M-O-P-D-I-B-B-B | 47-I-6205 | 44-P-92 |

$$D = \sum_{j=1}^{\#blocks} \left( \sum_{i=1}^{\#cycles} \frac{n_i}{N_{f_i}} \right)_j \tag{6.4}$$

As stated before in previous sections, this rule adds linearly the fatigue damage obtained in each loading path, which is an approach with good results when the loading spectrum is based in only one loading path type, even for complex ones. Several models based in the Palmgren-Miner's rule can be found in literature, one example is the Morrow's rule, where the Palmgren-Miner ratio is corrected with the material cyclic plasticity [169]. This correction is carried out for each loading path by using the ratio of the loading path damage to the maximum damage parameter found within the loading spectrum (all loading blocks). The Morrows damage accumulation rule is presented in Eq. 6.5.

$$D = \sum_{j=1}^{\#blocks} \left( \sum_{i=1}^{\#cycles} \frac{n_i}{N_{f_i}} \cdot \left( \frac{\sigma_{da}}{\sigma_{da\_spectrum}} \right)^d \right)_j \tag{6.5}$$

where $\sigma_{da}$ is the damage parameter maximum amplitude found within each loading path of a loading spectrum, and $\sigma_{da\_spectrum}$ is the maximum damage parameter found within the entire loading spectrum. The exponent $d$ is a material property; for the 2024-T4 aluminum alloy this value is equal to -0.45, for further treatment please see [134].

### 6.4.1 Constant amplitude loading paths

Regarding the experimental tests described in Figure 6.3 and Table 6.1, fatigue life estimates were carried out based on the SSF criterion presented in the previous Chapters 4 and 5. Figure 6.5 shows the fatigue life correlation between the SSF estimates and the aluminium alloy 2024-T4 experimental data. This fatigue life correlation is quite satisfactory, because the SSF damage map used in this calculation was not determined for this aluminium alloy neither adapted. Therefore, this results were obtained using the 42CrMo4 high strength steel damage map determined in Chapter 4.

Based on the SSF criterion performance discussed above, it can be hypothesise the idea of a general damage map that can be used to compute the SSF equivalent stress in any type of material, nonetheless this hypothesis requires further analysis and validation by experimental tests. However, it is advised the assessment of the SSF damage map for each material by experiments in order to achieve more reliable fatigue life estimates. Regarding the fatigue life correlation depicted in Figure 6.5, the outer boundary is defined based in a life factor of 3, and the inner one is defined in a life factor of two.

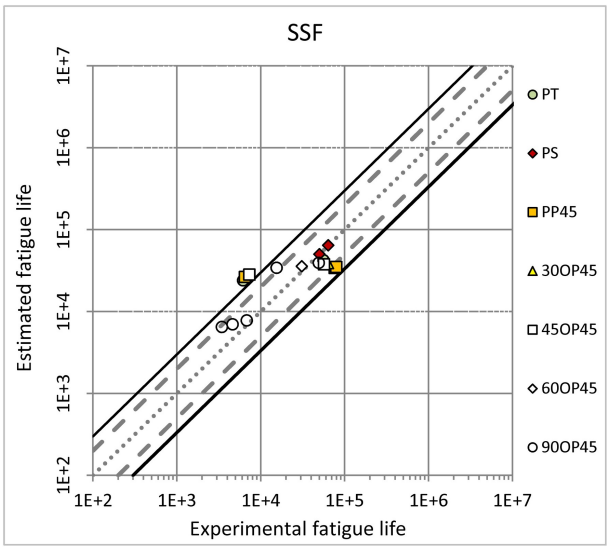


**Figure 6.5:** SSF fatigue life correlation for the 2024-T4 experimental data under constant amplitude loading.

### 6.4.2 Random fatigue life evaluation

Regarding the experimental tests described in Table 6.2 (random loading sequences), fatigue life estimates were carried out based in Eq.(s) 4.4 and 4.14 and using the damage accumulation rules presented in Eq. 6.4 and 6.5.

Figure 6.6 shows the results obtained for the damage accumulated estimates using the Palmgren-Miner and Morrow damage accumulation rules. In both damage accumulation rules the SSF equivalent shear stress was used to account the unitary damage of the

loading paths considered here. Each loading path used in the random loading sequence is well defined, thus it was not needed any method to extract loading blocks or use a cycle counting techniques such as the virtual cycle counting method presented in Chapter 5, for instance.

The results depicted in Figure 6.6 show to be non-conservative for the three first loading sequences, where the accumulated damage at rupture is lower than 1. Moreover, the fourth loading sequence has a accumulated damage greater than 1 at failure, being a conservative result. The most conservative of the two accumulated damage rules, was the Morrow's rule, essentially this rule estimates an accumulated damage 10% greater than the one estimated by the Palmgren-Miner rule.

Recalling the results of Figure 6.6 under a structural health monitoring perspective, non-conservative estimates given by graphic bars lower than 1, indicate a residual fatigue life when the sample is already broken, being a rather disturbing result. Therefore, only in two runs out of eight, it would be possible to avoid the specimen collapse by stopping the load sequence at damage summation equal to 1.

One important aspect to have in mind regarding damage accumulation estimates is the probabilistic behaviour of experimental fatigue data where it is obtained different experimental fatigue lives for the same damage parameter. Due to that, it is usual to show fatigue life correlations like the one shown in Figure 6.5, with fatigue life factors of two or three. Therefore, it is possible to have a survive sample with an accumulated damage greater than one, which is the case of the fourth loading sequence depicted in Figure 6.6. On the other hand, it is also possible to have a fail sample with an accumulated damage much lower than 1, which is the cases of the loading sequences 1, 2, and 3. In this sense, arguing that the "survive" or "not-survive" condition is based in accumulated damages greater or lower than 1 is an inaccurate approach, and an unsuitable criterion to be used in structural health monitoring. This is a crucial aspect of random damage accumulation that needs to be analysed in deep and solved, i.e. it is necessary to rethink the failure condition (trigger) for damage accumulation under random loading conditions.

One idea that can be used to overcome the probabilistic influence on the trigger paradigm is to establish a upper and lower boundary to the trigger value like the one used in fatigue data correlation, as presented in Figure 6.5 (life factors). One way to ensure a conservative damage accumulation result, to avoid unexpected failures in the field, is to increase the damage parameter amplitude in a certain percentage. This percentage must be determined according to the probabilistic pattern of each material family such as steels, aluminium alloys, magnesium alloys, among others. Thus, the damage parameter increase will compensate the probabilistic effect and their propagation during the damage accumulation process of each loading block extracted from a loading spectrum. In this way, under a structural health monitoring perspective,

the instantaneous accumulated damage less than 1 will give a greater confidence regarding the structural component integrity. Thus, the structural component will stand until reach an accumulated damage equal to 1, at this point the sample must be safely replaced.

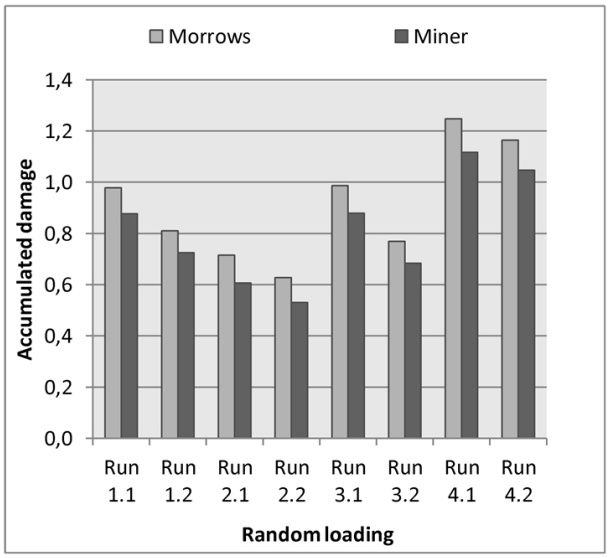


**Figure 6.6:** Damage accumulation results, obtained using the SSF fatigue life estimates and the Morrow and Miner damage accumulation rules.

The damage accumulation results achieved by Xia et al. [134] were obtained without the use of fatigue life criterion. In its calculations, it was used the experimental fatigue life to obtain the ratio between the number of cycles performed vs number of cycles at failure (block fatigue life). Here, a different approach was used in order to evaluate the SSF performance under random loading conditions. Xia et al. [134] used the experimental fatigue life for each loading block to evaluate damage accumulation in their random loading sequences, which is a valid approach.

However, in this study, the fatigue damage accumulation of the random loading sequences mentioned above was obtained by estimating the loading blocks fatigue life through the SSF package. This approach was used because for a general random loading in the field, it is not possible to have the experimental fatigue data for all kind of loading blocks, being necessary the use of fatigue life estimates.

## 6.5 Final comments

In this chapter the SSF equivalent shear stress, presented in Eq. 4.4 and the SSF damage map presented in Eq. 4.14, were used to evaluate fatigue damage accumulation under random loading conditions. To do that, it was gathered fatigue data from literature where random loading spectra were achieved by an aleatory combination of 16 loading paths. Two damage accumulation rules were used, the Palmgren-Miner, and the Morrow's rule, to

evaluate accumulated damage at the fatigue failure instant. Results show good correlations between the SSF estimates and the experimental fatigue data. However, the accumulated damage results were inconclusive due to the "not-survive" trigger paradigm used in the accumulated damage rules. The trigger concept based in damage accumulation greater or lower than 1 is not suitable for field applications such as structural health monitoring procedures. Some alternatives to the trigger concept were discussed based on a field application perspective.

# Chapter 7

# SSF assessment based in damping properties

## 7.1 Introduction

In this chapter, it is evaluated the hypotheses in which the SSF function (damage map) can be estimated based on damping properties of a given material. The present method to obtain the SSF damage map, requires five S-N curves, where each one of them needs at least five valid experiments as described in Chapter 4. In Chapter 4, it was also discussed the necessity to obtain the SSF damage map by experiments for each material in order to obtain optimal results.

However, during the work developed in this thesis, the 42CrMo4 SSF damage map was used to estimate fatigue lives in other materials with acceptable correlations. Thus, it makes some sense to consider the 42CrMo4 SSF damage map as an *universal damage map*, as seen in the von Mises equivalent stress with the $\sqrt{3}$ constant, however this hypothesis requires further validation. In this sense, here it is studied an alternative way to obtain the SSF damage map based in vibration modes and their inherent damping ratios.

## 7.2 Concepts and assumptions

The material damping ratio evaluation has been a controversy subject during years, in particular due to measurement difficulties, where several experimental factors can influence the damping values such as the boundary conditions used in experiments. Due to that, it is usual to evaluate the material damping ratio under a free-free boundary conditions being considered a material property independent from the loading type (material deformation type).

This assumption has indirectly resulted from the difficulties found to excite testing samples with loads different from the pure axial excitation typically used under free-free boundary

conditions. Therefore, a key question is how to measure the damping of a free-free supported sample subjected to a multiaxial (axial plus shear) vibration modes (combined vibration modes), which is a very challenging and interesting problem but outside of the scope of this thesis.

To overcome the drawback of the unavailability of tools to evaluate damping ratios from combined vibration modes, the aforementioned hypotheses was focused in the two uniaxial vibration modes, i.e. the pure axial and pure torsion. The axial damping calculation is straightforward procedure being easy to determine, however, the pure torsion damping is much more difficult to achieve, but its measurement is possible.

The material damping is usually a very small value, especially in steels. In some cases, the measurement error usually found in experiments has the same order of magnitude of the damping value, therefore special care in lab is required in order to minimize measurements errors. However, magnesium alloys have higher damping ratios, being suitable materials for exploratory studies in damping measurements, due to this feature it was selected the AZ31B-F magnesium alloy for this study.

As seen in the previous section, the SSF damage map for the uniaxial loading cases (pure axial damage reduce to the shear damage scale) is computed as $\tau_a/\sigma_a$ . Thus, the hypotheses that motivates this study is as follows in Eq. 7.1.

$$ssf = \frac{\tau_a}{\sigma_a} \approx \frac{D_{shear}}{D_{axial}} \tag{7.1}$$

Where $D_{shear}$, and $D_{axial}$ are the material damping ratio in pure torsion and pure axial, respectively. In this hypotheses, the ratio of shear to axial damping ratios is equal to the SSF given by the ratio of shear to axial stress amplitude (SFF for uniaxial loading conditions).

As seen in Chapter 4, the fatigue damage of axial and shear loadings are strongly related with the deformation pattern on a given material. Similarly, the material damping is the material capability to damp external stimuli which is strongly related to the material micro-structure, which in turn has different responses accordingly to the external stimuli type. Thus, based on this reasoning, the material damping may also vary for different type of stimuli as seen in multiaxial fatigue strength.

For instance, and generally speaking, hysteretic damping can be measured based in elastic and plastic energies computed from hysteresis loops (stress-strain patterns) [170], which in turn are strongly related to the material capability to resist cyclic loadings. Elastic and plastic energies can be related to S-N curves [148], therefore it is hypothesises here that the hysteretic damping of a given material can be also related with S-N curves, which means that hysteretic damping variation can be associated with the fatigue life variation.

## 7.3 Viscous damping ratio ($\zeta$)

### 7.3.1 Half power bandwidth method

It is possible to measure damping ratios using the FRF (Frequency Response Function) results and using the Half-power bandwidth method [171]. This method computes the viscous damping ratio using three specific frequencies of the vibration mode. These frequencies are the natural frequency of the vibration mode, $\omega_n$, the other two are the $\omega_1$, and $\omega_2$, which are calculated by subtracting 3 dB from the $\omega_n$ magnitude. Figure 7.1 depicts the Half-power bandwidth method and its characteristic frequency points used to calculate viscous damping.

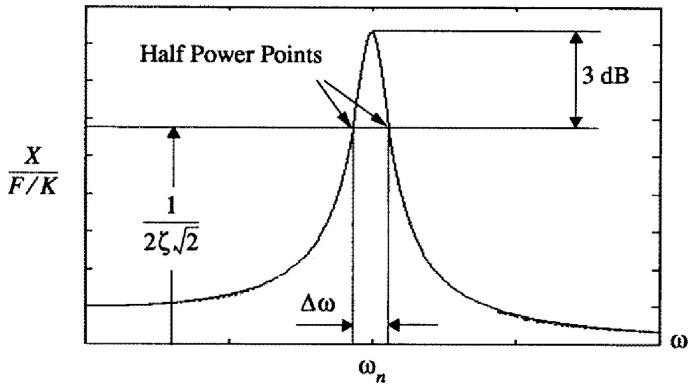


**Figure 7.1:** Half-power bandwidth method and its frequencies to determine viscous damping [172].

Equation 7.2 represents the viscous damping formulation using the Half-power bandwidth frequencies.

$$\zeta = \frac{\omega_2^2 - \omega_1^2}{2\omega_n^2} \tag{7.2}$$

### 7.3.2 Half-power bandwidth method & Nyquist

The Nyquist method [171] is a tool to estimate, with accuracy, the frequencies needed in the Half-power bandwidth method to calculate viscous damping. The FRF experimentally obtained is a discrete function that is strongly dependent on the acquisition rate. In order to estimate the frequency magnitudes in the acquisition gaps the Nyquist method is used (a circle fit method). Essentially, this method represents in the Argand plane the imaginary and real magnitude components of the acquired frequencies, afterwards this values are fitted with a circle. Based on the circle diameter it is possible to accurately estimate any natural frequency that was not caught with the acquisition rate used in experiments. Figure 7.2, shows Argand plane, for the receptance case. For the first vibration mode the

loci can be fairly represented by a circle with negative imaginary values and positive and negative real values.

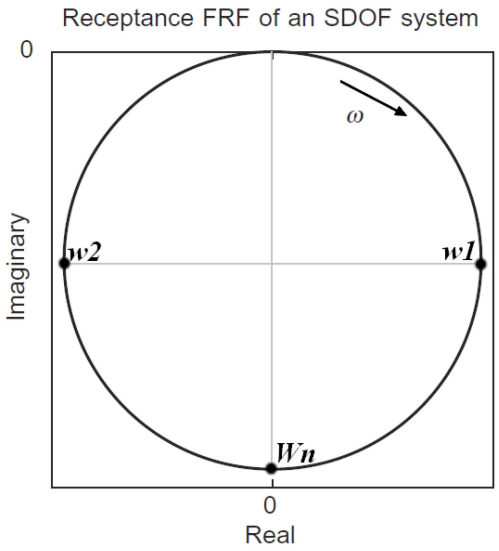


**Figure 7.2:** Nyquist plot to obtain the frequencies used in the material damping determination.

Considering the case shown in Figure 7.2, the receptance amplitude of the natural frequency is given by the circle diameter, because it is the highest amplitude value. The amplitude of $\omega_1$, and $\omega_2$ are estimated by the hypotenuse of two circle radius. To obtain the $\omega_1$, $\omega_2$ and $\omega_n$ frequencies, a linear regression is performed using experimental data and the amplitudes estimated by the circle fit method.

### 7.3.3 Logarithmic decrement

Considering the viscous damping model, the logarithmic decrement method is used in order to estimate the material damping in time domain; basically the response to an impulse in free vibration is measured and recorded in time. Moreover, the material damping in free vibration has amplitude decay with peaks enveloped by an exponential function, as depicted in Figure 7.3. The logarithmic decrement can be determined by the natural logarithm of two successive displacement peaks. The following equations describe in which way the logarithmic decrement is related to the material damping.

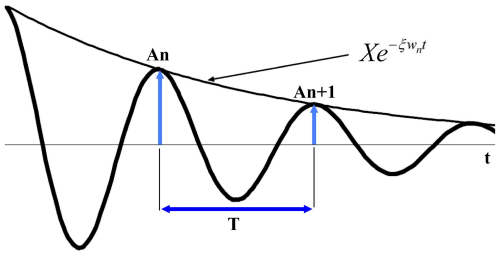


**Figure 7.3:** Free vibration displacement amplitude decay.

It is possible to show in [173] that:

$$\frac{A_n}{A_{n+1}} = e^{[\zeta\omega_n(t_{n+1}-t_n)]} \tag{7.3}$$

The period between peaks is given by:

$$(t_{n+1} - t_n) = T_d = \frac{2\pi}{\omega_d} = \frac{2\pi}{\omega_n\sqrt{1-\zeta^2}} \tag{7.4}$$

$$\ln\left[\frac{A_n}{A_{n+1}}\right] = \left[\frac{2\pi\zeta}{\sqrt{1-\zeta^2}}\right] \tag{7.5}$$

Where $T_d$ is the damped period, the $\omega_d$ is the damped frequency, $\omega_n$ is the natural frequency and $\zeta$ is the viscous damping. The $\zeta$ damping is determined by interaction steps.

### 7.3.4 Linear regression method

The linear regression method is only valid in cases where the material damping ratio is linear in a semi-log scale [171]. The viscous damping is determined by plotting the ratio between An and An+1 versus n, which is the number of periodic intervals between those amplitudes. The slope from the resultant trend line is related to the material viscous damping. Figure 7.4 shows the logarithmic value of An/An+1 versus n.

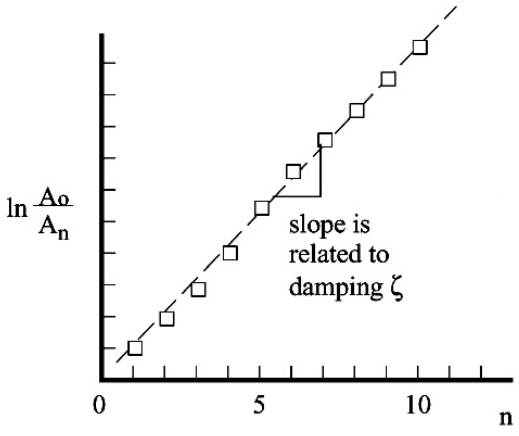


**Figure 7.4:** Linear regression method to determine viscous damping.

### 7.3.5 Area Method

The damping ratio can also be estimated using the areas inherent to each peak or valley represented in Figure 7.5 as Sn; these areas are determined between two consecutive

amplitude zero points; the procedure is similar to the one used in the logarithmic decrement method with some nuances; moreover, this method proved to be a very anti-noise method [173].

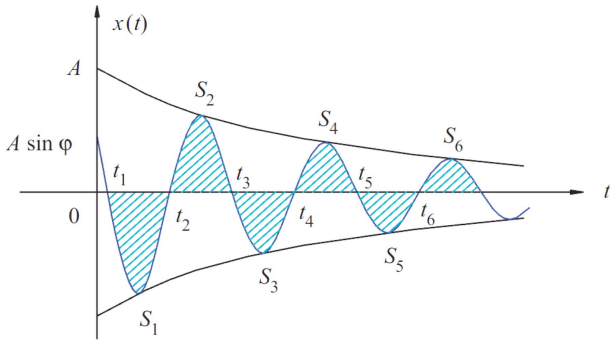


**Figure 7.5:** Free vibration response of the system [173].

$$\frac{S_1 + S_2 + .... + S_N}{S_{N+1} + S_{N+2} + .... + S_{2N}} = \frac{S_1 + S_2 + .... + S_N}{(S_1 + S_2 + .... + S_N)\, e^{-\zeta\omega_n n T_d}} = e^{\zeta\omega_n n T_d} = e^{\frac{2n\pi\zeta}{\sqrt{1-\zeta^2}}} \tag{7.6}$$

The damping ratio is given by:

$$\zeta = \frac{1}{\sqrt{1 + \left(2n\frac{\pi}{E}\right)^2}} \tag{7.7}$$

where:

$$E = \ln\left(\frac{\sum S_k}{\sum S_{k+N}}\right) \tag{7.8}$$

### 7.3.6 Proposal of the Exponential regression method

In the following, it is presented a new way to calculate viscous damping based in free vibration decay. The peaks from a free vibration decay can be fitted with an exponential trend line as shown in Figure 7.6.

From the period decay obtained by experiments the damped frequency can be calculated as follows in Eq. (s) 7.9 and 7.10:

$$\omega_d = \frac{2\pi}{T_d} \tag{7.9}$$

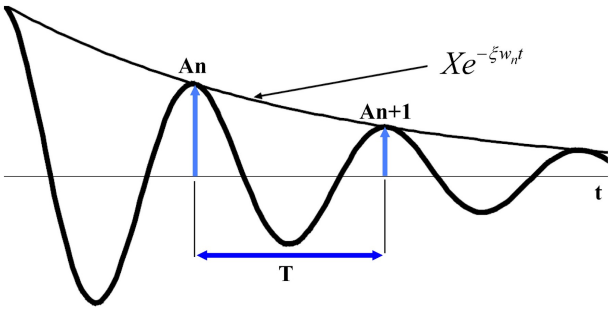


**Figure 7.6:** Free vibration displacement amplitude decay.

$$\omega_d = \omega_n \sqrt{1 - \zeta^2} \tag{7.10}$$

The natural and damped frequencies can be related as follows in Eq. 7.11.

$$\omega_d = \sqrt{\omega_n^2 - (\omega_n \zeta)^2} \Rightarrow \omega_n = \sqrt{\omega_d^2 + (\omega_n \zeta)^2} \tag{7.11}$$

where the $w_n\zeta$ value is obtained from the exponential trend line equation of the free-decay of the vibration amplitude. Based in these equations (7.9 to 7.11), the viscous damping can be computed as follows in Eq. 7.12.

$$\zeta = \sqrt{1 - \left(\frac{\omega_d}{\omega_n}\right)^2} \tag{7.12}$$

## 7.4 SSF results based in S-N curves

Figure 7.7 a) shows the S-N results for the AZ31-BF magnesium alloy under uniaxial loading conditions, i.e. the pure axial and pure shear loading cases. Moreover, the trend line of each loading case is also presented in Figure 7.7. As one can see, the uniaxial shear and axial stress amplitudes required to cause the same fatigue life are quite different, as seen in Chapter 4 for the 42CrMo4 material. Also, it can be concluded that the relative damage between axial and shear stress is not maintained constant in the finite fatigue life-time range, as seen in Figure 7.7 b). Figure 7.7 b) shows the relative damage between shear and axial stress through the SSF trend line, which was calculated based in the two S-N curves depicted in Figure 7.7 a). The SSF experimental values have a trend line with a negative slope, where the SSF value decreases as the fatigue life increases, please see Table 7.1 .

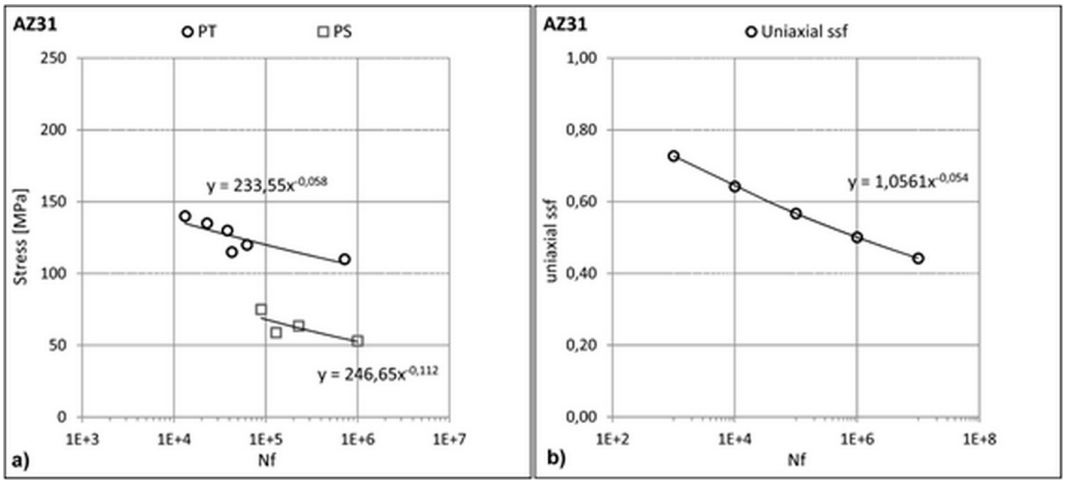


**Figure 7.7:** AZ31B-F magnesium alloy results a) uniaxial S-N trend lines b) SSF trend line based in the uniaxial trend lines.

**Table 7.1:** AZ31B-F SSF variation with fatigue life.

| Nf | Axial stress | Shear stress | SSF |
|---|---|---|---|
| 1.00E+03 | 156.5 | 113.8 | 0.73 |
| 1.00E+04 | 136.9 | 87.9 | 0.64 |
| 1.00E+05 | 119.8 | 67.9 | 0.57 |
| 1.00E+06 | 104.8 | 52.5 | 0.50 |
| 1.00E+07 | 91.7 | 40.6 | 0.44 |
| 1.00E+08 | 80.2 | 31.3 | 0.39 |

## 7.5 Experimental set-up

In this section it is presented the experimental set-up used to measure the axial and shear viscous damping. The magnesium alloy AZ31B-F was tested as received from factory, i.e. the specimen test was a rod with 26 mm of diameter and 1000 mm in length.

### 7.5.1 AZ31B-F axial damping experiments

Figure 7.8 illustrates the set-up implemented to measure the axial viscous damping. The magnesium bar was maintained on the horizontal using two thin rubber bands in order to simulate a free-free supported bar. The bar was hit with an instrumented impact hammer, which has a force transducer connected to the data acquisition module. On the opposite end of the impact zone, the specimen test had a glued accelerometer connected to the data acquisition module. With the information from these two sources the frequency response function was obtained.

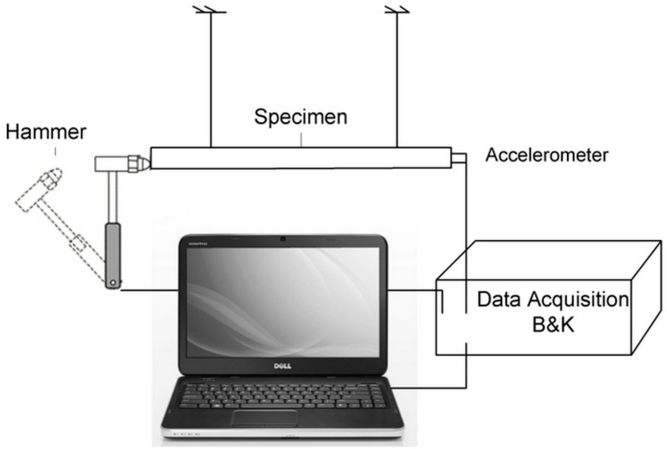


**Figure 7.8:** Magnesium alloy axial damping determination via FRF procedure.

### 7.5.2 AZ31B-F shear damping experiments

In order to calculate the viscous shear damping of the AZ31B-F magnesium alloy, two different set-ups were implemented. One was implemented for frequency domain methodologies (set-up 1) and the other one for time domain methodologies (set-up 2).

**Set-up 1**

The magnesium bar was glued to the floor with a cyanoacrylate adhesive in order to create a free-fixed end boundary condition. This boundary condition is similar to the one verified in the fatigue testing machine, i.e. the lower grip is static during the fatigue tests, being the load torque performed by the upper grip. In order to create instantaneous torque an aluminium cross was coupled to the bar as can be seen in Figure 7.9. The aluminium cross was glued to the magnesium bar with the cyanoacrylate adhesive.

Three accelerometers were used in specific locations at the aluminium cross branches, please see Figure 7.9. The data acquired from these accelerometers was used to perform a post processing data filtering of the FRF results in order to remove any influence of the bending moment (resultant from the impact excitation) on the experimental results. The impact was performed in the cross branches which do not have any applied accelerometers with a instrumented impact hammer connected to the the data acquisition module.

**Set-up 2**

Figure 7.10 presents the set-up 2 designed for free vibration tests. The magnesium rod was machined in both extremities in order to improve the experiments procedures and data acquisition. In one extremity it was machined the clapping region to optimize the boundary condition and in the other end it was machined small grooves to facilitate the measurements of torsional velocities. The velocities were measured using a polytec doppler laser, which was connected to the data acquisition module, the same used in set-up 1. The bar was excited using a electric shaker and an aluminum rod as shown in Figure

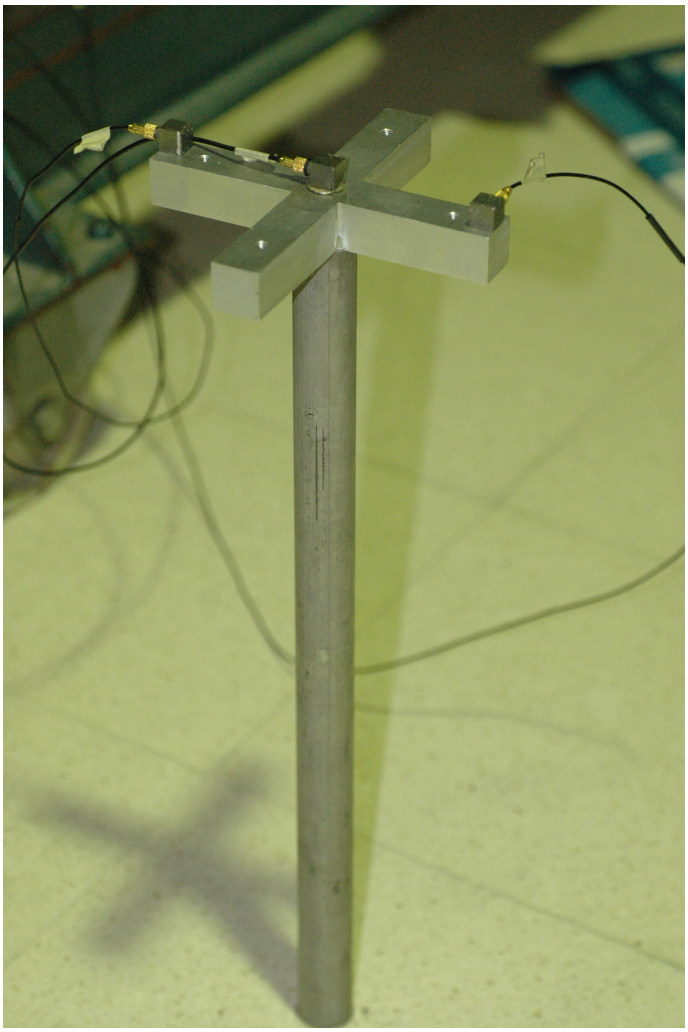

**Figure 7.9:** Torsion experimental set-up 1.

7.10. The magnesium rod was excited by contact near the clamping region in order to reduce the bending moment influence on the free vibration results. The excitation was performed with first torsional natural frequency previously determined with a commercial FEM package. The experiment starts by exciting the magnesium rod until reach a fully developed resonant response, at this point the excitation is removed and the free vibration decay is registered and stored.

### 7.5.3 Natural frequency estimates using FEM

The natural frequency of axial and torsional vibration modes were firstly estimated using ANSYS, a commercial FEM package, where the axial and torsional testing samples were numerically modulated having into account the samples geometry and boundary conditions used in experiments. The idea was to obtain a estimate for the natural frequency of each vibration mode, to make easier the natural frequency identification in the FRF results. Also, in the FEM simulations it is possible to visually inspect the vibration mode animation, which helps to eliminate any doubt about the vibration mode selection

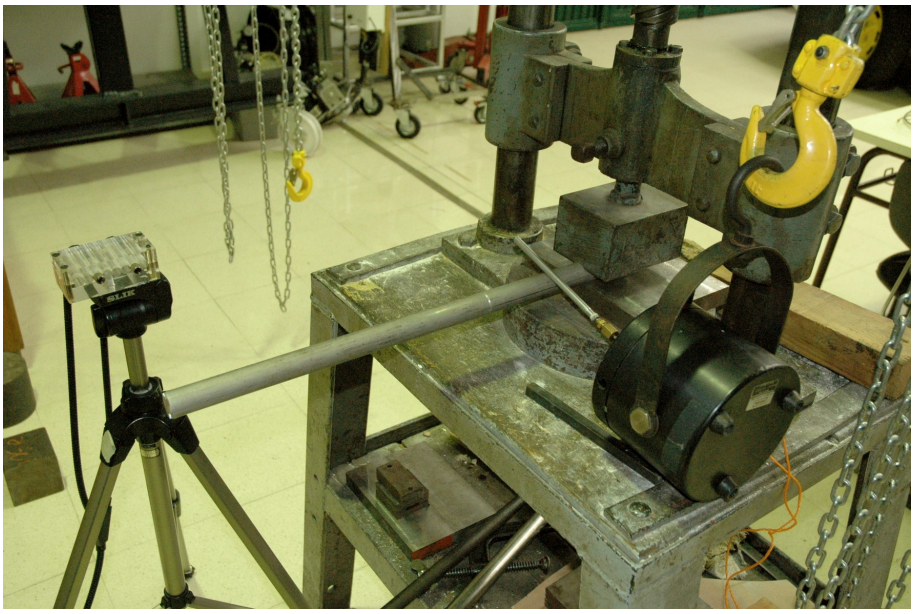

**Figure 7.10:** Torsion experimental set-up 2.

and inherent natural frequency identification. Moreover, the maximum sum displacement is also an alternative way to identify modes of vibration using FEM. Figure 7.11 shows the maximum sum displacement for the first axial and torsional modes of vibration. The natural frequencies estimates were 5979 Hz for the 1º axial mode of vibration and 255.4 Hz for the 1º torsional mode of vibration.

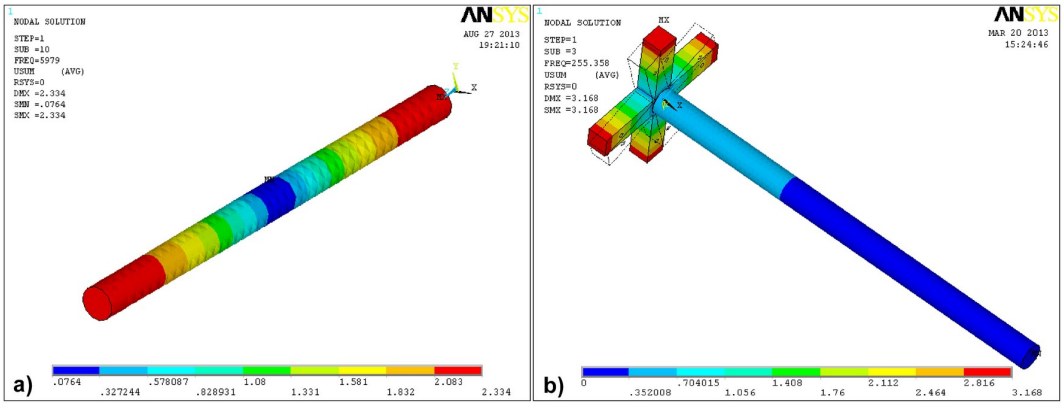


**Figure 7.11:** FEM results of the natural frequency estimates for a) 1º vibration axial mode b) 1º vibration torsion mode.

## 7.6 FRF experimental results

In this section, it is presented the FRF results obtained to identify the natural frequency of the 1º axial and torsional vibration modes. Figure 7.12 a) shows the FRF results for the first axial mode, and Figure 7.12 b) shows the FRF results for the first torsional mode. From the results depicted in Figure 7.12, it can be identified distinct vibration modes with a natural frequency near the numeric estimate for both vibration modes.

Without the results obtained in the numeric simulations, the vibration modes identification would be much more difficult to obtain, because from the FRF spectrum it is only possible identify natural frequencies, therefore the FRF do not give any information regarding the displacement of the vibration mode. However, there will be always differences between natural frequency estimates and experimental values. This is so because the mechanical properties used in simulations are usually slightly different from the ones found in the testing sample, also the dimensions and boundary conditions used in simulations may also differ from the experimental set-up. Moreover, the natural frequency estimates from modal analysis are undamped natural frequencies, but the ones obtained by experiments are damped natural frequencies, thus there always be a difference between these two estimates for the natural frequency. However, due to the low damping ratio found in metals the damped and undamped natural frequencies are very alike, which turns the numeric simulation a powerful tool for the identification of vibration modes and their inherent natural frequencies.

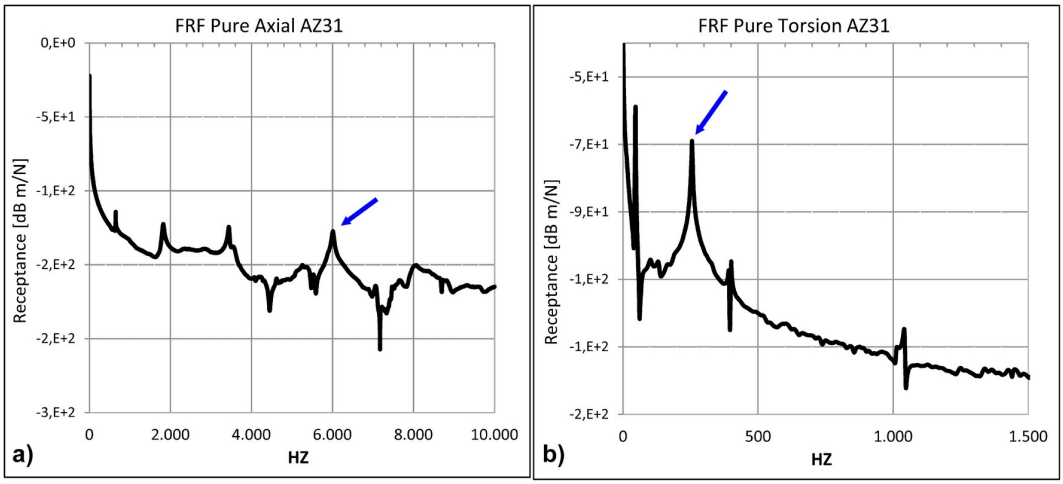


**Figure 7.12:** FRF experimental results: a) 1º axial mode b) 1º torsion mode.

Figure 7.13 a) and b) depicts a zooming around the peaks of the 1º axial and torsional vibration modes in order to inspect if there is any influence of other vibration modes in these ones. In these results, it can be found at least a 100 Hz window around the natural frequencies in both vibration modes, indicating that the FRF is well-behaved around the natural frequencies peaks, which allows the natural frequencies calculation of the 1º axial and shear modes of vibration without any interference of other undesired vibration modes.

## 7.7 Damping calculations

### 7.7.1 Half power bandwidth estimates

The FRF data is not a continuous data, i.e the FRF results is composed by discrete frequencies and amplitudes that can be accelerance or receptance. Due to the FRF discrete nature, a local maximum obtained experimentally may not be the true maximum i.e. the

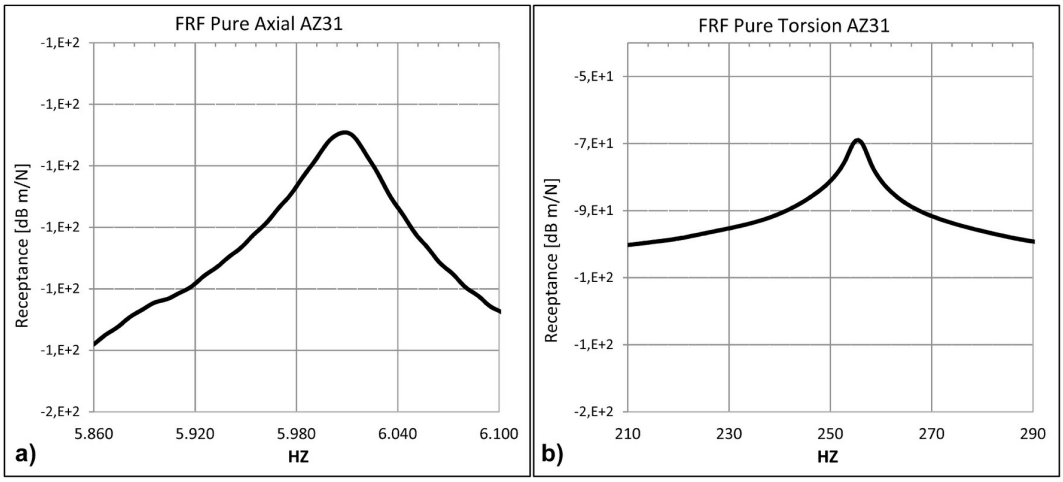


**Figure 7.13:** Zooming around the natural frequencies: a) 1º axial vibration mode, b) 1º torsion vibration mode.

natural frequency may be within the interval between two frequencies experimentally determined. In these cases, the Nyquist circle method can be used to obtain the natural frequency and the frequencies required to calculate the viscous damping. Figure 7.14 a) and b) shows the Nyquist circle for the axial and shear vibration modes, respectively. In these circles, it is used the receptance in the complex format, in the vertical axis it is represented the receptance imaginary part and in the horizontal axis it is represented the real part. For the first modes of vibration these circles most initiate and terminate at graph origin, then the natural frequency will have the maximum magnitude given by the antipodal point relatively to the graph origin.

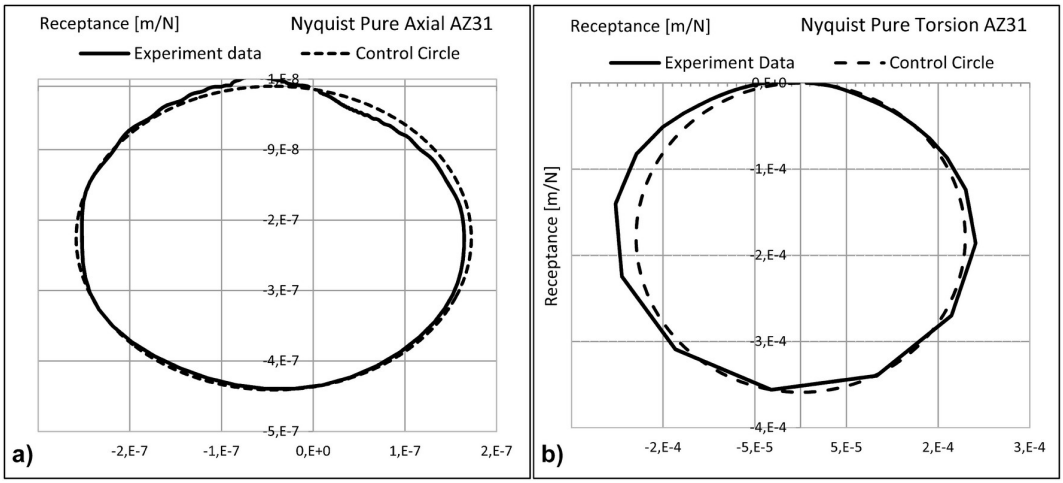


**Figure 7.14:** Nyquist circle for axial and shear vibration modes a) 1º axial vibration mode b) 1º torsional vibration mode.

Table 7.2 shows the axial and shear natural frequencies obtained from the axial and shear FRF using the Half-power bandwidth method and the Nyquist methodology. In the last row of Table 7.2 it is presented the viscous damping results for the axial and shear first

vibration modes. As one can seen, the shear damping is greater than the axial one.

**Table 7.2:** FRF results for the axial and shear 1º vibration modes, frequencies tuned by Nyquist method.

| | Axial | Shear |
|---|---|---|
| $\omega_n[Hz]$ | 6009.88 | 255.36 |
| $\omega_1[Hz]$ | 5987.06 | 253.95 |
| $\omega_2[Hz]$ | 6026.82 | 256.77 |
| Damping | 0.00661 | 0.011 |

### 7.7.2 Exponential regression results

Figure 7.15 a) shows the data recorded regarding the velocity decay at the time instant of the shaker removal. As one can see, the torsional velocity decay profile can be fairly approximated with an exponential trend line as depicted in Figure 7.15 b), which has an acceptable $R^2$.

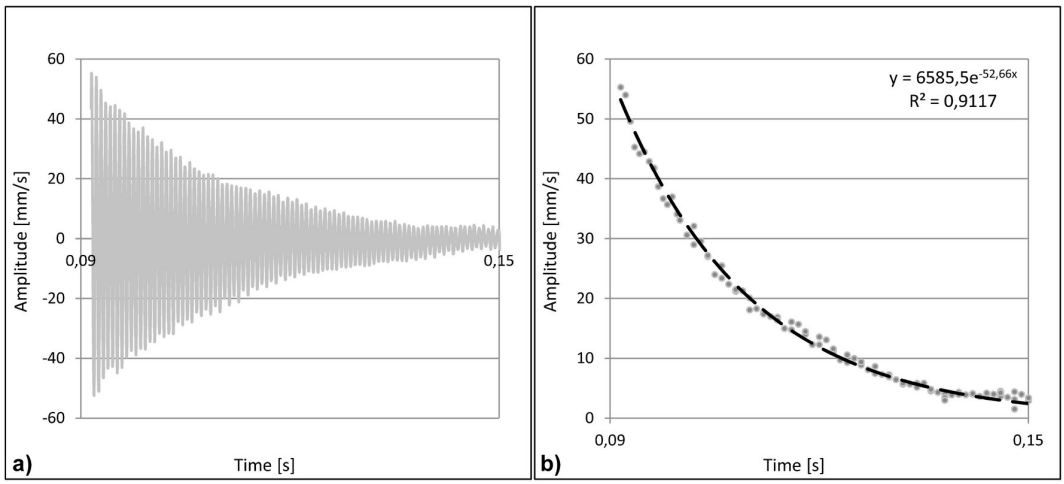


**Figure 7.15:** AZ31 free-fixed end at 1º torsion vibration mode in time domain, a) free decay velocity b) exponential regression on the velocity peaks.

The exponential trend line equation can be used to compute the viscous torsional damping as stated in Eq.(s) 7.9 to 7.12. Thus, damping estimate was 0.011733 for the exponential regression method which is very close to the shear damping obtained in the Half-power bandwidth method.

### 7.7.3 Linear regression results

Table 7.3 presents the hysteretic damping results obtained in the linear regression method calculations. The damping value was calculated considering the average value of the results obtained in five measurements. Also here, it was obtained a shear damping value in accordance to the FRF and exponential results.

**Table 7.3:** Linear regression results for pure shear free vibration mode.

| Sample | $\eta$ Linear regression |
|---|---|
| 1 | 0.014181 |
| 2 | 0.010759 |
| 3 | 0.010783 |
| 4 | 0.011284 |
| 5 | 0.009438 |
| Average | 0.011289 |

### 7.7.4 Areas method results

Table 7.4 shows the results for the area method, also here, it was performed five measurements, the average value of the shear damping was 0.0112.

**Table 7.4:** Areas method results for the damping determination of pure shear free vibration mode.

| Sample | $\eta$ Areas Method |
|---|---|
| 1 | 0.01354 |
| 2 | 0.01047 |
| 3 | 0.010579 |
| 4 | 0.01111 |
| 5 | 0.01026 |
| Average | 0.011192 |

## 7.8 Results interpretation

The damping values for the first axial and shear vibration modes are summarized in Table 7.5. The axial damping results were obtained using only the Half-power bandwidth method, being a reliable way to experimentally obtain the first axial vibration mode. However, the shear damping results were obtained by using two different experimental set-ups, and four different calculation methods, in order to avoid any biased result for the magnesium shear damping. The shear damping results shown in Table 7.5 are very alike, despite having been used different set-ups and calculation methods. The areas and FRF methods have the most similar values, in contrast, the result of the Exponential regression method is the most different. It can be concluded that the magnesium shear damping was calculated with success for the boundary conditions considered in this study, i.e. free–fixed end. The values of the magnesium axial and shear damping ratios are shown in the last

column of Table 7.5, where the exponential method result is not in accordance with the other methods trend.

**Table 7.5:** Magnesium alloy axial and shear damping ratio

| | $\zeta$ Axial | $\zeta$ Shear | $\zeta$ Axial / $\zeta$ Shear |
|---|---|---|---|
| FRF and Nyquist | 0.00661 | 0.011 | 0.6 |
| Exponential regression | | 0.011733 | 0.56 |
| Linear regression | | 0.011289 | 0.59 |
| Areas method | | 0.011192 | 0.59 |

## 7.9 Final comments

In this chapter, it was raised up the hypothesis in which the ratio of axial to shear damping ratio, determined under a mechanical vibration approach, can be an alternative to fatigue life experiments. The AZ31B-F magnesium alloy was used to scrutinize this hypothesis due to their high damping properties, instead of using the high strength steel 42CrMo4 which has much lower damping ratios. The magnesium sample used in experiments (axial and shear damping measurements) was a rod with 26 mm in diameter and 1000 mm in length. Based on the results achieved in this chapter some conclusions can be drawn:

First, the AZ31B-F magnesium alloy has different axial and shear damping ratios, which is a new finding. Thus, it can be concluded that the material damping is dependent on the vibration mode type. This finding can be supported by the conceptual idea in which different deformation patterns are obtained for different external loads (axial, shear or multiaxial) thus it makes sense to obtain different damping ratios for different deformation since a damping ratio is a measure of the material capability to eliminate vibration (lattice resistance to internal motion). Second, in this study it was found out that the AZ31B-F SSF damage map for uniaxial loading conditions varies with the energy level variation (variation of the stress-strain hysteresis loops) used in experiments, thus this variation can be correlated with the material hysteretic damping. One major drawback in this exploratory study is the lack of connection between the damping ratio and the material fatigue life. Thus, it is not possible to connect the measured damping to the material fatigue life at the present state of the art. The SSF value obtained here is in fact within the SSF values obtained by the S-N curves, however it is not possible to identify their inherent fatigue life. To do this, it is required a new approach in the lab to measure the material damping under high load levels. The loads involved in the FRF procedures are very low being impossible to cause any damage in the material. Thus, one possibility is to measure free vibrations with strains similar to the ones used in the S-N curves, in this way it becomes possible to account with the load level effect in the damping values and make a relation with their inherent fatigue life.

# Chapter 8

# Contributions to Level 5

## 8.1 Introduction

In this chapter, it is presented the thesis contribution to the state-of-the-art in regarding the level 5 depicted in Figure 8.1. Here, it was developed two models to estimate crack initiation planes according to the loading path type.

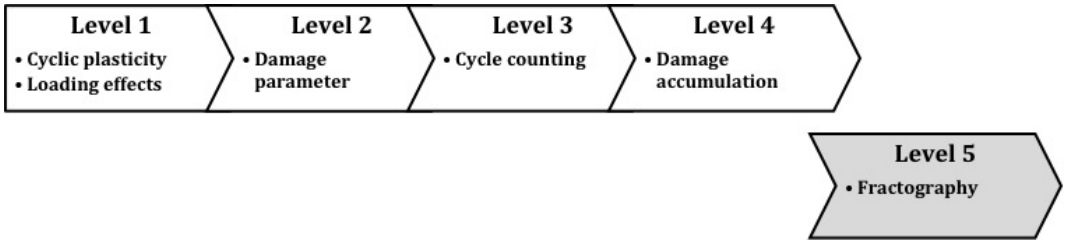


**Figure 8.1:** Multiaxial fatigue level focused in this chapter.

Multiaxial loading effects play an important role in the crack initiation at early crack growth stages, thus in this chapter, it is analysed these effects in two different crystallographic micro-structures, i.e. the body-centered cubic (BCC) and the hexagonal close-packed (HCP) micro-structures. The materials studied were the high strength steel 42CrMo4 with a BCC micro-structure, and the magnesium alloy AZ31B-F with a HCP micro-structure. Moreover, the multiaxial loading paths selected in this study promote the fatigue crack initiation and growth in both stages I and II, which are based in the combination of both axial and shear mechanisms during crack initiation and growth process. A series of experimental tests were carried out under multiaxial loading conditions in the AZ31B-F material in order to analyse its fatigue behaviour, regarding the 42CrMo4 results they were gathered from literature [3]. Moreover, a fractographic analysis was performed to depict the crack initiation an growth behaviour of two different micro-structures. In addition, critical plane models such as the Fatemi-Socie, SWT, and Liu as well as two models developed here were used to estimate the orientation of the crack initiation plane for each material and loading path. Moreover, the theoretical critical plane

estimates were correlated with the experimental data obtained in both materials. Different results were obtained for the crack initiation planes in both materials indicating a strong influence of the micro-structure on the critical plane direction under multiaxial loading conditions, further information regarding experiments will be given in the next sections. Structural failure is often caused by fatigue cracks, which frequently initiate and propagate at the most loaded regions, generally due to complex geometric shapes and/or multiaxial loading conditions. Fatigue crack initiation and early crack growth are two subjects that have created growing attentions in fracture mechanics research, because these subjects are crucial for an accurate assessment of fatigue crack propagation and to interpret the final fracture modes of cracked components or structures [174–176]. Multiaxial fatigue studies in magnesium alloys are quite few nowadays, especially fractography studies under multiaxial loading conditions. Bentachfine et al. [177] was a pioneer researcher of magnesium alloys and their mechanical behaviour under multiaxial loading conditions, he studied the mechanical behaviour of a lithium-magnesium alloy under proportional and non-proportional loading paths at low-cycle and high-cycle fatigue regimes. The research focus was the evolution of the deformation mode and cyclic plasticity. Several authors have reported that the phase shift angle found in non-proportional loading paths decreases the material fatigue strength. In these studies, the comparative parameter used to correlate experimental data was the von Mises equivalent stress/strain, which has the shortcomings already discussed in Chapter 3. Moreover, the von Mises equivalent stress under non-proportional loadings keeps a constant value during the loading period, therefore it indicates the same loading level in all loading directions, being unsuitable to identify crack initiation planes. However, the loading direction variation inherent to non-proportional loading paths increases the anisotropy of the material cyclic response at grain level, which may justify, for some materials, the decrease of the material fatigue strength [16] when subjected to this type of loading paths. Biaxial fatigue tests were performed by Ito and Shimamoto [178] using cruciform specimens made of a magnesium alloy. In this study, fatigue crack propagation was analysed as well as the effect of micro-structure in the material fatigue strength. Moreover, the experimental results for biaxial low cycle deformation led to conclude that the twinning density evolution is strictly related with crack initiation and slip bands formation on wrought magnesium alloys. Recently, Yu et al. [179], also performed in-phase and out-phase fatigue tests under strain control on the extruded magnesium alloy AZ61A using tubular specimens. The conclusions were similar to the ones found by Bentachfine et al. [177]. Yu et al. confirmed in their experiments the additional damage found in non-proportional loadings, where the presence of a shift angle lead to the material fatigue strength decrease comparatively to the in-phase loadings, for the same proportional and non-proportional equivalent strain amplitude. At low-cycle fatigue regime was reported a kink in the strain fatigue life curve, which is a typical behaviour usually reported in literature for uniaxial fatigue loading regimes in magnesium alloys [180]. Furthermore, in [180] the effect of compressive mean

stress was also evaluated, the authors reported a fatigue life enhancement due to the compressive mean stress. A critical plane study was performed comparing the agreement between experimental data and the theoretical results in magnesium alloy [181]. It was used the critical plane models Fatemi-Socie, SWT, Liu1, and Liu2 to estimate the direction of the crack initiation direction. The authors reported a poor prediction performance in some critical plane estimates, but good agreements in other ones. Magnesium alloys have mainly three types of shear transformations within their typical slip mechanism, namely deformation twinning, stress-induced martensitic transformations and kinking. Twinning deformation occurs in HCP materials when deformed at room temperatures, the same deformation pattern also occurs in BCC materials at low temperatures close to zero degrees. Twinning deformation mechanism occurs when it is created a boundary on the material lattice that defines a symmetric region due to shear strains at atomic level, please see Figure 8.2. This twin boundary defines a mirror image between deformed and un-deformed lattice grid [143, 144], from where resulted the so-called twinning effect. In

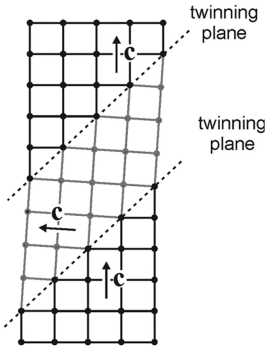


**Figure 8.2:** Twinning deformation found in magnesium alloys [182].

wrought Mg alloys, fatigue crack initiation has been associated to inclusions created during the casting process, but in the majority of the cases, the twinning deformation and the slip bands created during the twinning density flow are the main cause of the crack initiation process, where the crack propagation follows, in general, along the deformation twin's fields [183–185]. Currently, commercial FEM software do not have tools to modulate the mechanical behaviour (static and cyclic) found in magnesium alloys, which have a peculiar mechanical behaviour already described here in Chapter 3. Their main limitation is to follow the different yield stress at tension and compression found in magnesium alloys, [24]. In this work, it was performed several numeric simulations in Ansys, where it was used the stress-strain cyclic curve of the magnesium alloy AZ31B-F, however due to the limitations discussed above, here it was only considered the tensile branch of the AZ31B-F stress-strain curve, depicted in Figure 3.2 of Chapter 3. This decision was based in the fact that the tensile loading tends to be more damaging than the compression one. Figure 8.3 shows the four multiaxial loading paths considered in this study, where PS is the pure shear uniaxial loading, PT is the pure tensile uniaxial loading, OP is the 90º out-of-phase

loading, and PP is the proportional loading, respectively. The loading paths depicted in Figure 8.3 were used in the FEM simulations performed here and in the experiments carried out to characterize both materials, the 42CrMo4, and the AZ31B-F.

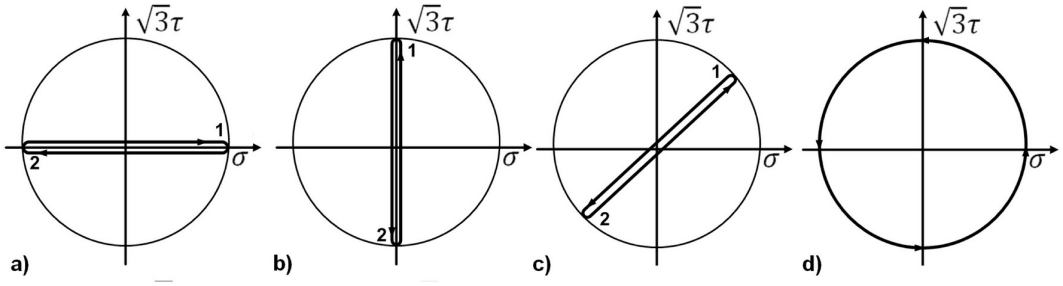


**Figure 8.3:** a) PS loading case, b) PT loading case, c) OP loading case, d) PP loading case.

**Table 8.1:** S-N results for the materials 42CrMo4 [3] and AZ31B-F.

| | 42CrMo4 | | | AZ31B-F | | |
|---|---|---|---|---|---|---|
| Case | **Sigma** | **Shear** | **Nf** | **Sigma** | **Shear** | **Nf** |
| **PT** | 700 | 0 | 6040 | 140 | 0 | 13164 |
| | 600 | 0 | 19951 | 135 | 0 | 22873 |
| | 500 | 0 | 215910 | 130 | 0 | 38102 |
| | 485 | 0 | 269178 | 120 | 0 | 62352 |
| | 445 | 0 | 2368959 | 105 | 0 | 721573 |
| | 455 | 0 | 247953 | | | |
| | 560 | 0 | 53752 | | | |
| | 550 | 0 | 56929 | | | |
| | 450 | 0 | 3263000 | | | |
| | 470 | 0 | 338170 | | | |
| | 480 | 0 | 284348 | | | |
| Case | **Sigma** | **Shear** | **Nf** | **Sigma** | **Shear** | **Nf** |
| **PS** | 0 | 374 | 1100000 | 0 | 75 | 88871 |
| | 0 | 545 | 2088 | 0 | 64 | 227808 |
| | 0 | 484 | 11302 | 0 | 75 | 88871 |
| | 0 | 440 | 70610 | 0 | 64 | 227808 |
| | 0 | 402 | 159854 | | | |
| | 0 | 395 | 315668 | | | |
| Case | **Sigma** | **Shear** | **Nf** | **Sigma** | **Shear** | **Nf** |
| **PP** | 425 | 245 | 1000000 | 106 | 61 | 16800 |
| | 435 | 251 | 564088 | 92 | 53 | 46878 |
| | 440 | 254 | 311401 | 78 | 45 | 69169 |
| | 445 | 257 | 239600 | 67 | 39 | 1000000 |
| | 465 | 269 | 109087 | 74 | 43 | 242685 |
| | 470 | 271 | 97366 | 71 | 41 | 353718 |
| | 495 | 286 | 48740 | | | |
| | 520 | 300 | 27204 | | | |
| | 610 | 352 | 4114 | | | |
| Case | **Sigma** | **Shear** | **Nf** | **Sigma** | **Shear** | **Nf** |
| **OP** | 450 | 260 | 1000000 | 106 | 61 | 7182 |
| | 465 | 269 | 618128 | 67 | 39 | 1173565 |
| | 475 | 274 | 316712 | 78 | 45 | 11986 |
| | 485 | 280 | 197548 | 74 | 43 | 167525 |
| | 490 | 283 | 107374 | 71 | 41 | 800000 |
| | 495 | 286 | 97548 | 95 | 55 | 8595 |
| | 510 | 294 | 56411 | 73 | 42 | 576336 |

Table 8.1 shows the S-N results for both materials. This tests were performed under load control and with loading frequencies between 5 to 6 Hz. The failure criterion was the sample total separation. Figure 8.4 shows the sample geometry used in the AZ31B-F experiments, the 42CrMo4 sample geometry can be found in Figure 3.30.

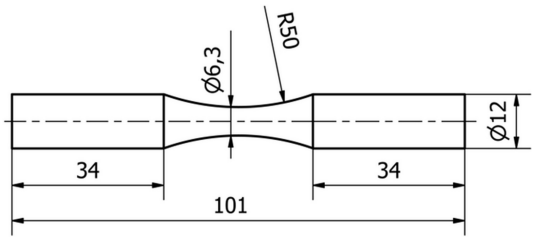


**Figure 8.4:** AZ31B-F specimen test used in experiments of Table 8.1 - geometry and it dimensions.

## 8.2 Estimates for the fatigue crack initiation plane

The orientation of the crack initiation plane is of utmost importance in fatigue damage characterization of loading paths. Because, it is obtained different orientations for different loading paths, even when they have the same stress level. Moreover, the crack orientation plane also changes with the stress level variation, as discussed in Chapter 4. Also, it is obtained different crack initiation planes in different materials for the same loading path and stress level. Thus, the crack initiation plane is sensitive to the loading path type, stress level, and material type, being a important experimental evidence of the fatigue damage process.

### 8.2.1 Virtual notch concept

As earlier stated in [16, 178, 179], loading paths have a strong influence on the crack nucleation and initiation process. In this process, the crack nucleation results mainly from cyclic intrusions and extrusions at the material surface creating local micro notches with cyclic plasticity at the micro notch root and surface, which governs the early crack initiation process. During this process, mode I governs the fatigue crack propagation where the crack growth is performed mainly by the load perpendicular to the cracked surface.

Based on this experimental evidence a new methodology to estimate the orientation of the fatigue crack initiation planes is presented here. This methodology was designed to be used in finite element analysis of structures and mechanical components with a well-known geometry, where the nominal stresses can be calculated and compared with the local stresses found at the notches discussed above. In this approach the main concept is based on the assumption that the crack tip has the greatest stress values, and they can be determined using numerical tools such as Ansys [186], Abaqus [187] or even an in-house developed FEM software. In the proposed approach, it is created a virtual notch in the FEM model of a given structure. This notch was named as virtual because in reality

doesn't exist in the structure, but is used here as a tool to estimate the direction of the crack initiation plane in the structure most loaded regions.

The cornerstone of this approach is based on the selection of the virtual notch geometry used in the numeric simulations, because the notch geometry may have a strong influence in the crack orientation estimates. Therefore, a spherical cap geometry with depth equal to This geometry does not have a favourable direction to induce particular stress risers since it has a equal geometry in all directions. In this way, the location of the stress risers are strictly dependent on the loading path type and stress level.

Figure 8.5 shows a FEM simulation of the virtual notch concept in a hour glass sample. Figure 8.5a) shows the nominal and local regions of the specimen test, where the nominal region is sufficiently far from the local one, which allows to compute the $K_t$ values at the virtual notch. Figure 8.5 b) shows the spherical cap (micro notch) numerically implemented, the spherical radius and spherical cap depth must be in agreement with the material average grain size which depends on its heat treatment and grain growth.

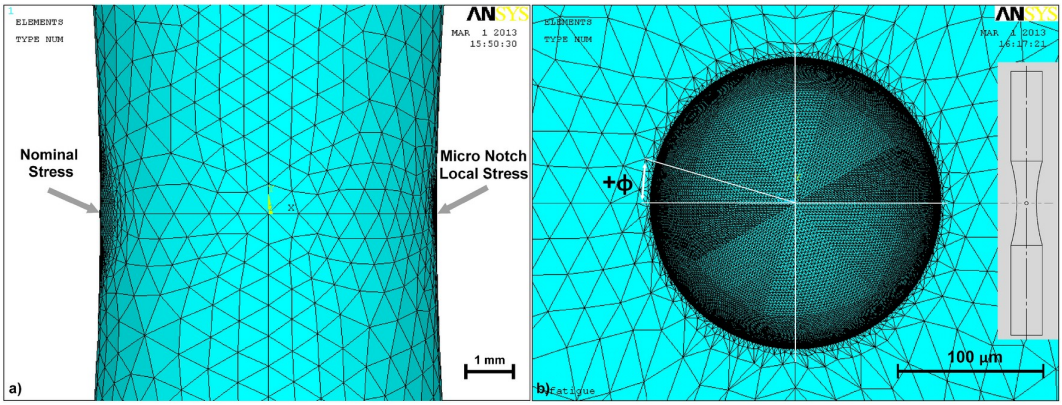


**Figure 8.5:** a) Identification of nominal and local stress points, b) Micro notch geometry and $\phi$ angle.

Regarding the mesh refinement in these simulations, a convergence study is required to avoid biased result in the critical plane estimates, which may result from deficient mesh. The virtual notch is monitored in two regions during the cyclic loadings performed in simulations. The first region, region 1, is defined around the cap edge at specimen surface, where the control nodes are evenly spaced in order to optimize the critical plane estimates. The second region is located at the micro notch root, where at maximum depth (0.2 mm) an additional node is also monitored.

The estimates of the virtual notch approach for the critical plane orientation in crack initiation stages are given based in the $K_t$ values found in the two virtual notch regions described above. Thus, the critical plane orientation is estimated by linking with a line the highest $K_t$ values found in the control nodes at region 1.

The equivalent stress concept is unsuitable to be used in the virtual notch approach,

because under non-proportional loadings its magnitude remains equal in all directions, thus the most loaded regions in the virtual notch can not be identified. Due to that, the axial and shear components of the multiaxial loadings are monitored in the virtual notch regions (1 and 2) and in the nominal region depicted in Figure 8.5.

The axial and shear $K_t$ values are computed separately by considering the local and nominal stresses in axial and shear, respectively. In this way, it is obtained at each node the axial and shear $K_t$ values during the loading period. Since two estimates are obtained for the critical plane orientation, one from the maximum axial $K_t$ and another from the maximum shear $K_t$, the critical plane selection is given by the estimate that has the highest $K_t$ value. This selection is based in the assumption that a crack starts to initiate and grow on the most loaded plane.

Fig.(s) 8.6 to 8.9 show the virtual notch concept in the FEM simulations of an hour glass sample subjected to the four loading paths depicted in Figure 8.3. In these figures, it is represented through several screen shots, the axial stress gradient time evolution in the virtual notch geometry during the loading period. These stress gradients are directly related to the axial $K_t$ values, where the highest stress values are depicted in red, therefore it is hypothesised that the crack initiation process will occur on these red regions.

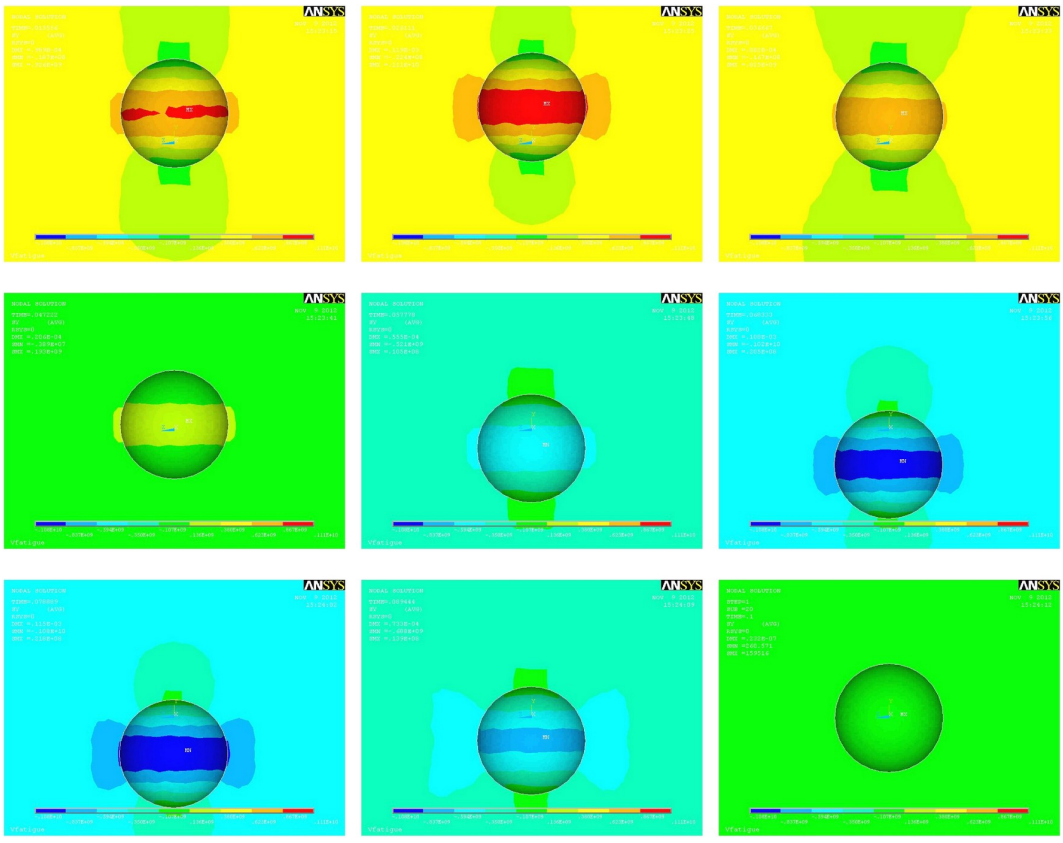

**Figure 8.6:** Time evolution within one loading cycle for the pure axial loading case.

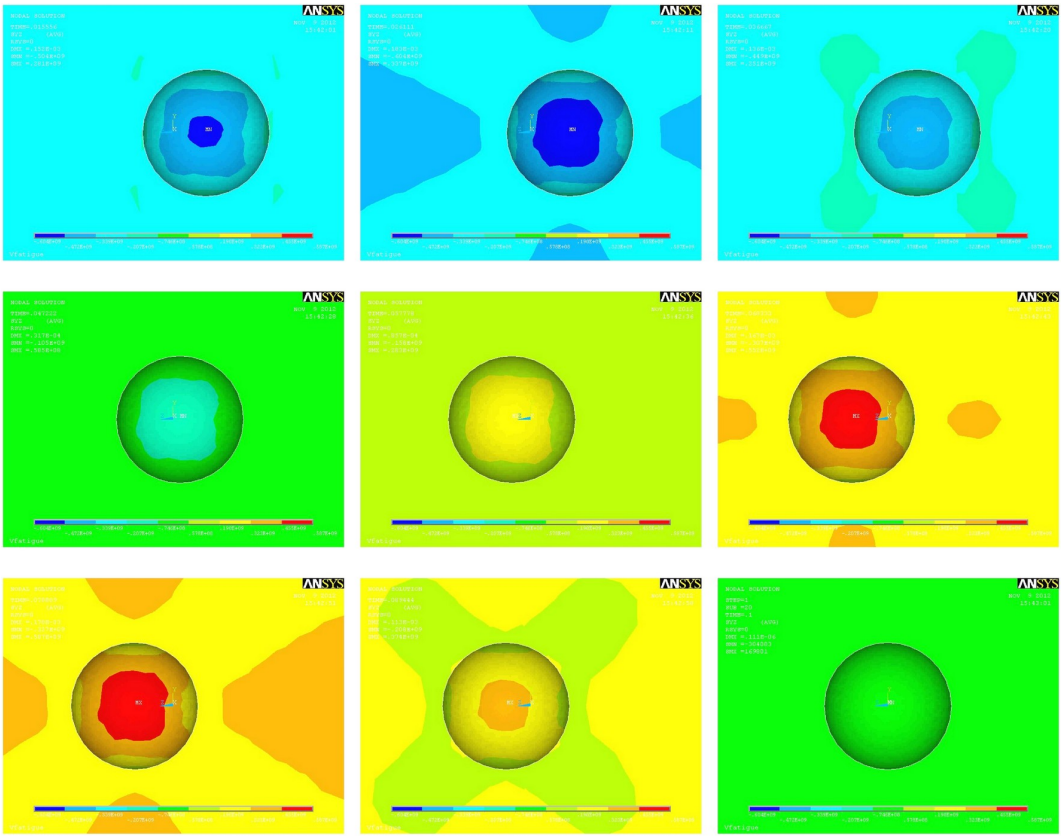

**Figure 8.7:** Time evolution within one loading cycle for the pure shear loading case.

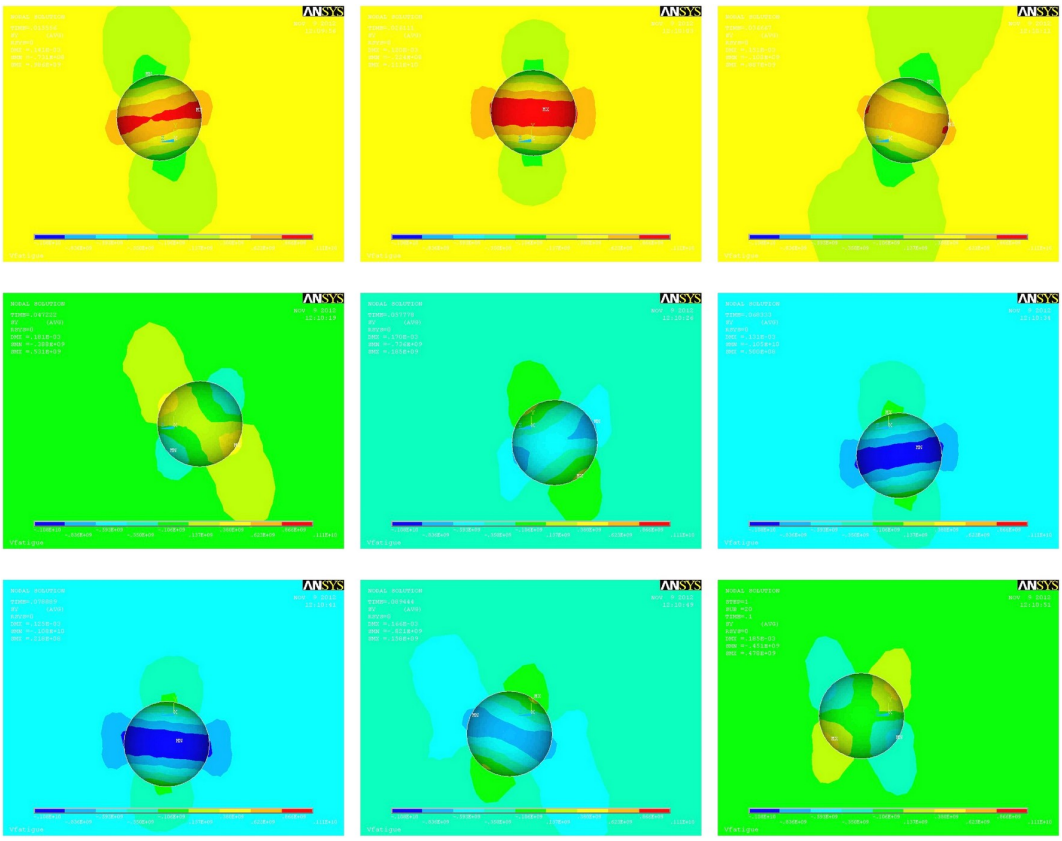

**Figure 8.8:** Out-of-phase time evolution within one loading cycle.

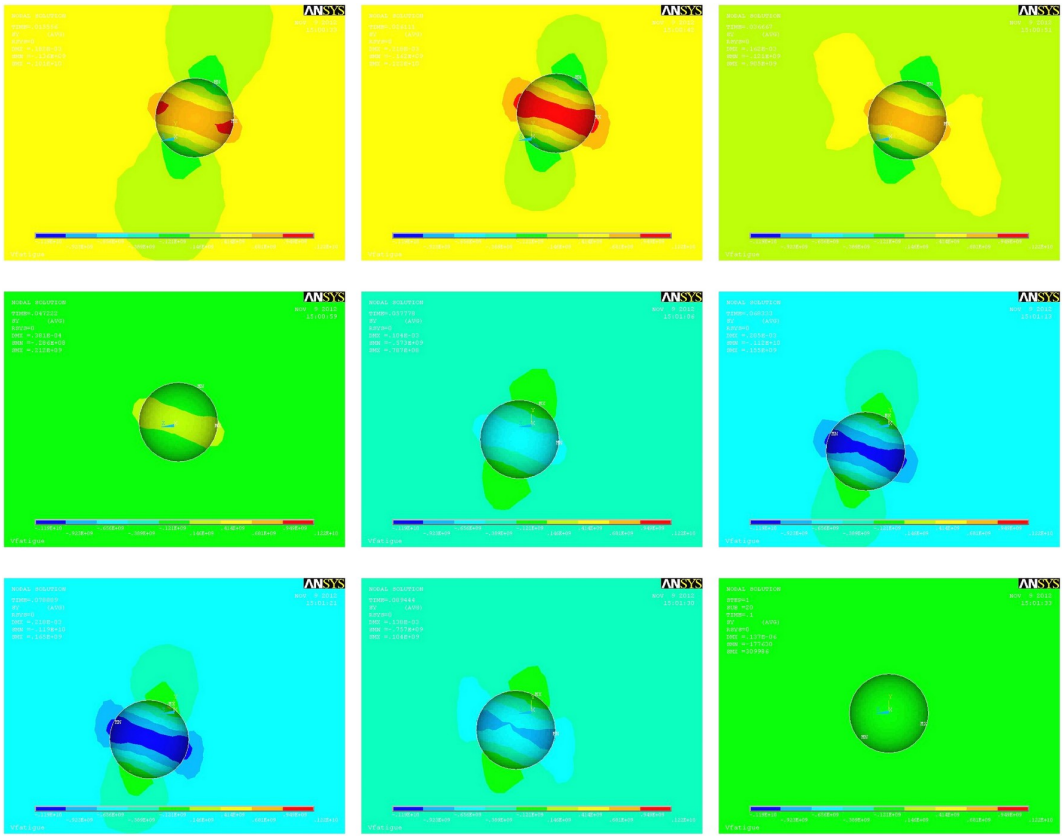

**Figure 8.9:** Proportional loading path time evolution within one loading cycle.

### 8.2.2 Critical plane orientation based in the Mohr's circle

The Mohr's circle method [175] is a useful methodology to project a stress state (stress tensor) in any desired direction. With this method it is possible to project a known stress state, at certain direction, to another one in which the stress state is unknown. In this procedure it is possible to establish different relations between axial and shear stresses just by rotating the projection direction, i.e by rotating the axes of the reference system. Among all possible rotating directions, two specific direction can be obtained, where two specific stress states can be evaluated. In one direction the shear stress components can be eliminated from the stress tensor; this direction is the so-called principal direction, which can be calculated using Eq. 8.1. The other direction is the so-called maximum shear stress direction, where the shear stress components of the stress tensor have their maximum values in this direction. The maximum shear stress direction is given by Eq. 8.2.

$$2\theta_p = \tan^{-1}\left(\frac{2\tau_{xy}}{\sigma_x - \sigma_y}\right) \tag{8.1}$$

$$2\theta_s = \tan^{-1}\left(\frac{\sigma_x - \sigma_y}{2\tau_{xy}}\right) \tag{8.2}$$

In this study, another approach to estimate the orientation of the crack initiation plane is proposed. Thus, it is hypothesised the idea in which the orientation of the crack initiation plane can be estimated by the two aforementioned directions calculated based in the Mohr's circle.

### 8.2.3 Critical plane orientation estimates

Structural materials have different properties under monotonic and cyclic loading regimes, for instance the cyclic yield stress can be quite different from the monotonic one, which depends of the material cyclic behaviour. As seen in Chapter 2 and 3, some materials can soften or hardening or even maintain the same monotonic properties under a cyclic regime [188]. When a cyclic softening occurs the cyclic yield stress is lower than the monotonic one, usually all cyclic curve are under the monotonic curve for all total strains. In other hand, material hardening occurs when the cyclic regime creates cyclic plasticity in such way that the cyclic yield stress becomes higher than the monotonic yield stress.

Magnesium alloys tend to have a cyclic hardening behaviour in tension and a softening one in compression, being these cyclic behaviours highly depend on the grain refinement, purity, lattice intrinsic behaviour like twinning or foundry transformation processes found in these alloys [189, 190]. On the other side the high strength steel 42CrMo4 also cyclically hardens. Thus, it is of utmost importance identify the material cyclic behaviour to estimate the local stress states.

Under strain control, the softening cyclic process lead to have a local stress states lower than the ones estimated using the material monotonic curve. However, cyclic total strains will be greater than the monotonic ones under stress control experiments. In cyclic hardening, it is achieved opposite results i.e. the local stresses are greater than the monotonic ones under strain control, and the total strains decrease their amplitude under a stress control loading regime.

Based on these facts, it can be concluded that fatigue models must be implemented having in to account the material cyclic behaviour since their crack initiation and fatigue life estimates are based in stress/strain amplitudes. Thus, these values must be corrected/updated according to the material cyclic properties [16].

In finite element analysis, the material cyclic behaviour can be accounted by using the material cyclic curve, however the micro-notches resulted from fatigue slip bands at surface or due to the material defects (casting impurities for instance) can create local stress risers with high local plasticity. This non-linear behaviour can affect substantially the crack initiation plane orientation.

Fatigue crack nucleation at grain level also can induce a micro notch presence during the fatigue process. Moreover, the fatigue crack has also high levels of plasticity in the crack

tip due to their geometry. Based in the aforementioned facts, one can conclude that the cyclic plasticity influence on the stress states and strains cannot be neglected in the crack initiation plane assessment [184, 191, 192]. Thus, it is advised to perform an update to the stress/strain time histories by using a cyclic elastic-plasticity model before any critical plane search [16].

In this study the critical plane identification was performed based on stresses and strains for each loading path obtained from numerical simulations. The most loaded spots in the testing sample were monitored for each loading path with and without the ANSYS/Chabone plasticity model. The numeric stress/strain data were afterwards used in a spreadsheet to identify the critical plane estimates using the proposed models and the critical plane models selected in this study.

#### 8.2.3.1 Critical plane estimation - direct approach (without plasticity model)

The critical plane models used to estimate the crack initiation planes were the SWT, Fatemi-Socie, Liu1, and Liu2. These models are the most used critical plane models among the critical plane criteria, due to that they were selected here to evaluate their performance for the 42CrMo4 and AZ31B-F materials. Figure 8.10 shows the critical plane damage parameter variation in $\theta$ for the loading paths considered in this study and depicted in Figure 8.3. The results presented in Figure 8.10 are valid for both 42CrMo4, and AZ31B-F materials, where the critical plane identification procedure yields the same estimates for the critical plane orientation in both materials. However, in fatigue life estimates it is necessary to compute the inherent damage parameter for each criterion and material. The critical plane orientation $\theta$ is identified for each loading path through the maximum damage parameter obtained along the loading period. The theoretical results depicted in Figure 8.10 were determined for the same stress level, i.e. it was used the same axial and shear stress components in each critical plane in order to avoid any stress level influence on the critical plane estimates. Based on these results, it can be concluded that the SWT and Liu 1 criteria have the same values of damage parameter in all $\theta$, moreover the Fatemi-Socie criterion has its highest value in the OP loading case, which indicates a lower fatigue life estimate for this loading path comparatively to the other three loadings considered here.

#### 8.2.3.2 Loading path influence on $K_t$

Tables 8.2 and 8.3 show the numerical results for the stress concentration factors $K_t$ calculated for each loading path considered here. Table 8.2 gathers together the results for the high strength steel 42CrMo4 calculated in Ansys and using its intrinsic Chaboche's plasticity model. The stress analysis was performed in the nodes found at notch root and at the intersection boundary between the notch cap and the specimen surface. The analyses was performed at each node considering each loading component, axial and shear

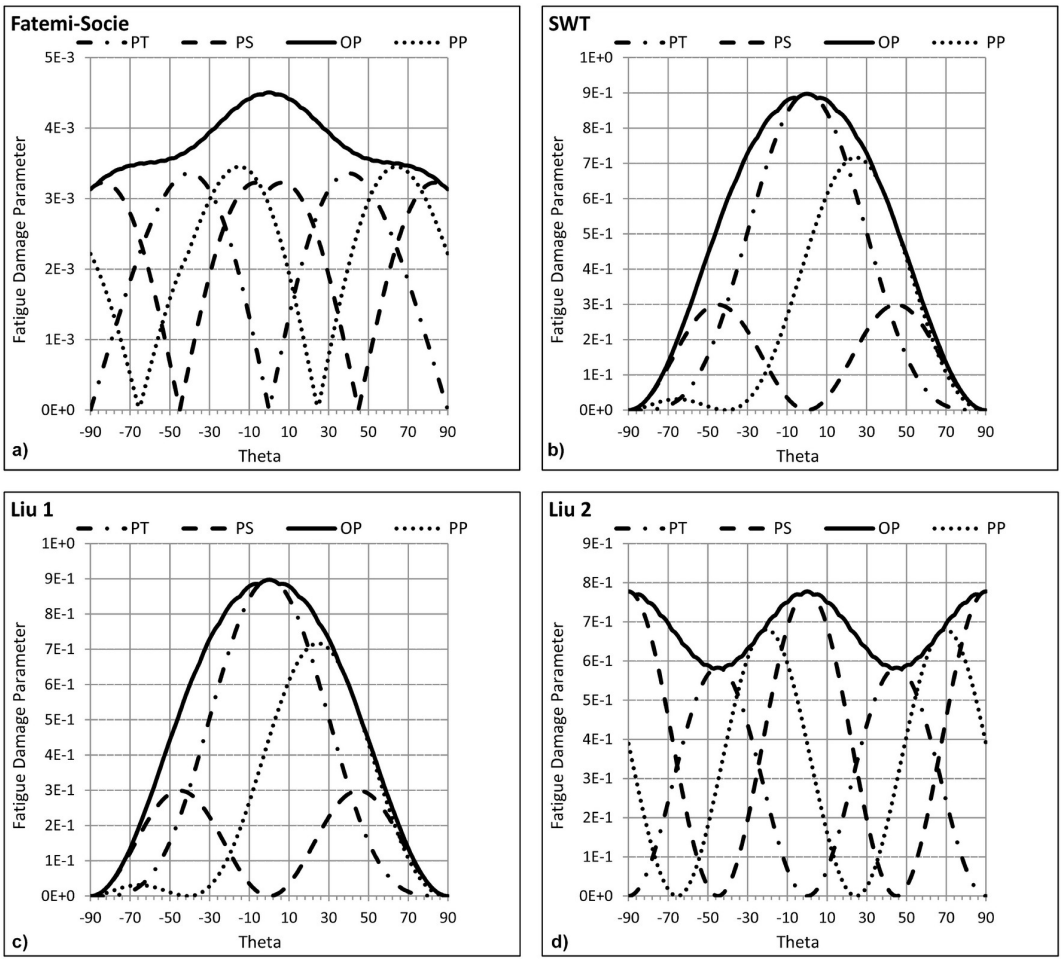


**Figure 8.10:** Critical plane damage parameter and its critical plane orientation for the 42CrMo4, and the AZ31B-F materials.

stress time evolution, as independent stresses. This can be made because the axial and shear stresses numerically computed at each node, have already into account the shear contribution to the axial stress and the axial force contribution to the shear stress. The local axial and shear instantaneous stresses at notch root and notch cup interface with the specimen outer surface, were divided by their antipodal nominal instantaneous values of the axial and shear stress, respectively. This approach was adopted to compute the stress concentration factors $K_t$, because equivalent stress approaches do not capture the $K_t$ variation in some loading paths as discussed in previous Chapters. Therefore, in this study, it was determined a $K_t$ for the axial loading component and other for the shear one. The stress level of the nominal stresses used in the FEM simulations were 30% lower than the material cyclic yield stress, in order to avoid any cyclic plasticity in the remote stress control region i.e. antipodal nominal region. Tables 8.2 and 8.3 show the 42CrMo4 $K_t$ numerical results obtained with and without the Chaboche plasticity model, respectively. Based on the results gathered in Tables, 8.2 and 8.3, it can be concluded that the $K_t$ values obtained with the plasticity model approach are lower than the ones obtained without it. Therefore, numeric simulation without using an plasticity model

can result on higher stress values at notch root and respective boundary. This result is justified through the Chaboche plasticity input, where it was used the 42CrMo4 cyclic curve instead the monotonic one. Excepting in the PP loading case, the highest axial and shear $K_t$ values occur at the notch root, which were obtained with and without plasticity model.

**Table 8.2:** $K_t$ for each loading path at notch root and surface calculated with plasticity model. Maximum values found during the loading period.

| with Plasticity Model - 42CrMo4 | | | |
|---|---|---|---|
| Loading Path | Location | $K_t$ Axial | $K_t$ Shear |
| OP | Root | 1.69 | 1.48 |
| | Surface | 1.60 | 1.20 |
| PP | Root | 1.47 | 1.08 |
| | Surface | 1.48 | 1.22 |
| PS | Root | nan | 1.51 |
| | Surface | nan | 1.09 |
| PT | Root | 1.69 | nan |
| | Surface | 1.60 | nan |

**Table 8.3:** $K_t$ for each loading path at notch root and sample surface calculated without plasticity model. Maximum values found during a loading cycle period.

| without Plasticity Model - 42CrMo4 | | | |
|---|---|---|---|
| Loading Path | Location | $K_t$ Axial | $K_t$ Shear |
| OP | Root | 1.83 | 1.73 |
| | Surface | 1.80 | 1.24 |
| PP | Root | 1.83 | 1.67 |
| | Surface | 2.06 | 1.43 |
| PS | Root | nan | 1.72 |
| | Surface | nan | 1.08 |
| PT | Root | 1.83 | nan |
| | Surface | 1.80 | nan |

In the PP loading case, the $K_t$ results obtained without the plasticity model indicates the biggest axial and shear $K_t$ values at the sample surface being the shear $K_t$ at notch root higher than the one at surface, please see Table 8.3. In contrast at Table 8.2, the opposite scenario occurs, the results obtained for the PP loading case with the plasticity model indicates a shear $K_t$ at notch surface higher than at notch root. These results lead to conclude that the loading path type has influence in the stress concentration factors. Therefore, the $K_t$ values are dependent on the crack geometry (which is of common

knowledge) and on the loading path type, which is a new finding regarding multiaxial fatigue. Also, the $K_t$ values are dependent on the stress level where elastic-plastic cyclic models play a important role. In this study, the multiaxial loading components, the axial and shear stress of the loading path, have a stress amplitude ratio equal to $\tau/\sigma = 1/\sqrt{3}$ being the shear stress amplitude $\sqrt{3}$ times less than the axial one. In this way, the stress level could be defined based in the von Mises equivalent stress, for each loading path. The average values of the axial $K_t$ obtained in the cases OP and PP are greater than the shear ones, in both simulations (with and without plasticity model). The numeric results of the axial $K_t$ obtained with the Chaboche's plasticity model are 25% greater at notch root and 35% at notch interface with the sample surface, comparatively to the shear $K_t$ results. Moreover, in the simulations performed without the Chaboche plasticity model, the axial values of $K_t$ were 7% greater at notch root and 45% greater at the notch surface.

Table 8.4 shows the $K_t$ variation in percentage at the notch root for each loading path. These variations were calculated by comparing the $K_t$ results obtained with and without the Chaboche plasticity model. For instance, the axial value of $K_t$ increases 20% in the PP loading case, when the simulation is performed without plasticity model, please see Table 8.4. The greatest variation occurs in the PP loading, where the axial $K_t$ is reduced about 20%, and the shear one in 35%, when it is used a plasticity model. In the other cases, it was found a similar reduction, i.e. about 7% for the axial $K_t$ and 12% for the shear one.

Table 8.5 shows the mean values of axial and shear $K_t$ at the notch cap surface obtained with the Chaboche plasticity model; the greatest values were obtained in the OP loading case, and the lowest ones were obtained in the PP loading case. From these results, it can be concluded that the OP loading case, during the loading period have in average, the highest stress level at notch, comparatively to the stress level found in the PP loading case.

**Table 8.4:** $K_t$ variation in % due to the loading path type at notch root and surface computed without plasticity model.

| At notch root - 42CrMo4 | | |
|---|---|---|
| Loading Path | $K_t$ Axial [%] | $K_t$ Shear [%] |
| OP | 7 | 14 |
| PP | 20 | 35 |
| PS | nan | 12 |
| PT | 7 | nan |

**Table 8.5:** $K_t$ mean values at notch surface along the loading period.

| with Plasticity Model - 42CrMo4 | | | |
|---|---|---|---|
| Loading Path | Location | $K_t$ Axial | $K_t$ Shear |
| OP | Surface | 0.85 | 0.93 |
| PP | Surface | 0.65 | 0.7 |
| PS | Surface | nan | 0.85 |
| PT | Surface | 0.85 | nan |

#### 8.2.3.3 Maximum $K_t$ approach

Figure 8.11 shows the estimates of the maximum $K_t$ approach for the orientation of the crack initiation plane in each loading path. Since the $K_t$ has an important influence on the crack nucleation and initiation process, this method was numerically implemented to verify the loading path effect in the fatigue life and orientation of the crack initiation plane. Fatigue micro-cracks can be considered as micro-notches, which for the majority of materials are created during 80% of fatigue life.

Thus, it is important to investigate the loading path effect on the stress state distribution at yearly crack stages simulated here with a virtual notch. In the approach presented here, the maximum value for axial and shear $K_t$ is determined along the loading period, and assigned to each node of the notch cup. Thus, the crack initiation plane estimated by the axial $K_t$ is obtained by linking the maximum axial $K_t$ values. The same reasoning is used to estimate the crack initiation plane using the shear $K_t$. From these two $K_t$ estimates, the one with the greatest value of $K_t$ (in axial or in shear) will give the orientation of the crack initiation plane for each loading path.

The graphs of Figure 8.11 depicts the $K_t$ magnitudes, in shear and axial, associated to each node at the interface between the notch cup and the sample surface. For instance, in the PT loading case, Figure 8.11 a) shows the highest $K_t$ value in axial located at $0^o$ and $180^o$ degrees, whereas at $90^o$ and $270^o$ direction the $K_t$ is zero. It is possible to have an idea of the $K_t$ maximum magnitude in any direction during the loading period by linking the graph origin to the $K_t$ curves depicted in Figure 8.11. These curves were determined at nodes located in the interface between the notch cup and the test sample surface. Moreover, it is also represented two circles with two different radius, one is the axial $K_t$, and the other is the shear one, both determined at the notch root.

The circle based in the axial $K_t$ radius is depicted by a dotted line, and the shear one by a full line, as shown in Figure 8.11. These two circles allow to perform a direct correlation between the $K_t$ values found at notch root and sample surface, where it is possible to identify the location of the surface $K_t$ values which are greater or equal to the ones found at notch root.

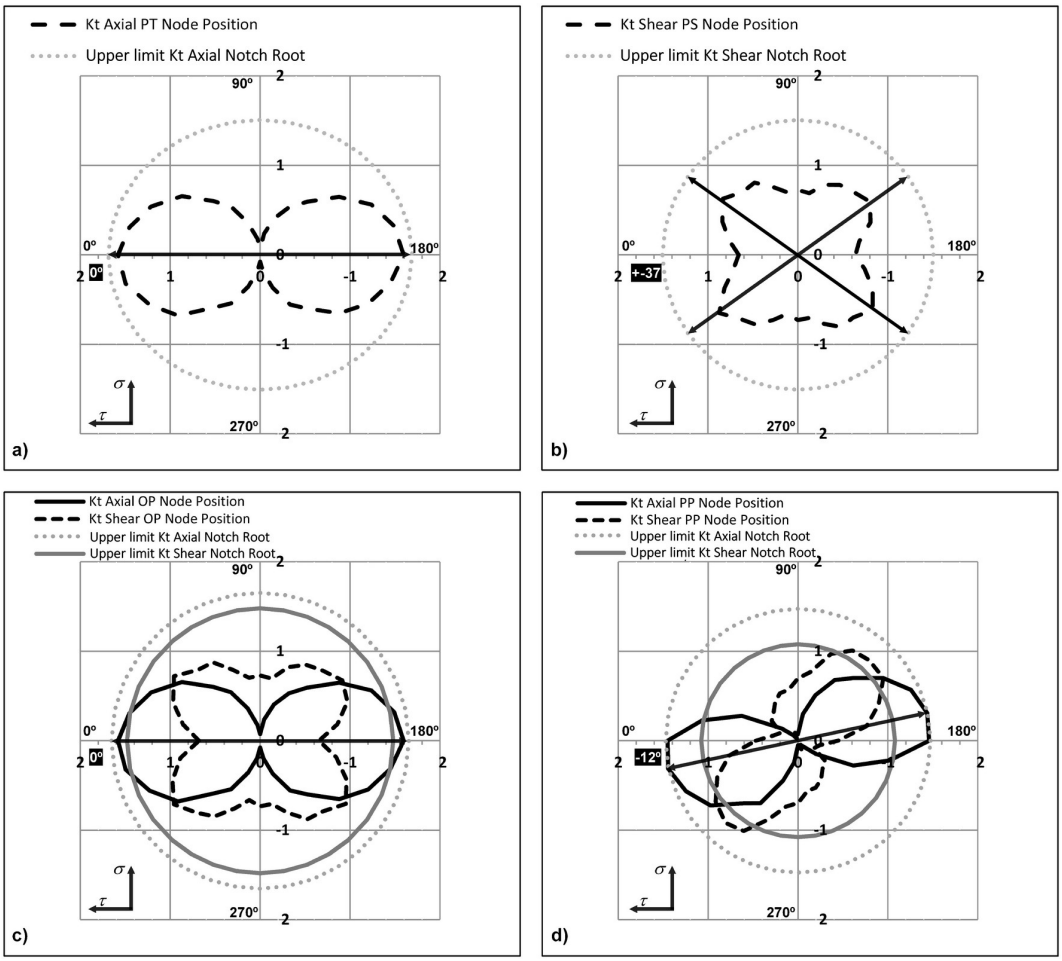


**Figure 8.11:** Critical plane estimates based in the maximum $K_t$ approach for the loading cases a) PT, b) PS, c) OP, and d) PP.

Figure 8.11 a) shows the critical plane orientation estimates for the loading case PT, where the maximum axial $K_t$ values indicate the critical plan at $0^o$, and the highest $K_t$ value occurs at notch root. Figure 8.11 b) shows the shear $K_t$ magnitude variation in the loading case PS, where the highest values of $K_t$ found at notch surface occur at $\pm 37^o$ direction, and the highest $K_t$ value was found at notch root.

Figure 8.11 c), shows the results obtained for the OP loading case; the highest $K_t$ values were found in the axial curve, where the direction of the crack initiation plane is estimated at $0^o$ degrees. In this case, the axial $K_t$ value at notch root is almost equal to the maximum ones found at notch surface. Moreover, the axial $K_t$ is greater than the shear one, therefore the orientation of the crack initiation plane is estimated by the axial $K_t$ curve; the same pattern is observed on the PP loading case, please see Figure 8.11 d). This result can be explained through the stress amplitude ratio used in this study, where the axial stress amplitude is $\sqrt{3}$ times greater that the shear one, which creates an axial stress predominance in the loading path stress level. This stress amplitude ratio is traditionally used in fatigue life experiments and is based on the von Mises stress space.

Figure 8.11 d) shows the results for the PP loading case; here, the critical plane orientation is estimated by the maximum axial $K_t$ found at $\pm 12^o$ direction, also at the surface notch, the axial $K_t$ values are very similar to the one found at the notch root. However, the shear $K_t$ found at the notch root is less than the maximum shear $K_t$ values found at surface. This result can be seen in Figure 8.11 d), where the circle depicted by a full line intercepts the shear $K_t$ dotted line around the $-45^o$ and $135^o$ directions. Thus, from the results discussed above, it can be hypothesised that the stress amplitude ratio has a strong influence in the orientation of the crack initiation plane, which may result from a shear or axial stress predominance.

#### 8.2.3.4 Gradient approach

The interpretation of the $K_t$ estimates can be facilitated by using the gradient of the axial and shear $K_t$ results in the notch cup. Moreover, with this gradient it becomes possible to use this approach in numerical simulations. Figure 8.12 shows the axial and shear $K_t$ gradients at the notch cap obtained under the PT loading case. In Figure 8.12 a) can be found the highest axial $K_t$ values located at $0^o$ and $180^o$ degrees, please see $\phi$ referential depicted in Figure 8.5 b). Moreover, the highest values of shear $K_t$ were obtained at $\pm 45^o$, as seen in Figure 8.12 b) Based on the maximum $K_t$ approach, the orientation of the crack initiation plane is given based in one of these two $K_t$ gradients (axial or shear). The $K_t$ values are determined for each node of the micro notch cap in order to obtain the $K_t$ gradient, however, the orientation estimates of the crack initiation plane are based in the maximum values found at the specimen surface. Thus, for the PT loading case, Figure 8.12 a), the maximum axial $K_t$ approach estimates the orientation of the crack initiation plane at $0^o$, and the highest axial $K_t$ value occurs at notch root. Figure 8.13 a) shows the axial $K_t$ gradient for the PS loading case, where the maximum axial $K_t$ was found at $\pm 45^o$. However, in this loading case (PS), the highest maximum $K_t$ is the shear one, as expected. Figure 8.13 b) shows the locations of the highest shear $K_t$ found in the micro notch interception with specimen surface, which were located at $\pm 45^o 2$; the highest shear $K_t$ was found at the micro notch root. Figure 8.14 a) shows the results obtained for the OP loading case, where the highest $K_t$ occurs in the axial gradient, which suggests a crack initiation plane at $0^o$ degrees. In this loading case (OP), the $K_t$ at the micro notch root is almost equal to the ones verified at notch cap interception with specimen surface. The axial $K_t$ gradient has the greatest values comparatively to the shear one, please see Figure 8.14 b), thus the maximum $K_t$ estimate for the critical plane in this loading path is given through the axial $K_t$, which estimate the crack initiation plane at $0^o$. Figure 8.15 a) shows the axial $K_t$ gradient for the PP loading case, which estimates the critical plane at the $\pm 13^o$ direction. Moreover, in this loading case (PP), the axial $K_t$ values are greater than the one verified at the micro notch root, the same results was found for the shear $K_t$ gradient, i.e. the $K_t$ values at surface are greater than the one verified at notch root. The

results obtained for the PP loading case have the maximum values of $K_t$ at the sample surface, which is contrary to the results obtained for the other loading paths, where the maximum $K_t$ occurs at the notch root. Based on the aforementioned results, it can be concluded that the $K_t$ gradient approach is sensitive to the loading path type.

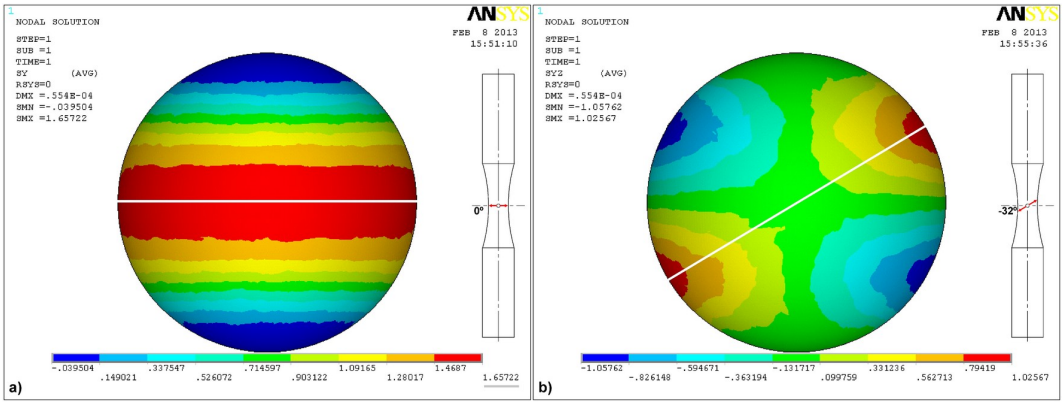


**Figure 8.12:** Critical plane estimation based on maximum $K_t$ for PT loading with plasticity model, case : a) Axial, and b) Shear.

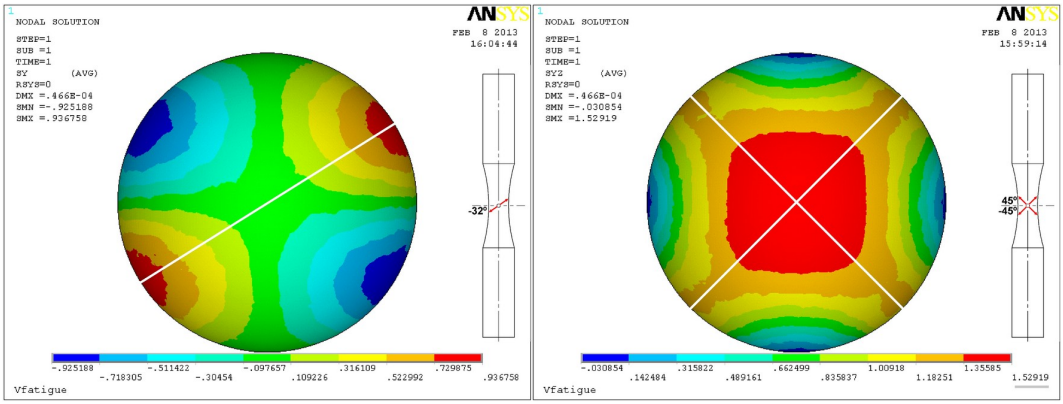


**Figure 8.13:** Critical plane estimation based on maximum $K_t$ for PS loading with plasticity model, case : a) Axial, and b) Shear.

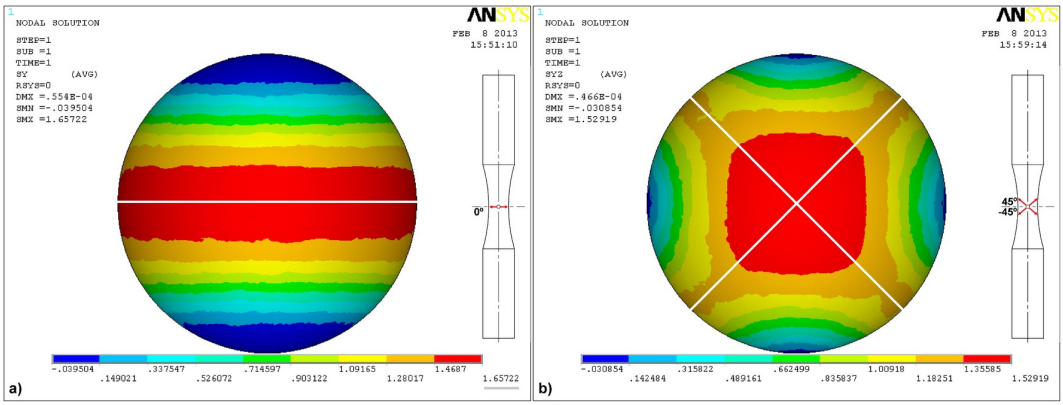


**Figure 8.14:** Critical plane estimation based on maximum $K_t$ for OP loading with plasticity model, case : a) Axial, and b) Shear.

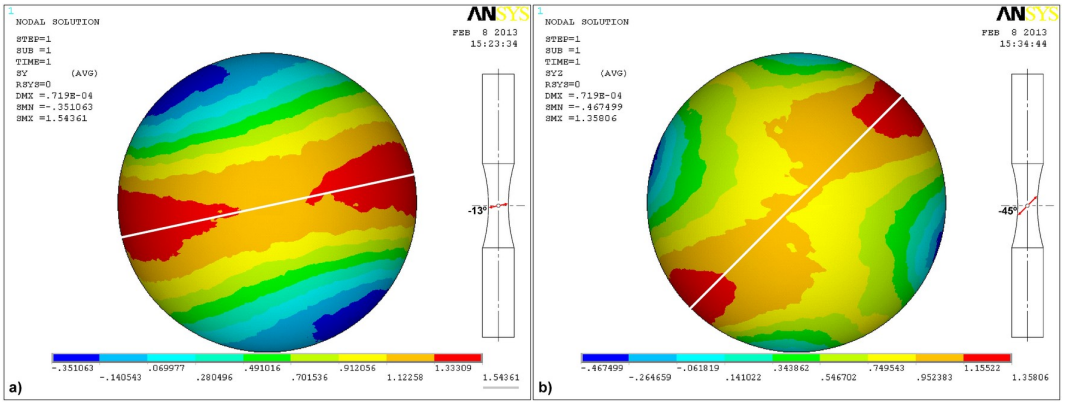


**Figure 8.15:** Critical plane estimation based on maximum $K_t$ for PP loading with plasticity model, case : a) Axial, and b) Shear.

#### 8.2.3.5 Critical plane estimates based in the Mohr's circle

Figure 8.16 shows the Mohr's circle estimates for the critical plane orientations of the loading paths considered in this study. In figure 8.16, it is depicted the critical plane estimates based in the maximum principal stress directions, where the critical plane direction is perpendicular to the principal stress orientation.

In Figure 8.17, it is shown the results of the critical plane estimates based in the maximum shear stress direction given by the Mohr's circle. In the maximum principal stress approach, the crack opening process (initiation plus growth) is based on tensile mechanisms, thus the fatigue crack growth is perpendicular to the opening stress direction. On the other hand, in the maximum shear stress approach, it is proposed that the crack opening process is based in shear stress mechanisms, which can be promoted by tensile stress or constrained by compressive stress.

The estimates of the principal stress direction approach for cases PT, PS and PP were, $0^o$, $-45^o$ and $-25^o$, respectively. This procedure do not give a direct result for the critical plane direction under out of phase loading cases, because under non-proportionality the principal directions changes during the loading period.

Figure 8.16 d) shows the principal directions variation on the OP loading case, starting with a pure shear stress state (sub-Figure 8.16 d1), passing through a biaxial loading condition (sub-Figure 8.16 d2), and ending on a pure tensile (sub-Figure 8.16 d3). In this loading case, it was considered the principal direction that has the maximum principal stress value in order to estimate the critical plane orientation, which in this case it was at $0^o$. The same reasoning can be applied to the results of the maximum shear stress approach for the OP loading case, where the direction of the crack initiation plane is at $90^o$. For the PT, PS and PP loading cases, the maximum shear stress approach estimates the crack initiation plane at $-45^o$, $90^o$ and $-70^o$, respectively.

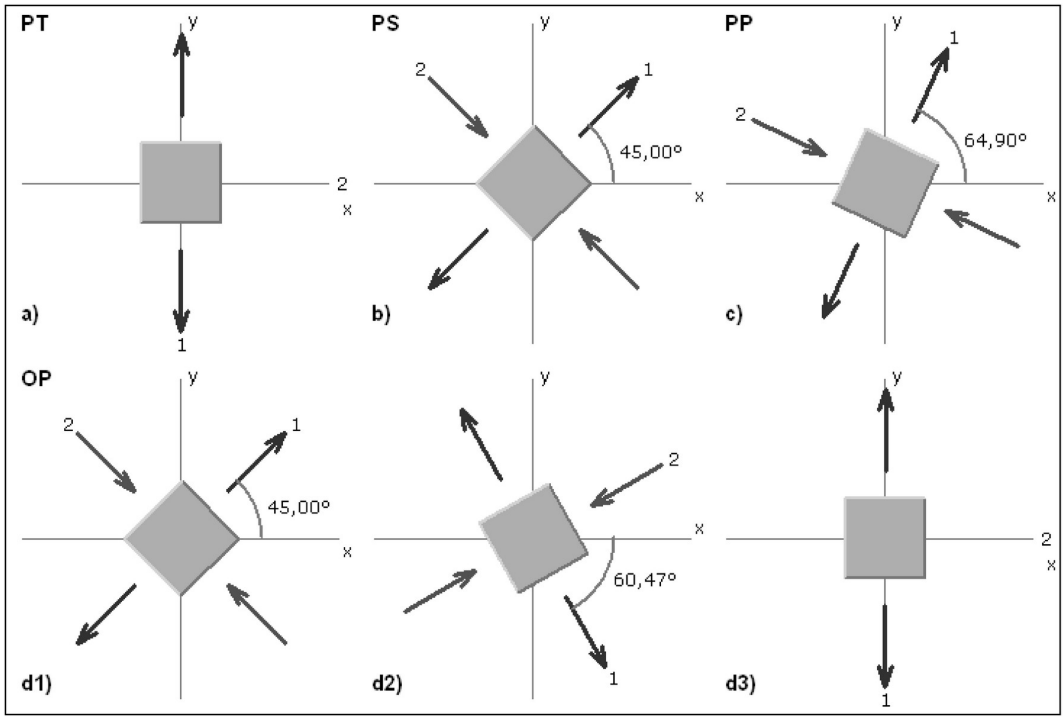


**Figure 8.16:** Critical plane estimates based in the principal stress directions obtained for loading case a) PT, b) PS, c) PP, and d) OP

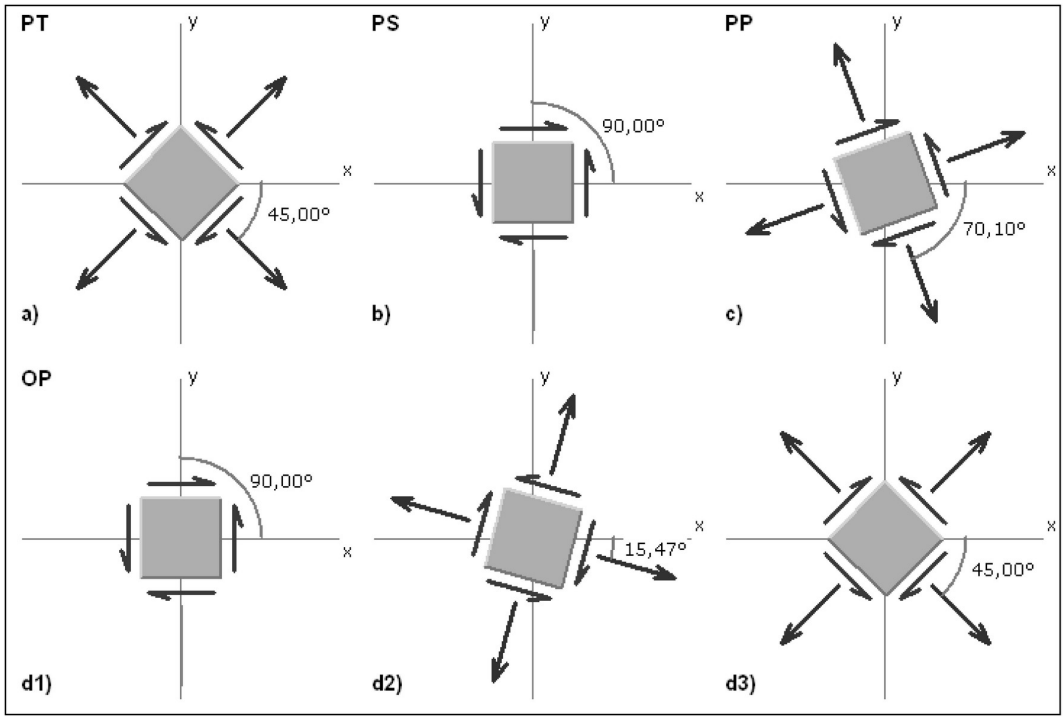


**Figure 8.17:** Critical plane estimates based on the maximum shear stress directions for the loading case a) PT, b) PS, c) PP, and d) OP.

## 8.3 Experimental fatigue crack analysis

Figure 8.18 shows the fracture surfaces and the crack initiation planes for the PT loading case, in both materials considered here. The 42CrMo4 specimen failed at 247953 cycles under 455 [MPa] and the Mg alloy failed at 13164 cycles under 140 [MPa]. Despite that fatigue failure occurs at different fatigue life regimes in each material, one at HCF and other near the upper limit of the LCF regime, the fracture surface shows a similar topography for this loading case. Both surfaces suggest a ductile fatigue failure mechanism with two different zones and roughness, i.e. the fatigue zone (FZ), with a smooth roughness, and an instantaneous zone (IZ), with accentuated roughness.

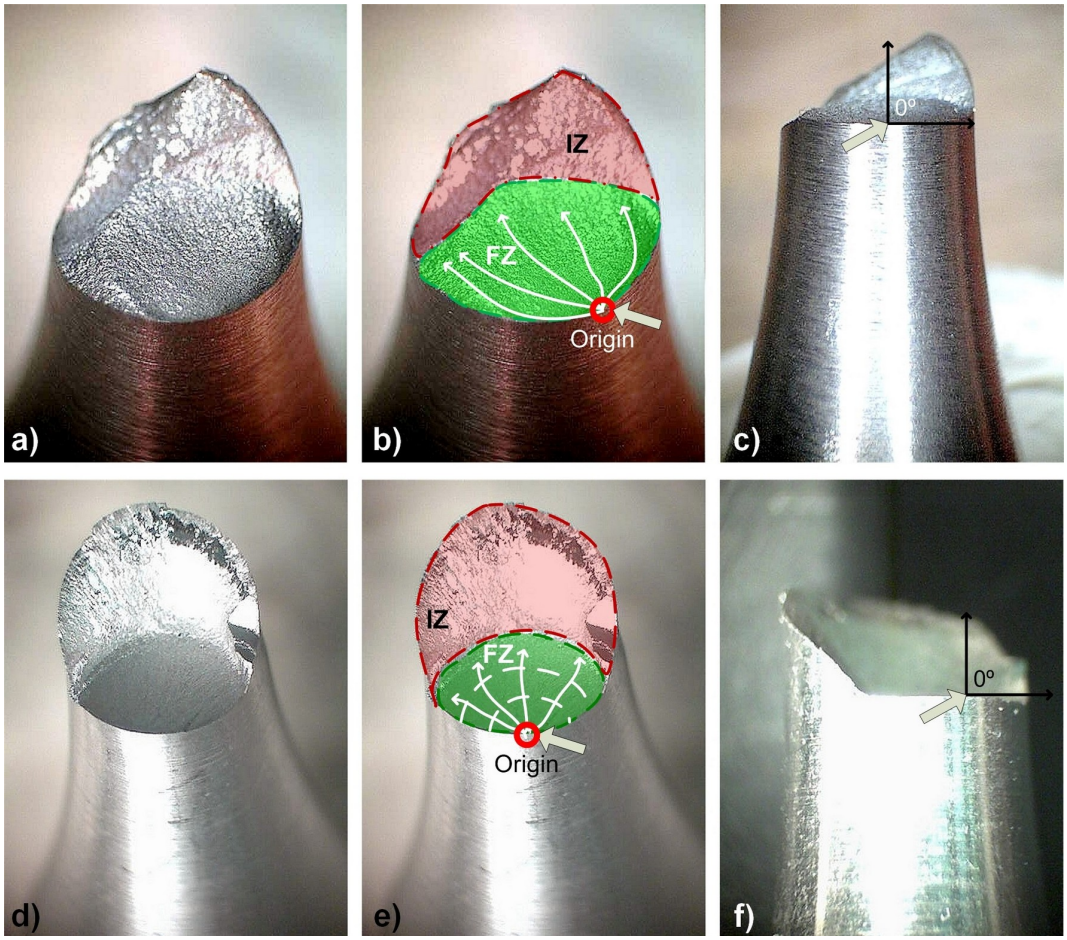


**Figure 8.18:** Loading case PT: Fracture surface for a), b) 42CrMo4 and d) e), Mg AZ31B-F. Crack initiation angle for c) 42CrMo4, and f) Mg AZ31B-F.

In the smoothest area of the fatigue zone, it is possible to identify the crack initiation spot, and in the instantaneous zone the final fracture can be analysed. The roughness change in the fracture surface shows different speeds of crack growth indicating that the failure didn't happen suddenly. In this loading case, most of the fatigue life is spent mainly in mode I crack growth, and it finishes with a rough and crystalline appearance at the IZ. The final fracture (IZ) occurred with a crack separation in mode II through slip

mechanism in the maximum shear plane. No expressive propagation marks were observed in the high strength steel, however in the Mg alloy it was observed a slight river marks starting near the crack initiation spot which progressed into the crack growth direction. In both materials, the experimental crack initiation planes of the PT loading path were measured at $0^o$ degrees. Figure 8.19 shows the fatigue crack results for the PS loading case, where it is depicted the fatigue crack surface in both materials. The steel sample was cyclic loaded with a von Mises equivalent stress amplitude equal to 685 [MPa], and it failed at 315668 cycles. The Mg alloy sample was subjected to a von Mises equivalent stress amplitude equal to 120 [MPa] and it failed at 128719 cycles. The fracture surface found in the steel sample shows a unique initiation spot with a initiation plane oriented at $45^o$, which is a typical result for twisting loads in ductile materials [16, 187]. Under multiaxial loadings the crack initiation process has a mixed mode, thus it is expected a reduction of this angle due to the axial component.

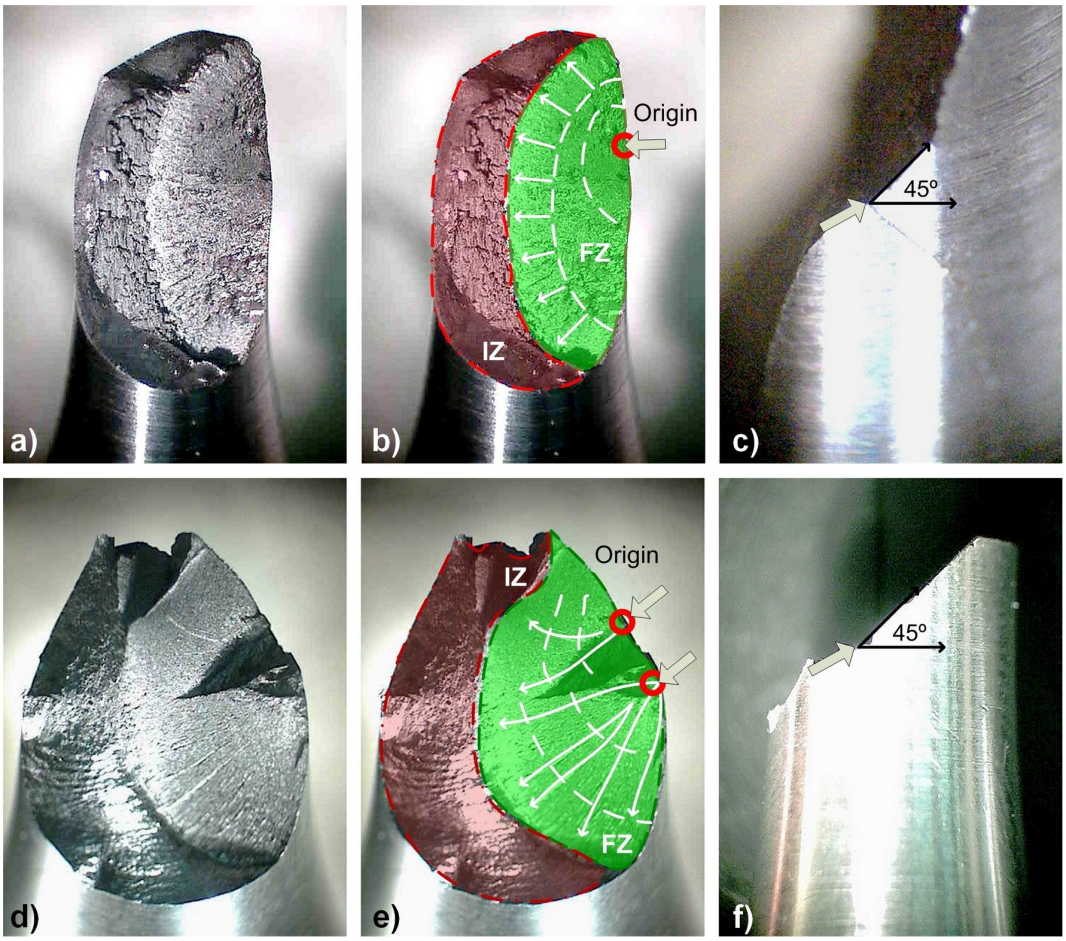


**Figure 8.19:** Loading case PS: Fracture surface for a), b) 42CrMo4 and d) e), Mg AZ31B-F. Crack initiation angle for c) 42CrMo4, and f) Mg AZ31B-F.

The fatigue and instantaneous zones depicted in Figure 8.19 show a strong granulated surface in the steel specimen, however in the Mg specimen the fracture surface is smoother. Both fracture surfaces have a similar pattern in the FZ and IZ. However, in the Mg fracture

surface, it was observed ratchet marks with two initiation spots, which grew towards the centre of the specimen. Moreover, in the instantaneous zone, it can be seen some rifling grooves similar to progression marks. Figure 8.20 shows the fracture surfaces obtained in the proportional loading (PP) experiments. The steel sample was cyclic tested with a von Mises equivalent stress amplitude equal to 622 [MPa], and their failure occurred at 311201 cycles. The Mg specimen was subjected to a von Mises equivalent stress amplitude equal to 150 [MPa], and it failed at 16800 cycles.

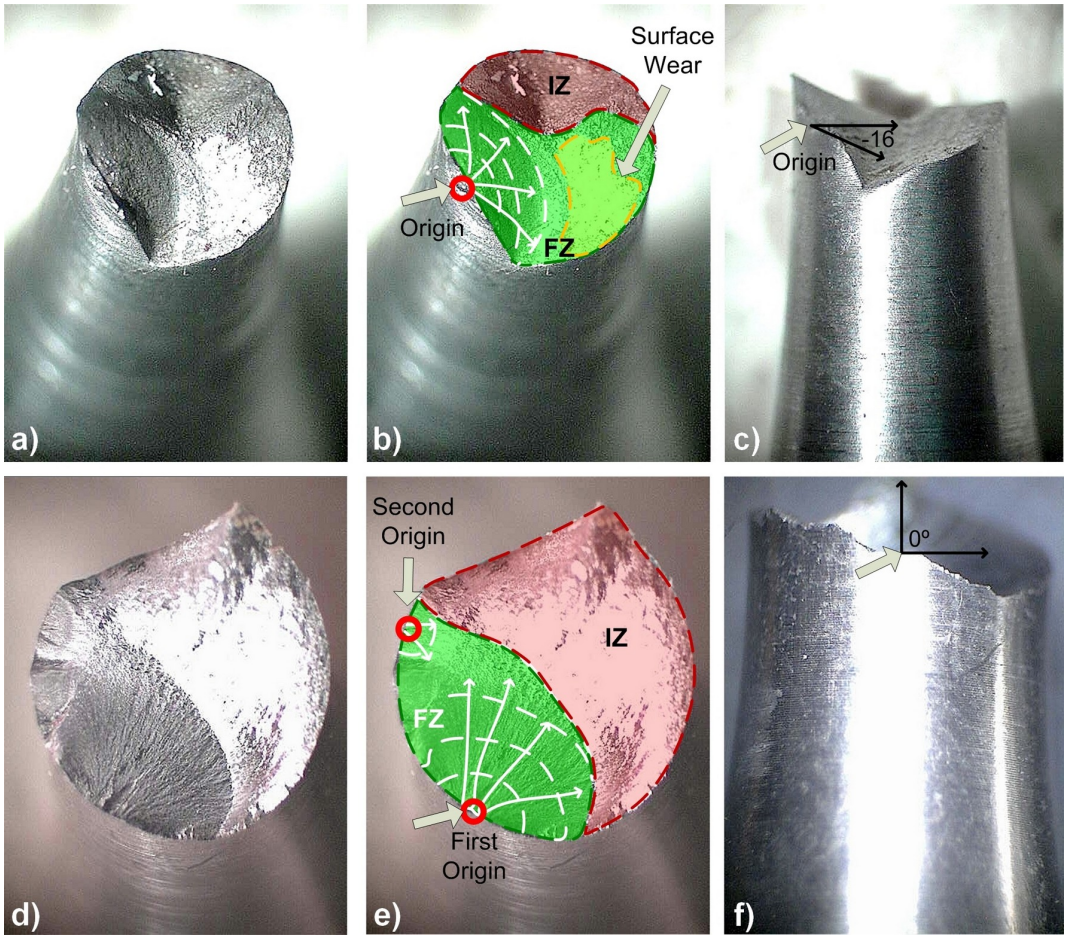


**Figure 8.20:** Loading case PP: Fracture surface for a), b) 42CrMo4 and d) e), Mg AZ31B-F. Crack initiation angle for c) 42CrMo4, and f) Mg AZ31B-F.

Also here, the samples were tested at different fatigue life regimes as seen in the PT loading path. Different stress levels changed the size of the instantaneous zones found in both samples. Due to that, it was obtained different fracture surface's topologies for the same loading path. Thus,under multiaxial loading conditions, the fracture surface topography is dependent on the stress level, which is a result in opposition to the observed in the loading cases PT and PS. The fracture surface of the steel sample has one fatigue crack origin, and three distinct zones: the usual FZ and IZ zones and a wear region. The Mg fracture surface shows two fatigue crack origins, and many river marks pointing to the first crack origin. It is expected that under the same fatigue regime the fatigue fracture surface be

more similar in both materials. The experimental direction of the crack initiation plane was $\pm 16^{o}$ in the steel sample, and $0^{o}$ in the magnesium alloy. Recalling the premise in which the axial component of a multiaxial loading changes the crack initiation angle from $\pm 45^{o}$ (pure shear) to a value between $\pm 45^{o}$ and $0^{o}$ (pure axial) accordingly to the stress amplitude ratio, it can be concluded that the Mg alloy is much more sensitive to the axial component than to the torsional one. This result is corroborated by the magnesium cyclic behaviour discussed in Chapter 3. Figure 8.21 shows the fatigue crack surfaces obtained in the OP loading path, where the steel sample was cyclic loaded with a von Mises equivalent stress amplitude equal to 686 [MPa], the sample fatigue life was 197548 cycles. The Mg sample was cyclic loaded with a von Mises equivalent stress amplitude equal to 72.5 [MPa] which caused the sample collapse at 576336 cycles. In both materials, the fracture surfaces were very similar in this loading path, which supports the hypothesis in which the fracture topography is similar in both materials for a high cycle loading regime. In the Mg fracture surface, the IZ has a diagonal riffle grooves, which started from the FZ and evolved throughout the end of the IZ. Diagonal riffle grooves in instantaneous zone indicate a biaxial loading at the fracture instant.

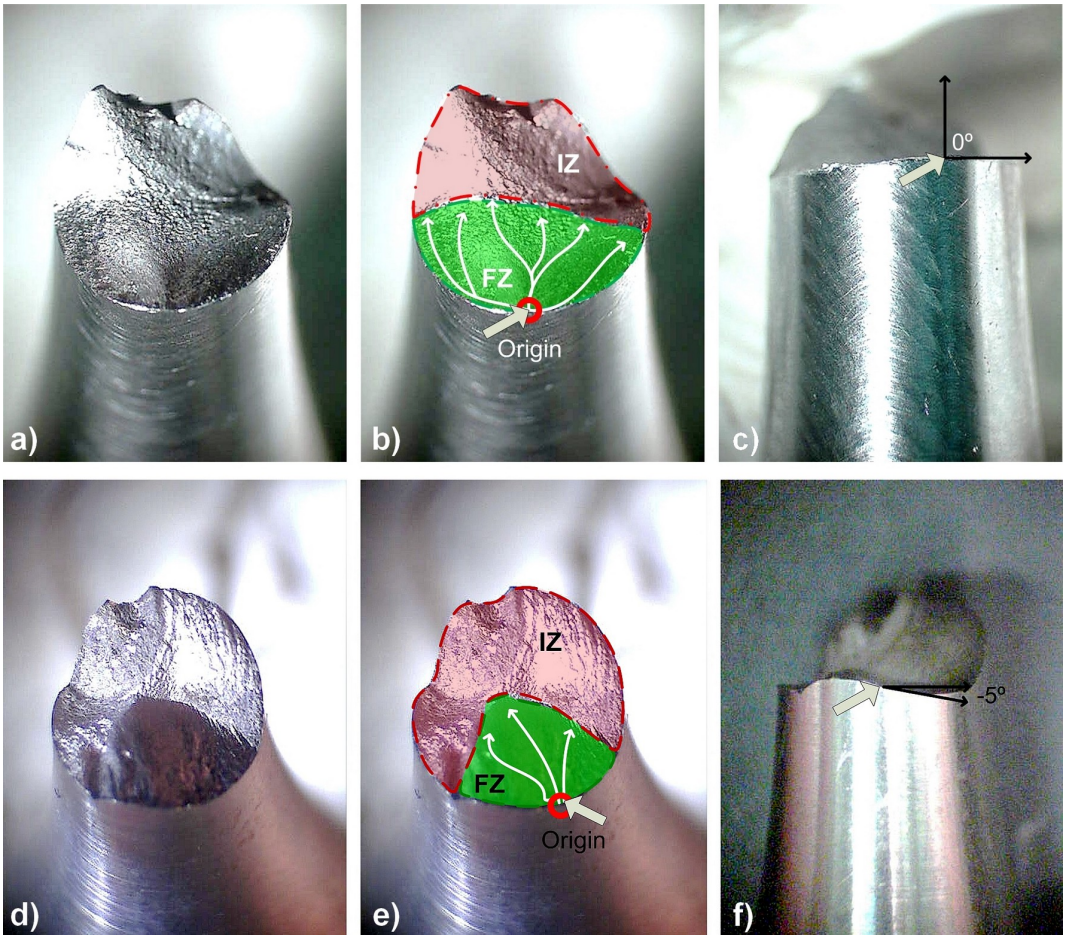


**Figure 8.21:** Loading case OP: Fracture surface for a), b) 42CrMo4 and d) e), Mg AZ31B-F. Crack initiation angle for c) 42CrMo4, and f) Mg AZ31B-F.

## 8.4 Fatigue crack estimates and experimental data correlation

This chapter is focused in the early crack growth on the crack initiation plane, which occurs in a very thin layer at the sample surface and where the shear stress gradient effect is relatively small. Thus, in the previous section, it was analysed the fracture surface topography for each loading path depicted in Figure 8.3. Moreover, the crack initiation spots were identified and the directions of the crack initiation plane were measured. In this section, it is performed a correlation between the experimental results and the theoretical estimates. Table 8.6 summarizes both experimental and theoretical results for the crack initiation planes. The 42CrMo4 experimental results were gathered from literature [3], regarding the AZ31B-F results they were measured using a digital USB microscope.

The theoretical estimates were obtained using the well-known critical plane criteria: FS, SWT, Liu I, Liu II, and the three criterion proposed here: the maximum $K_t$ approach, the principal direction approach, and the maximum shear direction approach. The SWT and Liu I estimates are in accordance with the PT and PS experimental results obtained in both materials, where the first principal strain amplitude used in their formulations has a key role in this performance. Moreover, the FS and Liu II estimates are very far from the the results obtained in experiments for these two loading paths. However, in the PP loading case, the FS and Liu II results are satisfactory in the 42CrMo4, in contrast, for the Mg alloy, the these estimates strongly differ from the experimental data.

Regarding the OP loading case, the critical plane criteria estimates are in accordance with the experimental data in both materials. The results of the maximum $K_t$ approach are in accordance with the experimental results obtained in the PT and OP loading cases. Also, in the PS and PP loading cases, the maximum $K_t$ estimates are very close to the experimental data.These estimates could be improved by refining the notch mesh in the boundary between the notch cap and the sample surface.

In this study, in the notch boundary where the values of $K_t$ were measured, the mesh has a $12^o$ gap between nodes, thus reducing this gap may improve the estimates. However, due to the notch reduced dimensions (about 200 microns as depicted in Figure 8.5) the mesh refinement may lead to convergence problems, specially when plasticity options are used.

The maximum principal direction approach shows to be the most accurate and easy way to estimate the direction of the crack initiations planes using a FEM environment, their critical plane estimates are quite similar to the ones achieved in the SWT and LIU 1 models. On the other hand, the estimates of the maximum shear direction approach are very alike to the ones obtained with the LIU 2 criterion, where the critical plane estimates are very far from the experimental results.

The good results obtained in the axial stress/strain based models can be explained by the stress amplitude ratio used in the experiments performed in this study, where the axial stress amplitude is greater than the shear one yielding an axial damage predominance. Despite the results obtained in the maximum $K_t$ approach, it may be the most sensitive approach to the stress amplitude ratio variation being sensitive to axial or shear damage predominance within a multiaxial loading, which is a plus comparatively to the other approaches considered here, which are only sensitive to axial or shear fatigue damages.

**Table 8.6:** Critical plane experimental orientation and their theoretical estimates for the 42CrMo4 [3] and AZ31B-F materials.

| | Case PT | | Case PS | | Case PP | | Case OP | |
|---|---|---|---|---|---|---|---|---|
| | AZ31 | 42CrMo4 | AZ31 | 42CrMo4 | AZ31 | 42CrMo4 | AZ31 | 42CrMo4 |
| Measured | 0 | 0 | 45 | 45 | -40 | -16 | -5 | 0 |
| FS | ±40 | ±40 | ±3; ±87 | ±3; ±87 | -13 | -13 | 0 | 0 |
| SWT | 0 | 0 | ±45 | ±45 | 25 | 25 | 0 | 0 |
| Liu I | 0 | 0 | ±45 | ±45 | 25 | 25 | 0 | 0 |
| Liu II | ±45 | ±45 | ±90; 0 | ±90; 0 | -20; 70 | -20; 70 | ±90; 0 | ±90; 0 |
| Max $K_t$ | 0 | 0 | -37 | -37 | -12 | -12 | 0 | 0 |
| PD | 0 | 0 | -45 | -45 | -25 | -25 | 0 | 0 |
| MSD | -45 | -45 | 90 | 90 | -70 | -70 | 90 | 90 |

## 8.5 Final comments

Base on the experimental data, and theoretical estimates carried out for the two materials considered in this chapter, a low-alloy steel and a magnesium alloy, some remarks can be drawn:

Fatigue life analysis shows different scatter patterns in both materials, which indicates different sensibility to the loading level. Moreover, similar slopes were found in the fatigue life correlation trend lines inherent to each loading path, excepting the loading case OP where the slope of the correlation trend line is much more pronounced.

Regarding the fractographic analysis results in the uniaxial loading cases, PT and PS; the fracture surface topography in both 42CrMo4 and Az31B-F materials were very similar and independent from the equivalent stress level. However, under multiaxial loading conditions, the loading path type and loading level do have influence in the magnesium alloy surface topography. For a high number of loading cycles, the fracture surface is strongly dependent on the loading path type, but for the same loading path the fatigue fracture surface tends to be similar in both materials.

Regarding the experimental measurements of the crack initiation planes, the orientation of the crack initiation plane, in pure axial (PT) and pure torsion (PS) loading cases, does

not change with the stress level variation, however, under multiaxial loading conditions the critical plane orientation varies with the stress level variation.

The principal direction approach based in the Mohr's circle methodology presented here, proved to be a fast way to estimate the orientation of the crack initiation plane, however for non-proportional loading cases this method can lead to inconsistent results due to the principal directions variation always present in non-proportional loading paths. Moreover, the maximum shear stress direction based in the Mohr's circle methodology has poor estimates for the orientation of the crack initiation plane.

Finally, the maximum $K_t$ approach and the principal stress methodology have a similar performance in their estimates, but the maximum $K_t$ approach proved to be more sensitive to non-proportional loadings, stress amplitude ratios, and local stress states due to their synergy with cyclic elastic-plastic models.

# Chapter 9

# Final remarks and possible future research

## 9.1 Final remarks

At the actual state-of-the-art in multiaxial fatigue criteria, the loading path effect on the materials fatigue strength remains to be fully understood and accounted specially under multiaxial random loading conditions. For instance, the equivalent stress concept under multiaxial loading conditions remains independent from the loading path type, i.e. it can be reached the same equivalent stress for different combinations of axial and shear stress amplitudes. However, experimental results show that the fatigue strength varies with different combinations of axial and shear stress amplitudes. Thus, fatigue life estimates under equivalent stress criteria under multiaxial loading conditions give inconsistent results. This document proposes a new set of tools for multiaxial fatigue in order to capture the several effects within the fatigue damage of multiaxial random loadings. Multiaxial fatigue damage of random loadings is the ultimate challenge in multiaxial fatigue characterization, because random loadings usually activates almost all multiaxial loading path effects. In order to capture multiaxial random damages, it was developed here a new equivalent shear stress, the SSF equivalent stress. This equivalent stress is able to capture partially the non-proportionality of a loading path, in order to overcome this limitation it was developed a non-proportional parameter, the non-proportional sensitivity factor, Y, that corrects the SSF equivalent stress to the material non-proportional response. Further, based on the SSF equivalent stress time evolution, it was developed a new cycle counting methodology, which was validated for block fatigue damage assessment. In order to evaluate random fatigue, it was developed a block extraction method that yields loading block regions within multiaxial loading spectra. For each extracted block, the fatigue damage is calculated using the SSF equivalent stress, and the virtual cycle counting method (vcc), afterwards the overall

damage of a loading spectrum is computed block by block using the Miner's rule. In the end, it was proposed three methodologies to estimate crack initiation planes for multiaxial loading conditions.

## 9.2 Possible future research

During the journey of this work several paths of great interest came along such as:

1. Investigate by experiments the relation between shear and axial strains, in order to inspect the accuracy of the von Mises estimates.
2. Investigate the integration of non-proportionality effects in the HYS model.
3. Investigate the HYS model integration in commercial FEM packages such as ANSYS or Abaqus.
4. Additional experiments are required to exploit the Y concept (non-proportional sensitivity) under broad non-proportional loading conditions.
5. Investigate alternative ways to obtain the material SSF damage map without or reduced amount of fatigue tests.
6. Investigate the hypotheses of an universal SSF damage map.
7. Perform a integration of the virtual cycle counting (vcc) in commercial FEM packages.
8. Investigate the material damping dependence of the material deformation type.
9. Development of a probabilistic trigger for multiaxial fatigue damage accumulation under random loadings.
10. Perform a integration of the $K_t$ approach in FEM packages.
11. Implement the SSF package in the field using SHM procedures for damage accumulation assessment on the fly.

# Bibliography


[1] Eschede train disaster, March 2015. URL `http://en.wikipedia.org`.

[2] ATSB Transport Safety. In-flight uncontained engine failure overhead batam island. Technical report, Australian Transport Safety Bureau, 2010.

[3] Luis Reis. *Comportamento mecânico de aços em fadiga multiaxial a amplitude de carga constante e sincrona*. PhD thesis, Universidade Técnica de Lisboa, Instituto Superior Técnico, 2004.

[4] E.E. Gdoutos. *Fracture of Nano and Engineering Materials and Structures*. Springer Netherlands, 2006.

[5] Nima Shamsaei. *Multiaxial fatigue and deformation including non-proportional hardening and variable amplitude loading effects*. PhD thesis, University of Illinois at Urbana-Champaign, 2010.

[6] Henrique Fonseca. Avaliação do comportamento mecânico da liga de magnésio az31b sob fadiga multiaxial com um entalhe. Master's thesis, Universidade Técnica de Lisboa, Instituto Superior Técnico, 2013.

[7] Bin Li, JLT Santos, and M de Freitas. A unified numerical approach for multiaxial fatigue limit evaluation. *Mechanics of Structures and Machines*, 28(1):85–103, 2000.

[8] Ioannis V Papadopoulos, Piermaria Davoli, Carlo Gorla, Mauro Filippini, and Andrea Bernasconi. A comparative study of multiaxial high-cycle fatigue criteria for metals. *International Journal of Fatigue*, 19(3):219–235, 1997.

[9] João Louro. Avaliação do dano acumulado gerado por sequências de carregamentos biaxiais na vida à fadiga no aço 42crmo4. Master's thesis, Universidade Técnica de Lisboa, Instituto Superior Técnico, 2010.

[10] L Susmel, R Tovo, and P Lazzarin. The mean stress effect on the high-cycle fatigue strength from a multiaxial fatigue point of view. *International Journal of Fatigue*, 27(8):928–943, 2005.

[11] Darrell F Socie, Linda A Waill, and Dennis F Dittmer. Biaxial fatigue of inconel 718 including mean stress effects. *Multiaxial Fatigue*, pages 463–481, 1985.

[12] Manuel da Fonte and Manuel de Freitas. Stress intensity factors for semi-elliptical surface cracks in round bars under bending and torsion. *International Journal of Fatigue*, 21(5):457–463, 1999.

[13] Jagabanduhu Chakrabarty. *Theory of plasticity*. Butterworth-Heinemann, 2006.

[14] Yanyao Jiang and P Kurath. Nonproportional cyclic deformation: critical experiments and analytical modeling. *International journal of plasticity*, 13(8): 743–763, 1997.

[15] Hs Lamba and Om Sidebottom. Cyclic plasticity for nonproportional paths part 1 cyclic hardening, erasure of memory, and subsequent strain hardening experiments. *Journal of Engineering Materials and Technology*, 100(1):96–103, 1978.

[16] GB Marquis and DF Socie. *Multiaxial fatigue*. Society of Automotive Engineers, Warrendale, Pa, USA, 2000.

[17] Steven M Tipton et al. Coiled tubing deformation mechanics: Diametral growth and elongation. *SPE Gulf Coast Section/ICoTA North American Coiled Tubing Roundtable*, 1996.

[18] Niels Saabye Ottosen, Robert Stenström, and Matti Ristinmaa. Continuum approach to high-cycle fatigue modeling. *International Journal of Fatigue*, 30(6): 996–1006, 2008.

[19] Kenji Kanazawa, KJ Miller, and MW Brown. Cyclic deformation of 1% cr-mo-v steel under out-of-phase loads. *Fatigue & Fracture of Engineering Materials & Structures*, 2(2):217–228, 1979.

[20] Jianyu Zhang, Xinhong Shi, and Binjun Fei. High cycle fatigue and fracture mode analysis of 2a12–t4 aluminum alloy under out-of-phase axial–torsion constant amplitude loading. *International Journal of Fatigue*, 38:144–154, 2012.

[21] Yanyao Jiang and Peter Kurath. Characteristics of the armstrong-frederick type plasticity models. *International Journal of Plasticity*, 12(3):387–415, 1996.

[22] Luis Reis, Vitor Anes, and Manuel de Freitas. Az31 magnesium alloy multiaxial lcf behavior: theory, simulation and experiments. *Advanced Materials Research*, 891: 1366–1371, 2014.

[23] Fenghua Wang, Jie Dong, Miaolin Feng, Xingwei Zheng, and Wenjiang Ding. Application of drucker–prager plasticity to predict fracture in rectangular cup drawing of az31 alloy sheet. *Materials Science and Engineering: A*, 532:316–324, 2012.

[24] ST Pietruszczak and Z Mroz. Finite element analysis of deformation of strain-softening materials. *International Journal for Numerical Methods in Engineering*, 17(3):327–334, 1981.

[25] Wai-Fah Chen and Da-Jian Han. *Plasticity for structural engineers*. J. Ross Publishing, 2007.

[26] Jean-Louis Chaboche. Constitutive equations for cyclic plasticity and cyclic viscoplasticity. *International Journal of Plasticity*, 5(3):247–302, 1989.

[27] JL Chaboche. A review of some plasticity and viscoplasticity constitutive theories. *International Journal of Plasticity*, 24(10):1642–1693, 2008.

[28] Y Jiang and P Kurath. A theoretical evaluation of plasticity hardening algorithms for nonproportional loadings. *Acta mechanica*, 118(1-4):213–234, 1996.

[29] Yanyao Jiang and Huseyin Sehitoglu. Multiaxial cyclic ratchetting under multiple step loading. *International journal of plasticity*, 10(8):849–870, 1994.

[30] Shafiqul Bari. *Constitutive modeling for cyclic plasticity and ratcheting*. PhD thesis, North Carolina State University, 2001.

[31] R v Mises. Mechanik der festen körper im plastisch-deformablen zustand. *Nachrichten von der Gesellschaft der Wissenschaften zu Göttingen, Mathematisch-Physikalische Klasse*, 1913:582–592, 1913.

[32] Marco Antonio Meggiolaro, JTP Castro, and ACO Miranda. Evaluation of multiaxial stress-strain models and fatigue life prediction methods under proportional loading. In *Proceedings of the Second International Symposium on Solid Mechanics*, pages 365–384, 2009.

[33] L Reis, B Li, and M De Freitas. Analytical and experimental studies on fatigue crack path under complex multi-axial loading. *Fatigue & fracture of engineering materials & structures*, 29(4):281–289, 2006.

[34] Manuel de Freitas, Luis Reis, and Bin Li. Comparative study on biaxial low-cycle fatigue behaviour of three structural steels. *Fatigue & Fracture of Engineering Materials & Structures*, 29(12):992–999, 2006.

[35] G Sines. *Metal Fatigue*. McGraw-Hill, 1959.

[36] Bong-Ryul You and Soon-Bok Lee. A critical review on multiaxial fatigue assessments of metals. *International Journal of Fatigue*, 18(4):235–244, 1996.

[37] A Aid, M Bendouba, L Aminallah, Abdelwaheb Amrouche, Noureddine Benseddiq, and M Benguediab. An equivalent stress process for fatigue life estimation under

multiaxial loadings based on a new non linear damage model. *Materials Science and Engineering: A*, 538:20–27, 2012.

[38] A Cristofori and R Tovo. An invariant-based approach for high-cycle fatigue calculation. *Fatigue & Fracture of Engineering Materials & Structures*, 32(4): 310–324, 2009.

[39] B Crossland. Effect of large hydrostatic pressures on the torsional fatigue strength of an alloy steel. In *Proc. Int. Conf. on Fatigue of Metals, Institution of Mechanical Engineers, London*, pages 138–149, 1956.

[40] YS Garud. A new approach to the evaluation of fatigue under multiaxial loadings. *Journal of Engineering Materials and Technology*, 103(2):118–125, 1981.

[41] Y Jiang. A fatigue criterion for general multiaxial loading. *Fatigue and fracture of engineering materials and structures*, 23(1):19–32, 2000.

[42] P Lazzarin and L Susmel. A stress-based method to predict lifetime under multiaxial fatigue loadings. *Fatigue & Fracture of Engineering Materials & Structures*, 26(12): 1171–1187, 2003.

[43] Jan Papuga. A survey on evaluating the fatigue limit under multiaxial loading. *International Journal of Fatigue*, 33(2):153–165, 2011.

[44] EN Mamiya, FC Castro, RD Algarte, and JA Araújo. Multiaxial fatigue life estimation based on a piecewise ruled s-n surface. *International Journal of Fatigue*, 33(4):529–540, 2011.

[45] George Sines. The prediction of fatigue fracture under combined stresses at stress concentrations. *Bulletin of JSME*, 4(15):443–453, 1961.

[46] George Sines and George Ohgi. Fatigue criteria under combined stresses or strains. *Journal of Engineering Materials and Technology*, 103(2):82–90, 1981.

[47] K Dang Van, B Griveau, et al. On a new multiaxial fatigue limit criterion: Theory and application. In *ICBMFF2*, 2013.

[48] K Dang-Van. Macro-micro approach in high-cycle multiaxial fatigue. *ASTM Special Technical Publication*, 1191:120–120, 1993.

[49] DL McDiarmid. A shear stress based critical plane criterion of multiaxial fatigue failure for design and life prediction. *Fatigue & Fracture of Engineering Materials & Structures*, 17(12):1475–1484, 1994.

[50] DL McDiarmid. A general criterion for high cycle multiaxial fatigue failure. *Fatigue & Fracture of Engineering Materials & Structures*, 14(4):429–453, 1991.

[51] Tomokazu Matake. An explanation on fatigue limit under combined stress. *Bulletin of JSME*, 20(141):257–263, 1977.

[52] Andrea Carpinteri and Andrea Spagnoli. Multiaxial high-cycle fatigue criterion for hard metals. *International Journal of Fatigue*, 23(2):135–145, 2001.

[53] Andrea Carpinteri, Andrea Spagnoli, and Sabrina Vantadori. Multiaxial fatigue assessment using a simplified critical plane-based criterion. *International Journal of Fatigue*, 33(8):969–976, 2011.

[54] Darrell Socie. Critical plane approaches for multiaxial fatigue damage assessment. *ASTM special technical publication*, 1191:7–7, 1993.

[55] MW Brown and KJ Miller. A theory for fatigue failure under multiaxial stress-strain conditions. *Proceedings of the Institution of Mechanical Engineers*, 187(1):745–755, 1973.

[56] L Reis, V Anes, B Li, and M de Freitas. Damage accumulation due to sequential loading effect. *Procedia Engineering*, 10:1396–1401, 2011.

[57] Ralph Döring, Jens Hoffmeyer, Timm Seeger, and Michael Vormwald. Short fatigue crack growth under nonproportional multiaxial elastic–plastic strains. *International Journal of Fatigue*, 28(9):972–982, 2006.

[58] Nima Shamsaei, Ali Fatemi, and Darrell F Socie. Multiaxial fatigue evaluation using discriminating strain paths. *International Journal of Fatigue*, 33(4):597–609, 2011.

[59] Leslie P Pook. Comments on fatigue crack growth under mixed modes i and iii and pure mode iii loading. *Multiaxial Fatigue, ASTM STP*, 853:249–263, 1985.

[60] Jaap Schijve. *Fatigue of structures and materials*. Kluwer Academic Publishers, 2001.

[61] Harald Zenner, Armin Simbürger, and Jiping Liu. On the fatigue limit of ductile metals under complex multiaxial loading. *International Journal of Fatigue*, 22(2): 137–145, 2000.

[62] ASME Boiler and Pressure Vessel Code. Case n-47-23 class 1 components in elevated temperature service. *Section III, Division*, 1, 1986.

[63] CM Sonsino. Multiaxial fatigue of welded joints under in-phase and out-of-phase local strains and stresses. *International Journal of Fatigue*, 17(1):55–70, 1995.

[64] CM Sonsino. Influence of load and deformation-controlled multiaxial tests on fatigue life to crack initiation. *International Journal of Fatigue*, 23(2):159–167, 2001.

[65] Rodney Hill. A theory of the yielding and plastic flow of anisotropic metals. *Proceedings of the Royal Society of London. Series A. Mathematical and Physical Sciences*, 193(1033):281–297, 1948.

[66] G Sines. Behavior of metals under complex static and alternating stresses. *Metal fatigue*, 1:145–169, 1959.

[67] IV Papadopoulos. Critical plane approaches in high-cycle fatigue: on the definition of the amplitude and mean value of the shear stress acting on the critical plane. *Fatigue & Fracture of Engineering Materials & Structures*, 21(3):269–285, 1998.

[68] Joseph Edward Shigley, Richard Gordon Budynas, and Charles R Mischke. *Mechanical engineering design*. McGraw-Hill, 2004.

[69] QH Vu, D Halm, and Y Nadot. Multiaxial fatigue criterion for complex loading based on stress invariants. *International Journal of Fatigue*, 32(7):1004–1014, 2010.

[70] H Kakuno and Y Kawada. A new criterion of fatigue strength of a round bar subjected to combined static and repeated bending and torsion. *Fatigue & Fracture of Engineering Materials & Structures*, 2(2):229–236, 1979.

[71] B Li, L Reis, and M De Freitas. Comparative study of multiaxial fatigue damage models for ductile structural steels and brittle materials. *International Journal of Fatigue*, 31(11):1895–1906, 2009.

[72] Camilla de Andrade Gonçalves, José Alexander Araújo, and Edgar Nobuo Mamiya. A simple multiaxial fatigue criterion for metals. *Comptes Rendus Mecanique*, 332 (12):963–968, 2004.

[73] Ali Fatemi and Darrell F Socie. A critical plane approach to multiaxial fatigue damage including out-of-phase loading. *Fatigue & Fracture of Engineering Materials & Structures*, 11(3):149–165, 1988.

[74] JA Araújo, A Carpinteri, C Ronchei, A Spagnoli, and S Vantadori. An alternative definition of the shear stress amplitude based on the maximum rectangular hull method and application to the c-s (carpinteri-spagnoli) criterion. *Fatigue & Fracture of Engineering Materials & Structures*, 2014.

[75] E Maggiolini, P Livieri, and R Tovo. Implicit gradient and integral average effective stresses: relationships and numerical approximations. *Fatigue & Fracture of Engineering Materials & Structures*, 2014.

[76] Enrico Maggiolini, Paolo Livieri, and Roberto Tovo. On numerical integration for effective stress assessment at notches. *Fracture and Structural Integrity*, 25: Pages–117, 2013.

[77] William Nicholas Findley. *A theory for the effect of mean stress on fatigue of metals under combined torsion and axial load or bending*. Engineering Materials Research Laboratory, Division of Engineering, Brown University, 1958.

[78] William Nichols Findley. *Fatigue of metals under combinations of stresses*. Division of Engineering, Brown University, 1956.

[79] RD Lohr and EG Ellison. A simple theory for low cycle multiaxial fatigue. *Fatigue & Fracture of Engineering Materials & Structures*, 3(1):1–17, 1980.

[80] KN Smith, TH Topper, and P Watson. A stress-strain function for the fatigue of metals(stress-strain function for metal fatigue including mean stress effect). *Journal of materials*, 5:767–778, 1970.

[81] KC Liu. A method based on virtual strain-energy parameters for multiaxial fatigue life prediction. *ASTM special technical publication*, 1191:67–67, 1993.

[82] G Glinka, G Wang, and A Plumtree. Mean stress effects in multiaxial fatigue. *Fatigue & fracture of engineering materials & structures*, 18(7-8):755–764, 1995.

[83] G Glinka, G Shen, and A Plumtree. A multiaxial fatigue strain energy density parameter related to the critical fracture plane. *Fatigue & Fracture of Engineering Materials & Structures*, 18(1):37–46, 1995.

[84] Wen-Fung Pan, Chao-Yu Hung, and Lieh-Lin Chen. Fatigue life estimation under multiaxial loadings. *International Journal of Fatigue*, 21(1):3–10, 1999.

[85] Ahmad Varvani-Farahani. A new energy-critical plane parameter for fatigue life assessment of various metallic materials subjected to in-phase and out-of-phase multiaxial fatigue loading conditions. *International Journal of Fatigue*, 22(4): 295–305, 2000.

[86] J Liu and H Zenner. Berechnung der dauerschwingfestigkeit bei mehrachsiger beanspruchung—teil 1. *Materialwissenschaft und Werkstofftechnik*, 24(7):240–249, 1993.

[87] VV Novoshilov. Theory of elasticity. *Sherrkon, JJ, trans.*, 1961.

[88] Milton A Miner et al. Cumulative damage in fatigue. *Journal of applied mechanics*, 12(3):159–164, 1945.

[89] CH Wang and MW Brown. On plastic deformation and fatigue under multiaxial loading. *Nuclear engineering and design*, 162(1):75–84, 1996.

[90] Roberto Brighenti and Andrea Carpinteri. A notch multiaxial-fatigue approach based on damage mechanics. *International Journal of Fatigue*, 39:122–133, 2012.

[91] Marco Antonio Meggiolaro and Jaime Tupiassú Pinho de Castro. An improved multiaxial rainflow algorithm for non-proportional stress or strain histories–part i: Enclosing surface methods. *International Journal of Fatigue*, 42:217–226, 2012.

[92] Marco Antonio Meggiolaro and Jaime Tupiassú Pinho de Castro. An improved multiaxial rainflow algorithm for non-proportional stress or strain histories–part ii: The modified wang–brown method. *International Journal of Fatigue*, 42:194–206, 2012.

[93] JA Bannantine and DF Socie. A multiaxial fatigue life estimation. *Advances in fatigue lifetime predictive techniques*, 1(61801):249, 1992.

[94] TE Langlais, JH Vogel, and TR Chase. Multiaxial cycle counting for critical plane methods. *International journal of fatigue*, 25(7):641–647, 2003.

[95] H Chen, D-G SHANG, and E-T LIU. Multiaxial fatigue life prediction method based on path-dependent cycle counting under tension/torsion random loading. *Fatigue & Fracture of Engineering Materials & Structures*, 34(10):782–791, 2011.

[96] Pingsha Dong, Zhigang Wei, and Jeong K Hong. A path-dependent cycle counting method for variable-amplitude multi-axial loading. *International Journal of Fatigue*, 32(4):720–734, 2010.

[97] ASTM Standard. E1049-85. *Standard Practices for Cycle Counting in Fatigue Analysis*, 1999.

[98] CH Wang and MW Brown. A path-independent parameter for fatigue under proportional and non-proportional loading. *Fatigue & fracture of engineering materials & structures*, 16(12):1285–1297, 1993.

[99] Mahera Musallam and C Mark Johnson. An efficient implementation of the rainflow counting algorithm for life consumption estimation. *Reliability, IEEE Transactions on*, 61(4):978–986, 2012.

[100] CH McInnes and PA Meehan. Equivalence of four-point and three-point rainflow cycle counting algorithms. *International journal of fatigue*, 30(3):547–559, 2008.

[101] M Matsuishi and T Endo. Fatigue of metals subjected to varying stress. *Japan Society of Mechanical Engineers, Fukuoka, Japan*, pages 37–40, 1968.

[102] P Colombi and K Dolinski. Fatigue lifetime of welded joints under random loading: rainflow cycle vs. cycle sequence method. *Probabilistic engineering mechanics*, 16 (1):61–71, 2001.

[103] RJ Anthes. Modified rainflow counting keeping the load sequence. *International journal of fatigue*, 19(7):529–535, 1997.

[104] Z Wei and P Dong. A rapid path-length searching procedure for multi-axial fatigue cycle counting. *Fatigue & Fracture of Engineering Materials & Structures*, 35(6): 556–571, 2012.

[105] CH Wang and MW Brown. Life prediction techniques for variable amplitude multiaxial fatigue—part 1: theories. *Journal of Engineering Materials and Technology*, 118(3):367–370, 1996.

[106] CH Wang and MW Brown. Life prediction techniques for variable amplitude multiaxial fatigue—part 2: comparison with experimental results. *Journal of engineering materials and technology*, 118(3):371–374, 1996.

[107] Stephen D Downing and DF Socie. Simple rainflow counting algorithms. *International Journal of Fatigue*, 4(1):31–40, 1982.

[108] Arvid Palmgren. Die lebensdauer von kugellagern. *Zeitschrift des Vereins Deutscher Ingenieure*, 68(14):339–341, 1924.

[109] Milton A. Miner. Cumulative damage in fatigue. *Journal of applied mechanics*, 12 (3):159–164, 1945.

[110] A. Fatemi and Lianxiang Yang. Cumulative fatigue damage and life prediction theories: a survey of the state of the art for homogeneous materials. *International Journal of Fatigue*, 20(1):9–34, 1998.

[111] Donald Lewis Henry. *A theory of fatigue damage accumulation in steel*. PhD thesis, Ohio State University, 1953.

[112] S. M. Marco and W. L. Starkey. A concept of fatigue damage. *Trans. ASME*, 76 (4):627–632, 1954.

[113] Horace J. Grover. An observation concerning the cycle ratio in cumulative damage. *Fatigue in Aircraft Structures, STP*, 274:120–124, 1960.

[114] S. S. Manson. Interfaces between fatigue, creep, and fracture. *International Journal of Fracture Mechanics*, 2(1):327–327, 1966.

[115] SS Manson, AJ Nachtigall, CR Ensign, and JC Freche. Further investigation of a relation for cumulative fatigue damage in bending. *Journal of Manufacturing Science and Engineering*, 87(1):25–35, 1965.

[116] S. Subramanyan. A cumulative damage rule based on the knee point of the SN curve. *Journal of Engineering Materials and Technology*, 98(4):316–321, 1976.

[117] Tiiu V. Kutt and M. P. Bieniek. Cumulative damage and fatigue life prediction. *AIAA journal*, 26(2):213–219, 1988.

[118] M. Ben-Amoz. A cumulative damage theory for fatigue life prediction. *Engineering Fracture Mechanics*, 37(2):341–347, 1990.

[119] J. L. Chaboche and P. M. Lesne. A non-linear continuous fatigue damage model. *Fatigue & fracture of engineering materials & structures*, 11(1):1–17, 1988.

[120] J. Lemaitre and A. Plumtree. Application of damage concepts to predict creep-fatigue failures. *Journal of Engineering Materials and Technology*, 101(3): 284–292, 1979.

[121] Changchun Li, Zhixiong Qian, and Guangxia Li. The fatigue damage criterion and evolution equation containing material microparameters. *Engineering Fracture Mechanics*, 34(2):435–443, 1989.

[122] Liang Xue. Damage accumulation and fracture initiation in uncracked ductile solids subject to triaxial loading. *International Journal of Solids and Structures*, 44(16): 5163–5181, 2007.

[123] A. Seweryn, A. Buczyński, and J. Szusta. Damage accumulation model for low cycle fatigue. *International Journal of fatigue*, 30(4):756–765, 2008.

[124] F. Casciati, S. Casciati, L. Faravelli, and A. Marzi. Fatigue damage accumulation in a cu-based shape memory alloy: preliminary investigation. *Computers Materials and Continua*, 23(3):287, 2011.

[125] Zhi Yong Huang, Danièle Wagner, Claude Bathias, and Jean Louis Chaboche. Cumulative fatigue damage in low cycle fatigue and gigacycle fatigue for low carbon–manganese steel. *International Journal of Fatigue*, 33(2):115–121, 2011.

[126] Vijay Rathod, Om Prakash Yadav, Ajay Rathore, and Rakesh Jain. Probabilistic modeling of fatigue damage accumulation for reliability prediction. *International Journal of Quality, Statistics, and Reliability*, 2011, 2011.

[127] T. Zarrin-Ghalami and A. Fatemi. Cumulative fatigue damage and life prediction of elastomeric components. *Fatigue & Fracture of Engineering Materials & Structures*, 36(3):270–279, 2013.

[128] P. J. Huffman and S. P. Beckman. A non-linear damage accumulation fatigue model for predicting strain life at variable amplitude loadings based on constant amplitude fatigue data. *International Journal of Fatigue*, 48:165–169, 2013.

[129] Ihab El Aghoury and Khaled Galal. A fatigue stress-life damage accumulation model for variable amplitude fatigue loading based on virtual target life. *Engineering Structures*, 52:621–628, 2013.

[130] S. Taheri, L. Vincent, and J.-C. Le-roux. A new model for fatigue damage accumulation of austenitic stainless steel under variable amplitude loading. *Procedia Engineering*, 66:575–586, 2013.

[131] Philipp Hilgendorff, Andrei Grigorescu, and Martina Zimmermann. The effect of damage accumulation in slip bands on the resonant behavior in the very high cycle fatigue (VHCF) regime. In *ICF13*, 2013.

[132] Ying-Yu Wang and Wei-Xing Yao. A multiaxial fatigue criterion for various metallic materials under proportional and nonproportional loading. *International journal of fatigue*, 28(4):401–408, 2006.

[133] Huiying Gao, Hong-Zhong Huang, Shun-Peng Zhu, Yan-Feng Li, and Rong Yuan. A modified nonlinear damage accumulation model for fatigue life prediction considering load interaction effects. *The Scientific World Journal*, 2014, 2014.

[134] Tian-xiang Xia and Wei-xing Yao. Comparative research on the accumulative damage rules under multiaxial block loading spectrum for 2024-t4 aluminum alloy. *International Journal of Fatigue*, 48:257–265, 2013.

[135] Neville W Sachs. *Practical plant failure analysis: a guide to understanding machinery deterioration and improving equipment reliability*. CRC Press, 2006.

[136] Les Pook. *Why Metal Fatigue Matters*. Springer, 2007.

[137] Yanyao Jiang and Jixi Zhang. Benchmark experiments and characteristic cyclic plasticity deformation. *International Journal of Plasticity*, 24(9):1481–1515, 2008.

[138] Jafar Al Bin Mousa. *Multiaxial Fatigue Characterization and Modeling of AZ31B Magnesium Extrusion*. PhD thesis, University of Waterloo, 2011.

[139] H Wang, PD Wu, J Wang, and CN Tomé. A crystal plasticity model for hexagonal close packed (hcp) crystals including twinning and de-twinning mechanisms. *International Journal of Plasticity*, 49:36–52, 2013.

[140] C Bruni, A Forcellese, F Gabrielli, and M Simoncini. Post-welding formability of az31 magnesium alloy. *Materials & Design*, 32(5):2988–2991, 2011.

[141] Myoung-Gyu Lee, RH Wagoner, JK Lee, K Chung, and HY Kim. Constitutive modeling for anisotropic/asymmetric hardening behavior of magnesium alloy sheets. *International Journal of Plasticity*, 24(4):545–582, 2008.

[142] MG Lee, SJ Kim, RH Wagoner, K Chung, and HY Kim. Constitutive modeling for anisotropic/asymmetric hardening behavior of magnesium alloy sheets: application to sheet springback. *International Journal of Plasticity*, 25(1):70–104, 2009.

[143] MR Barnett. Twinning and the ductility of magnesium alloys: Part ii."contraction" twins. *Materials Science and Engineering: A*, 464(1):8–16, 2007.

[144] MR Barnett. Twinning and the ductility of magnesium alloys: Part i:"tension" twins. *Materials Science and Engineering: A*, 464(1):1–7, 2007.

[145] H Wang, B Raeisinia, PD Wu, SR Agnew, and CN Tomé. Evaluation of self-consistent polycrystal plasticity models for magnesium alloy az31b sheet. *International Journal of Solids and Structures*, 47(21):2905–2917, 2010.

[146] H Wang, PD Wu, and J Wang. Modeling inelastic behavior of magnesium alloys during cyclic loading–unloading. *International Journal of Plasticity*, 47:49–64, 2013.

[147] L Wu, A Jain, DW Brown, GM Stoica, SR Agnew, B Clausen, DE Fielden, and PK Liaw. Twinning–detwinning behavior during the strain-controlled low-cycle fatigue testing of a wrought magnesium alloy, zk60a. *Acta Materialia*, 56(4):688–695, 2008.

[148] Jafar Albinmousa, Hamid Jahed, and Steve Lambert. An energy-based fatigue model for wrought magnesium alloy under multiaxial load. In *ICMFF9*, 2013.

[149] Jafar Albinmousa, Hamid Jahed, and Steve Lambert. Cyclic axial and cyclic torsional behaviour of extruded az31b magnesium alloy. *International Journal of Fatigue*, 33(11):1403–1416, 2011.

[150] J Koike. Enhanced deformation mechanisms by anisotropic plasticity in polycrystalline mg alloys at room temperature. *Metallurgical and Materials Transactions A*, 36(7):1689–1696, 2005.

[151] Myoung-Gyu Lee, Daeyong Kim, Chongmin Kim, Michael L Wenner, and Kwansoo Chung. Spring-back evaluation of automotive sheets based on isotropic–kinematic hardening laws and non-quadratic anisotropic yield functions, part iii: applications. *International Journal of Plasticity*, 21(5):915–953, 2005.

[152] Arthur Peter Boresi, Richard Joseph Schmidt, and Omar M Sidebottom. *Advanced mechanics of materials*, volume 5. Wiley New York, 1993.

[153] Yongming Liu and Sankaran Mahadevan. Multiaxial high-cycle fatigue criterion and life prediction for metals. *International Journal of Fatigue*, 27(7):790–800, 2005.

[154] MA Meggiolaro and JTP Castro. Statistical evaluation of strain-life fatigue crack initiation predictions. *International Journal of Fatigue*, 26(5):463–476, 2004.

[155] Adam Niesłony and Cetin M Sonsino. *Comparison of some selected multiaxial fatigue assessment criteria.* Fraunhofer-Inst. für Betriebsfestigkeit und Systemzuverlässigkeit LBF, 2008.

[156] Armin Simbürger. *Festigkeitsverhalten zäher Werkstoffe bei einer mehrachsigen, phasenverschobenen Schwingbeanspruchung mit körperfesten und veränderlichen Hauptspannungseinrichtungen.* Fraunhofer-Gesellschaft, 1975.

[157] B Atzori, G Meneghetti, and L Susmel. Material fatigue properties for assessing mechanical components weakened by notches and defects. *Fatigue & Fracture of Engineering Materials & Structures*, 28(1-2):83–97, 2005.

[158] C Amzallag, JP Gerey, JL Robert, and J Bahuaud. Standardization of the rainflow counting method for fatigue analysis. *International journal of fatigue*, 16(4):287–293, 1994.

[159] E Macha, T Łagoda, A Niesłony, and D Kardas. Fatigue life under variable-amplitude loading according to the cycle-counting and spectral methods. *Materials Science*, 42(3):416–425, 2006.

[160] Vitor Anes. Efeito da sequência de cargas axial e de torção na previsão de vida em fadiga multiaxial. Master's thesis, Universidade Técnica de Lisboa, Instituto Superior Técnico, 2009.

[161] Wilson Henriques. Análise do dano acumulado devido a carregamentos multiaxiais na vida à fadiga no aço 42crmo4. Master's thesis, Universidade Técnica de Lisboa, Instituto Superior Técnico, 2009.

[162] Gançalo Perpétuo. Análise do efeito de carregamentos multiaxiais assíncronos na vida à fadiga no aço 42crmo4. Master's thesis, Universidade Técnica de Lisboa, Instituto Superior Técnico, 2009.

[163] RW Hyers, JG McGowan, KL Sullivan, JF Manwell, and BC Syrett. Condition monitoring and prognosis of utility scale wind turbines. *Energy Materials*, 1(3): 187–203, 2006.

[164] Douglas Adams, Jonathan White, Mark Rumsey, and Charles Farrar. Structural health monitoring of wind turbines: method and application to a hawt. *Wind Energy*, 14(4):603–623, 2011.

[165] CM Sonsino, W Fricke, F De Bruyne, A Hoppe, A Ahmadi, and G Zhang. Notch stress concepts for the fatigue assessment of welded joints–background and applications. *International Journal of Fatigue*, 34(1):2–16, 2012.

[166] V Chaves, C Madrigal, and A Navarro. Biaxial fatigue tests and crack paths for aisi 304l stainless steel. *Fracture and Structural Integrity*, 30:273–281, 2014.

[167] Andrea Carpinteri, Camilla Ronchei, Andrea Spagnoli, and Sabrina Vantadori. Lifetime estimation in the low/medium-cycle regime using the carpinteri–spagnoli

multiaxial fatigue criterion. *Theoretical and Applied Fracture Mechanics*, 73:120–127, 2014.

[168] A Bolchoun, J Wiebesiek, H Kaufmann, and CM Sonsino. Application of stress-based multiaxial fatigue criteria for laserbeam-welded thin aluminium joints under proportional and non-proportional variable amplitude loadings. *Theoretical and Applied Fracture Mechanics*, 73:9–16, 2014.

[169] JD Morrow. The effect of selected sub-cycle sequences in fatigue loading histories. *Random fatigue life predictions*, 72:43–60, 1986.

[170] Benjamin Joseph Lazan. *Damping of materials and members in structural mechanics*, volume 214. Pergamon press Oxford, 1968.

[171] Nuno Manuel Mendes Maia and Júlio Martins Montalvão e Silva. *Theoretical and experimental modal analysis*. Research Studies Press Taunton, 1997.

[172] David J Ewins. *Modal testing: theory and practice*, volume 2. Research studies press Letchworth, 1986.

[173] Fang-Lin Huang, Xue-Min Wang, Zheng-Qing Chen, Xu-Hui He, and Yi-Qing Ni. A new approach to identification of structural damping ratios. *Journal of sound and vibration*, 303(1):144–153, 2007.

[174] Jack A Collins. *Failure of materials in mechanical design: analysis, prediction, prevention*. John Wiley & Sons, 1993.

[175] George Ellwood Dieter and David Bacon. *Mechanical metallurgy*, volume 3. McGraw-Hill New York, 1986.

[176] Norman Edward Frost, Kenneth James Marsh, and Leslie Philip Pook. *Metal fatigue*. Courier Dover Publications, 1999.

[177] S Bentachfine, G Pluvinage, LS Toth, and Z Azari. Biaxial low cycle fatigue under non-proportional loading of a magnesium-lithium alloy. *Engineering fracture mechanics*, 54(4):513–522, 1996.

[178] Yasumi Ito and Akira Shimamoto. Effect of microstructure on fatigue crack growth resistance of magnesium alloy under biaxial stress. *Key Engineering Materials*, 297: 1559–1564, 2005.

[179] Qin Yu, Jixi Zhang, Yanyao Jiang, and Qizhen Li. Multiaxial fatigue of extruded az61a magnesium alloy. *International Journal of Fatigue*, 33(3):437–447, 2011.

[180] Li Qizhen, Yu Qin, Zang Jixi, and Jiang Yanyao. Effect of strain amplitude on tension-compression fatigue behaviour of extruded mg6al1zna magnesium alloy. *Scripta Materialia*, 62(10):778–781, 2010.

[181] Xiong Ying Cheng Lixia. Multiaxial fatigue life prediction for extruded az31b magnesium alloy. *Acta Metall Sin*, 48(12):1446–1452, 2012.

[182] Dirk Mohr, Marc-Antoine Chevin, and Lars Greve. Deformation behavior of magnesium extrusions with strong basal texture: Experiments and modeling. *Journal of Applied Mechanics*, 80(6):061002, 2013.

[183] S Begum, DL Chen, S Xu, and Alan A Luo. Low cycle fatigue properties of an extruded az31 magnesium alloy. *International Journal of Fatigue*, 31(4):726–735, 2009.

[184] F Yang, SM Yin, SX Li, and ZF Zhang. Crack initiation mechanism of extruded az31 magnesium alloy in the very high cycle fatigue regime. *Materials Science and Engineering: A*, 491(1):131–136, 2008.

[185] H Mayer, M Papakyriacou, B Zettl, and SE Stanzl-Tschegg. Influence of porosity on the fatigue limit of die cast magnesium and aluminium alloys. *International journal of fatigue*, 25(3):245–256, 2003.

[186] Erdogan Madenci and Ibrahim Guven. *The finite element method and applications in engineering using ANSYS®*. Springer, 2007.

[187] E Giner, N Sukumar, JE Tarancon, and FJ Fuenmayor. An abaqus implementation of the extended finite element method. *Engineering fracture mechanics*, 76(3): 347–368, 2009.

[188] Zuzana Zúberová, Ludv Kunz, TT Lamark, Y Estrin, and M Janeček. Fatigue and tensile behavior of cast, hot-rolled, and severely plastically deformed az31 magnesium alloy. *Metallurgical and Materials Transactions A*, 38(9):1934–1940, 2007.

[189] Marko Knezevic, Amanda Levinson, Ryan Harris, Raja K Mishra, Roger D Doherty, and Surya R Kalidindi. Deformation twinning in az31: influence on strain hardening and texture evolution. *Acta Materialia*, 58(19):6230–6242, 2010.

[190] J Polak, M Klesnil, and P Lukáš. High cycle plastic stress-strain response of metals. *Materials Science and Engineering*, 15(2):231–237, 1974.

[191] Z Cedric Xia and John W Hutchinson. Crack tip fields in strain gradient plasticity. *Journal of the Mechanics and Physics of Solids*, 44(10):1621–1648, 1996.

[192] H Li and N Chandra. Analysis of crack growth and crack-tip plasticity in ductile materials using cohesive zone models. *International Journal of Plasticity*, 19(6): 849–882, 2003.

# Appendices

# Appendix A

# Mechanical properties

## A.1 Introduction

In this appendix it is presented the materials used in this research focusing their mechanical properties and industrial applications. It was analysed four steels, i.e. a high strength steel, two medium-carbon steels and one stainless steel. In addition, it was also analysed an aluminium alloy commonly used in aerospace airframes, the 2024T4 (aluminium alloyed with copper and heat treated), and a magnesium alloy usually used in transportation industry, the AZ31B-F, a magnesium alloy with 3 wt% of Aluminium and 1 wt% of Zinc. Some information presented here was gathered from literature, but other it was obtained by experiments during this research, which was the case of some properties and fatigue data of the 42CrMo4 and AZ31B-F materials.

## A.2 42CrMo4 (AISI 4140)

The 42CrMo4 material is a high strength steel that is alloyed with Chromium, and Molybdenum being a special structural steel. It is commonly used in high and moderately stressed components for automotive industry such as: shafts, connecting rods, crankshafts, screws.

## A.3 Ck 45

The Ck45 is a medium carbon steel is usually used when greater strength and hardness is required having good machinability. This material has an extreme size accuracy, straightness and concentricity. It is normally used in component parts for vehicles, shafts, bushings, crankshafts, connecting rods and parts for the machine building industry. it is also used as steel for axes, knives, hammers. It is considered as a wear resistant steel.

## A.4 Medium-carbon steel C40

The C40 (AISI 1040) is a high carbon structural steel with 0.4 wt% carbon, has poor welding capabilities and is mainly used for manufacturing wear parts, like gears and so on. Also, it is commonly used in plastic mould, cold work die and mould bases.

## A.5 Stainless steel AISI 303

The AISI 303 is an austenitic stainless steel with an excellent machinability compared with others austenitic stainless steels. It is primarily used when production involves extensive machining. The AISI 303 typical applications are nuts, bolts, bushings, shafts, electrical switchgear components and food related equipment. In general, the AISI 303 is used in components that should be heavily machined and/or in cases where good corrosion resistance is required.

## A.6 Aluminum alloy 2024-T4

The 2024-T4 is an aluminium alloy commonly used in the aircraft industry such as load-bearing applications. This aluminium alloy has good machinability and surface finish capabilities. It is a high strength material with adequate workability and high resistance to fatigue crack due to the copper and age hardening. However, also due to the copper precipitates their corrosion resistance is very low. The major corrosion types found in this alloys are intergranular corrosion and exfoliation. The mechanical properties of 2024-T4 depends greatly on the temper type, in this case the aluminum alloy has a T4 heat treatment, (solution heat-treated and naturally aged to a substantially stable condition).

## A.7 Magnesium alloy AZ31B-F

Magnesium alloys have been a raw material with successful industrial applications; the major advantages are based on the reduced weight and high specific strength. The world magnesium production increases exponentially each year; new improvements on corrosion and mechanical properties had led to sustaining the industry demanding specially at automotive and aerospace industries where the driving force has settled on a weight reduction policy. Magnesium is the sixth most abundant metal on planet earth with high recycling properties and can be obtained from sea water. Also, it is a non-toxic material being a good candidate to be used in human implants and replace aluminium alloys on structural and mechanical components. However, their mechanical behaviour is quite different from steel or aluminum alloys, the hexagonal closest-packed structure, HCP, have some specific properties such as the reduced number of slip planes, only 3 against 12 found in steels, which gives a non-standard mechanical behaviour at room temperature.

## A.8 Mechanical properties

**Table A.1:** Available monotonic and cycle properties for the selected materials [3, 134, 155].

| | 42CrMo4 | Ck45 | AISI 303 | C40 | 2024-T4 | AZ31B-F |
|---|---|---|---|---|---|---|
| Micro-structure type | bcc | bcc | fcc | bcc | | hc |
| Poisson's ratio | 0.3 | 0.3 | 0.3 | 0.3 | 0.33 | 0.3 |
| Density (Kg/m3) | 7830 | 7870 | 8000 | 7800 | 2770 | 1770 |
| Hardness (HV) | 362 | 195 | 174 | 149 | 137 | 86 |
| Tensile strength (UTS) (MPa) | 1100 | 660 | 625 | 630 | 469 | 290 |
| Yield strength (MPa) | 980 | 410 | 330 | 530 | 400 | 203 |
| Elongation (%) | 16 | 23 | 58 | 22 | 16 | 14 |
| Young's modulus (GPa) | 206 | 206 | 178 | 210 | 73 | 45 |
| Cyclic yield strenght | | 350 | | | | |
| Strain hardening exponent | | 0.001 | | | | |
| Fatigue strength (endurance limit) | 420 | 300 | | | 140 | |
| $\sigma'_f$ Fatigue strength coefficient (MPa) | 1154 | 948 | 534 | | 643 | 450 |
| $b$ Fatigue strength coefficient | -0.061 | -0.102 | -0.07 | | | -0.12 |
| $\varepsilon'_f$ Fatigue ductility coefficient | 0.180 | 0.17 | 0.052 | | 0.18 | 0.26 |
| $c$ Fatigue ductility exponent | -0.53 | -0.44 | -0.292 | | | -0.71 |

## A.9 Chemical composition

**Table A.2:** Material chemical composition by weight % [3, 134, 155].

| | **42CrMo4** | **Ck45** | **C40** | **AISI 303** | **2024-T4** | **AZ31B-F** |
|---|---|---|---|---|---|---|
| C | 0.38-0.43 | 0.43-0.50 | 0.37-0.44 | 0.15 | | |
| Mn | 0.75-1.00 | 0.60-0.90 | 0.60-0.90 | 2.00 | 0.3 - 0.9 | Min 0.20 |
| P | Max 0.035 | Max 0.04 | Max 0.04 | 0.2 | | |
| S | Max 0.04 | Max 0.05 | Max 0.05 | Max 0.15 | | |
| Si | 0.15-0.30 | | | 1.00 | Max 0.5 | Max 0.10 |
| Cr | 0.80-1.10 | | | 17.0-19.0 | Max 0.1 | |
| Mo | 0.15-0.25 | | | | | |
| Ni | | | | 8.0-10.0 | | Max 0.0050 |
| Cu | | | | | 3.8 - 4.9 | Max 0.050 |
| Fe | | | | | Max 0.5 | Max 0.0050 |
| Mg | | | | | 1.2 - 1.8 | |
| Ti | | | | | Max 0.15 | |
| Zn | | | | | Max 0.25 | 0.60 - 1.4 |
| Al | | | | | | 2.5 - 3.5 |
| Ca | | | | | | Max 0.040 |

# Appendix B

# HYS's Matlab code

Here, it is presented the Matlab code of the elastic-plastic cyclic model presented in Chapter 3.

## B.1 MATLAB – Main Axial Routine

```
clear all;

global A B C D

global P1 P2 P3 P4 P5 P6

strain = csvread('Load incre 1 ciclo axial.csv');

data=zeros(length(strain(:)),5);

% FLAG if equal to -1 is going down, if equal to 1 is rising, if equal to 0 is a turn-point
% DATA = stress — strain — flag — backbone field — strain to hysteresis

for n=1:length(strain(:))

data(n,2)=strain(n);

end

for n=1:length(strain(:))-1

if strain(n+1)-strain(n)>0

flag=1; data(n,3)=1;

else

flag =-1; data(n,3)=-1;

end

end
```

```
data(length(strain(:)),3)=flag;
% Turn Points
i=1;
while i < length(strain(:))
if sign(data(i,3))+sign(data(i+1,3))==0
data(i+1,3)=0;
end
i=i+1;
end
% Backbone Field
rp=0;
for n=1:length(strain(:))
if data(n,3)>0 && data(n,2)>= rp
data(n,4)=1;
elseif data(n,3)==0 && data(n,2)>rp
rp = data(n,2);
data(n,4)=2;
end
end
rp=0;
for n=1:length(strain(:))
if data(n,4)==2 && data(n,2)>=rp
rp=data(n,2);
end
data(n,5)=rp;
end
for n=1:length(strain(:))
Point(data(n,2));
if data(n,4)==1 || data(n,4)==2
```

data(n,1)=P1;

end

Point(data(n,5));

if data(n,3)==-1 && data(n,4)==0

P=polyfit([data(n,5); P2; 0;-data(n,5)],[P1; 0; P3;P4],3);

$data(n,1) = P(1) * data(n,2)^3 + P(2) * data(n,2)^2 + P(3) * data(n,2) + P(4);$

end

if data(n,3)==0 && data(n-1,3)==1

P=polyfit([data(n,5); P2; 0;-data(n,5)],[P1; 0; P3;P4],3);

$data(n,1) = P(1) * data(n,2)^3 + P(2) * data(n,2)^2 + P(3) * data(n,2) + P(4);$

end

if data(n,3)==1 && data(n,4)==0

P=polyfit([-data(n,5); P5; 0;data(n,5)],[P4; 0; P6; P1],3);

$data(n,1) = P(1) * data(n,2)^3 + P(2) * data(n,2)^2 + P(3) * data(n,2) + P(4);$

end

if data(n,3)==0 && data(n-1,3)==-1

P=polyfit([-data(n,5); P5; 0;data(n,5)],[P4; 0; P6; P1],3);

$data(n,1) = P(1) * data(n,2)^3 + P(2) * data(n,2)^2 + P(3) * data(n,2) + P(4);$

end

end

plot(data(:,2),data(:,1));

## B.2 MATLAB – Main Shear Routine

clear all;

global P1 P2 P3 P4 P5 P6

strain = csvread('PS 0.4 2ciclos.csv');

data=zeros(length(strain(:)),5);

% FLAG if equal to -1 is going down, if equal to 1 is rising, if equal to 0 is a turn-point
% DATA = stress — strain — flag — backbone field — strain to hysteresis

```
for n=1:length(strain(:))
data(n,2)=strain(n);
end
for n=1:length(strain(:))-1
if strain(n+1)-strain(n)>0
flag=1; data(n,3)=1;
else
flag =-1; data(n,3)=-1;
end
end
data(length(strain(:)),3)=flag;
% TurnPoints
i=1;
while i < length(strain(:))
if sign(data(i,3))+sign(data(i+1,3))==0
data(i+1,3)=0;
end
i=i+1;
end
% backbone field
rp=0;
for n=1:length(strain(:))
if data(n,3)>0 && data(n,2)>=rp
data(n,4)=1;
elseif data(n,3)==0 && data(n,2)>rp
rp = data(n,2);
data(n,4)=2;
end
end
```

rp=0;

for n=1:length(strain(:))

if data(n,4)==2 && data(n,2)>=rp

rp=data(n,2);

end

data(n,5)=rp;

end

for n=1:length(strain(:))

Spoint(data(n,2));

if data(n,4)==1 || data(n,4)==2

data(n,1)=P1;

end

Spoint(data(n,5));

if data(n,3)==-1 && data(n,4)==0

P=polyfit([data(n,5); P2; 0;-data(n,5)],[P1; 0; P3;P4],3);

$data(n,1) = P(1) * data(n,2)^3 + P(2) * data(n,2)^2 + P(3) * data(n,2) + P(4);$

end

if data(n,3)==0 && data(n-1,3)==1

P=polyfit([data(n,5); P2; 0;-data(n,5)],[P1; 0; P3;P4],3);

$data(n,1) = P(1) * data(n,2)^3 + P(2) * data(n,2)^2 + P(3) * data(n,2) + P(4);$

end

if data(n,3)==1 && data(n,4)==0

P=polyfit([-data(n,5); P5; 0;data(n,5)],[P4; 0; P6; P1],3);

$data(n,1) = P(1) * data(n,2)^3 + P(2) * data(n,2)^2 + P(3) * data(n,2) + P(4);$

end

if data(n,3)==0 && data(n-1,3)==-1

P=polyfit([-data(n,5); P5; 0;data(n,5)],[P4; 0; P6; P1],3);

$data(n,1) = P(1) * data(n,2)^3 + P(2) * data(n,2)^2 + P(3) * data(n,2) + P(4);$

end

end

plot(data(:,2),data(:,1));

## B.3 MATLAB – Axial Points Routine

function [P1, P2, P3, P4, P5, P6]= Point(x)

global P1 P2 P3 P4 P5 P6

% x is the total strain % P1 is also the backbone

$P1 = 1612.48253449885 * x^7 - 9001.65583509937 * x^6 + 18990.5020952381 * x^5 - 18708.7282776579 * x^4 + 8547.57549175112 * x^3 - 1813.33571350405 * x^2 + 563.137085626194 * x - 4.76156172801138;$

% point 2 ( max error < 1% )

$P2 = -5.61728763324252 * x^7 + 31.310215828382 * x^6 - 66.8588782668116 * x^5 + 67.9999455558678 * x^4 - 33.1600903362105 * x^3 + 7.5210194883675 * x^2 - 0.675107654745615 * x + 2.15930065232407E - 02;$

% point 3 ( max error < 1% )

$P3 = 3205.96736505311 * x^7 - 16533.1719376398 * x^6 + 32943.737525031 * x^5 - 31603.0892036718 * x^4 + 14851.7963251929 * x^3 - 3297.00442656992 * x^2 + 293.317956033942 * x - 9.28864060310319;$

% point 4 ( max error < 1% )

if x<= 0.7

$P4 = -1724.51736010434 * x^4 + 2666.5055163261 * x^3 - 1029.0277569031 * x^2 - 282.021113164475 * x - 4.70001569608806;$

elseif x>0.7 && x<=1.4

$P4 = 3796.52087217134 - 4066.94784209075 * log(x) - 10980.616334377 * exp(-x);$

end

% point 5 ( max error < 1% )

if x<= 0.9

$P5 = -0.746391184235674 * x^5 + 3.61699194757608 * x^4 - 4.14317437186328 * x^3 + 1.45532858067314 * x^2 - 0.241326691061546 * x + 6.1460339490965E - 03;$

elseif x>0.9 && x<=1.4

$P5 = -0.226693656177561 - 0.774834235247346 * log(x)/x^2;$

end

% point 6 ( max error < 1% )

if x<=0.9

$P6 = 1350.68526517161 * x^5 - 3380.897469962 * x^4 + 2774.52155069743 * x^3 - 848.438040596614 * x^2 + 122.960739463697 * x - 3.24204992256947;$

elseif x>0.9 && x<=1.4

$P6 = 5779.51246461137 - 5643.82166319652 * log(x) - 15623.6005797354 * exp(-x);$

end

end

## B.4 MATLAB – Shear Points Routine

function [P1, P2, P3, P4, P5, P6]= Spoint(x)

global P1 P2 P3 P4 P5 P6

$P1 = -22.5107143654461 * x^{10} + 201.854998204418 * x^9 - 644.893587525743 * x^8 + 589.807792293021 * x^7 + 1430.93790923576 * x^6 - 4529.29434921615 * x^5 + 5129.10090675619 * x^4 - 2689.65237023041 * x^3 + 476.038605716444 * x^2 + 176.445398314215 * x + 3.59424205647902E - 02;$

$P2 = -0.121507127994832 * x^{10} + 1.5546297103227 * x^9 - 8.24383378545519 * x^8 + 23.7164284672066 * x^7 - 40.4660019459346 * x^6 + 41.9734744869975 * x^5 - 26.1944602437782 * x^4 + 9.42900640243149 * x^3 - 1.45961323569132 * x^2 + 4.50637543251064E - 02 * x - 2.75984233608916E - 04;$

$P3 = 24.6533431726864 * x^{10} - 292.72308712462 * x^9 + 1480.86238369206 * x^8 - 4168.0553676122 * x^7 + 7143.84701291341 * x^6 - 7660.14965960386 * x^5 + 5063.48496388391 * x^4 - 1917.81664050227 * x^3 + 312.436816613724 * x^2 - 11.2831886725052 * x + 9.35899650991619E - 02;$

$P4 = 42.5384244894889 * x^{10} - 426.986141656398 * x^9 + 1724.3989168212 * x^8 - 3465.80144527909 * x^7 + 3210.12678961038 * x^6 - 94.8787618819251 * x^5 - 2374.90919675872 * x^4 + 1815.40465011995 * x^3 - 378.091432395103 * x^2 - 172.009816070145 * x - 0.14752603498711;$

$P5 = 0.585030844902098 * x^{10} - 6.32353758132731 * x^9 + 28.8864133619076 * x^8 - 72.4416286562295 * x^7 + 108.334936430662 * x^6 - 98.2293234426468 * x^5 + 52.6799364225525 * x^4 - 15.6409570130916 * x^3 + 1.8745706258009 * x^2 - 8.52533212031502E - 02 * x - 7.63411843645122E - 04;$

$P6 = -64.2641216179107 * x^{10} + 715.849413123197 * x^9 - 3389.28366128172 * x^8 + 8879.85897034258 * x^7 - 14032.5004541184 * x^6 + 13658.7630212986 * x^5 - 8000.47811708188 * x^4 + 2591.33563475175 * x^3 - 339.867237908221 * x^2 + 18.5072444857954 * x + 9.67429174377977E - 02;$

end